CRANFIELD UNIVERSITY

D. D. HARWIG

ARC BEHAVIOUR AND METAL TRANSFER OF THE VP-GMAW PROCESS

SCHOOL OF INDUSTRIAL AND MANUFACTURING SCIENCE

PhD Dissertation

2003

CRANFIELD UNIVERSTIY

SCHOOL OF INDUSTRIAL AND
MANUFACTURING SCIENCE

PhD Dissertation

Academic Year 2000-3

Dennis D. Harwig

ARC BEHAVIOUR AND METAL TRANSFER OF THE VP-GMAW PROCESS

Supervisor S. Blackman

ABSTRACT

This project evaluated the metal transfer behaviour of the variable polarity (VP) GMAW process. Analysis was performed using high speed video that was synchronised with high speed data acquisition. Melting rate measurements were found to be very dependent on current waveform, polarity, and droplet size, and metal transfer if it occurred, for each waveform period. The transient conditions of current waveform and metal transfer produced rapid changes in arc behaviour which influenced the melting at the electrode tip and growing droplet.

The concentrated melting theory was developed to explain the significant increase in electrode extension burnoff and droplet growth rate that occurred at short EN time as a function of current, and during EP peak pulse when the pre-pulse droplet volume was small. The highest electrode extension burnoff and droplet growth rate occurred when the arc was permitted to climb over the solid electrode tip producing rapid concentrated melting. Likewise, large molten droplets were found to promote a negative electrode extension burnoff and a decreased droplet growth rate. The arc rooted on large droplets providing additional heating but limited electrode melting.

The droplet burnoff rate (DBR) method was developed and found to yield good experimental measurements for the arc and resistive heating coefficients used in a 2^{nd} order melting rate equation developed for a complex waveform process, like VP-GMAW. For the EN period, the EN time affected the melting rate as a function of EN current. The greater melting rate that occurred at low EN time was measured by the changes in the resistive heating coefficient. Concentrated arc melting of the electrode extension at low EN time caused the slope of the burnoff diagram to increase, which represented the resistive heating coefficient. The melting rate of the EP pulse was related to the pre-pulse droplet volume. Large pre-pulse droplets decreased the arc heating coefficient, which could be negative, which meant the electrode extension was increasing and the arc length was decreasing in that waveform period.

VP-GMAW power supplies offered stable operation for welding sheet structures on both carbon steel and stainless steel. Higher travel speeds were required as the %EN of the waveform increased to produce acceptable constant deposit area fusion. Welding speeds were up to 300% higher with VP-GMAW compared to the GMAW-P process when welding lap joints on 1.8 mm thick material with a 1.8 mm gap. VP-GMAW heat input was up to 47% less than GMAW-P for the same melting rate.

TABLE OF CONTENTS

LIST OF TABLES

LIST OF FIGURES

LIST OF APPENDICES

LIST OF ABBREVIATIONS

AC-GMAW	alternating current gas metal arc welding
AIP	average instantaneous power
BR	burnoff rate
BDT	burnoff diagram technique
CCD	charged coupled device
CTWD	contact tip-to-work distance
CV	constant voltage
DAQ	data acquisition
DBR	droplet burnoff rate method
e	electron charge
EN	electrode negative
EP	electrode positive
f	frequency
FET	field emission transistors
F_L	electrode extension heating factor
GMAW	gas metal arc welding
GMAW-P	pulse gas metal arc welding
H	heat in joules
H_o	heat per unit volume to melt a drop
HI	heat input
Hz	Hertz
HSV	high speed video
i_e	thermionic current
i_p	positive ion current
I	current
I_{EPB} , I_b	current electrode positive background
I_{EPP} , I_p	current electrode positive peak
I_-	current electrode negative
I_+	current electrode positive
j	current density
k	Boltzmann constant
L	electrode extension
MR	melting rate
MR_{ac}	melting rate alternating current
MR_{dc}	melting rate direct current
MR_{vp}	melting rate variable polarity
OCV	open circuit voltage
P	power
PWM	pulse width modulation
q_e	heat loss to electrode
RMS	root mean square
SAW	submerged arc welding
SMAW	shielded metal arc welding
t	thickness
t_{EN}, t_-	time electrode negative

t_{EP}, t_+	time electrode positive
t_{EPB}, t_b	time electrode positive background
t_{EPP}, t_p	time electrode positive peak
T	temperature
TS	travel speed
VOF	volume of fluid
VP-GMAW	variable polarity gas metal arc welding
V	voltage
V_d	droplet volume
V_D	droplet volume growth rate
V_{pp}	pre-pulse droplet volume
WFS	wire feed speed
α ,C_a	arc heating coefficient
β ,C_R	resistive heating coefficient
γ	pulse burnoff factor
η	arc process efficiency
ϕ	work function
Δx	electrode extension burnoff

1.0 INTRODUCTION

Gas metal arc welding (GMAW) technology has advanced considerably over the past two decades due to the development of microprocessor-controlled, solid-state power supplies. The most common solid-state power supplies include secondary choppers, series regulators, and inverters. Inverters allow rapid changes in the electrical waveform, which controls the metal transfer dynamics. Currently, power supplies are designed for constant voltage (CV) GMAW, pulse GMAW (GMAW-P), and pulse short circuit GMAW (Ref. 1-4) using CV and/or constant current control, and more recently variable polarity (VP) GMAW (Ref. 5-11).

Microprocessor controlled inverter power supplies offer control of the current and voltage waveform at very high speeds. There are numerous waveforms available for pulse GMAW where the ability to vary waveform magnitude and shape within a pulse offer unlimited choices. Current pulsing permits spray transfer welding at mean currents below the globular-to-spray transition current, providing spatter-free welds on light gauge materials and out-of-position welding applications. Pulse parameter algorithms are readily developed throughout the power supply industry to permit synergic (one knob) control of pulse parameters as a function of wire feed speed. Adaptive pulse GMAW power supplies have been developed that sense arc instability due to short circuits and provide corrections through algorithm control to regain stability (Ref. 1-4).

Microprocessor control technology has also permitted the development of practical VP-GMAW power supplies (Ref. 5-11). This process takes advantage of the large increase in melting rate that occurs when the GMAW process operates in the electrode negative (EN) polarity mode. The electrical waveform combines pulse GMAW droplet transfer technology, the ability to pinch and propel drops associated with electrode positive (EP) polarity, with the low heat input and high deposition of EN polarity. The net result is the ability to weld thin gauge structures with very low heat inputs, large gaps, minimal spatter, and higher welding speeds.

The majority of VP-GMAW power supply technology is from Japan and was introduced in 1988 (Ref. 5-7). Since the early 1990's, several hundred power supplies have been sold in the U.S. Unfortunately, many industrial users do not understand the benefits of this technology since limited research has been published in the U.S. (Ref. 3, 4, 10, 11). This has deterred wide-scale implementation of VP-GMAW throughout industry. The power supplies offered by the Japanese manufacturers have pre-programmed algorithms and are presently limited to welding of mild steel, stainless steel and aluminium at currents up to 350 amps where the benefit has been the welding of thin gauge structures with large gaps (Ref. 10).

The metal transfer process for VP-GMAW begins with droplet formation in the EN period where large droplets form on the end of the electrode. The waveform switches to the EP background period to maintain the arc based on the wire feed speed and melting rate balance. The EP peak period is used to transfer the droplets by using a high current pulse which squeezes the droplet off the electrode tip forming a drop. The drops

transfer across the arc into the weld pool. The VP-GMAW waveform can be designed to provide a range of heat input for a given wire feed speed, thus allowing optimization of the travel speed for different weld deposit size applications.

There are many factors the affect the droplet formation and transfer process which are not understood. As will be described in this dissertation, the behaviour of VP-GMAW welding arcs and metal transfer has not been published in the literature.

The objectives of this project were to determine the arc and metal transfer behaviour of the VP-GMAW process. Measurement techniques were developed to permit systematic study of the relationships between VP-GMAW waveform to melting rate, droplet growth, and drop transfer. A state-of-the-art VP-GMAW power supply was evaluated in great detail on steel using 90% argon -10% CO_2 mixed gas. A new melting rate measurement technique, named the Droplet Burnoff Rate (DBR) method, was developed using synchronized high-speed video and data acquisition. Here the electrode melting and droplet growth was measured closely and related to the exact waveform parameter and arc behaviour. These measurements accounted for the change in electrode extension during the droplet formation process, rather than assuming a constant electrode extension like prior research. This investigation showed that the melting rate potency of each waveform period was dependent on how the arc concentrates on the growing droplet and / or the electrode tip. Measurements using this technique are believed to produce accurate second order relationships based on the melting rate equation developed by Lesnewich (Ref. 12, 13). An advanced melting rate equation was developed for VP-GMAW by integrating Lesnewich's equation over time for one waveform period. New observations have been made relating the effects of arc behaviour to the melting rate of VP-GMAW and GMAW-P. This knowledge offers future researchers the ability to better predict melting rate based on the shape of the waveform.

In addition, a productivity benchmarking study was performed using the ARCWISE method on 1.8 mm steel and stainless steel lap joints. These tests showed that VP-GMAW offered an increase in travel speeds compared to the GMAW-P process due to the lower heat inputs for the same melting rate. The maximum travel speed was limited by the stability of the metal transfer waveform and the current capacity of the power supply.

2.0 LITERATURE SURVEY

In 1930, H.M. Hobart and P.K. Devers were issued patents 1746081 and 1746191, respectively for "Arc Welding" using a concentric nozzle with wire feed. Their invention later became known as gas metal arc welding (GMAW). The process evolved from the study of various arc welding shielding gases that started in 1926. The GMAW process became commercial in 1948 (Ref. 14). Since then, and with the development of microprocessor power supplies, the GMAW process has become widely used throughout the world. The many process variants that exist are largely based on metal transfer mode, and the development of advanced waveforms for enhanced process control.

The definition of GMAW (Ref. 14) is an arc welding process that uses an arc between a continuous filler metal electrode and the weld pool. The process is used with shielding from an externally supplied gas and without the application of pressure. The electrode can be solid metal or metal-cored, which is considered a subset of the GMAW process. Shielding can be supplied with inert gas, argon, helium, or a mixture thereof, or using reactive gas such as CO_2. Today, there are literally hundreds of possible combinations for electrode type and size, shielding gas, and power supply waveform. The process can be used in all positions to weld almost any commercially available alloy that is considered weldable.

There are many factors that affect the GMAW process. Engineers and scientist have studied electrode composition and form; shielding gases; power supply type, dynamics, and waveform; the physics of metal transfer; weld metal properties, etc. There are still many gaps on the physics, thermal dynamics and chemistry of the process associated with the gas metal arc. The literature review performed here is focused on the state-of-the-art in GMAW process with emphasis on waveform control for metal transfer. Metal transfer involves the melting of the electrode tip to form a droplet and the transfer of the drop into a weld pool. The droplets are melted from the heat generated by current flow in the electrode extension and by the arc at the electrode tip. Today, molten droplets can be transferred through short circuiting, pulse-short circuit, spray, pulse-spray, rotating spray, globular and more recently pulse-globular using the VP-GMAW process. These process modes are made possible by controlling the melting rate and metal transfer characteristics for each shielding gas and electrode type.

2.1 Principles of Operation

The GMAW process uses a consumable wire electrode that is continuously fed into a welding torch (Figure 2.1). The process is most commonly used in the semi-automatic mode where the welder initiates the process by squeezing a torch trigger. The process can easily be adapted to an automatic welding system using robots or automation. Equipment required for the process include a torch that is interfaced to a power supply, a wire feeder, electric cables for current delivery, and a hose for shielding gas delivery (Figure 2.2). The work piece is attached to the other pole of the power supply to complete the electric circuit. The current is transferred to the electrode through a contact tip on the end of the torch. The current used by the process is a function of the

wire electrode type, diameter, extension, and feed speed. The current passing through the electrode extension provides resistive preheating.

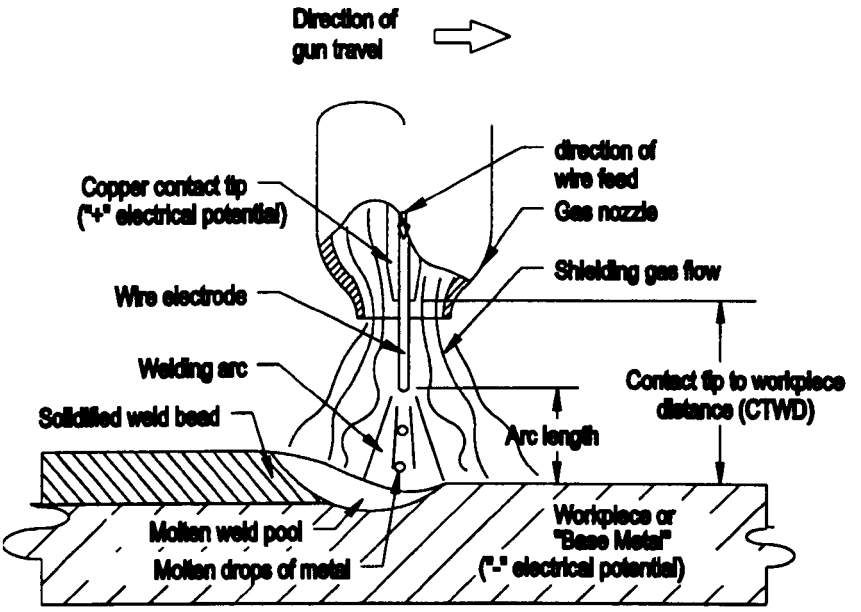

Figure 2.1 Cross-Sectional View of the Gas Metal Arc Welding Process

The voltage of the process is set to accommodate the voltage drops at the cathode, anode, electrode extension, and arc column (Ref. 15,16). Conventional GMAW uses a power supply with CV characteristics. The slope of these power supplies is matched to provide self-regulation (Ref. 14). Here, if the operator changes the torch tip-to-work distance, the resistance change in the electrode extension is matched to the slope of the power supply to maintain a constant arc length. Constant current (CC) power supplies with drooping characteristics are also used for GMAW, mostly on aluminium, where the resistance is too low in the electrode extension to provide self-regulation except for electrodes that are smaller than 1.2 mm diameter. For CC arc length control, the wire feed speed must match the current. Precise contact tip-to-work (CTWD) and current control provide stable metal transfer for constant current welding with aluminium electrodes.

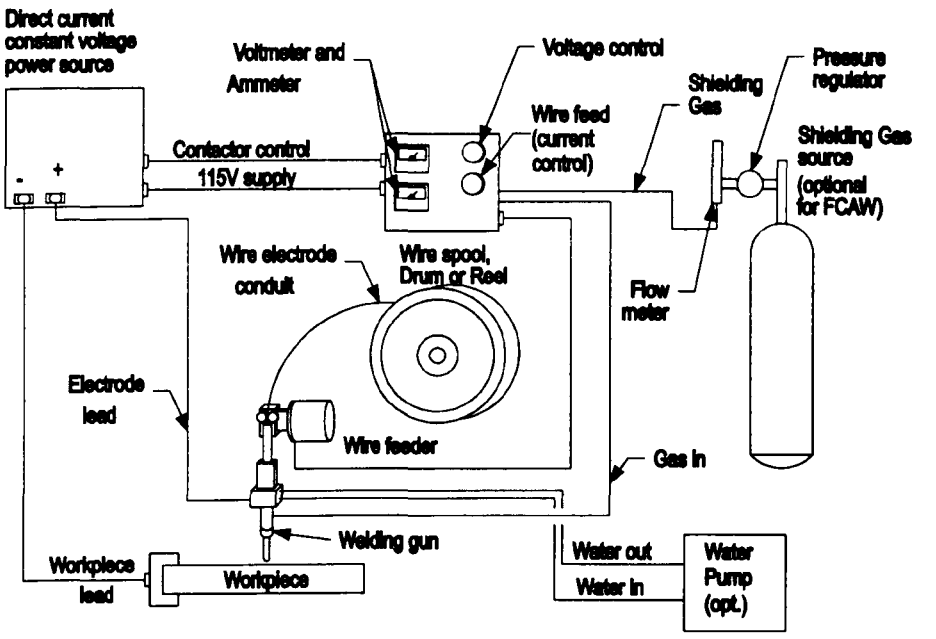

Figure 2.2 GMAW/FCAW Equipment Diagram

2.2 Arc Heating and Melting Rate Characteristics

The gas metal arc is stable when the voltage and current are matched for a given combination of electrode type, electrode extension, wire feed speed, and arc length (Ref. 12-20). The welding voltage between the contact tip and work piece can be described using an equation that accounts for the voltage drops in each region as follows:

$$V_w = V_L + V_a + V_p + V_c \tag{2.1}$$

where V_w is the welding voltage which is the sum of the voltage drops at the electrode extension, V_L, anode, V_a, arc plasma, V_p and cathode, V_c.

Cathode Heating

The voltage drop at the different arc regions varies for different welding processes. In GMAW, the cathode is a non-thermionic emitter, versus GTAW where the tungsten electrode is a thermionic emitter. Thermionic emitters are very efficient at electron emission where the voltage drop for GTAW is approximately 4.8 to 5.3 volts for a tungsten cathode (Ref. 15). The voltage drop by a thermionic cathode emitter has been represented by the following equation:

$$V_c = \left(\phi + \frac{3kT}{2e}\right) + \frac{q_e}{I} \tag{2.2}$$

where: ϕ = work function of the electrode material (volts)

q_e = heat loss to the electrode (Joules)

T = temperature of the gas (Kelvin)

$\frac{3kT}{2e}$ = thermal energy of the electrons.

Boltzmann constant, k is equal to 1.38 x 10^{-23} J/K and the electron charge, e is 1.602 x 10^{-19} coulomb. The temperature of the tungsten cathode is well below the melting point for current densities of 10^6 to 10^8 A/m^2 (Figure 2.3) used in arc welding. The figure also shows that transition metal like iron, copper, and nickel have melting points below the equilibrium temperature for the current density seen in GTAW.

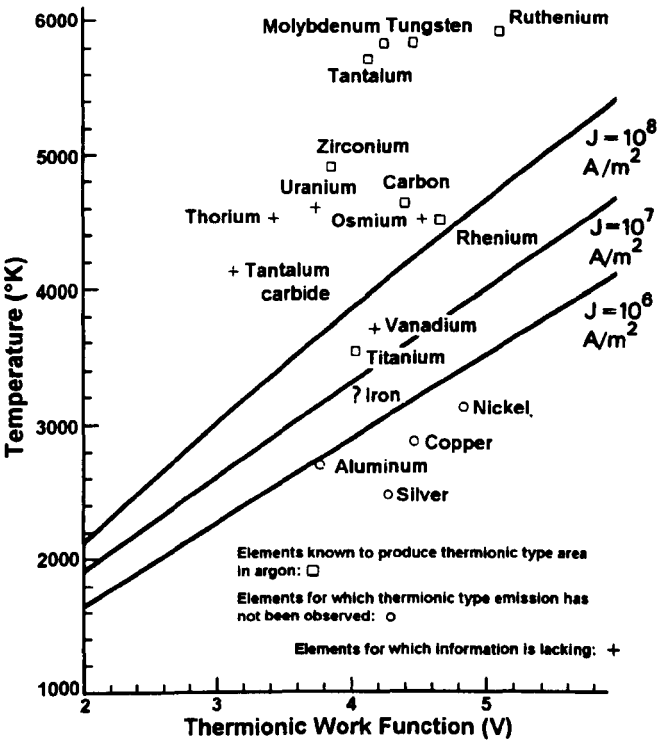

Figure 2.3 Temperature for Thermionic Emission at Various Current Density Levels (Ref. 15) (individual points show boiling point of pure elements vs. work function)

For steel cathodes, the voltage drop has been reported to vary between 10 to 20 volts during welding (Ref. 15-17, 21-26). The current flow through the cathode sheath for non-thermionic cathodes is largely due to field emission. Surface boiling and ionised gas promote a cloud (or sheath) of positive and negative charges that support current flow. As a result, the cathode supplies a large portion of the electrons needed to conduct welding current through the arc stream (Ref. 12, 15). The cathode is believed to be surrounded by a cloud of positive charged ions. These ions come from metal vapour and ionised shielding gas. The ion sheath acts to accelerate ions with an increase in energy proportional to the potential fall, V_c at the cathode surface. Ion energy is also

released at the surface when the ions become neutralised where this energy is proportional to the ionisation potential of the ion. The energy released during cathode current flow causes the surface melting and the large voltage drop. The field theory for electron emission assumes that vapour pressure may be above ambient near the cathode spot. The mechanisms for field emission are very complex and have not been simply modelled by physicists. Heating is believed to occur on a micro-scale. The very thin cathode sheath is believed to raise the voltage gradient at the cathode surface to millions of volts per cm which provides the driving force for removing electrons by field emission. Both positive ions and electrons carry current at the cathode surface. The ratio of positive ions to electrons is determined by the work function, boiling temperature, and shape and area of the cathode surface. Factors such as surface roughness, oxide films, non-metallic impurities affect the work function voltage required for electron emission.

In view of this theory, a change in work function or boiling temperature is expected to change the fraction of current carried by positive ions or electrons. A reduction in work function or increase in boiling temperature will increase the fraction of thermionic electrons at the expense of ionised gas and metal vapours and cause cathode heating effect to decrease. A simple equation to describe cathode heating H_c (Joules) was proposed by Lesnewich to account for these competing effects as follows:

$$H_c = i_p(V_c - \phi) + i_p V_i - i_e \phi \tag{2.3}$$

where: V_c = cathode fall voltage
V_i = ionisation potential
i_p = positive ion current
i_e = thermionic electron current
ϕ = work function of the electrode material (volts).

The cathode typically generates more than twice the heat of the anode for steels and other common alloys. The cathode fall voltage increases as the boiling temperature of the metal decreases since thermionic electrons are harder to emit.

The dependence of melting rate on changes in work function and boiling point has been evaluated during EN welding tests by activating the surface of the consumable electrodes which improves electron emission and reduces the cathode drop (Ref. 27, 28). Electrode surface activation decreased the melting rate for a given current. Equation 2.3 explains why the melting rate is much higher in EN welding and deeper weld penetration is achieved in EP welding when both materials (electrode and work) used at the cathode and anode are the same.

Anode Heating

Research has shown that the voltage drop at the anode varies between 3 to 5 volts for GMAW of steels (Ref. 16, 21). The anode is not believed to be a direct source of positive ions to the arc. The high temperature of the anode releases free electrons.

These electrons do not have sufficient energy to overcome the attractive forces of the anode (Ref. 12, 15). As a result, the electrons form a very thin cloud immediately about the electrode. A very steep voltage gradient develops across this region. The voltage drop is small compared to the cathode but since electrode cloud region is small, the voltage gradient is very high. Electrons are accelerated to very high velocities over this short distance developing considerable kinetic energy. The energy converts to heat at the point of impact. Additional energy is also supplied when the electrons are absorbed into the metal lattice and this energy is considered the "energy of condensation', which is represented by the thermionic electron work function of the anode material. The heat developed by these basic reactions was described by Lesnewich by the following equation:

$$H_a = c(V_a + \phi)I \tag{2.4}$$

where: H_a = heat generated by the anode reaction (J)
V_a = anode drop
ϕ = anode thermionic work function
I = welding current
c = constant.

All this heat is transferred to the anode. Some of the kinetic energy from the electrons is lost when ionising gas molecules. Heat is also lost when metal vapours boil off the anode. These reactions are considered to be a major source of positive ions in the arc. Radiation and conduction losses through the electrode and shielding gas also occur but are considered negligible. Therefore, the heat at the anode is not affected by the type of shielding gas.

A simple thermal model for electrode melting assumes that the droplets melt and detach at their melting point. The total heat content of the drops, H_o is considered constant and approximates to the heat at the melting point. Under these conditions, the heat at the anode is proportional to the wire feed speed, v. The heat developed by the melting of drops can also be used to explain (Ref. 17-20) the total heat content produced at the anode as:

$$vH_o = \left[\phi + \frac{3}{2}\frac{kT}{e} + V_a\right]j \tag{2.5}$$

where: H_o = total heat of drops (J/mm^3)
j = current density ($amps/mm^2$)
v = wire feed speed (mm/s).

This equation is similar to Equation (2.4) with additional heat from free electrons and a better relationship to electrical parameters. The total voltage drop at the anode can be determined by dividing the melting rate heat content by the current density. The current density factors the effects of electrode diameter and this simple equation assumes the heat is uniform over the electrode tip.

2.2.1 Effect of Welding Variables on Anode Melting Rate

The effects of welding variables on anode electrode heating used in GMAW were well studied by Lesnewich (Ref. 12). He performed tests which isolated the effects of electrode extension and diameter, arc length, and current to empirically determine the anode voltage drops for steel electrodes. He determined an anode heating coefficient which was a function of electrode cross sectional area by extrapolating the effects of electrode extension to zero from the data shown in Figure 2.4. This figure was for one electrode diameter and shows that melting rates increase with electrode extension at constant current and arc length. The anode heating coefficient, C_a was determined by dividing intercepts by the welding current which was found to give a constant relationship as shown by the slope in Figure 2.5. The effects of anode heating on melting rate were constant for a given electrode diameter and material, and was only affected by the current. Lesnewich defined the following simple equation to factor the effects of anode heating on melting rate, MR_a:

$$MR_a = C_a I \tag{2.6}$$

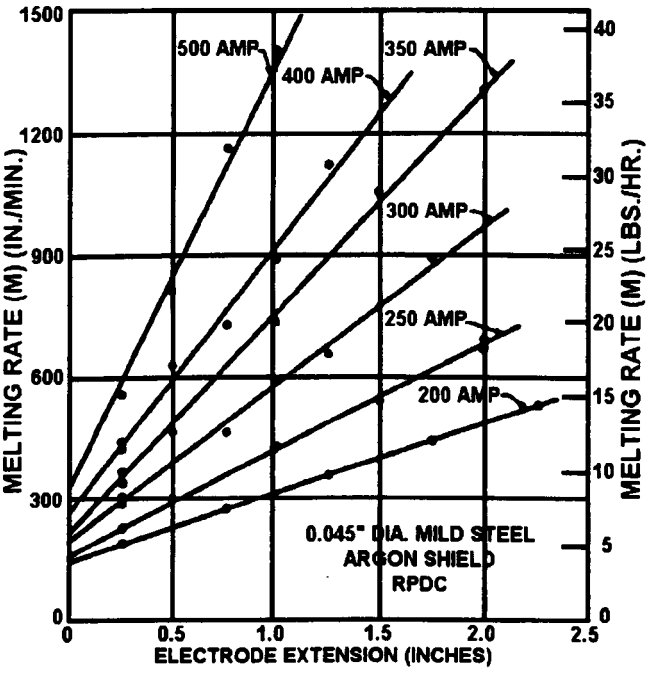

Figure 2.4 Effect of Electrode Extension and Welding Current on the Electrode Melting Rate (Ref. 12)

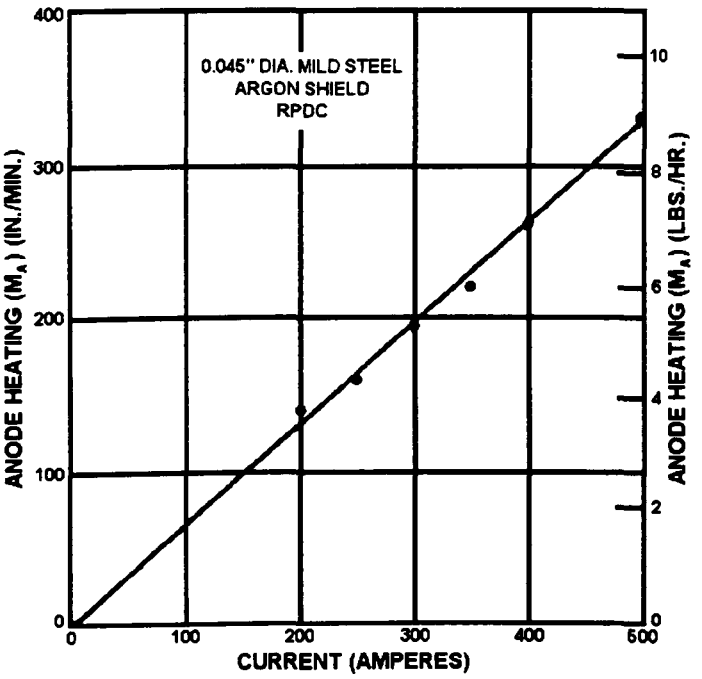

Figure 2.5 The Effect of Welding Current on Anode Heating as Measured by Melting Rate (Ref. 12)

Melting rate can be expressed in wire feed speed, which is a welding parameter, or in deposition rate by factoring wire area and density. This equation was very similar to the theoretical Equation (2.4). The slope of Figure 2.5, C_a, is therefore related to the anode voltage drop and the electrode work function. This process was repeated for several electrode diameters. The results of these tests show that the anode heating coefficient, C_a (lbs/hr amp) increased as the electrode area increased (Figure 2.6). His experiments proved that the heating at the anode was independent of other factors such as arc length and electrode extension. In addition to electrode area, changes in C_a are dependent upon the specific heat of the material, and therefore their chemistry. Anode heating effects are restricted as the electrode tip area decreases. Lesnewich noted that the data in Figure 2.6 was based on the theoretical diameter and did not include the shape of the electrode tip and the arc. The electrode tip was tapered since his tests focused on the spray mode of the process. Therefore the actual area of the electrode tip was much greater. He argued that it was this effect that gave lower values for C_a compared to data extrapolated for the AC submerged arc process shown in the same figure. The submerged arc data showed that very larger electrodes do not develop a conical shape and the arc may not envelop the tip depending on the current. The tip geometry seen in Figure 2.6(c) has been observed on very large electrodes used for gas metal arc furnace melting but this is not applicable to GMAW. For most industrial GMAW applications, the relationship defined by Equation (2.6) and values for C_a from Figure 2.6 are valid for spray transfer using argon-based gases and C_a can be related to just the electrode diameter. Here the electrode tip and arc behaviour are relatively constant over the range of electrode sizes used by industry.

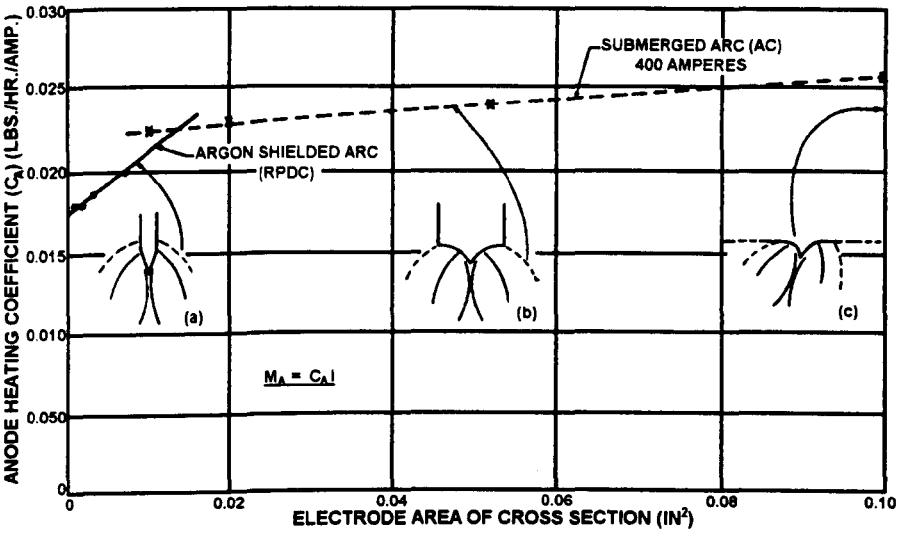

Figure 2.6 Relationship of the Coefficient of Anode Heating to the Electrode Area of the Cross Section (Ref. 12)

Lesnewich repeated many of the melting rate tests using a variety of shielding gases including helium, nitrogen, and carbon dioxide to evaluate the effects on anode heating coefficient. Shielding gas showed significant variation in metal transfer, weld soundness and bead shape, but changes to electrode melting rate were quite small and considered negligible compared to argon shielding gas. This was not surprising since the heat at the anode was due to the absorption of electrons from the arc and the source of the electrons was not a factor.

Activation coatings that change the work function of the electrode were shown to have a strong effect upon the electrode when it was in the negative pole (Ref. 27, 28). This effect was explored for EP welding too by Lesnewich (Ref. 12). According to Equation (2.4), electrode activation could affect the anode heating by changing the work function. His experiments evaluated the effects of caesium (which has a low work function) surface treated wire and found no appreciable effect on the anode work function of steel. Therefore, the heat generated by the anode drop is significantly greater than the work function.

2.2.2 Effect of Welding Variables on Cathode Melting Rate

Energy is supplied to the cathode by the acceleration of positive ions across a steep voltage gradient through the cathode sheath. As a response, the cathode releases electrons in an attempt to neutralize the arc. Cooling of the cathode occurs when electrons evaporate off the surface. As the fraction of electrons increase, the net heat released at the cathode decreases. Stabilization has been used to reduce the heat at the cathode by using rare earth elements to activate the surface of the cathode which provides more electrons to carry the current (Ref. 27, 28). In addition, argon based shielding gases that have at least 5% oxygen (or mixtures of oxygen and carbon dioxide that exceeded a critical oxidation potential) have been shown to provide arc stabilisation with EN (Ref. 29).

Lesnewich (Ref. 12) performed tests which evaluated the melting rate behaviour of EN welding and the effects of electrode activation. The melting rate relationship for EN was similar to EP in that it was directly related to current. However, activation provided by wire surface treatment or through the use of oxidizing shielding gases was found to reduce the melting rate coefficient for EN. Therefore, the melting rate due to cathode heating could be defined using Equation (2.6) except that C_c was dependent on shielding gas type, activation, and current.

Shielding gases are defined as either being inert or oxidizing. Oxidising shielding gases promote the formation of a thin iron oxide layer on the wire electrode near the tip. The thin oxide, as described by Lesnewich (Ref. 12), reduced the cathode voltage drop, and therefore the melting rate, for argon-based shielding gases that have small concentrations of either oxygen or CO_2. Neutral gases, such as helium or argon, or mixtures thereof, have not shown an effect on the activation of the negative electrode. The melting rate for the latter inert gases is the same at a given current and electrode extension. High concentrations of CO_2 or pure CO_2 were shown to increase in EN melting rate (Ref. 12). This effect was attributed to the volume fraction of dissociated CO_2 molecules providing increased positive ion bombardment across the cathode sheath.

Norrish (Ref. 29) performed tests to determine the preferred shielding gas mixtures for EN welding with 1.0 and 1.6 mm steel electrodes. Tests were performed to establish the deposition rate and arc behaviour of pure helium and argon, argon – helium mixtures, argon – O_2 mixtures, and argon – O_2 – CO_2 mixtures. There was a range of optimized Ar – O_2 –CO_2 gas mixtures which provided stable arc behaviour. His tests also showed an increase in melting rate for EN compared to EP, but the benefits were not quantified as the emphasis was on metal transfer stabilization.

Melting rate tests performed by Lesnewich showed that melting due to cathode heating was almost twice that of anode heating for the same size electrode using argon – 1% oxygen shielding gas. The melting rate due to cathode heating was linear as shown by the uppermost curve in Figure 2.7 for 0.062 in. (1.6 mm) electrodes. Characterisation of EN welding was limited by the unstable metal transfer, so his tests on this polarity were not as complete as EP. The lower curves for 0.045 in. (1.2 mm) electrodes in this figure show how surface activation can be used to lower melting rates and improve metal transfer. This electrode was considered partially activated and larger changes were observed with fully activated electrodes. The cathode heating coefficient, C_c, for the activated electrode decreased slightly at lower currents and then rapidly at currents above 300 amps (Figure 2.8). At currents above 550 amps, the melting rate with activated wire in the EN became lower than the EP wire. The changes observed were due to the electron emission characteristics, which were not only dependent on the degree of activation but also the welding current. The current changes the thermal distribution at the electrode tip. Electrode extension changes also affect the thermal distribution and the cathode heating coefficient, C_c. Lesnewich found an increase in electrode extension caused a decrease in cathode heating. The amount of this decrease was also dependent on the current. He did not elaborate on this relationship but concluded that calculations for EN melting rate are far more complex than EP.

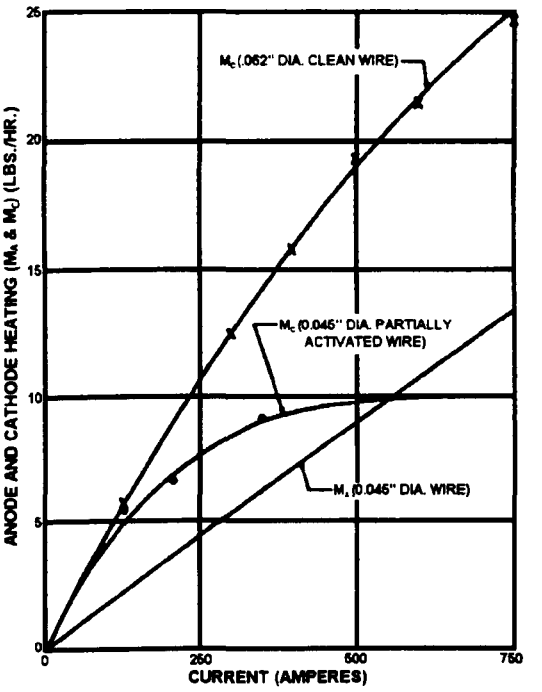

Figure 2.7 Dependence of Melting Rate Due to Cathode and Anode Heating on the Magnitude of Welding Current (Ref. 12) (mild-steel electrode, argon + 1% oxygen shield)

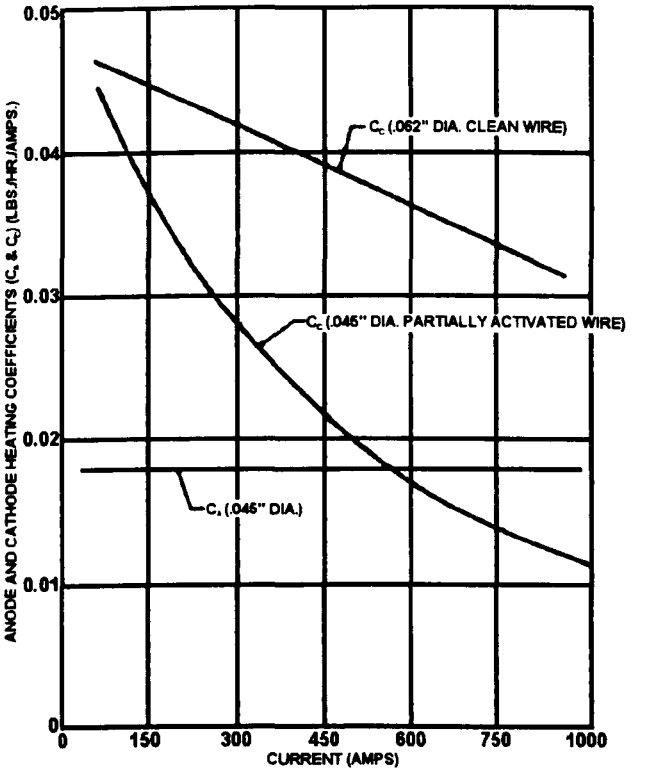

Figure 2.8 Change in the Cathode-Heating Coefficient Due to the Magnitude of Welding Current (Ref. 12) (mild-steel electrode, argon + 1% oxygen shield)

To summarise, Lesnewich found that cathode heating was similar to anode heating in that the former approaches a linear relationship to current on very clean (non-activated) wires in inert gas. Surface activation with alkali, alkali-earth, and rare earth metals produce a non-linear melting rate relationship to current. Activation is also provided by the use of oxidizing shielding gases, which could change the melting rate up to 10%. A non-linear relationship existed between cathode heating and electrode extension, but the departure from linearity was far less than its dependence on current. Wire diameter was believed to have an effect on cathode heating but no relationships were developed.

The same thermal model for electrode melting described in Equation (2.5) for anode heating can be applied to cathode heating. Again, the heat content of the drops, H_o, is considered constant and approximates to the heat at the melting point. Under these conditions, the heat at the cathode is proportional to the wire feed speed, v. Heat from thermionic emission causes a reduction in melting rate as described above and cools the electrode. The total heat content produced at cathode electrodes (Ref. 17) may be written as:

$$vH_o = \left[V_c - \phi + \frac{3}{2}\frac{kT}{e}\right]j \tag{2.7}$$

2.2.3 Effects of Electrode Extension on Melting Rate

In the electrode extension, the voltage drop is proportional to the resistance in the electrode extension times I as follows:

$$\begin{aligned} V_L &= IR \\ R &= \rho L/A \end{aligned} \tag{2.8}$$

This is Ohms law which needs no explaining where the resistance in the electrode extension, R is proportional to the resistivity, ρ, times the electrode extension length, L, divided by the wire cross sectional area, A. Resistivity is a function of temperature, which varies along the electrode extension from room temperature to the melting point at the electrode tip. Resistivity is also a functional of alloy and prior metallurgical history. The voltage drop in the electrode extension times the welding current determines the heating of the electrode extension and is given by:

$$H_R = \rho\frac{L}{A}I^2 \tag{2.9}$$

Longer electrode extensions provide more heating and increase the melting rate for a given current. Likewise, smaller electrodes increase the heating at constant current due to decreased cross section area.

The actual contribution to electrode melting by the electrode extension was determined by Lesnewich by subtracting the anode heating melting rate in Figure 2.5 from Figure

2.4 as a function of current. The results of these calculations are shown in Figure 2.9. The linearity of Figure 2.9 was surprising to Lesnewich who concluded that for this to occur the average temperature and resistance must be constant in different electrode extensions. He did notice a deviation from this behaviour in extremely long electrode extensions and high currents where a more exponential temperature profile was developed, but these values were not practical for welding. The fact that deviations from linearity did not occur over electrode extensions less than 2 in. proved that the electrode temperature, on average, was the same for each current. The reason for this behaviour was that wire feed speed was increased to maintain the melting rate and arc length. At constant current, wire feed speed is increased as electrode extension is increased to maintain the melting rate so the time each element of wire spends in the electrode extension is about the same.

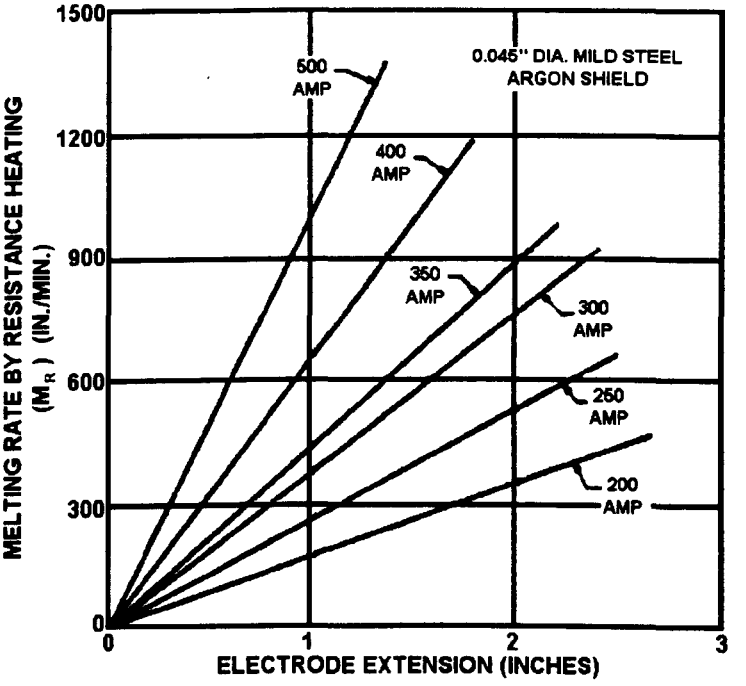

Figure 2.9 Effect of Welding Current and Electrode Extension on the Electrode Melting Rate Due to its Electrical-Resistance Heating (Ref. 12)

The melting rate achieved by different electrode extensions was found to be dependent on current as shown in Figure 2.9. The relationship to current was not linear since the heating was by the current squared which causes the slope of each line in Figure 2.9 to change with current. He determined the exact melting rate relationship for electrode extension heating by plotting the results on a logarithmic scale (Figure 2.10). From here, the resistive heating coefficient, C_R, was determined which was 42.1 x 10^{-4} (lbs/hr in amps^2) for this data using 0.045 in. electrodes. A simplified equation for resistive heating melting rate was developed as follows:

$$MR_R = C_R L I^2 \tag{2.10}$$

The units for C_R are expressed in terms of deposition rate (or wire feed speed) per inch amp squared. For this example, the units were in lb/hr in amp^2. The resistance was dependent on electrode diameter so a different constant was required for each electrode type and size. Lesnewich solved the relationship for the effects of wire diameter for steel electrodes where the following equation was determined:

$$MR_R = \frac{3.68x10^{-8}}{A^{1.26}} LI^2 (lb./hr.) \tag{2.11}$$

The equation shows that the resistive heating coefficient has the units of resistivity when the equation is in this form. However, Lesnewich noted that the exponential relationship to wire area deviates from the theoretical equation shown in Equation (2.9). This deviation was believed to be due to variances in the actual temperature distribution and, hence, average resistance with different size electrodes.

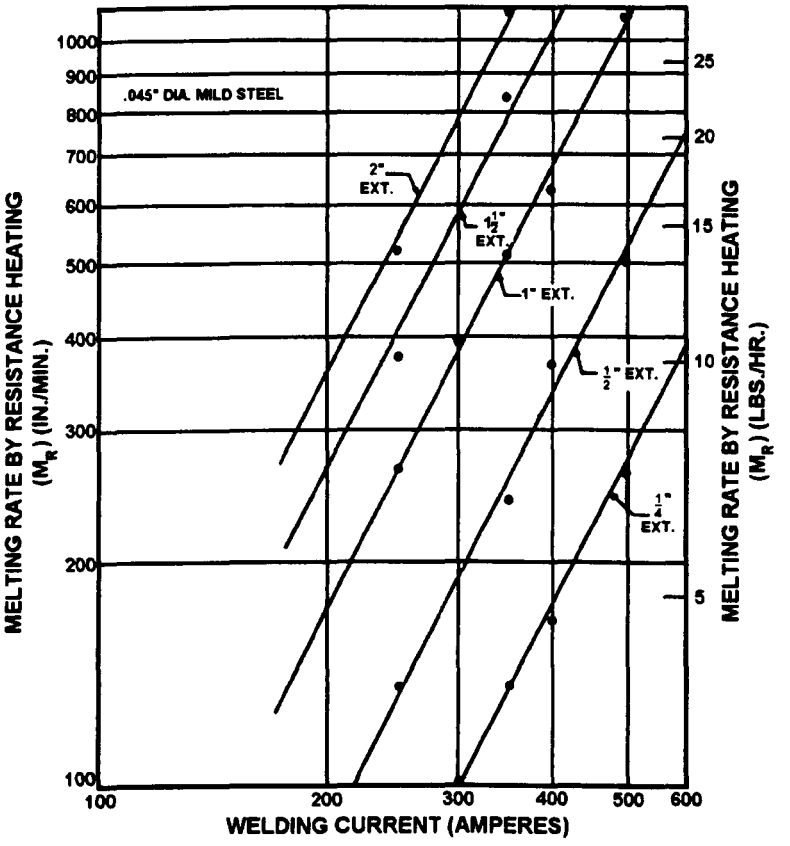

Figure 2.10 Effect of Welding Current and Electrode Extension on the Electrode Melting Rate Due to its Electrical-Resistance Heating (Ref. 12)

2.2.3.1 Electrode Wire Heating in Terms of Welding Parameters

Twenty years later, Halmoy performed tests that complemented Lesnewich's theory by measuring the actual resistivity, ρ, in the electrode extension (Ref.19). The relationship between resistance and energy required to heat the electrode extension was determined

instead of the relationship to temperature. This approach simplified the experiments. His method involved passing current through a short piece of wire while recording the voltage and current as a function of time. The energy was proportional to the time integral $\int VI\,dt$ and the resistivity was proportional to V/I by factoring electrode extension parameters. This relationship was developed for mild steel, Si-Mn steel, and stainless steel (Figure 2.11). The unique finding of these tests was that the resistivity was almost constant for all three materials above energy levels of approximately 4 J/mm^3, which corresponds to the resistivity transition point of 800°C, up to the melting point.

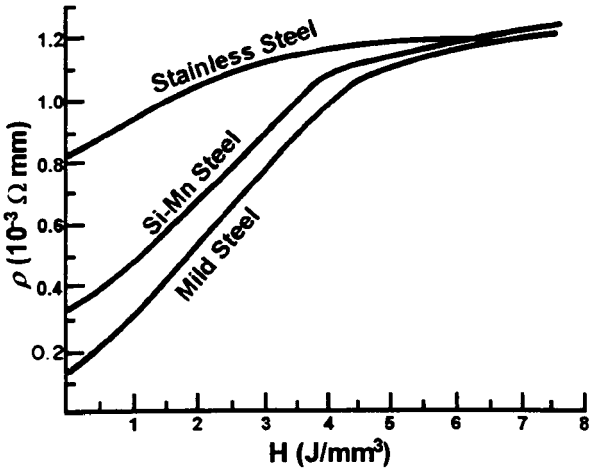

Figure 2.11 The Resistivity of Some Steel Wires as Functions of the Specific Heat Content (Ref. 19)

Halmoy developed an analytical equation to predict the heat produced in the electrode extension based on these resistivity measurements and the welding parameters as follows:

$$H_{oL} = \rho_L \frac{Lj^2}{v} + b \qquad (2.12)$$

Where: H_{oL} = Resistive heat content (J/mm^3)
ρ_L = Resistance (Ω mm)
L = electrode extension
j = current density (A/mm^2)
v = wire feed speed (mm/s)
b = Heat content constant (intercept from Figure 2.12)

Figure 2.11 shows that heat content H_{oL} caused by resistivity was a nonlinear function of Lj^2/v at lower temperature. The linear equation shown above is valid for high values of energy greater than 4 J/mm^3 where resistance is constant, like near the electrode tip in GMAW. Since this equation used a constant resistivity, ρ_L, the constant b was used to factor the heat developed from room temperature as shown in Figure 2.12. The

constant, b, was dependent upon room temperature resistivity, and was material specific. Steel alloys with low room temperature resistivity had large b values. Each alloy studied by Halmoy had a different b value. For all three alloys shown in Figure 2.11, the resistivity, ρ_L was 1.2 x 10^{-3} Ωmm at the electrode tip near the melting point.

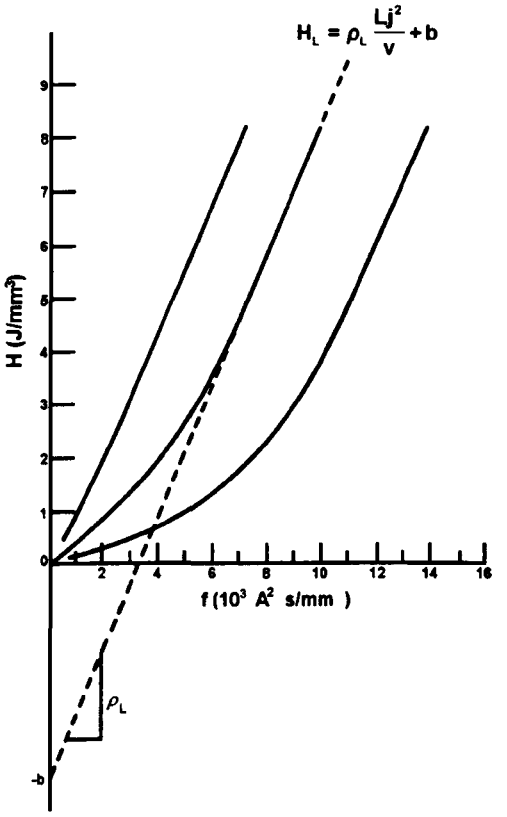

Figure 2.12 The Resistive Heat Content as a Function of f = $\int dH/\rho$ (Ref. 19)

2.2.4 Other Melting Rate Factors

The arc column is defined as the part of the arc that is located between the cathode and anode. It is considered electrically neutral in that there are an equal number of negative and positive electric charged carriers. The arc temperature determines many properties of the arc column including the degree of ionisation and dissociation of the shielding gas if it is diatomic. The voltage drop in the arc column is related to the arc length and the resistance of the plasma column, which is non-linear. Different shielding gases change the heat field above the weld pool due to differences in ionisation potential and thermal conductivity, and have been shown to have a strong effect on the weld nugget area at constant current, arc length, and travel speed. Tests performed by researchers (Ref. 12, 17, 18, 30, 31) have shown that the type of shielding gas and arc length did not affect the melting rate in the EP mode. Travel speed and arc length tests were also performed by Lesnewich and he found no effect from these variables on melting rate even though the weld pool size varied significantly with travel speed and arc length. The weld nugget size has been shown to be directly related to welding heat input, travel speed, and process efficiency, which factors how much energy is absorbed by the work piece.

2.2.5 General Melting Rate Equations

Based on the extensive work performed by Lesnewich, a general form for the melting rate equation has been established and used extensively since his initial publication in 1958. The general form of the melting rate equation was based on combining the anode (or cathode) heating as per Equation (2.6) with resistive heating as per Equation (2.10) as follows:

$$MR = C_a I + C_R L I^2 \tag{2.13}$$

This equation has been widely used to characterise CV GMAW processes. Today, modern power supplies based on inverter technology permit the use of waveform controlled GMAW processes. The most notable is the pulse GMAW process, here-in referred to as GMAW-P. In addition, there are pulse-short circuit, AC, and VP-GMAW processes, to name a few, that have unique melting rate relationships based on the effects of current waveform. Lesnewich's equation can be applied to these waveform-based processes by integrating the MR equation current waveform over time.

A more physical general model has been proposed by Halmoy (Ref. 18-20). His model was physically intuitive since it used the temperature dependent resistivity based on Equation (2.12) and wire electrode dimensions. A constant value for the resistivity of steel was determined for energy above 4 J/mm^3 and an energy offset constant was used to account for changes in resistance from room temperature for each material. Halmoy's model was based adding the heat content, H_o in (J/mm^3) in the electrode extension and anode using the following equation:

$$H_{oL} + \phi_m \frac{j}{v} = H_o \tag{2.14}$$

The melting potential, ϕ_m in volts describes the potential drop at the anode surface used for melting. Substituting the linearised expression Equation (2.12) into this equation yields a useful linearised equation for wire feed speed:

$$v = \frac{1}{H_o + b}\left(\phi_m j + \rho_L L j^2\right) \tag{2.15}$$

The mass melting rate (or deposition rate) in kg/hr can be calculated by factoring mass density, m in kg/mm^3:

$$M = \frac{m}{H_o + b}\left(\phi_m I + \rho_L \frac{L}{A} I^2\right) \tag{2.16}$$

For standard carbon steel wire electrode, the numerical values by experiments were:

H_o= 11.1 J/mm^3
b = 4.0 J/mm^3
ϕ_m = 3.5 volts
ρ_L = 1.2x10^{-3} ohm mm

Halmoy's equations were only valid when the ohmic heating in the electrode extension was not too small as the case with most industrial GMAW application. By solving for H_o, b, ϕ, and ρ_L, the validity and range of his model was determined and shown graphically (Figure 2.13). Numerically, his model requires H_L to be greater than 4 J/mm^3. In this regime, the accuracy of Equation (2.15) was verified for several electrode diameters and different carbon steel electrodes. The latter mainly affects the resistive heating constant, b. For the common solid steel electrodes, b does not vary much. Equation (2.15) has the same heating dependency as Lesnewich's Equation (2.13) where separate factors are used for arc and resistive heating.

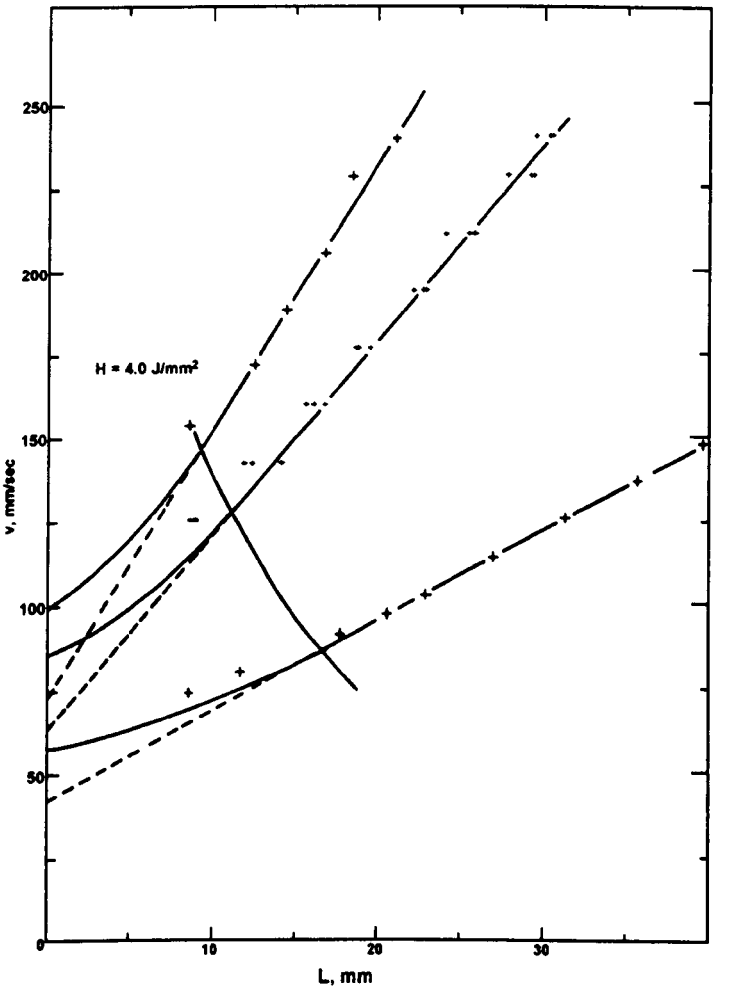

Figure 2.13 Wire Feed Speed as a Function of Extension and Current [large crosses are average of three data points; small crosses are single points (Ref. 18) (1 – j = 317.3A/mm^2, I = 347A; 2 – j = 271.6A/mm^2, I = 297A; 3 – j = 182.9A/mm^2, I = 200A)]

Overall, Halmoy's equation offers the same predictive capability as Lesnewich's model except more quantitative measurements are required to determine the electrode extension resistivity. Because of this, most engineers prefer to characterise the effects of more advanced GMAW processes using Lesnewich's general equation. His equation uses two simple constants to factor arc and resistive heating permitting quick analytical correlation to welding parameters.

2.2.6 Numerical Models

In recent years, numerical models have been used to model the GMAW process (Ref. 32-40). These models have evaluated the heat flow in the electrode extension, the melting rate, the droplet formation process, the power in the arc, and the interaction with the power supply for self-regulation. These analyses have led to some important insight on the capability of numerical analysis for prediction (Ref. 33) as summarised by Kim:

- Thermal conduction in the solid electrode may be approximated as a quasi-steady process except in the immediate vicinity of the molten droplet.
- Dimensional and time scale analyses including a number of transient thermal phenomena involved in droplet formation and detachment found no significant simplification to apply for analysing droplet formation.
- Given the transient nature of the convection within the droplet, the relative significance of so many thermal phenomena, and poorly quantified conditions, accurate solutions for within the droplet are very difficult.

Simple numerical models were static, and assumed the droplets were round and had stationary electrode extension interface. The volume of fluid (VOF) method (Ref. 34, 37) is becoming more common as it can predict the dynamic effects of drop transfer. These methods have become available only in recent years with the use of high power computers. There are still many limitations for accurately deploying these models in industry. Many of these limitations are related to accurate measurement of material properties at high temperatures. Numerical modelling will continue to factor more details that affect the heating at the electrode tip, the shape of the arc, the current flow into the droplet, the droplet formation process, and the interdependent dynamics between the areas.

Numerical models have focused on CV waveform with focus on the melting rate and droplet formation process, and the transition between metal transfer modes. No numerical models were found that attempted to factor the effects of complex waveforms on droplet formation or the effects of VP. The transient effects that occur during arc re-ignition, current pulsing, and VP will require even more advanced models. In VP, the arc heating process will need to separate the effects of electrode anode and cathode heating, shielding gas activation, and arc ignition and growth on a time scale based on the waveform.

2.3 GMAW Metal Transfer Modes

A review of GMAW metal transfer is required before the theories for GMAW-P and VP-GMAW can be presented properly. Metal transfer begins with the formation of molten droplets on the tip of the electrode. The droplets are detached forming drops based on the mode of transfer. Metal transfer affects the control of the weld pool, positional weldability, stability of the process, and compositional changes to the filler metal due to reactions in the arc. In addition, the melting rate efficiency of this process is dependent on the metal transfer mode that is controlled by the power supply waveform and electrode conditions. Shielding gases do not directly affect melting rate for EP welding but do influence metal transfer (Ref. 12, 17, 18, 29, 30, 31). Oxidizing shielding gases do affect the melting rate of EN welding and metal transfer (Ref. 12, 29). Losses through fume and spatter, and sometimes weld defects are a result of poor metal transfer.

2.3.1 IIW Classification

Welding processes offer a wide range of metal transfer modes. The International Institute of Welding developed a classification in 1976 to describe these modes (Table 2.1). The GMAW process offers the largest range of metal transfer modes. Many GMAW modes provide regular transfer of drops which can be quantified and related to welding parameters. This is not always the case with SAW and SMAW, and GMAW with pure carbon dioxide shielding gas. These processes may have drops that vary in volume over time.

Table 2.1 IIW Classification of Metal Transfer (Ref. 17)

Designation of Transfer Type	Welding Processes (examples)
1. Free flight transfer	
1.1 Globular	
1.1.1 Drop	Low-current GMAW
1.1.2 Repelled	CO_2 shielded GMAW
1.2 Spray	
1.2.1 Projected	Intermediate-current GMAW
1.2.2 Streaming	Medium-current GMAW
1.2.3 Rotating	High-current GMAW
1.3 Explosive	SMAW (coated electrodes)
2. Bridging transfer	
2.1 Short-circuiting	Short-arc GMAW
2.2 Bridging without interruption	Welding with filler wire addition
3. Slag-protected transfer	
3.1 Flux-wall guided	SAW
3.2 Other modes	SMAW, cored wire, electroslag

The GMAW process is industrially applied using the short circuit mode. This mode uses a low voltage that inhibits a free burning arc. The droplets form in the arc period between shorts that are made between the electrode tip and the weld pool (Ref. 41-49).

With proper control of the short circuit process, the droplets that formed can be transferred during short circuits with the pool without excessive spatter during re-ignition. High quality welds can be made on sheet metal and under controlled conditions on thick plate.

For GMAW, at low currents using voltages that inhibit short circuiting, the metal transfer mode is characterised as globular (Figure 2.14). Globular drops are defined as drops that have a diameter significantly larger than the electrode diameter. The globular mode has two sub-modes; drop and repelled. In the drop globular mode, the drops transfer to the weld pool when the forces, largely due to the droplet weight, cause the drop to detach. This mode can be controlled and here-in is just called globular. With carbon dioxide shielding gas, the globular drops can be repelled at high currents away from the weld pool. The repelled globular mode found in high current CO_2 welding is related to the high thermal gradients that constrict the arc (Ref. 13, 17, 27, 28). The carbon dioxide molecules absorb a lot of heat as they are dissociated and ionised. This constricts the arc, which forces the current flow into the bottom of the droplet where a strong reaction force exits. Repelled globular transfer is also common in EN GMAW where massive droplets have been seen to grow, and sometimes transfer is only by a short circuit.

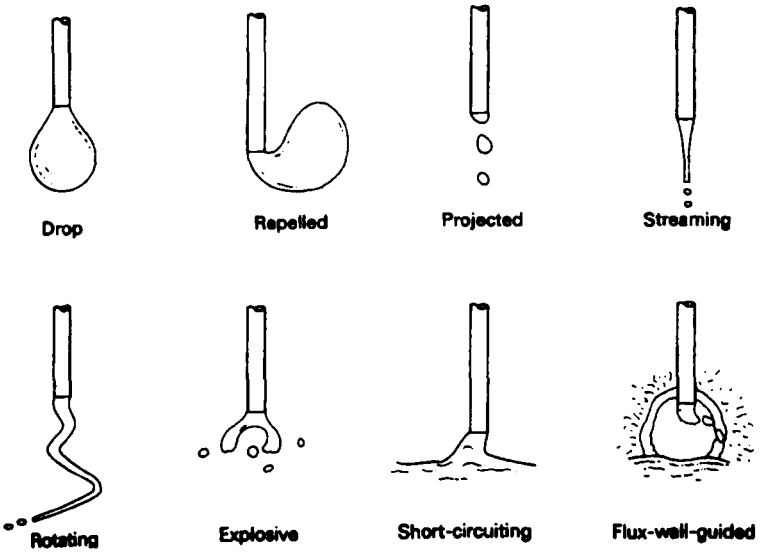

Figure 2.14 Metal Transfer Modes According to the IIW Classification (Ref. 17)

The polarity has a strong effect on the droplet form. For anode electrodes, the arc has been observed to form symmetrically around the bottom or entire droplet in argon based shielding gases (Ref. 13, 17, 27, 28). When the electrode is negative (cathode), a mobile cathode spot has been observed on the bottom of the droplet (Ref. 13, 17). The cathode spot can support a large droplet and is very unstable. For this reason, EN GMAW is not industrially used except with special electrodes that have activated surfaces or with shielding gases that have sufficient oxidation potential (Ref. 29). With activated electrodes, regular and stable transfer can be achieved in EN with the same transfer modes achieved in the EP mode (Ref. 13, 28).

Norrish (Ref. 29) showed that stable globular and spray transfer can be achieved in EN welding when the shielding gas provided sufficient activation. Argon mixtures having more than 5% oxygen, or 2%O_2 and 10% CO_2 to 10%O_2 and 10%CO_2 provided stable transfer. His work found that the optimum shielding gas for arc stability and weld bead shape was argon with 5%O_2 and 6%CO_2 but other mixtures gave almost similar results.

In pure argon, Norrish observed that the cathode arc oscillated between two modes; the multi-spot cathode and the single-spot cathode. The two modes oscillated at lower wire feed speeds and currents where the multi-spot mode started the droplet formation process. Here, the arc travelled up the electrode extension and rapidly consumed virgin electrode. Once a large droplet formed, the arc root on the droplet and transitioned to the single-spot cathode mode until drop detachment. At higher weld current, the two modes were found to co-exist during droplet formation but metal transfer occurred in the single-spot mode. With argon oxygen or O_2-CO_2 mixtures that provide sufficient activation, the cathode area was stable and covered the tip of the electrode. At 25% CO_2 the arc formed a dominant cathode spot on the bottom of the electrode tip. This resulted in non-axial transfer and spatter.

The driving force for metal transfer is related to the geometry of the arc-droplet interface which is probably more important than the direction of current flow (Ref. 27, 29, 50, 51, 52). Symmetric current flow above and around the droplets promotes stable detachment. Current flow into the bottom of the droplet results in significant repulsive force. The work function of ferrous materials is too high for thermionic emission of electrons to carry current. The electrode cathode spot, formed in shielding gases that do not have sufficient activation, strongly depends on the fraction of ions carrying current and naturally forms on the bottom of the droplet close to the arc where ions are available. Activation by shielding gas or surface activating elements provides for some thermionic emission and makes the arc more stable (Ref. 27, 28, 53-57). Cerium, caesium, and other rare earth metals have commercially been used to activate the electrode (Ref. 58, 59). The arc that forms on an activated electrode has been observed to cover the entire electrode tip and forming droplet (Ref. 27, 28).

In argon-based shielding gases with EP, globular transfer can be stable and regular. Small additions of oxygen or CO_2 help drop transfer by reducing the surface tension of the droplets (Ref. 53, 54). Arc length is critical and must be long enough to avoid short circuiting.

The globule drop volume is directly related to the forces on the droplet where drop volume decreases as the current is increased (Figure 2.15) (Ref. 17). At a critical current, a transition in metal transfer occurs where the drop volume significantly changes often by more than an order of magnitude. This is called streaming spray transfer (Figure 2.15d) as the fine metal drops stream across the arc.

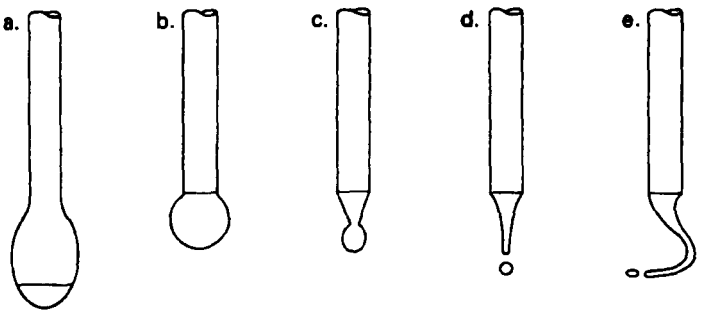

Figure 2.15 Successive Modes of Transfer in GMAW with Increasing Current Density from Left to Right (Ref. 17) (a - large globular, b - globular, c - project spray, d - streaming spray, e - rotating spray)

There are three sub-groups for spray transfer; projected, streaming, and rotating (Table 2.1). Researchers (Ref. 13, 17) have studied the spray transition current. Here, the drop volume significantly decreased with a corresponding increase in drop frequency. Lesnewich was the first to document the relationship between drop frequency and volume as a function of current through the transition range (Figure 2.16). The transition current was dependent on current and electrode type, diameter, extension, composition, and activation. Activation was caused by oxidizing shielding gases which change the surface tension or work function of the electrode. The relationship between transition current and electrode extension for steel using Ar-1%O_2 is shown in Figure 2.17. The transition current decreased as the electrode diameter decreases and/or electrode extension increases. For 1.14 mm (0.045 in.) electrodes, the transition currents using normal electrode extensions of 12 to 25 mm were between 200 to 180 amps, respectively. For the most part, this figure was for the streaming spray mode, which is typically defined as just the spray mode.

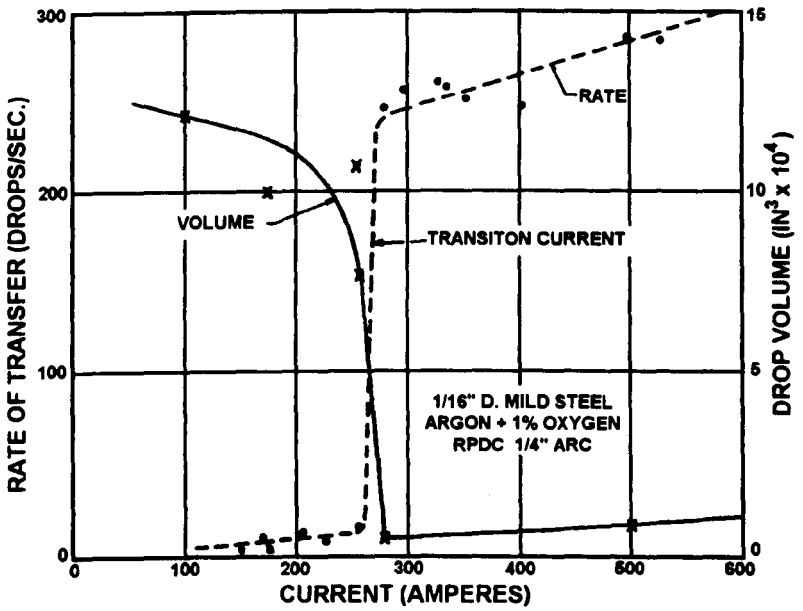

Figure 2.16 Effect of Current on the Size and Frequency of Drops Transferred in an Argon-Shielded Arc (Ref. 13)

At even higher current densities, the metal transfer mode can undergo a transition to rotating spray (Figure 2.15e). This mode is more common with long electrode extensions that soften the electrode. The rotating spray mode occurs when the hot soft electrode becomes deflected under the influences of the Lorentz magnetic field force. The transition current from spray to rotating spray is dependent on polarity, electrode diameter, extension, composition, and activation (Ref. 13, 17, 28, 53-55). At extremely long electrode extensions, the transition currents for both spray and rotating spray merge. At this condition, a further increase in electrode extension resulted in a transition from globular to rotating spray that skipped the streaming spray mode.

For most practical purposes, the rotating spray mode is not industrially used and is not achieved in modern power supplies using current waveform technology. Phillips Electric developed a hybrid process called plasma-MIG in the 1980's which enhanced the preheating of the electrode extension and promoted this transfer mode (Ref. 60). The process was claimed to offer benefits for cladding since the rotating arc distributed the heat input and deposited metal reducing base metal dilution. Stability of this metal transfer mode made plasma-MIG marginally successful and hence, the company has abandoned supplying this welding system.

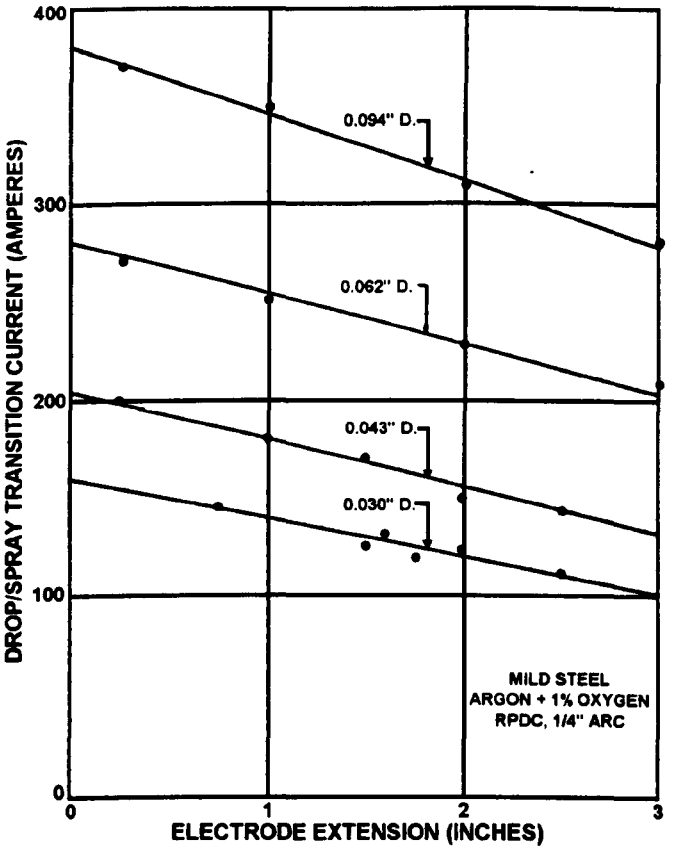

Figure 2.17 Relationship Between the Drop/Spray Transition Current, Electrode Diameter, and Extension (Ref. 13)

2.3.2 Drop-Spray Mode

Researchers (Ref. 61-63) have studied metal transfer for the GMAW-P process. Focus was on the projected spray mode of metal transfer (Figure 2.15c) with emphasis on a small subset of this mode known as "drop-spray". The drop-spray mode was subsequently preferred because the goal of most pulse parameters was to achieve one drop per pulse using a spray like arc. The drop-spray droplet diameter was within +/- 20% of the wire diameter and the drop was accelerated from the current pulse providing arc stiffness. Ma and Apps (Ref. 61, 62) studied the phenomena at the transition current and found that current range for stable drop-spray transfer was less than 20 amps above the transition current. This was for steady-state metal transfer using CV power supplies. In industry, this mode of transfer was hard to control using CV power supplies because variation in wire composition and activation may cause a frequent transition into streaming spray or back to projected-globular.

During the transition from globular to spray using a current pulse, the first drop that formed as current increased was found to be drop-spray (Ref. 61, 62). With long current pulses, the electrode tip began to neck and subsequent drops progressively got smaller as the process transitioned into streaming spray. The metal transfer transition phenomena was easily controlled by pulsing the current at a regular frequency. Depending on the pulse parameters, one or more drops may form per period. The drops that form after the drop-spray drop at currents above the spray transition current have a smaller drop diameter depending on the height and length of the pulse current.

The shielding gas used for GMAW-P was important in achieving stable drop-spray transfer. French (Ref. 64) concluded that the shielding gas must have less than 20% CO_2 to produce this type of metal transfer. This was in good agreement with the 29% criteria (Ref. 52) that was obtained by Jacobson. A similar effect was observed using helium-rich shielding gases (Ref. 33). Here, Kim found that the mode transition between globular and spray disappeared when more than 50% helium was used in helium-argon shielding gases, or when pure CO_2 was used with GMAW-P.

In the drop-spray mode, metal fume is minimized and the arc is stiff providing directional metal transfer. The fume is minimized by the greater surface area to drop volume compared with streaming spray (Ref. 61, 62). As the drops travel through the arc, vapour is generated off the surface from the intense heat. Drop surface area increases as the drop size decreases for a given melting rate. Streaming spray promotes significant fume which can exceed 5% of the electrode burnoff volume, which is measured by the filler deposition efficiency. Metal vapour is the main cause of fume based on the relationship between drop surface area to drop volume, arc length, and oxidation potential of the shielding gas. Longer arcs provide more time for drop superheating and fume formation. Increased oxidation potential increases fume by the exothermic reaction of oxide formation, which accelerates drop boiling.

Control of fume is important in modern industry to meet regulations relative to welder exposure. The metal transfer mode can be used to reduce fume and requirements for protective equipment like active filter masks and extraction equipment. As will be

described later, the VP-GMAW process can significantly reduce fume and at the same time provide improve productivity (Ref. 10).

2.4 Metal Transfer Forces

Metal transfer is controlled in GMAW by the forces on the droplet. Researchers have represented these forces using simple static models that did not include the movements in the electrode extension interface (Ref. 32, 50-52, 61, 62, 65-72). Modern studies have factored the effects of fluid flow within the droplet which affect temperature distribution and surface tension. The simple static model (Ref. 32, 65) for forces on a droplet (Figure 2.18) is based on the competition of surface tension F_γ, and vaporisation F_v (repulsive) forces against the electromagnetic F_{em} (pinch), gas drag F_d, and gravitational F_g forces. Metal transfer occurs when the latter forces exceed the surface tension and vaporisation forces. The gravitational force is assumed to be positive since most welding is downhand. The static model for forces on the droplet can be expressed as follows:

$$F_\gamma + F_v = F_{em} + F_d + F_g \tag{2.17}$$

Of the above forces, the gas drag force and vaporisation force can be ignored for most practical welding applications. These applications use good welding parameters and normal welding torches. The force of gravity is simply the mass of the droplet multiplied by gravitational acceleration. This force is significant for the drop globular mode at low current and large droplet diameters. For most GMAW-P applications, the force of gravity can be ignored too since the droplets are near to or smaller than the electrode diameter of small electrodes (Ref. 50), and current densities are high. Therefore, in simple terms, metal transfer occurs when the Lorentz force exceeds the surface tension force. Under most GMAW-P applications, the Lorentz force accelerates the droplets off the tip of the electrode providing direction metal transfer and out-of-position welding capability.

The vaporisation force is related to the arc droplet interface. The vaporisation force is negligible when argon-based shielding gases are used with EP. These gases promote an arc that covers the drop-spray and streaming spray droplets. Argon based arcs provide a more uniform anode that distributes the heat caused by the acceleration of current flow into the droplet surface. The vaporisation force may be very dominant in the case of EN with CV power supplies or with CO_2 based shielding gases in the EP mode. Here, the anode or cathode spot may be constricted superheating the bottom droplet surface. The localized vaporisation provides for a repulsive force. For most industrial applications using GMAW-P, the surface tension force is the dominant force resisting drop transfer since most shielding gases are argon-based and the metal transfer mode is drop-spray.

The surface tension force is strongly dependent on droplet temperature and superheat, and effects of surface active elements which act to reduce surface tension. Small quantities of oxygen in the shielding gas, or sulphur and phosphorus in the filler material, can have a strong effect on reducing surface tension (Ref. 53-56).

The electromagnetic force, which is also known as the Lorentz force, is caused by reaction between the electromagnetic field and current density. This force is controlled by the current and the wire diameter, and is the dominant force controlling the transition from spray to globular transfer. The Lorentz force (Ref. 50) is believed to pinch the droplet surface and accelerate the liquid drops off the tip of the electrode. The Lorentz force is present when the magnetic field is changing as in the case of current flow through a forming droplet and after transfer. Again, this force is strongly dependent on the interface between the droplet surface and the anode (or cathode) arc root that shapes the current flow into the droplet (Ref. 50-52), especially in GMAW-P.

In streaming spray GMAW, the arc envelope the entire electrode tip and a current density gradient along this taper drives liquid along the surface. The liquid column covering the electrode tip is accelerated and generates a spray of fine drops off the tip. The spray of drops has been given the analogy of water emitting from a high pressure orifice where the liquid column breaks into a fine spray.

The Lorentz force can be repulsive if the current flowing into the droplet begins at the centre of the droplet bottom. As the current travels along the droplet surface, the Lorentz force can act to resist metal transfer. Therefore, the vaporisation force and Lorentz force may be acting together in the case of EN welding where there is a dominant cathode spot, and CO_2 welding where the arc is constricted by the temperature gradients. Spray transfer with pure helium shielding gas can also be difficult due to a constricted arc. The high thermal conductivity of helium promotes behaviour similar to CO_2 GMAW, and because of this, pure helium is not used for most GMAW applications. In applications that need the larger heat field for improved weld fusion, like GMAW of titanium, mixtures of helium and argon are used to improve metal transfer. For non-reactive metal like stainless steel, small addition of oxygen or CO_2 may be used to further improve metal transfer with helium rich shielding gases (Ref. 55, 57).

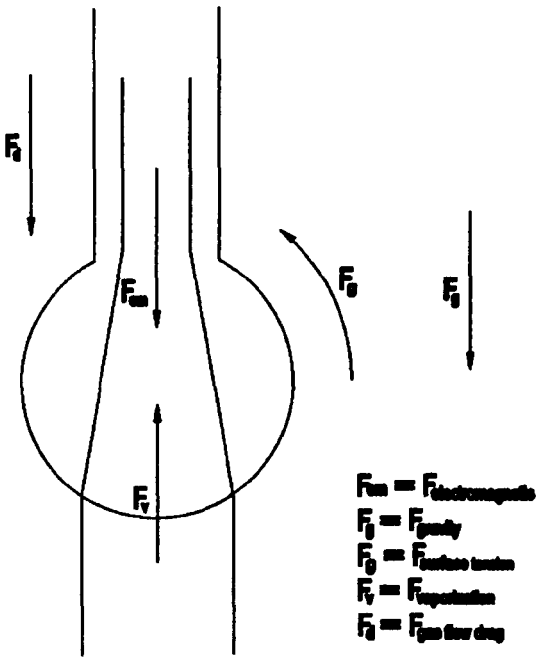

Figure 2.18 Forces on a Consumable Electrode Droplet (Ref. 65)

The static force theory has been developed since 1960 (Ref. 60). This theory predicted a generally larger drop size than what was observed by experiments. Allum (Ref. 70, 71) proposed a different theory in 1985 and it was based on pinch instabilities in a liquid column at the electrode tip. This theory has been found to predict a smaller drop size in the lower current range for globular transfer. The pinch theory (Ref. 72) was invalid for globular transfer since a liquid column would never form on the electrode tip at low currents. The pinch-instability theory was also found to predict drops smaller than experiments for spray transfer where a liquid column exists. This error was attributed to the electrode tip taper and anode heating on the electrode sides. As mentioned in Section 2.2.6, new numerical models offer the possibility to link droplet calculations with arc column calculations. In addition, the dynamics of the droplet formation process and interactive arc behaviour for advanced waveforms needs to be factored in these future models.

2.5 GMAW-P Waveform Parameters

Before the development of modern power supplies using transistors, GMAW-P was limited to low fixed frequencies of 60 or 120 Hz (Ref. 73). Invertor power supplies, which were offered by the mid-1980's, offer significant control over pulse waveform. The main driving force for application of GMAW-P was improved metal transfer, out-of-position weldability, and reduced currents for a given melting rate (Ref. 73-87). The process competes with short circuit GMAW on many applications, but this process suffers from spatter from short circuit induced metal transfer. Process control for GMAW-P strongly relies on controlling the forces on the droplet and metal transfer mode.

Drop-spray metal transfer has been considered the optimum mode for the majority of GMAW-P applications (Ref. 61-63). The drop-spray mode exists over a very small current range just above the transition current in the steady-state (Figure 2.19). This detailed diagram, which was developed by Allum, for 1.2 mm steel shows burnoff rate and drop frequency as a function of current using a 5 mm constant arc length and three electrode extensions (Ref. 63). The current range was less than 15 amps at each electrode extension for drop-spray. The drop spray range decreased with decreasing electrode extension. The shielding gas for this figure was 95%Ar-5%CO_2. Overall, the window for steady-state control of this mode was small.

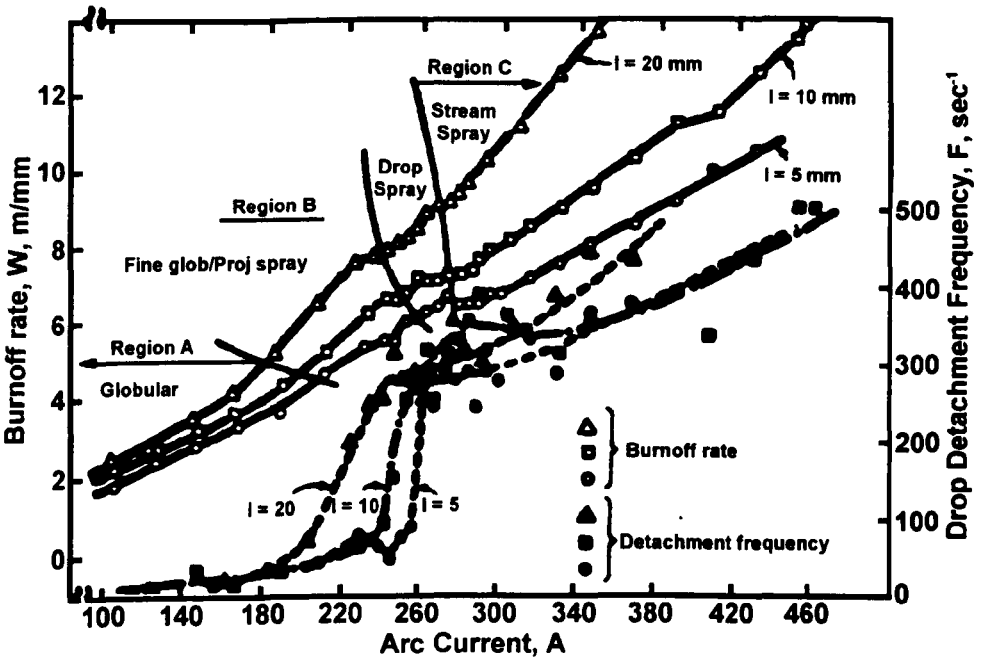

Figure 2.19 Influence of Current and Electrode Extension on Burnoff Rate and Metal Transfer Frequency Using 1.2 mm Mild Steel, with Ar-5CO_2 Shield, Arc Length 5 mm (nom), Electrode Stickout, l, as Shown (Ref. 63)

Drop-spray transfer was hard to control using CV or constant current power supplies since small changes in electrode diameter, extension or activation caused a full transition into streaming spray or reversion back to globular. Current pulses above and below the transition current provided control for the drop-spray mode (Figure 2.20). This figure shows two simple strategies that have been evaluated for synergic control of pulse parameters (Ref. 63). The definition of synergic meant the pulse parameters were systematically changed to provide drop-spray transfer over the full range of wire feed speeds offered by the process. The goal was to get one drop per pulse. These first synergic power supplies used very square waveforms to maximize the melting potential of the waveform. Today, most power supplies use a more trapezoidal waveform (Ref. 92). The latter waveforms provide a softer arc and less audible noise.

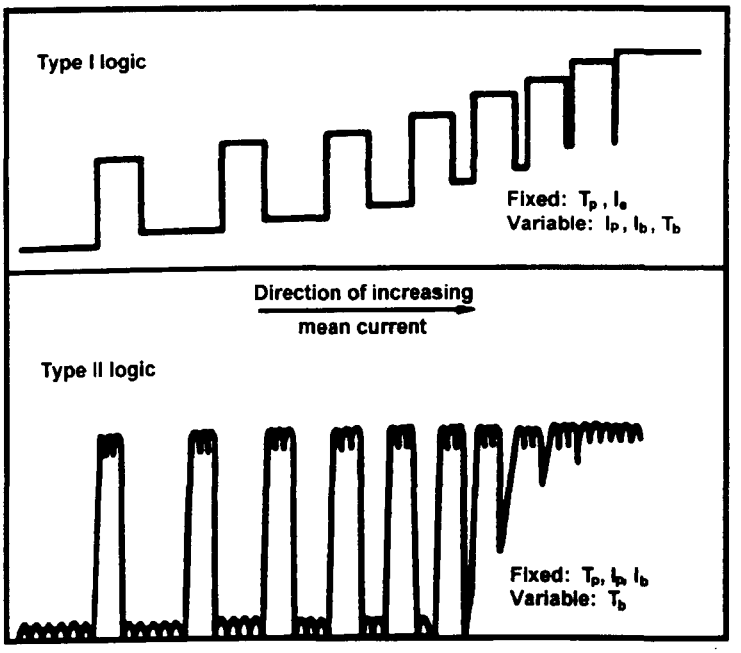

Figure 2.20 Changes in Pulse Shape as Mean Current is Continuously Increased for Synergic Logics (Ref. 63)

The general strategy for modern GMAW-P power supplies is to use a pulse waveform that provides "one drop per pulse". The first metal drop to transfer during the current pulse that exceeds the spray transition current is drop-spray. Multi-drop per pulse parameters are common in many procedures used in industry. In general, there is no pulse waveform that can be considered optimum for GMAW-P. There are many pulse waveform solutions that can provide working procedures that have good stable metal transfer and weld quality, Figure 2.21 for example (Ref. 83). This example shows a large range for peak pulse current and peak time, and the regions for one or multiple drops per pulse. The relationship between these two variables for a specific type of transfer, like one drop per pulse, is called the detachment parameter (Ref. 63, 77, 78, 81) which is defined as follows:

$$D = I_p{}^n t_p \tag{2.18}$$

where D is the characteristic detachment parameter, I_p is the pulse current, t_p is the peak time and n is a constant usually between 1.5 to 2.5 . The curves shown in Figure 2.21 were defined by the detachment parameter. Based on this theory, similar results were achieved with a broad range of pulse parameter combinations by using Equation (2.18) within the windows shown in this figure.

Preferences in welding applications make some pulse parameters better than others. Preferences that influence pulse parameter selection may improve the (1) melting rate, (2) out-of-position weldability, (3) fume, (4) noise and/or (5) weld bead shape. These factors can be application dependent so what works on one application may not be preferred on another.

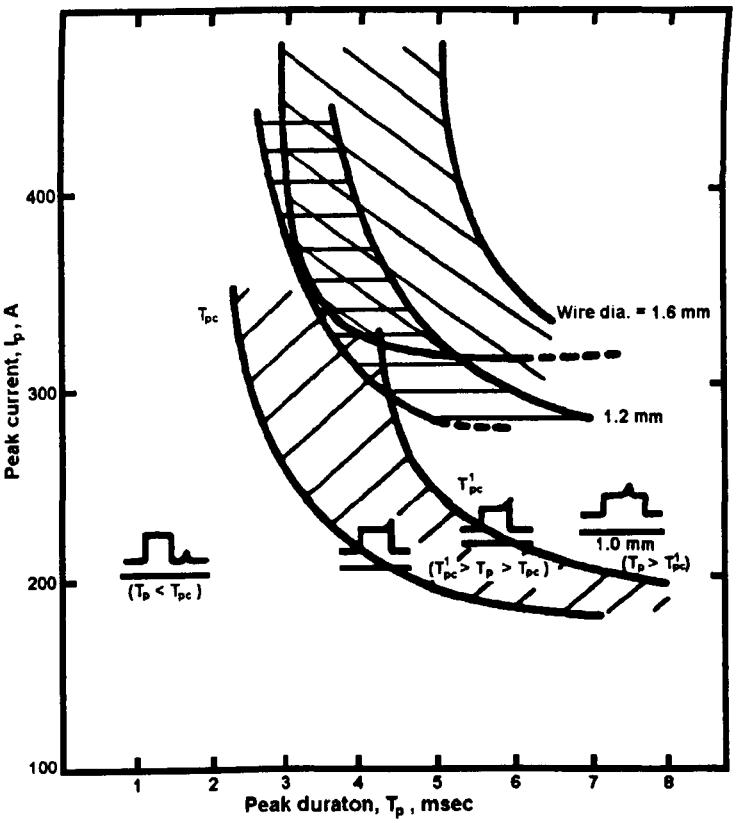

Figure 2.21 Influence of Peak Parameters on Droplet Detachment for Mild Steel Wire in Ar-5%CO_2 (Ref. 83)

There are a variety of waveform shapes that can be used to achieve pulse metal transfer. The typical waveform parameters for GMAW-P include the peak and background current, the peak and background time, and the wave shape in the transitions. For trapezoidal waveforms, a common parameter is the slew rate to and from the background current to the peak current. More modern waveforms may have other properties like pulse on pulse, exponential slew rate, or short circuit adaptive control waveforms for spatter minimization (Ref. 1-10).

Early researchers focused on square waveforms. In reality, almost all their tests had some slew rate due to the limitations of the power supply response rate. Some of the general principles of GMAW-P waveform technology (Ref. 79-81) were as follows:

1) A minimum background current, I_b, is required to maintain the arc. This was typically greater than 40 amps but can be set as high as 50 amps below the transition current.
2) The background current, I_b, is usually minimized to reduce heat input and inhibit the formation of globular droplets before pulsing the current above the spray transition.
3) The current waveform is rapidly pulsed to currents above the transition current to grow the droplet and force metal transfer.
4) The peak current time, t_p is set long enough to grow the droplet and force a pinch force instability.

5) The peak current magnitude is usually set at least 50 amps above the transition current and can be 200 amps or greater than the transition current.
6) The peak current and time are usually optimised to provide one metal drop per pulse.
7) The droplet can detach from the electrode tip at the end of the peak period or during the following background period to produce different arc characteristics (i.e., a hard or soft arc).
8) The first drop to detach is approximately equal to the wire diameter depending upon the material, shielding gas, waveform shape, and electrode diameter. These are related to the governing forces which were discussed in Section 2.4.
9) Multiple drops are transferred if the peak parameters are too great where the first drop is of drop-spray dimensions and subsequent drops rapidly decrease in size as the electrode develops a tapered tip to support steady-state streaming spray.
10) Frequency is the main pulse parameter used to control changes in wire feed speed by usually adjusting the background time to balance the requirements for melting rate, arc length control, and stability. This is not universal as many equipment suppliers also make small adjustments to peak and background variables to provide different strategies and avoid patent infringement.

Most GMAW-P power supplies that offer synergic algorithms are tolerant to a range of shielding gases. The shielding gas affects the activation of the electrode and the droplet surface tension. Spray transition current can change up to 35 amps for 1.2 mm steel by changing the CO_2 content from 5 to 20% (Table 2.2). Most commercial power supplies simply offer one set of pulse parameters for a full range of Ar-CO_2 shielding gases. Here, the strategy is to use a peak current that is significantly higher than all the transition currents shown in this table. Peak pulse currents near 350 amps are common on many power supplies (Table 2.3). This results in a pulse that is 75 to 100 amps greater than the transition current for 1.2 mm steel.

Table 2.2 Spray Transition Currents for Steel Wires (amps) (Ref. 81)

Wire Diameter	Shielding Gas		
	Ar-5CO_2	Ar-15CO_2	Ar-20CO_2
0.8	140	155	160
1.0	180	200	200
1.2	240	260	275
1.6	280	280	280

There may be other factors that affect waveform strategy too. This includes synchronisation of pulse parameter for hyperbaric conditions to deal with high pressure arcs (Ref. 86, 87) or in hybrid welding processes, like tandem GMAW (Ref. 88-91). Waveform synchronisation may be used to have tandem electrode waveforms in or out of phase. The preference has a strong influence on metal transfer stability, the resultant tandem GMA plasma jet, and weld bead shape, for example.

Table 2.3 Pulse Parameters Based on Mid-Point Detachment Parameter Conditions, I_p - Pulse Current; t_p – Pulse Duration (Ref. 81)

Wire/Gas Type	Wire Diameter (mm)							
	0.8		1.0		1.2		1.6	
	I_p	t_p	I_p	t_p	I_p	t_p	I_p	t_p
Ar-5O_2 Plain carbon steel (70S6)	300A (350A	2.7 ms 1.3 ms)	350A	2.5 Ms	350A	3.5 ms	400A	3.5 ms
Ar-12-15CO_2 Plain carbon steel (70S6)	300A	2.5 ms	325A	3.0 Ms	350A	3.5 ms	--	--
Ar-20CO_2 Plain carbon steel (70S6)	300A	3.0 ms	300A	3.0 ms	350A	3.2 ms	--	--
He-13.5Ar-1.5CO_2 Plain carbon steel (70S6)	--	--	--	--	350A	2.8 ms	--	--
He-38Ar-2CO_2 Plain carbon steel (70S6)	300A	2.75 ms	325A	3.0 ms	350A	3.5 ms	--	--
Ar-2O_2 Stainless steel (308)	300A	1.5 ms	300A	1.8 ms	350A	2.5 ms	--	--
He-13.5Ar-1.5CO_2 Stainless steel (308)	--	--	--	--	--	--	300A	4.0 ms
He-38Ar-2CO_2 Stainless steel (308)	--	--	325A	3.5 ms	350A	3.5 ms	--	--
Argon Aluminium (pure)	--	--	--	--	250A	2.5 ms	220A	4.0 ms

2.6 GMAW-P Melting Rate

In direct current (DC) GMAW-P, the pulsing waveform improves the electrode resistive heating efficiency of the process due to I^2R. Allum (Ref. 63) derived a melting rate equation for square waveform pulse GMAW. The melting rate for pulse DC waveforms, MR_{pdc}, was analysed in a time dependent form as follows:

$$MR_{pdc} = \frac{1}{t_p + t_b} \int_{\substack{one\ pulse \\ cycle}} MR_b(t)dt$$

$$MR_{pdc} = \left[\left(t_p \alpha I_p + \beta L I_p{}^2 t_p\right) + \left(t_b \alpha I_b + \beta L I_b{}^2 t_b\right)\right] \frac{1}{t_p + t_b}$$

$$= \alpha \frac{\left(I_p t_p + I_b t_b\right)}{\left(t_p + t_b\right)} + \frac{\beta L}{\left(t_p + t_b\right)} \left\{I_p{}^2 t_p + I_b{}^2 t_b\right\}$$

$$= \alpha \bar{I} + \frac{\beta L}{\left(t_p + t_b\right)^2} \left\{\left(I_p t_p + I_b t_b\right)^2 + \left(I_p{}^2 + I_b{}^2 - 2 I_p I_b\right) t_p t_b\right\}$$

$$MR_{pdc} = \alpha \bar{I} + \beta L \left\{\bar{I}^2 + \frac{\left(I_p - I_b\right)^2 t_p t_b}{\left(t_p + t_b\right)^2}\right\} \qquad (2.19)$$

where for simplicity:

I_p = current EP peak
I_b = current EP background

t_p = time at EP peak current
t_b = time at EP background current.

This equation was applied by a number of early researchers to relate pulse parameters to melting rate (Ref. 30, 31, 74). Allum developed a burnoff factor to graphically show the potency of pulse parameters for melting rate (Figure 2.22). This figure plots burnoff factor , γ, versus the time balance, x. = $t_p/(t_p + t_b)$. The burnoff factor is defined as follows:

$$\gamma = x(1-x)I_e^2 = \frac{MR_{pdc} - MR_{dc}}{\beta L} \qquad (2.20)$$

The burnoff factor is directly related to the difference in pulse melting rate minus the mean melting rate taken from the components of Equation 2.19 while ignoring the arc heating component. This figure shows that as excess current increases, $I_e = I_p - I_b$, the burnoff contribution from the pulse increases at a given mean current. The efficiency of the pulse parameters are the highest when the pulse time is balanced; peak fraction, x equals 0.5.

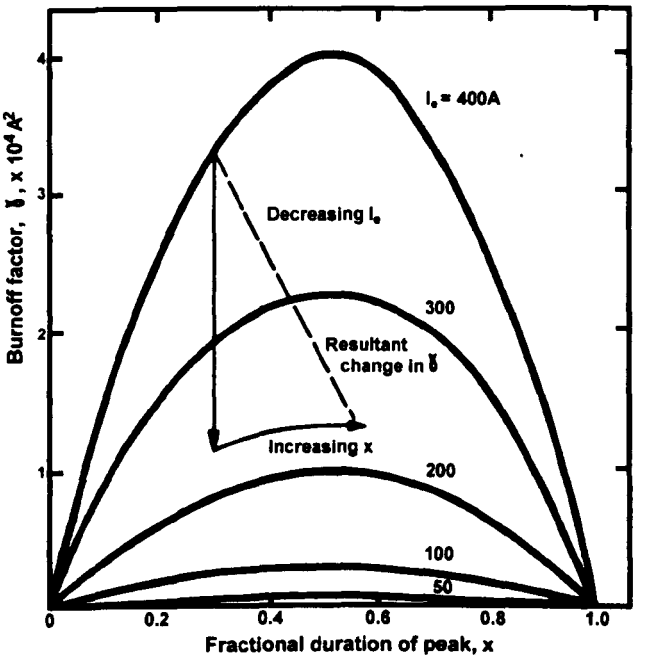

Figure 2.22 Influence of Fractional Duration of Peak ($x = t_p f$) and Excess Current ($I_e = I_p - I_b$) on the Burnoff Factor, γ (Ref. 63)

This equation ignored the effects of slew rate, which decreases the resistive heating efficiency of the pulse waveform. Modern power supplies use slew rate to soften the arc and reduce noise. Effects of EP slew rate, as shown in Figure 2.23, were characterised by Richardson, et al (Ref 75). His work was performed to better characterise power supply dynamics. The waveform shown in Figure 2.21 was divided into discrete time-

based components that describe a trapezoidal waveform. The current in the trapezoidal waveform can be divided into four pulse periods as follows:

$$I_1 = I_b + \frac{(I_p - I_b)}{t_1} t \tag{2.21}$$

$$I_2 = I_p \tag{2.22}$$

$$I_3 = I_p - \frac{(I_p - I_b)}{t_3} t \tag{2.23}$$

$$I_4 = I_b \tag{2.24}$$

On the rising edge of the pulse, the response rate is given by:

$$\frac{dI}{dt} = \frac{(I_p - I_b)}{t_1} \tag{2.25}$$

and on the trailing edge, the response rate is given by:

$$\frac{dI}{dt} = \frac{(I_p - I_b)}{t_3} \tag{2.26}$$

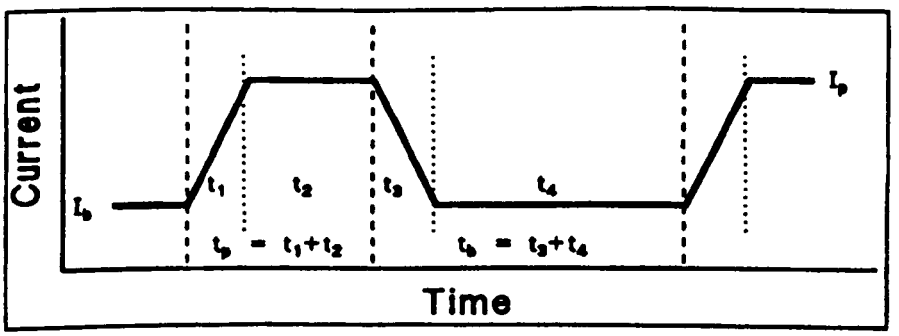

Figure 2.23 Trapezoidal Waveform and Pulse Parameters (Ref. 75)

Richardson, et al assumed that the rise and fall rates of the peak current pulse were equal so $t_1 = t_3$. The time period for t_p was equal to t_1 plus t_2 and the time period for t_b was t_3 plus t_4. Unequal slew rates led to a larger resultant equation although the basic mathematical behaviour remains unaltered. Performing the integral over one pulse cycle and rearranging the resulting equation to the form like Equation (2.19) yields:

$$MR_{pdc} = \frac{1}{t} \int_{\substack{one\ pulse \\ cycle}} MR_b(t)dt \tag{2.27}$$

$$MR_{pdc} = \alpha \bar{I} + \beta L \left\{ \bar{I}^2 + \frac{(I_p - I_b)^2 t_p t_b}{(t_p + t_b)^2} - \frac{(I_p - I_b)^3}{3(t_p + t_b)\frac{dI}{dt}} \right\} \tag{2.28}$$

The slew rate term in Equation (28) was found to have an important effect, up to 12%, on the melting rate of small diameter wires, long electrode extensions, or highly resistive electrodes. Under most circumstances, when welding steel the slew rate component of the resultant melting rate based on this equation was 3 to 8%.

2.6.1 Other Melting Rate Analysis Approaches

Kim and Eager (Ref. 76) proposed the "weighted sum method" for predicting the melting rate of GMAW-P. This method added the weighted (percent time) steady-state melting rates for the base and peak current levels used in the waveform. The melting rate was determined in CV tests so the base current was for globular transfer and the peak was for streaming spray. The theory was these steady-state properties could be added to predict pulse melting. This method was found to underestimate melting rate of GMAW-P. They had no explanation for this error. The error was probably due to a lower anode drop and arc heating coefficient for streaming spray versus drop-spray, which was shown to be more efficient; especially when pulsing current (Ref. 63).

2.7 Electrical Measurements in GMAW-P

There are multiple sets of pulse parameters that yield effectively the same result being deposition rate, arc length, arc power, and effective bead shape on an application. Joseph (Ref. 92) recently completed a study which characterised the effects of waveform shape with modern power supplies and found no major change in bead shape over a wide range of pulse parameters when deposit area and arc length were held constant. The main difference compared to CV welding was that all GMAW-P waveforms provided a significant decrease in power from the improved melting rate. The difference in power between waveforms only varied 10%. These power supplies offered a variety of waveform strategies. In original GMAW-P theory, the waveform shape was characterised by assuming an instantaneous change in current from background to peak levels forming a square waveform. In industry, most modern power supplies do not offer such a "hard" waveform since the noise and penetration can be excessive. The net effect is that almost all GMAW-P waveforms were trapezoidal in shape. Joseph did notice, as supported by other researchers, that the shape of the trapezoid and the relationship to drop transfer did produce differences in the penetration (papilla) under the arc, arc stiffness, audible noise, and fume. The most critical finding of his study was related to the measurement of power and heat input.

Joseph used high speed DAQ to measure the electrical parameters and calculate power. Power was calculated using mean and root mean square (RMS) measurements, and was compared with average instantaneous power (AIP). It was found that the only true measure of power, which is used to calculate welding heat input, was determined by using high speed DAQ to calculate AIP (Table 2.4).

Transference of pulse parameters between power supplies has plagued the industry for years. These problems were attributed to the measurement techniques, which before the invention of microprocessor DAQ were normally limited to average (mean) or RMS measurements of current and voltage (Ref. 93-101). Power calculated using the product of mean or RMS current and voltage did not capture effects of phase. In addition, there is significant power developed in processes where both current and voltage vary with time, are in phase, and increase in phase together as is the case with GMAW-P. Similar results were reported by Bosworth (Ref. 93, 94). In addition, Street and Rehfeldt (Ref. 95, 96) both noted that the true power in the arc, in general, should be based on the instantaneous product of voltage and current. These researchers studied the design of high frequency DAQ for welding to make these measurements. Other researchers recommended mean measurements for GMAW-P meters over the use of RMS, but did not have the capability to calculate AIP from waveform (Ref. 98-101).

Table 2.4 Calculations for Heat Input and Power (Ref. 92)

$H_{net} = P \bullet \eta / TS$	$I_{mean} = (\sum_{i=1}^{n} I_n)/n$
$P_{mean} = I_{mean} \bullet V_{mean}$	$V_{mean} = (\sum_{i=1}^{n} V_n)/n$
$P_{AIP} = \sum_{i=1}^{n} (I_n \bullet V_n / n)$	$I_{RMS} = \sqrt{(\sum_{i=1}^{n} (I_n^2)/n)}$
$P_{RMS} = I_{RMS} \bullet V_{RMS}$	$V_{RMS} = \sqrt{(\sum_{i=1}^{n} (V_n^2)/n)}$
P = power, η = efficiency, TS = travel speed, I = current, V = voltage	

In general, Joseph and Bosworth found that RMS power was always higher and mean power always lower than AIP. The error in measurement was the greatest at low pulse frequencies and wire feed speeds as shown in Table 2.5. This data from Joseph showed that the error in power measurements varied from 30 to 17%. Joseph proved that AIP was the correct power measurement by performing liquid nitrogen calorimetry measurements (Figure 2.24). The slope of each line in this figure was compared to the heat absorbed by the calorimeter. The only slope which equalled the heat absorbed by the calorimeter was heat calculated using AIP measurements. Based on the AIP curve intercept, the process efficiency η was calculated to be approximately 70% for GMAW-P bead-on-plate tests.

Table 2.5 Voltage and Current Measurements for One GMAW-P Power Supply (Ref. 92) (0.045-in. ER70S-6 wire with 90%Ar-10%CO_2 at 40 cfh)

WFS (in./min)	V_{RMS} (V)	I_{RMS} (A)	V_{mean} (V)	I_{mean} (A)	P_{RMS} (watts)	P_{mean} (watts)	P_{inst} (watts)	%Difference $100(P_{inst} - P_{mean})/P_{mean}$
100	21.40	119.10	20.83	69.69	2548	1450	1915	32.0
200	25.90	178.35	25.16	127.37	4619	3203	3931	22.7
300	27.69	225.44	26.98	180.63	6242	4874	5694	16.8
400	29.42	267.61	28.58	217.06	7873	6204	7245	16.7
500	31.70	297.67	30.95	250.20	9436	7740	8841	14.2

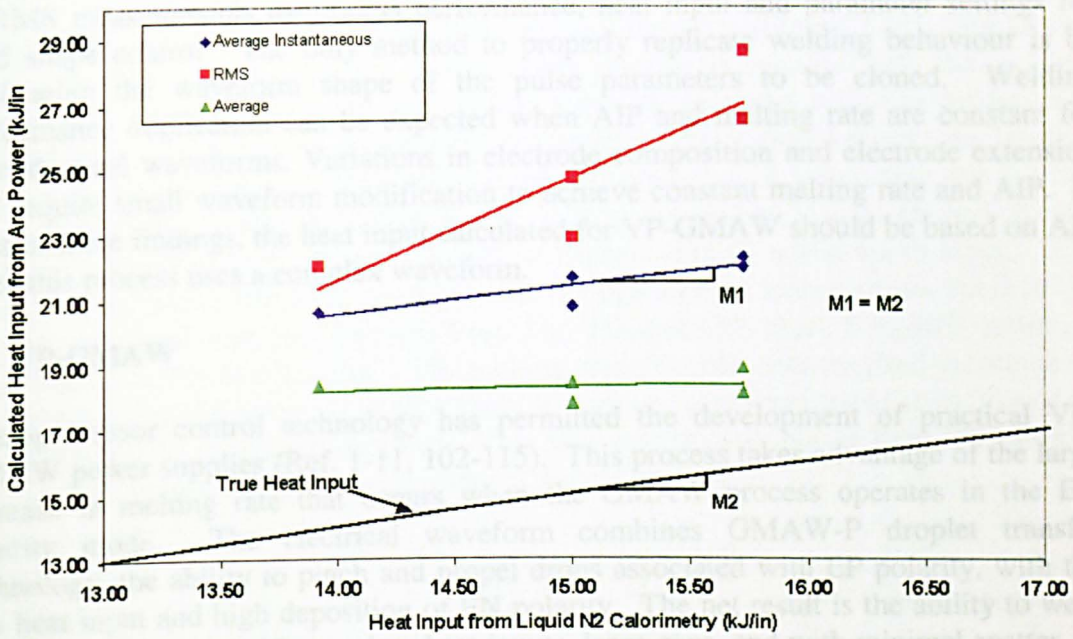

Figure 2.24 Comparison of Calculated Heat Input to Actual Heat Input for GMAW-P (Ref. 92)

2.7.1 Process Efficiency and Heat Input Measurements

Process efficiency, η calculated using calorimetry is determined by dividing the heat absorbed by the solution by the total heat supplied by the welding processes. Heat input (energy per unit length) calculations for arc welding processes have been established for years. This calculation is based on process efficiency times the product of voltage and current divided by the travel speed (TS):

$$\eta = \frac{H_{absorbed}}{H_{power\ sup\ plied}} \tag{2.29}$$

$$HI = \eta \frac{VxI}{TS} \tag{2.30}$$

As mentioned above, heat input, HI calculated using AIP is required to capture the true power of a GMAW-P arc, therefore this equation is modified as follows:

$$HI_{GMAW-P} = \eta \frac{AIP}{TS} \tag{2.31}$$

In light of these modern findings, much of the prior research in GMAW-P research is flawed and is the reason for much controversy over procedure transference and power supply calibration in industry. Many reports have been published trying to relate mean or RMS measurements to process performance, heat input and parameter settings for bead shape control. The only method to properly replicate welding behaviour is by duplicating the waveform shape of the pulse parameters to be cloned. Welding performance duplication can be expected when AIP and melting rate are constant for near identical waveforms. Variations in electrode composition and electrode extension will require small waveform modification to achieve constant melting rate and AIP. In light of these findings, the heat input calculated for VP-GMAW should be based on AIP since this process uses a complex waveform.

2.8 VP-GMAW

Microprocessor control technology has permitted the development of practical VP-GMAW power supplies (Ref. 1-11, 102-115). This process takes advantage of the large increase in melting rate that occurs when the GMAW process operates in the EN polarity mode. The electrical waveform combines GMAW-P droplet transfer technology, the ability to pinch and propel drops associated with EP polarity, with the low heat input and high deposition of EN polarity. The net result is the ability to weld thin gauge structures with very low heat inputs, large gaps, and with minimal spatter, or at higher welding speeds. The current is lower than most other forms of GMAW for a given wire feed speed except pure EN polarity GMAW, which is usually too unstable for most GMAW applications (Ref. 10).

The majority of VP-GMAW power supply technology is from Japan and was introduced in 1988 (Ref. 5-7). Since the early 1990's, several hundred power supplies have been sold in the U.S. Unfortunately, many industrial users do not understand the benefits of this technology since limited research has been published (Ref. 3, 4, 10, 11). This has deterred wide-scale implementation of VP-GMAW throughout industry. The power supplies offered by the Japanese manufacturers have pre-programmed algorithms and are presently limited to welding of mild steel, stainless steel and aluminium at currents up to 350 amps where the benefit has been the welding of thin gauge structures with large gaps (Ref. 10).

2.8.1 VP-GMAW Power Supply Development

The first power supplies that were used for alternating current (AC) GMAW had a drooping characteristic (Ref. 102-104). The current was controlled by using external conductors in stepped switches. The open circuit voltage (OCV) was typically 75 volts. The GMAW AC arc was stable only at 250 volts OCV or greater. This was considered an unsafe OCV for workers. Early researchers found that higher OCV's were needed with AC processes compared to DC processes to help with arc re-strikes after each zero. This was especially true as the arc went from EN to EP. The EN arc extinguished as the current went through zero. The arc was found to maintain a plasma of low conductance after the EP period so the re-ignition from EP to EN often occurred without delay.

Lucas (Ref. 102, 103) was the first to develop a surge ignition system which superimposed a high voltage surge at both zeros of the cycle (Figure 2.25). The charge circuit was basically a capacitor and damping resistor in parallel with the welding circuit. A detector firing circuit was used to sense the zero and pulse the voltage with the capacitor. The damping resistor inhibited reverse current flow between the ignition circuits. He found that the OCV could be safely lowered to 75 volts using this system, which provided a steady AC-GMAW arc. Using the system, Lucas studied several shielding gases that had different oxygen or carbon dioxide additions to argon. The focus was on which shielding gases provide enough surface activation to stabilize the EN arc and metal transfer. Oxygen from 2 to 5% and CO_2 from 5 to 20% additions were found to stabilize transfer. The melting transfer was characterised as projected where stable transfer occurred in EP. Useable melting rates were found to be from 5 to 16 m/min for 1.2 mm steel electrode. This was significantly higher than DC positive welding which only offered a melting rate of 8 to 11 m/min.

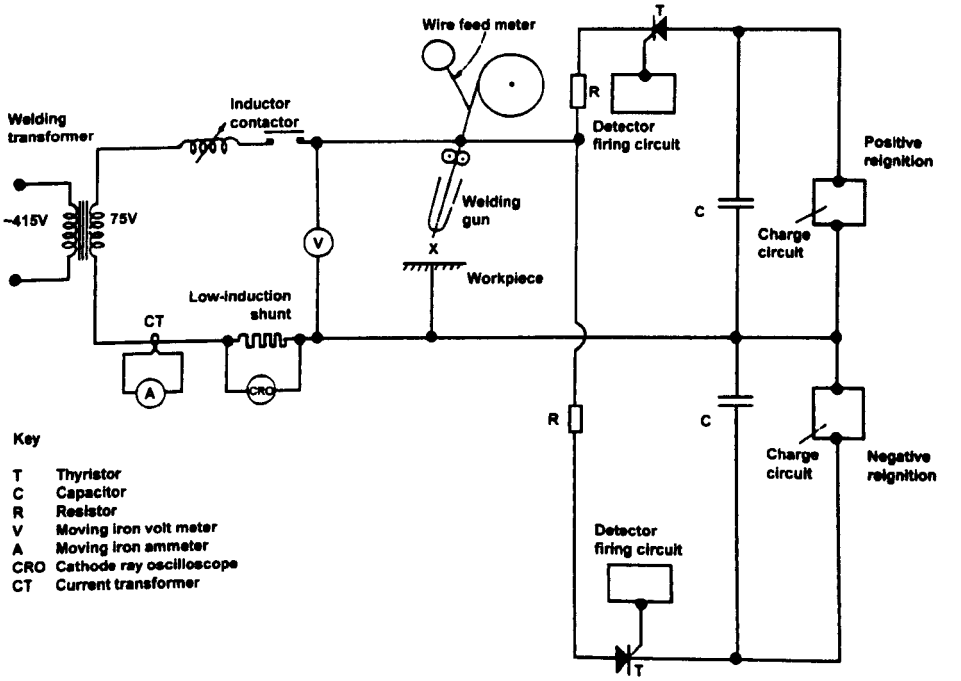

Figure 2.25 Welding Circuit for AC MIG with Surge Injection (Ref. 102)

In the mid-1980's, high current AC-GMAW was developed for the fabrication of line pipe in Japan (Ref. 105-109). Early research was successful at developing welding procedures using SAW power supplies that had a drooping characteristic and offered an excess of 1000 amps (Ref. 105). AC-GMAW was preferred over SAW on 9% Ni steels to achieve both good properties and reduced arc blow. The AC waveform promoted resistance to arc blow which had plagued the welding of this steel. Arc stability was obtained by activating the surface of solid wires at first. Cored wires were then developed to further improve activation. Titanium dioxide was the preferred constituent of the flux core where approximately 10% by weight gave the best stability. These electrodes were considered semi-flux cored as a light slag layer was produced. Silicon controlled power supplies were found to give better power control and process stability (Ref. 106). Tandem AC-GMAW techniques were fully developed to further improve productivity and arc stability. The phase relationship between each wire was used to control penetration and arc stability. This process used large electrodes, 4.8 mm, and very high currents compared with that used in work performed by Lucas. The high currents and arc stabilizers made the process very stable for heavy section fabrication. This process was not relevant to semi-automatic welding applications that typically use 150 to 350 amps for sheet to thin plate.

Standard AC power supplies with special re-ignition circuits like that developed by Lucas have seen very little use in industry. The approach taken to develop modern power supplies has changed from saturable reactors (like Lucas') through thyristor (SCR) and transistor control to inverter control. Development of power electronics using bi-polar transistors and later field emission transistors (FET's) led to the development of inverter power supplies (Ref. 1-11). Modern VP-GMAW power supplies were developed in the mid-1980's using inverter technology to permit welding of thinner materials. These power supplies have inverter switching frequencies from 10 to 40 kHz. These power supplies provided almost a pure DC control with little ripple after secondary rectification. Recent VP power supplies use a secondary inverter to shape the waveform (Figure 2.26) (Ref. 10).

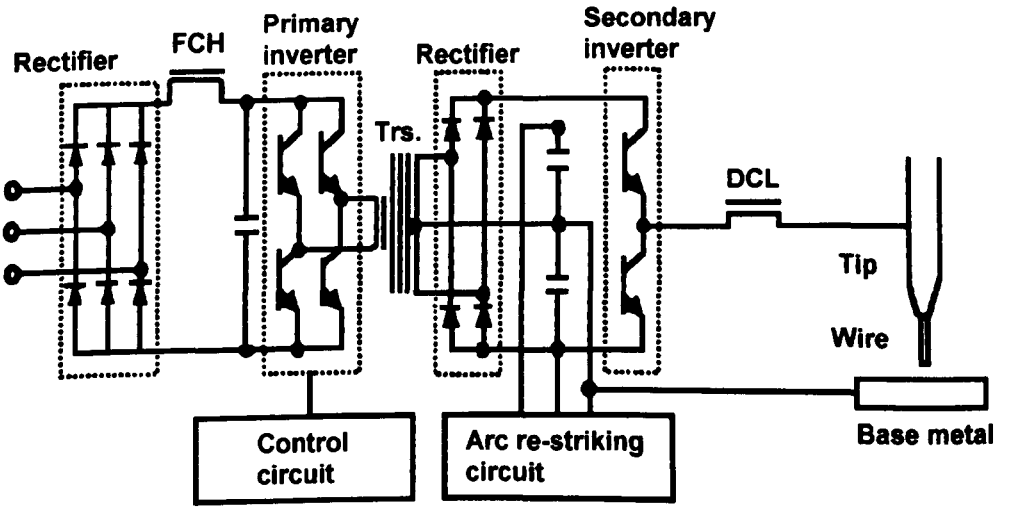

Figure 2.26 Schematic Diagram of the AC-GMAW-P Power Supply (Ref. 10)

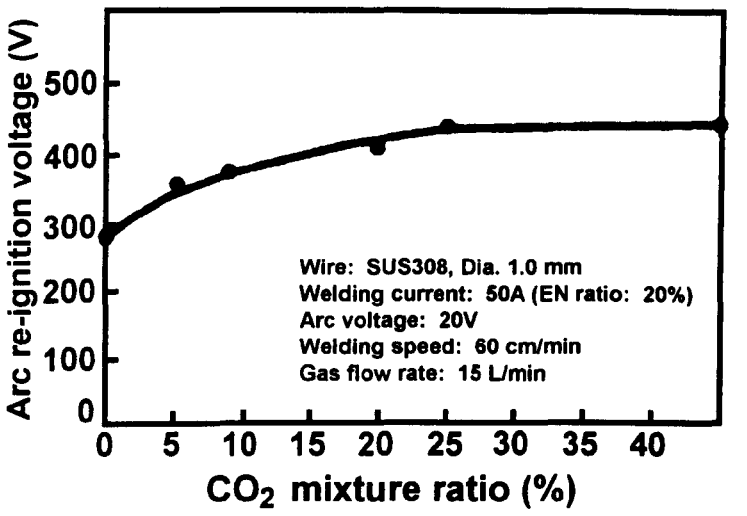

Figure 2.27 The Minimum Necessary Arc Re-Striking Voltage When Switching from EN Polarity to EP Polarity (Ref. 10)

This figure shows the block diagram of a modern VP type of power supply. The main circuit composes of a primary inverter. This inverter takes rectified AC line power and converts it to high frequency AC power. The output frequency from the primary inverter to the second rectifier is typically 2 to 30 kHz. In the primary inverter, pulse width modulation (PWM) is used to output current to the secondary inverter. Current from the primary inverter after rectification is almost pure DC (i.e., almost no line ripple). The secondary inverter is used to control the switching between EP and EN and, hence, control the %EN or polarity ratio, and waveform shape. The secondary inverter was designed with an arc re-ignition circuit to assure excellent arc stability through the current zeros. This circuit applies a high voltage surge across the zeros of a couple of hundred volts. Depending on the CO_2 content of the shielding gas, the re-ignition voltage was over 400 volts (Figure 2.27). These modern power supplies have employed IGBT's (Insulated Gate Bipolar Junction Transistors) that have a switching time of 1 to 2 μ sec. This is several hundred times faster than SCR's permitting the waveform shaping.

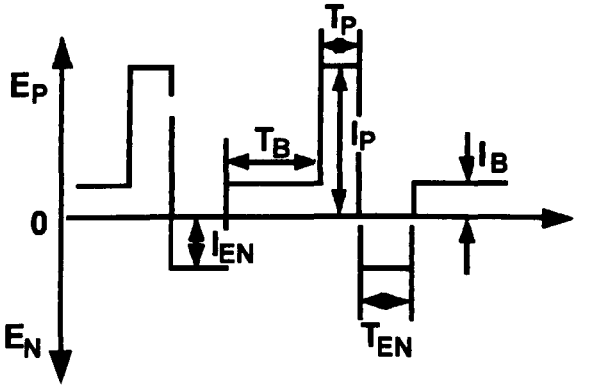

Figure 2.28 Waveform of AC-GMAW-P (Ref. 10)

The percent of EN can be defined as the EN time divided by the pulse period. The EN ratio is defined by the product of EN time times current divided by the absolute product sum of current times time over that period. The former method (%EN) is easier to calculate since the latter requires current integration over time, which can be difficult if the waveform has curvature. The EN ratio and %EN for a typical VP-GMAW waveform as shown in Figure 2.28 are defined as:

$$ENratio = \frac{I_{EN}t_{EN}}{(I_p t_p)+(I_b t_b)+(I_{EN}t_{EN})} \tag{2.32}$$

$$\%EN = \frac{t_{EN}}{t_{EN}+t_{EP}} \tag{2.33}$$

2.8.2 VP-GMAW Waveform Technology

In waveform controlled AC-GMAW, the EN and EP periods are repeatedly alternated for polarity switching and waveform shaping to develop the VP waveforms. The nomenclature for VP and AC are used interchangeably but in the USA, VP normally indicates non-symmetric AC waveform. A number of waveforms are offered by commercial power supplies, which are all from Japan, as shown in Figure 2.29. These waveforms are controlled almost entirely by using software and microprocessor controls (Ref.10).

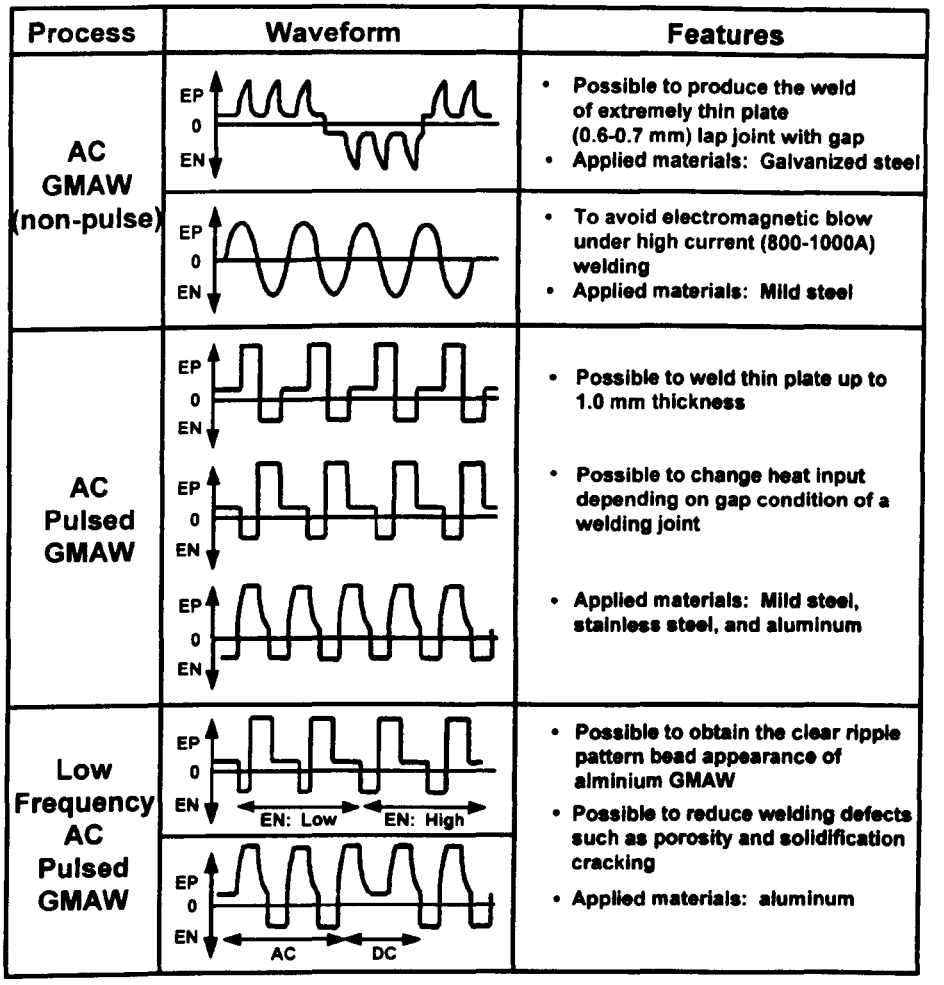

Figure 2.29 Welding Current Waveform Types of AC-GMAW (Ref. 10)

This figure shows seven different waveforms that can be used for AC- and VP-GMAW. The first category, AC-GMAW (non-pulse) defines waveforms for extremely thin materials, and high current SCR-based technology developed for line pipe welding (Ref. 105-109). The second category shows three types of VP-GMAW waveforms that are used for welding thin materials and provide a range of heat input. The latter characteristic permits welding of thin materials with large gaps where larger weld deposits are required.

The first waveform in the second category was studied in detail in this investigation. Here, a period starts with an EN pulse to melt a droplet. The EP background (EPB) current is used to maintain the droplet before switching to the EP peak (EPP) period which pinches off the droplet (Ref. 10). These waveforms have been developed for steel, stainless steel, and aluminium.

Different waveforms shown in Category 2 were developed by different suppliers to avoid patent infringement. These different waveforms may achieve the same goal, but the metal transfer stability may vary significantly depending on the robustness of the developed waveform.

The third category, also known as pulse on pulse was developed to produce VP-GMAW welds that appear like a GTAW weld. Some manufacturers prefer the appearance of coarse weld ripples on their products, like motorcycle frames. The waveforms have also been shown to improve grain structure by disrupting columnar solidification in materials like aluminium alloys. This also improved the resistance to porosity and solidification cracking.

All the above waveforms are designed to provide a pulse globular transfer. This is different from the projected transfer described by IIW in Section 2. Here, the droplets formed during the EN period grow to be of globular size. The difference lies in the high current EP pulse which provides a stiff arc and accelerates the globular drop towards the weld pool. The Lorentz force in low current projected transfer does not produce high drop velocities.

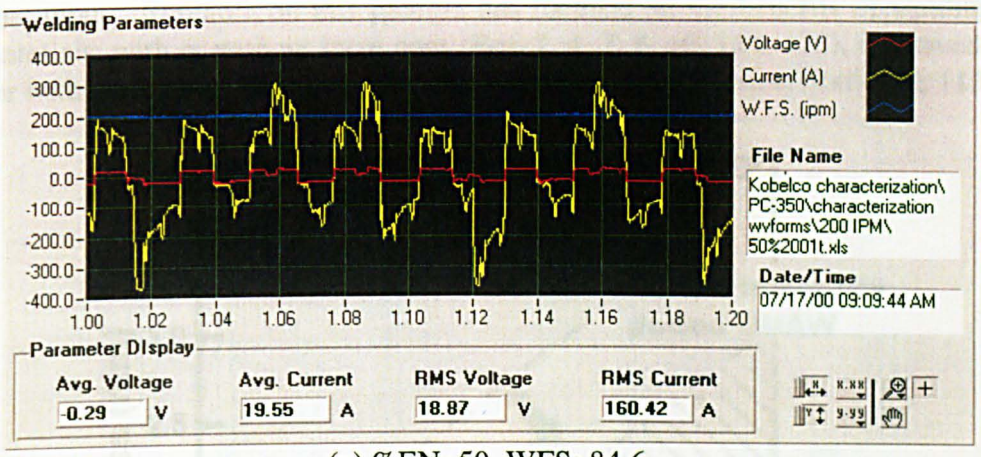

(a) %EN: 50, WFS: 84.6

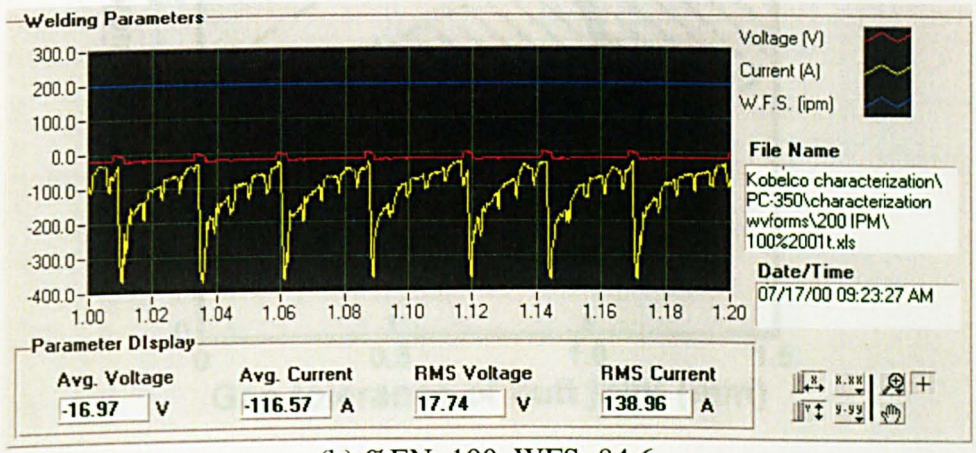

(b) %EN: 100, WFS: 84.6

Figure 2.30 Fuzzy Logic VP-GMAW Waveform with Short Circuit Anticipation Control; (a) EN ratio = 50% and (b) EN ratio =100% (Ref. 1, 8)

In addition to these waveforms, one equipment supplier has developed a hybrid VP-GMAW power supply that incorporates a short circuit anticipation control (Figure 2.30) (Ref. 1, 2, 8). This power supply constantly oscillates the current in both the EP and EN

periods and actually senses the weld pool. The current in each period is oscillated down to promote a low current short circuit droplet transfer. Depending on the %EN set by the control pendant, the fuzzy logic control will either switch polarities or repeat a pulse of the same period. The droplet transfer of this power supply has a more random frequency. The benefit of this power supply is to offer an even larger range in heat input control and provide droplet transfer with 100% EN waveforms.

2.8.3 Characteristics of VP-GMA Welds

The EN polarity of the GMAW process suffers from unstable globular transfer (Ref. 12, 13, 27, 28, 103 110) where drop sizes can be an order of magnitude larger than the wire diameter, unless high current are used with activating shielding gases (Ref. 29). VP-GMAW basically provides a pulse globular transfer where the drop size can be controlled, and is typically 1.5 to 3 times the wire diameter, permitting stable welding at low heat inputs. Research on this process has focused on the benefits of welding very thin materials, with or without large gaps (Ref. 2, 4, 7, 8, 10, 114, 115), improved metal transfer with aluminium electrodes (Ref. 9, 10), and fume reduction (Ref. 112, 113).

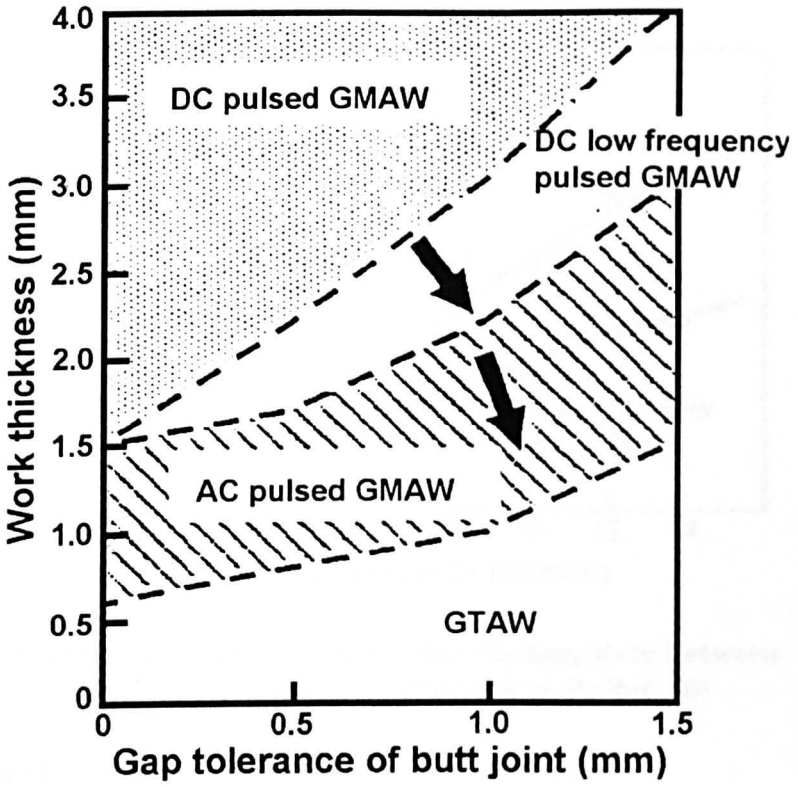

Figure 2.31 Comparison of Available Work Thickness and Gap Tolerance of Aluminium Among Various Welding Processes (Ref. 7)

The VP-GMAW process was found to provide good weldability on materials as thin as 0.6 mm with no gap (Figure 2.31). The process can easily tolerate gaps, T equal to 1T for materials up to 1.5 mm. The improved gap tolerance was a result of improved melting rate allowing the deposition of larger deposits at lower heat input (Ref. 7). The

process was found to provide heat inputs that were at least 25% less than GMAW-P and almost half that of CV spray for the same wire feed speed.

The process offered significant advantage for aluminium where fume was significantly lowered (Ref. 112, 113). The mechanism for reduced fume was related to droplet size and temperature. The EN arc was found to melt the droplet without significant heating. This resulted in a significant reduction in spatter in Al-Mg filler metals like 5356. Droplets in this material were found to explode due to vaporisation of magnesium inside the drop. In addition, the larger drops provided a larger drop surface area to volume ratio that minimized vaporisation of the drop surface during transfer in the EP period.

No systematic research on VP-GMAW was found that related melting rate characteristics to arc and resistive heating properties like that performed by Richardson (Ref. 75) on GMAW-P. Some research provided simple analysis on the effects of waveform parameters on droplet volume, stability, and susceptibility to spatter. Several researchers showed the current reducing effects of EN heating to maintain the melting rate in VP waveforms (Ref. 2, 5, 7, 10). These were simple plots, Figure 2.32 for example, that compared current to wire feed speed for different EN ratios.

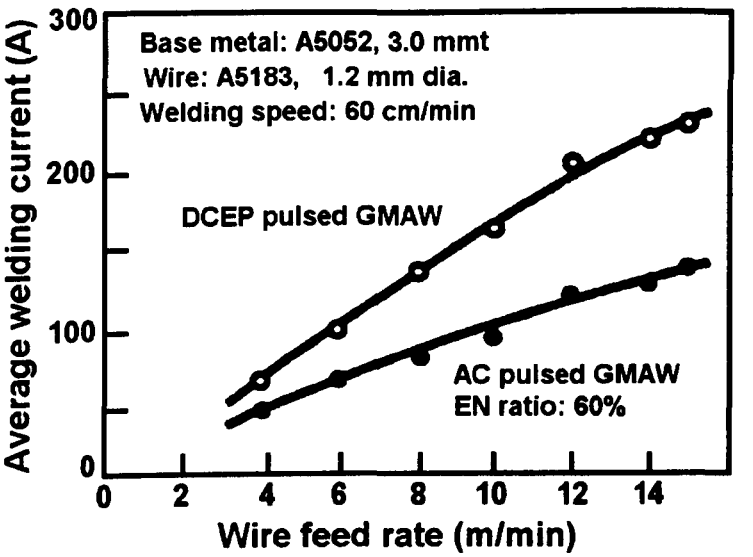

Figure 2.32 Comparison of Wire Melting Rate Between DCEP GMAW-P and AC-GMAW-P (Ref. 10)

2.8.4 VP-GMAW Review Summary

Based on the literature review provided here, there appeared to be a technology gap on the melting rate behaviour of the VP-GMAW process. The research presented has focused on the development of power supplies that permit waveform control, working VP pulse parameters, and commercialisation of equipment. Engineering relationships were needed to provide an analytical approach for designing waveforms and predicting the resulting melting rate. This knowledge may improve the strategy used to develop VP-GMAW processes and widen industrial deployment to new applications and

materials. This project sought to characterise the metal transfer of the VP-GMAW process with emphasis on how each VP waveform component affected the electrode melting and droplet growth.

2.9 Process Benchmarking

Process benchmarking is important for arc welding applications because there are so many choices in power supply waveforms, electrode types and sizes, and shielding gases. For mild steel welding applications, the number of process choices can easily exceed a hundred possible combinations. Since VP-GMAW offers improved welding travel speeds, and reduced heat input and fume, benchmarking tests were performed in this investigation to compare VP-GMAW to GMAW-P for welding sheet steel lap joints. The following review describes a preferred method for benchmarking that has been developed in the USA.

The author has been involved in welding process benchmarking since 1996 (Ref. 116-118). As a result of these efforts, a formal method was developed named ARCWISE™ which integrates preferred process measurements and test methodology to determine the capability of a welding process for an application. The definition of an application was a set of fixed design factors such as base materials, joint type, position, weld size, bead shape, and mechanical properties requirements.

In typical welding-related reference publications (Ref. 29, 30, 31, 39, 77-81, 199-121), the following types of operational characteristics for consumable electrode processes were common:

- Voltage versus current
- Wire feed speed versus current
- Deposition rate versus current.

Examples of these graphs were also provided by Lesnewich in Figure 2.4. These graphs show the effects of electrode diameter, shielding gas, electrode extension, and polarity. However, they ignore the effects of application weld size, joint design, CTWD, and arc length. Therefore, these graphs were not "application representative," making it difficult for an engineer to select actual weld parameters. The ARCWISE data have been shown to yield a set of graphs from welding tests that represent an application. The operational windows that were identified can be used to select preferred welding parameters for that application.

The objective of this method was to eliminate defects, develop welding strategy, establish benchmarking criteria, and optimise productivity. Most welding procedures have been developed by a trial and error approach. Some welding technicians and engineers have tried statistical parameter development techniques (Ref. 122-127) but these approaches only worked once a sound weld procedure was developed and the weld tests used boundary conditions which produce sound welds. Many weld applications have not had well defined weld property requirements for bead shape, mechanical properties, and soundness. For example, if fatigue strength is the dominant property for

an application, then weld parameters must be optimised to control weld bead shape and size; especially toe radius. Quality measurements used to select optimum welding parameter must relate to key control characteristics. The ARCWISE method factors these objectives and develops preferred process relationships for an application. The six elements of the ARCWISE method (Ref. 118) were described as follows:

1) Weld Bead Sizing Strategy and Acceptance Criteria
2) Constant Deposit Area Test Matrix
3) Constant Arc Length Testing
4) Graphical Data Analysis
5) Bead Shape Measurements and Map
6) Welding Productivity Window Analysis.

The unique aspect of this method was the constant arc length testing where arc length was adjusted for each test to a preferred distance. It has been well known amongst welders, that arc length was critical for proper weld pool performance, yet this important aspect of parameter development has been consistently overlooked. Constant deposit area tests have been shown to isolate the effects of parameters, weld position, and torch angles for a given application. It has also been shown that travel speed affects the base metal melting efficiency of the welding process based on the selected consumables, torch setup and waveform (Ref. 118, 128).

For each set of consumables and waveform, there was an optimum travel speed level that produced the preferred penetration and base metal fusion for that weld size. Different processes offer different electrode melting rate as a function of welding heat input. Basically, as the electrode melting rate efficiency of the process increased, higher travel speeds (productivity) were used to achieve the same base metal fusion quality compared with a process that has lower electrode melting rate.

An example of an ARCWISE data set for ¼ in. (6 mm) fillets made in the flat position is provided in Figures 2.33 and 2.34. Notice the good bead shape that was produced at 15 ipm travel speed. Lack-of-fusion was observed at 10 ipm travel speed with the buried arc length. Excessive penetration and convexity were observed at the highest travel speeds. The corresponding welding parameters for procedures can be quickly selected from the graphs in Figure 2.34.

From a relatively small group of 15 to 24 test welds, the ARCWISE method was shown to yield an integrated set of parameter relationships, corresponding weld bead shapes, and graphical representations that described operational and productivity operating capabilities of the tested welding process and filler metals. Done properly, it examined the full range of the process for a specific application, taking into consideration weld quality requirements.

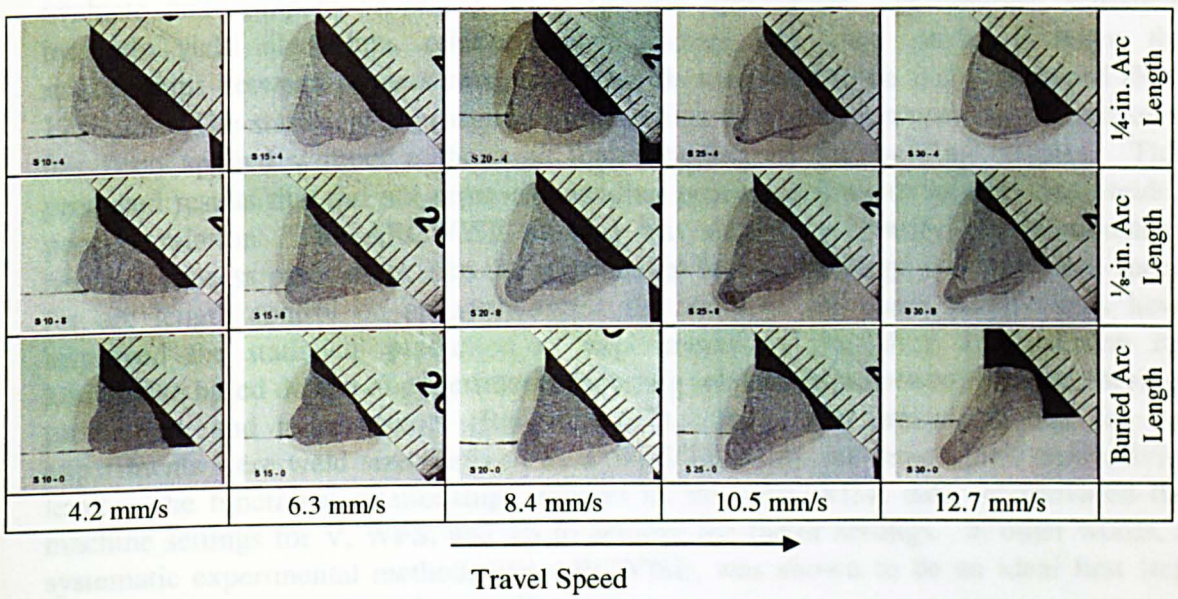

Figure 2.33 Bead Shape Photomacrographs for a GMAW Process (Ref. 118) (Average Deposit Area = 0.0362 in^2)

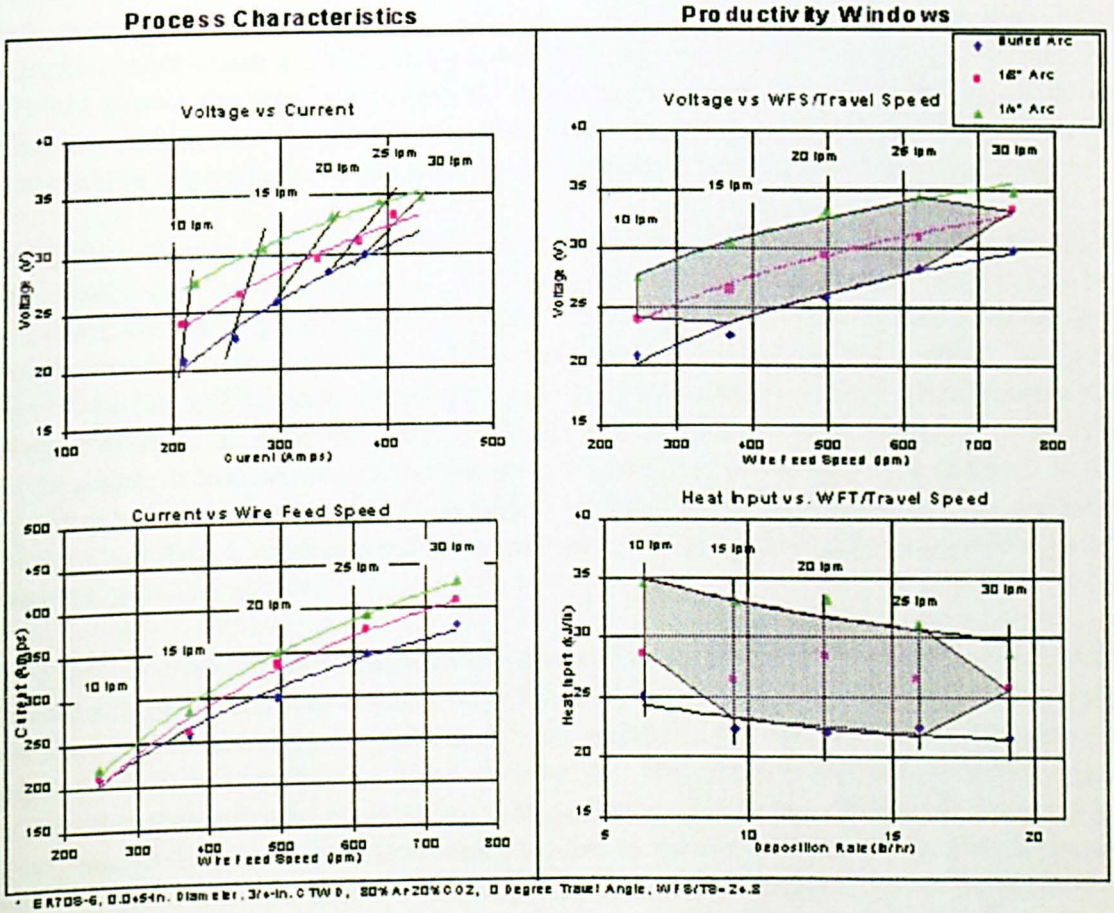

Figure 2.34 Parametric Graphs for ¼-in. Fillet Welds Using a GMAW Process

It is important to emphasize that the ARCWISE experimental method was best suited to evaluate and compare *processes* for a specific application. In contrast, statistical methods yield algorithms relating many factors and were preferred when the relationships between process and *production factors* need to be fully optimised (Ref. 125-127). The statistical approach required a high level of expertise and sometimes it has been applied without a thorough understanding of the welding process. This produced results that did not represent welding process behaviour reliably and yielded poor correlation. The ARCWISE method was shown to identify key relationships between process parameters, like the relationship between voltage and wire feed speed for arc length control on an application. In addition, the same relationships have improved the statistical prediction of experiments by providing a foundation for knowledge based design of experiments factoring relationships between process, design, production, and noise factors (Ref. 125-127). Here, key process factors for the experiments were weld size (defined by a WFS/TS ratio), arc length, and productivity level. The functional relationships defined by the ARCWISE data set provided the machine settings for V, WFS, and TS to achieve the factor settings. In other words, a systematic experimental method, like ARCWISE, was shown to be an ideal first step towards optimisation of welding applications.

3.0 RESEARCH AIMS AND OBJECTIVES

The literature review emphasised melting rate, metal transfer behaviour, and the development of waveform controlled GMAW processes, like GMAW-P and VP-GMAW. Based on the literature review provided here, there appeared to be a technology gap on the principles controlling melting rate, metal transfer, and arc behaviour of the VP-GMAW process.

The general melting rate equation was described in detail in Section 2. The relationship for DC GMAW was developed by Lesnewich (Ref. 12). Based on his research, a well accepted form of the melting rate equation has been established for a given electrode type and diameter for the spray metal transfer mode. This equation is a second order polynomial that uses terms for arc and resistive heating. The arc heating term is dependent on the polarity, and electrode type and size. For EN heating the arc heating term is also a function of shielding gas and electrode activation. The resistive heating term is based on I^2R heating that occurs in the electrode extension.

Allum (Ref. 63) and Richardson (Ref. 75) both attempted to use this fundamental melting rate equation to explain the behaviour of GMAW-P. Their research assumed the waveform was totally responsible for changes in melting rate. Under this assumption, the arc and resistive heating coefficients were believed to be constant for each polarity, and electrode type and size. The improved melting rate was solely attributed to increases in I^2R heating in the electrode extension. The research performed here has shown the transient behaviour of the arc at the electrode tip has a significant effect on melting rate for identical waveforms. The resistive heating (I^2R) effect was secondary in importance compared to the arc heating effect using pulsed waveforms.

Richardson showed that the burnoff diagram techniques (BDT) can be used to determine empirically the arc and resistive coefficients for GMAW processes, especially CV processes that have uniform metal transfer. When the BDT was applied to GMAW-P waveforms, both Allum and Richardson used an effective current parameter to make the data fit the burnoff diagram. This approach made quantitative prediction of melting rate using different waveforms very difficult and accuracy was marginal. In this investigation, it was decided to use the BDT to study electrode melting rate based on the droplet growth and position in each period of VP-GMAW waveforms. This approach gave a good data fit and allowed characterisation of arc and melting rate behaviour in complex waveforms.

To establish working pulse parameters, researchers (Ref. 63, 77, 78, 81) established a detachment parameter that described the GMAW-P pulse energy requirements for metal transfer. The detachment parameter was believed to satisfy the relationship for improved resistive heating for pulse waveforms. The detachment parameter was based on the energy required to achieve one drop per pulse conditions. However, industry has been plagued with cases that show that this simple relationship cannot be used to predict melting rate and metal transfer stability. In fact, most modern power supplies have empirically developed pulse parameters that are not based on a well defined algorithm (Ref. 92). To remedy the technology gap, most power supply manufacturers provide

waveform parameter development tools which allow the user to optimise metal transfer stability for a given melting rate. The user, lacking fundamental knowledge usually develops pulse parameters through trial and error. This investigation showed that the EN period and/or EP background period controlled the EP pre-pulse droplet volume. The melting rate of identical EP pulses was dependent on the pre-pulse droplet size. Based on these observations, the detachment parameter can only be used under a small range of pulse waveforms that have similar pre-pulse droplet size. Wide changes in pulse parameters that affect droplet size will surely lead to error using the detachment parameter approach.

For VP-GMAW, the research reviewed (Ref. 4-11, 102-115) has focused on the development of power supplies that permit waveform control, working VP pulse parameters, and commercialisation of equipment. Engineering relationships are needed to provide an analytical approach for designing waveforms and predicting the resulting melting rate. This technology will promote deployment of VP-GMAW in applications, like welding sheet steel and cladding vessels that can benefit from the lower heat input and higher melting rates of this process. In addition, the arc behaviour, and its interactive effects on melting rate, was not understood for VP-GMAW waveforms.

This project characterised the metal transfer of the VP-GMAW process with emphasis on how each VP waveform component affected the arc behaviour, electrode melting, and droplet growth. The projected started by benchmarking two VP-GMAW power supplies for welding sheet steel lap joints. The ARCWISE parameter development method (Ref. 116-118) was used to establish the welding parameter windows between voltage, current, wire feed speed, and travel speed, etc. looking at each waveform parameter set holistically. The ARCWISE graphs were found useful for relating weld heat input and travel speed to weld bead shape, and assessing the productivity potential of different waveforms. Burnoff diagrams, which are used to characterise melting rate, were plotted from this data and provided little insight on the effects of complex waveforms. It became apparent during these tests that a new method was needed to properly characterise the metal transfer behaviour of VP-GMAW. Initial high speed video observations showed that electrode melting rate and droplet growth were very dependent on the waveform, arc behaviour and droplet size.

The droplet burnoff rate (DBR) method was developed so the true melting rate at the electrode tip could be measured and used to separate the effects of waveform parameters and polarity. The DBR method was based on measuring the electrode melting rate of each period used high speed video that was synchronised with high speed data acquisition. The corresponding waveform parameters (current and time), and electrode and droplet dimensions were measured and used to calculate melting rate. The data was then used to create burnoff diagrams, based on the approach by Richardson that can be used to solve for melting rate coefficients. The burnoff diagram plots burnoff rate, BR versus the electrode extension heating factor, F_L. The intercepts and slopes of lines made with this diagram equal the arc heating and resistive heating coefficients, respectively for different waveform period conditions. The magnitude and changes in these coefficients for each period were related to arc behaviour and droplet size. The

DBR method was used to develop new understandings for how waveform and arc behaviour affect melting rate in advanced GMAW processes.

The concentrated melting theory was developed to explain the significant increase in electrode extension burnoff and droplet growth rate that occurred at short EN time as a function of current, and during EP peak pulse when the pre-pulse droplet volume was small. The highest electrode extension burnoff and droplet growth rate occurred when the arc was permitted to climb over the solid electrode tip producing rapid concentrated melting. Likewise, large molten droplets were found to promote a negative electrode extension burnoff and a decreased droplet growth rate. The arc rooted on large droplets providing additional heating but limited electrode melting. The concentrated melting theory is supported by work performed by Norrish (Ref. 29) who observed rapid melting during constant voltage EN metal transfer as the arc switched between the single and multi-spot cathode modes. In the multi-spot mode, the arc rapidly consumed virgin electrode, where in the single spot mode, the melting rate decreased as the arc rooted on the bottom of the droplet until transfer occurred.

The DBR method was developed and found to yield good experimental measurements for the arc and resistive heating coefficients used in a melting rate equations developed for VP-GMAW. The coefficients were not as physically linked to arc and resistive heating based on the work by Lesnewich, but provided good characterisation of second order behaviour for each period of the waveform. For the EN period, the EN time affected the melting rate as a function of EN current. The greater melting rate that occurred at low EN time was measured by the change in the resistive heating coefficient. The melting rate of the EP pulse was related to the pre-pulse droplet volume. Large pre-pulse droplets decreased the EP melting rate. The reduced melting rate was related to the position of the arc root relative to the electrode tip and droplet. The changes in EP melting rate due to pre-pulse droplet volume were measured by changes in the arc heating coefficient, which could be negative with large pre-pulse droplets.

Based on the developed approach and subsequent results, the objectives of this investigation were as follows:

1) Develop an electrode melting rate measurement method that can accurately solve for the arc and resistive heating coefficients of advanced waveform processes, like VP-GMAW and GMAW-P.
2) Determine the effects of VP-GMAW waveform on electrode melting, and the droplet growth and detachment process.
3) Measure the change in arc and resistive heating coefficients for a full range of VP-GMAW waveforms and determine the underlying mechanisms for differences due to polarity and waveform.
4) Compare the measured arc and resistive heating coefficients to measurements made by prior researchers to determine the validity of the DBR method which employed the BDT to solve for the coefficients.
5) Determine whether EN arc heating dominates the melting rate or does the electrode extension resistive heating (I^2R) dominate.

6) Determine the influence of droplet volume from EN melting on the melting rate of EP pulse.
7) Derive a melting rate equation for VP-GMAW and evaluate whether accurate predictions can be made using coefficients measured using the DBR method.
8) Provide benchmarking data to assess the benefits of improved melting rate and lower heats inputs with VP-GMAW compared to GMAW-P by comparing the travel speed potential for welding lap joints on sheet steel.

4.0 EQUIPMENT AND MATERIALS

This project evaluated the metal transfer behaviour of the VP-GMAW process. An assessment of welding systems that were commercially available was performed to determine the state-of-the-art. The majority of welding trials involved bead-on-plate and lap joint tests on sheet steel, and, to some extent, stainless steel coupons. Moving table welding stations were fabricated to permit analysis of metal transfer using high speed video (HSV) that was synchronised with high speed DAQ. The quality of welds was examined using standard metallographic procedures.

4.1 Equipment

4.1.1 Power Supplies

The power supplies evaluated in this work consisted of two CC inverter types that have pre-programmed EN/EP ratio control. The Kobelco PC350 (Figure 4.1) was developed for steel and, in addition to the variable EN/EP ratio control, it employs a short circuit anticipation drop transfer mechanism (Ref. 1, 2, 8). The waveform of this process uses a fuzzy logic control where the current peak waveform is varied continuously from peak levels downward anticipating the short circuit. Once the short circuit is detected, the process either increases current and repeats the process, or switches polarity. The overall waveform was observed to alternate between the peak current of each polarity. The EN and EP period length was also observed to vary based on the fuzzy-logic control. Here, the time in each period was believed to be controlled based on sensing the short circuit and continuously calculating the EN ratio. Based on the target EN ratio, the power supply would pulse the current again in the same polarity or switch polarity to control the EN ratio.

The OTC AC/MIG 200 (Figure 4.2) power supply was developed for steel and stainless steel, and provides a pulse globular free flight transfer mode. This power supply uses a traditional waveform for EP where a background and peak current is used for maintaining the arc and for droplet detachment. The EN waveform is square, can be varied for different amplitude and duration with the pendant settings, and is used to create the droplet.

Both power supplies automatically control the relationship between the pulse parameters (Figure 4.3), which includes the EN peak current and time, the EPP current and time, the EPB current, and frequency depended on the wire feed speed and EN setting on the control pendant. The EN pendant setting automatically changes the pulse parameter relationships for each wire feed speed providing a range of arc power. Arc length control is provided on the control pendants where the pulse frequency is increased to increase arc length or vice versa.

Figure 4.1 Kobelco PC350 Power Supply

Figure 4.2 OTC AC/MIG 200 Power Supply

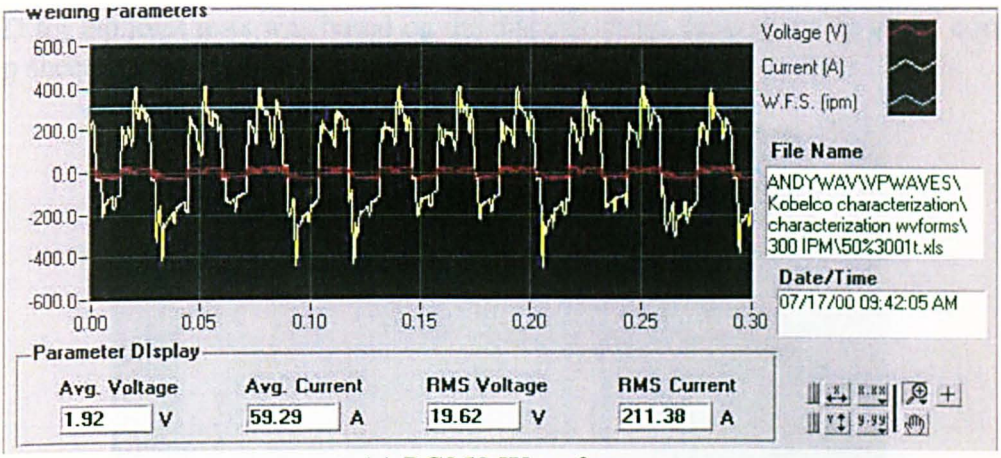

(a) PC350 Waveform

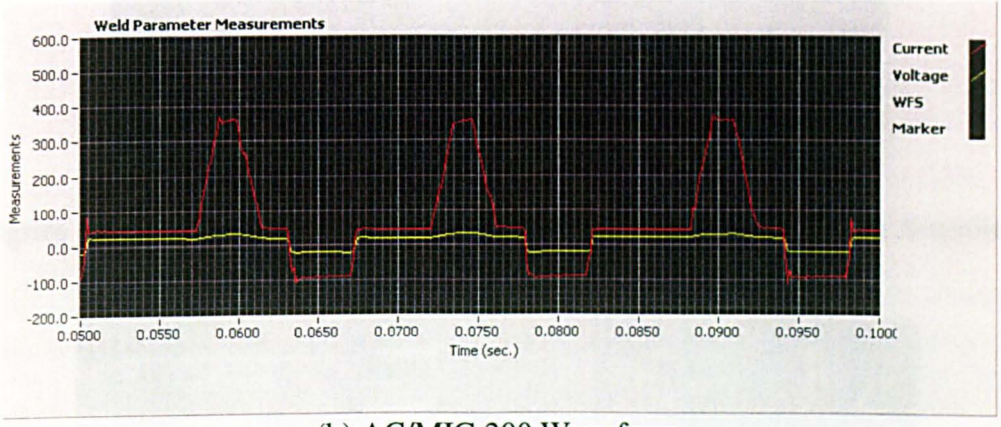

(b) AC/MIG 200 Waveform

Figure 4.3 Typical Waveforms for PC350 and AC/MIG 200 Power Supplies

4.1.2 Welding Stations

The power supplies were evaluated from bead-on-plate and lap joint tests made from sheet material. The bead-on-plate tests were used to study metal transfer. The lap joint application was selected to evaluate sheet metal weldability since the main benefit of VP-GMAW is the welding of thin sheet material where joint fit-up is prone to gaps. Tests were made using a stationary straight machine welding gun and a linear table that moved the base material at a constant speed (Figure 4.4). This setup allowed the HSV equipment to be stationary so the HSV lens could be focused directly on the welding arc and weld pool during each test.

The moving table was able to vary the welding speed from 4.2 to 25.3 mm/s. The travel driver/axis was manufactured by Jetline where controls were provided for arc start, travel delay, and stop. Pendants provided with each power supply were triggered manually to produce tests. During each weld the high speed DAQ and video was initiated to evaluate steady-state conditions. A simple fixture (Figure 4.5) was mounted on the travel axis to permit clamping of either bead-on-plate or lap joint specimens. The

CTWD for lap joint tests was based on the distance from the contact tip to the corner of the top sheet as shown in Figure 4.5.

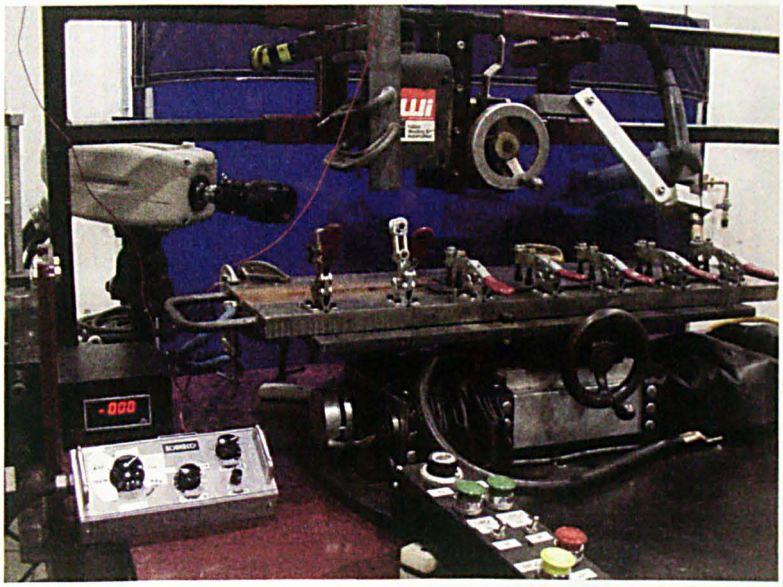

Figure 4.4 Lap Joint Test Setup for Evaluating VP-GMAW Power Supplies with Moving Table Welding Fixture

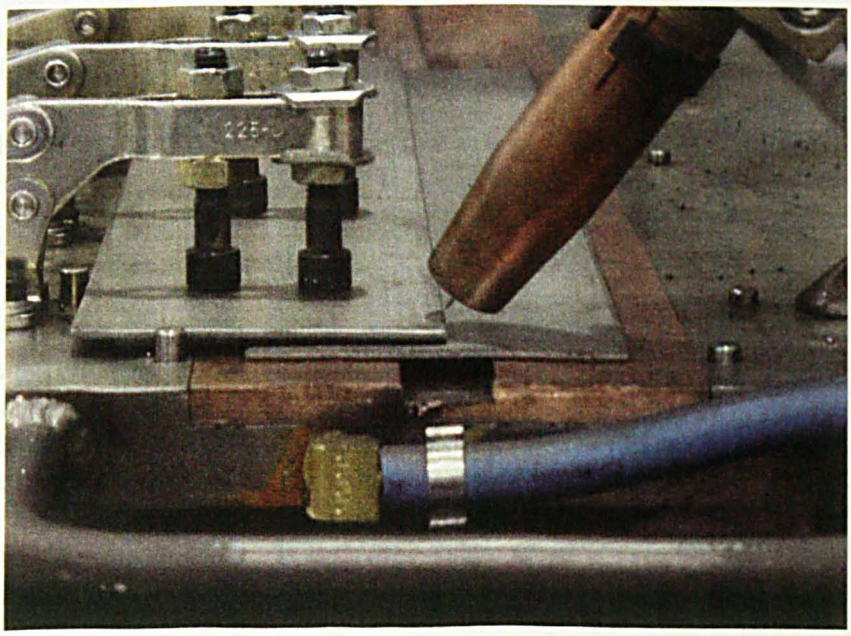

Figure 4.5 Lap Joint Test in Fixture

Lap joint specimens were also made using an OTC robot with the AC/MIG 200 power supply (Figure 4.6). This robot has a laser stripe vision system that can measure gap in real-time permitting adaptive VP-GMAW of sheet metal applications. The adaptive features of this robot were not utilized in this investigation, but the knowledge gained from the lap joint tests could be used to develop an adaptive algorithm.

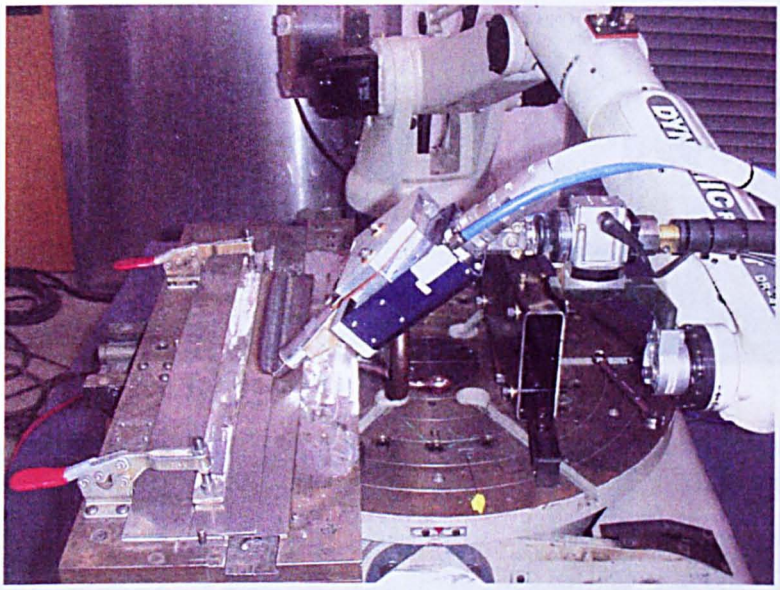

Figure 4.6 OTC Robot Used with AC/MIG 200 Power Supply for Lap Joint and Bead-on-Plate Tests

4.1.3 HSV Camera

A HSV camera (Figure 4.7) manufactured by Phantom was positioned to measure droplet transfer during VP-GMAW tests. The camera used a complementary metal oxide semi-conductor (CMOS) array. This type of camera is faster than charged coupled device (CCD) cameras. The higher frame speeds are a result of the digital signal produced by the CMOS sensor, which is immediately integrated into the image. CCD cameras require signal conversion from digital to analog to digital again for signal processing. In addition, the CMOS camera signals can be evaluated real-time and at any point in time.

The CMOS camera had frame speeds of 1000 to 60,000 fps. The control system with this camera permits control over both vertical and horizontal screen dimensions at frame speeds greater than 11,900 fps. The memory size ranged from 0.9 to 2 sec. The software permitted integrated acquisition, playback, recording, and viewing. Sections of memory can be downloaded, as preferred, reducing the download time to permanent memory as mpeg or compressed format. Measurement tools were used to populate an Excel™ spreadsheet for droplet and electrode dimensions as a function of time. Droplet surface boundary detection was aided with edge and colour functions.

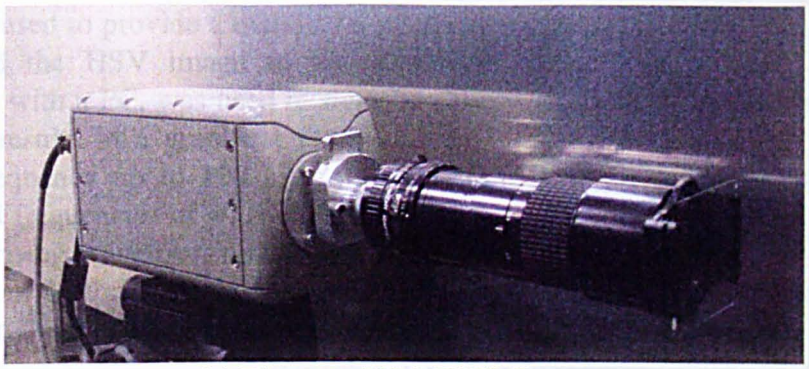

(a) Phantom V5.0 HSV Camera

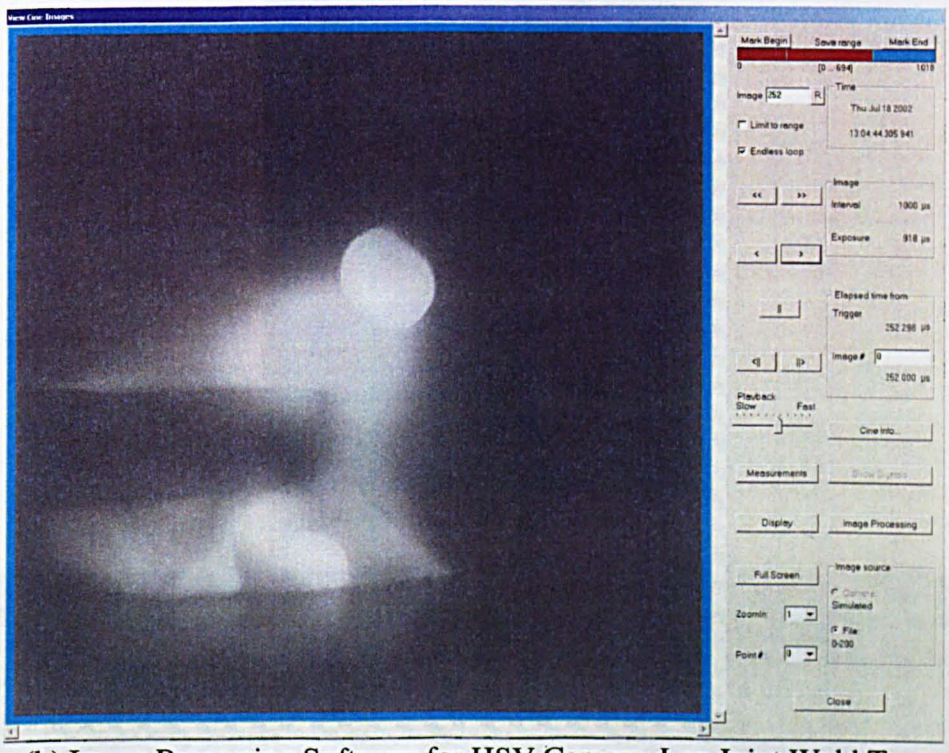

(b) Image Processing Software for HSV Camera; Lap Joint Weld Test

Figure 4.7 HSV Camera Used for Metal Transfer Measurements

The majority of tests performed in this investigation were performed using a frame speed of 3700 fps where the frame speed and shutter were adjusted to optimise the droplet image for different portions of the VP-GMAW waveform. The resolution at this frame speed was 512 by 512 pixels. This was required to accommodate the wide variation in light intensity from EP to EN current. The electrode extension neck position was closely measured and used in melting rate calculations with the wire feed speed.

4.1.4 High Speed DAQ

A high speed DAQ system, designed by EWI, was used for measurements of current, voltage, and wire feed speed (Figure 4.8). A trigger signal (marker) provided by the

camera was used to provide a marker on the graphical display of data waveforms. This synchronised the HSV image to the waveform of the DAQ. A DAQ card, in combination with a PC, was used to monitor voltage, current, and wire feed speed, and display the results in a graphical format. The DAQ software provided selection of sampling frequency up to 100 kHz for one channel. The power supply waveform typically had frequencies of 40 to 100 Hz. The sampling frequency was set at 8000 Hz for characterising waveform period effects on melting rate. This sampling frequency was more than 80 times the highest pulse frequency minimizing aliasing of the signal. A 5000 Hz low-pass filter was used to remove noise from the power supply.

(a) DAQ control cabinet

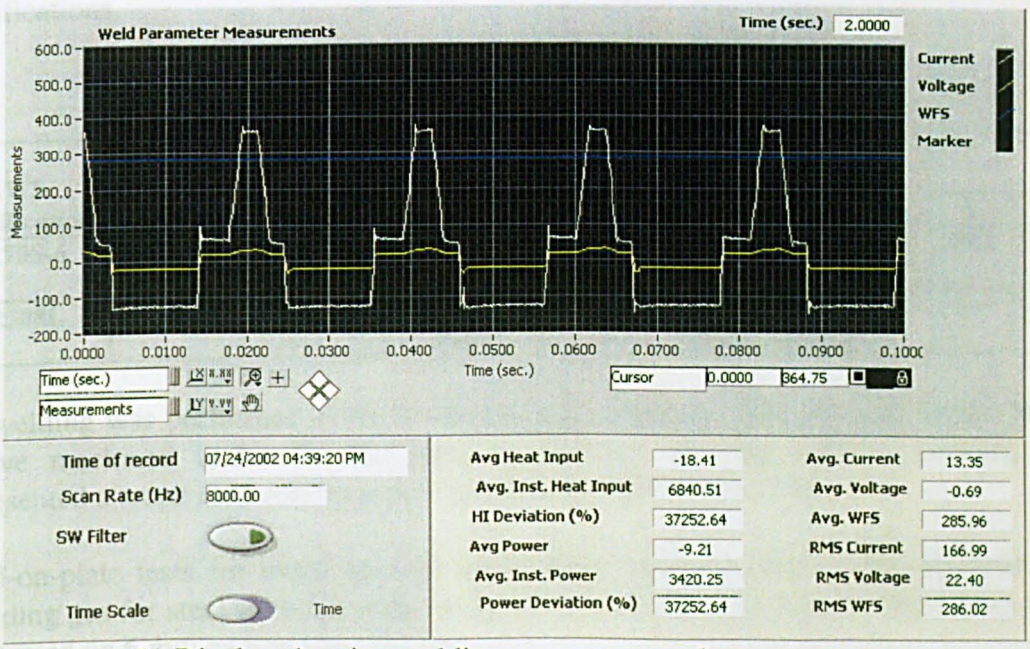

(b) Display showing welding parameters and measurements

Figure 4.8 High Speed DAQ System

Voltage was measured at the junction between the wire feeder and the welding gun, and the work. These points were considered as close to the arc as possible, and represent the approximate arc voltage. The shunt used for voltage measurement was supplied by CWT Model: T3A5031 Rev. A and had an output of 1 volt per 10 volts, up to 100 volts maximum. Current was measured using a Hall effect current sensor supplied by Ohio Semitronics, Model: CT-3474CY04, that had an output of 1 volt per 150 amps up to 750 amps maximum. The wire feed speed of the electrode was measured using a tachometer supplied by Computer Weld Technology (CWT), Model: A3A0051. Software design in LABVIEW™ by EWI was used to calculate the instantaneous power, average power, RMS current and voltage, and average current and voltage (Figure 4.8b). In addition, welding heat input was calculated without the effects of process efficiency (η) using the travel speed.

4.2 Materials

For the steel tests, the filler electrode was 1.14 mm (0.045 in.) diameter ER70S-6 uncoated steel wire used with 90Ar-10CO_2 shielding gas at 18.8 l/min. The steel electrode was manufactured by National Standard per AWS A5.18 by the trade name of NS-115. The lap joint (Figure 4.5) was made using 1.8 mm (0.060 in.) thick (t) low carbon steel that had a 1.8 mm (0.060 in.) thick shim placed between the joint to rigidly maintain a 1t gap. For stainless steel, the lap joint tests used 1.14 mm diameters ER308L with 95Ar-5CO_2 shielding gas at 18.8 l/min. The stainless steel electrode was manufactured by Harris Welco per AWS A5.9. The stainless steel lap joints were made from 304L sheet that was also 1.8 mm thick with a 1t gap. The nominal compositions of the electrodes are shown in Table 4.1. Note, the wire diameter was 1.14 mm, instead of 1.2 mm that is used in Europe, because the wire was purchased to AWS specifications.

Table 4.1 Electrode Filler Materials

AWS Classification	UNS No.	Weight Percent									
		C	Mn	Si	P	S	Ni	Cr	Mo	V	Cu
ER70S-6	K11140	0.06-0.15	1.40-1.85	0.80-1.15	0.025	0.035	0.15	0.15	0.15	0.03	0.50
ER308L	S30883	0.03	1.0-2.5	0.30-0.65	0.03	0.03	9.0-11.0	19.5-22.0	0.75	--	0.75

All welding was performed in the horizontal (2F) position. The welding fixture had a groove machined under the lap joint to simulate welding without backing and represented a worst case condition for susceptibility to burn-through.

Bead-on-plate tests for metal transfer study were made on steel. The electrode and shielding gas for steel were the same as the lap joint tests. The bead-on-plate tests were performed on 6 mm carbon steel flat bar.

5.0 EXPERIMENTAL PROCEDURE

This investigation characterised the metal transfer behaviour of the VP-GMAW process and assessed the state-of-the-art. Metal transfer was characterised using HSV and DAQ that were synchronised permitting accurate melting rate measurements. The droplet burnoff rate (DBR) method was developed, which provided the accurate melting rate measurements for advanced waveform processes, like VP-GMAW. This technique required detailed analysis of the electrical waveform and how it related to the droplet growth process for each period in the waveform. The technique accounted for variation in electrode extension during the droplet growth process. Each power supply was first evaluated by studying the functional relationship between wire feed speed and waveform for bead-on-plate and lap joint applications using the ARCWISE parameter development method. Welding parameters were selected from these data to assess the metal transfer of the OTC AC/MIG 200 power supply over the full range of operation.

5.1 Electrical Measurements

Mean and RMS voltage (V), and current (I) measurements were calculated using data supplied by a wire pair and Hall-effect transducer, respectively. From these measurements, RMS and AIP were calculated (Table 5.1) to determine which measurement was preferred for heat input calculations.

Table 5.1 Calculations for Heat Input and Power

$H_{net} = P \bullet \eta / TS$	$I_{mean} = (\sum_{i=1}^{n} I_n)/n$
$P_{mean} = I_{mean} \bullet V_{mean}$	$V_{mean} = (\sum_{i=1}^{n} V_n)/n$
$P_{AIP} = \sum_{i=1}^{n} (I_n \bullet V_n / n)$	$I_{RMS} = \sqrt{(\sum_{i=1}^{n} (I_n^2)/n)}$
$P_{RMS} = I_{RMS} \bullet V_{RMS}$	$V_{RMS} = \sqrt{(\sum_{i=1}^{n} (V_n^2)/n)}$
P = power, η = efficiency, TS = travel speed, I = current, V = voltage	

This information was used to develop process operating windows for relationships between voltage and current, voltage and wire feed speed, current and wire feed speed, and heat input versus deposition rate for the full waveform. In addition, these measurements were used to develop the same relationships for different periods of the waveform, which are the EN, the EPB, and EPP waveforms.

The current of each waveform component was used to determine burnoff rate once the melting rate was known. Waveform measurements, current and time, were made for each period by averaging a number of periods from the corresponding DAQ record. Electrical DAQ measurements were taken at either 4500 or 8000 Hz where the higher frequency was used to study the details of each waveform period.

5.2 DBR Measurements

The droplet burnoff rate (DBR) method was based on measuring the melting rate of each period, corresponding waveform (current and time), and electrode/droplet dimensions that may affect these measurements. The data was the used to create burnoff diagrams that can be used to solve for melting rate coefficients. The burnoff diagram plots electrode burnoff rate, BR versus the electrode extension heating factor, F_L. The intercepts and slopes of lines made with this diagram equal the arc heating and resistive heating coefficients, respectively for different waveform period conditions. The magnitude and changes in these coefficients for each period were related to arc behaviour. The DBR method was used to develop new understandings for how waveform and arc behaviour affect melting rate in advanced GMAW processes.

The HSV camera was set up to allow viewing of the growing droplet at the tip of the electrode and subsequent drop detachment. Shutter speed was adjusted to allow viewing of the metal transfer without using laser back lighting. The shutter speed was optimised for the waveform period being studied, and for measuring arc length on steady-state tests. The arc length was trimmed using the control pendant of each power supply to 3 mm nominal at drop detachment between the electrode tip and weld pool surface. The leading edge of the weld pool was almost flush with the plate during these tests. The HSV sampling frequency was nominally set at 3700 Hz. This frequency optimised the image size for measuring the droplet growth and electrode extension.

The wire diameter (1.14 mm) for all tests was used to calibrate the dimensional measurements taken at the electrode extension (L). During droplet formation, the electrode extension length either burned off or increased in length, with the current waveform to balance the melting rate.

For this project, the electrode melting rate for each period of the waveform was determined empirically by adding the electrode extension burnoff rate to the wire feed speed. The MR for each waveform period (EN, EPB, EPP) was:

$$MR_{(EN.EPP.EPB)} = \frac{\Delta x}{t_2 - t_1} + WFS_{DAQ} \tag{5.1}$$

Where Δx is the electrode extension burnoff, which equals the length of change in solid-liquid interface position from initial time (t_1) to final time (t_2) and WFS is wire feed speed measured with the data acquisition during that period.

The electrode extension burnoff was measured by calibrating the HSV frames to the wire diameter (1.14 mm) and recording the droplet - electrode interface position at initial and final times for each period. The sign convention used for Δx required that positive interface growth be upward (toward the solid wire). Figure 5.1a shows the interface position at the beginning of the EN cycle. Figure 5.1b shows the interface position at the end of the EN cycle. In this case, the time elapsed throughout the cycle is 0.01107 seconds and growth is in the positive direction ($\Delta x>0$).

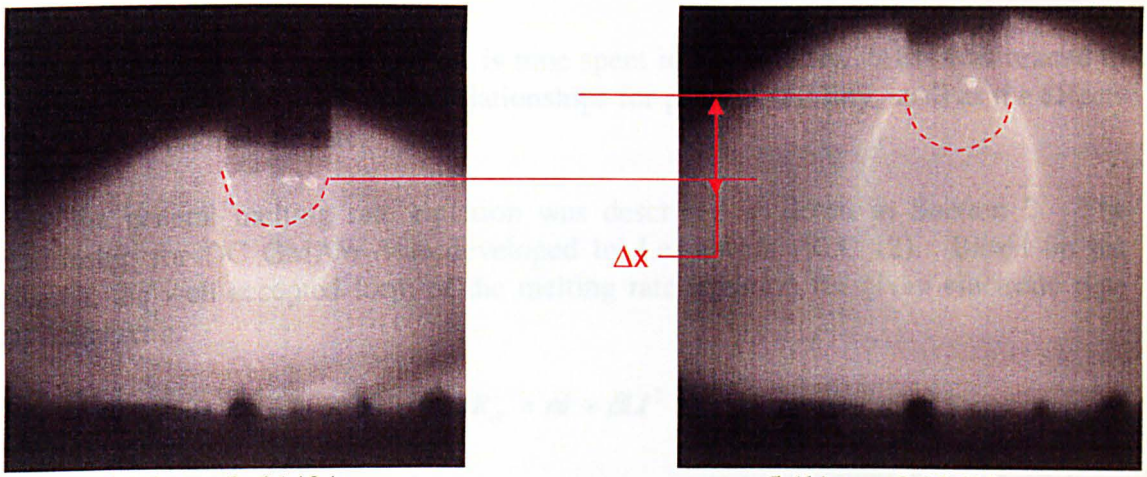

5.1a) $t_1 = 0.01404s$ 5.1b) $t_2 = 0.02511s$

Figure 5.1 Electrode Extension Burnoff During Droplet Growth in EN Period

The droplet volume growth rate for each waveform component was calculated by multiplying the electrode melting rate by the wire area, A_w which was 1.02 mm^2 (0.00159 in^2). Therefore, the droplet volume growth rate (V_D) in each period was:

$$V_D = \left(\frac{\Delta x}{t_2 - t_1} + WFS_{DAQ} \right) \cdot A_w \tag{5.2}$$

The electrode extension heating factor (F_L) for each waveform period was determined as follows:

$$F_{L(EN,EPB,EPP)} = L \cdot I_{EN,EPB,EPP} \tag{5.3}$$

The electrode extension used in these calculations was the average based on the change in electrode extension length during the period of evaluation;

$$L_{EN,EPB,EPP} = Lo + \frac{\Delta x}{2} \tag{5.4}$$

The average total melting rate for process stability can be determined by averaging the MR for each period times the waveform frequency with the following equation:

$$MR_{AVG} = \left(\left(MR_{(EN)} \cdot t_{EN} \right) + \left(MR_{(EPB)} \cdot t_{EPB} \right) + \left(MR_{(EPP)} \cdot t_{EPP} \right) \right) \cdot f \tag{5.5}$$

The average MR should equal the true melting rate for a VP-GMAW waveform.

The percent EN of each waveform based on time was determined from the waveform DAQ. The %EN was determined using the following equation:

$$\%EN = \left(f \cdot t_{EN}\right) \cdot 100\% \tag{5.6}$$

where f is the pulse frequency and t_{EN} is time spent in EN polarity. %EN was related to waveform parameters to determine relationships for process stability, such as the effects of I_{EN} and t_{EN} on melting rate.

Note, the general melting rate equation was described in detail in Section 2. The relationship for DC GMAW was developed by Lesnewich (Ref. 12). Based on his research, the well accepted form of the melting rate equation for given electrode type and diameter is:

$$MR_{dc} = \alpha I + \beta L I^2 \tag{5.7}$$

The first part of the equation (αI) represents the contribution from arc heating and the second part of the equation (βLI^2) represents the contribution from electrode extension resistance heating. The melting rate terms are as follows:

MR_{dc} = (mm/s)
α = arc heating coefficient (mm/s-amp)
I = current (amps)
β = resistive heating coefficient $(amps^2\text{-}s)^{-1}$
L = electrode extension (mm)

This equation can be integrated to relate the effects of waveform current on the melting rate for advanced waveforms. Process stability is achieved when the average MR equals the WFS. For pulse waveform processes, the melting rate increases dramatically from the improved electrode extension heating (i.e., by I^2R heating). Allum (Ref. 63) and Richardson (Ref. 75) have derived melting rate solutions for different waveforms for GMAW-P without and with slew rate, respectively. These mathematical relationships are treated in more detail in Section 5.3.

Once the melting rate, waveform, and other DBR measurements were made for each period, the Burnoff Diagram Technique (BDT) was used to empirically determine α and β. The BDT was demonstrated by Richardson (Ref. 75) as an efficient way to empirically determine the melting rate coefficients. A single line is yielded for CV processes that have a constant mode of transfer, like spray transfer, for a full range of operating conditions. The line produced on the BDT for CV processes characterizes the full range of electrode extensions, wire feed speeds, and currents for that process. A separate set of CV tests were performed to validate this approach for CV processes.

For the VP-GMAW process, this investigation showed that multiple BDT lines were needed for each polarity depending on the waveform conditions. Separate burnoff diagrams were created for each polarity, EN and EP for the AC/MIG 200 power supply using the 1.14 mm steel electrode and 90%Ar – 10%CO_2 shielding gas. For the EP polarity, the lines were fitted between DBR measurements made in EP background and peak period for different VP-GMAW waveforms. The coefficients measured for each

waveform period were compared to prior research for EP heating, and used to establish the melting rate properties of EN, EP background and EP peak heating in VP-GMAW.

5.3 Melting Rate Analysis

The melting rate equation for DC processes has been established for years. The effects of waveform were evaluated mathematically here to derive an equation for the VP-GMAW process. The melting rate coefficients, α and β, for each period determined using the approach described in Section 4.2 were used with the derived equation to compare predicted VP-GMAW melting rates versus actual WFS test data

5.3.1 GMAW-P Melting Rate Equations

In DC pulse GMAW, the pulsing waveform improves the resistive heating efficiency of the GMAW process due to I^2R heating. Allum (Ref. 63) derived a melting rate equation for square waveform pulse GMAW. The melting rate was analysed in a time dependent form as follows:

$$MR_{pdc} = \frac{1}{t_p + t_b} \int_{one\ pulse\ cycle} MR_b(t)dt \tag{5.8}$$

$$\begin{aligned} MR_{pdc} &= \left[\left(t_p \alpha I_p + \beta L I_p{}^2 t_p\right) + \left(t_b \alpha I_b + \beta L I_b{}^2 t_b\right)\right] \frac{1}{t_p + t_b} \\ &= \alpha \frac{\left(I_p t_p + I_b t_b\right)}{\left(t_p + t_b\right)} + \frac{\beta L}{\left(t_p + t_b\right)} \left\{I_p{}^2 t_p + I_b{}^2 t_b\right\} \\ &= \alpha \bar{I} + \frac{\beta L}{\left(t_p + t_b\right)^2} \left\{\left(I_p t_p + I_b t_b\right)^2 + \left(I_p{}^2 + I_b{}^2 - 2 I_p I_b\right) t_p t_b\right\} \\ MR_{pdc} &= \alpha \bar{I} + \beta L \left\{\bar{I}^2 + \frac{\left(I_p - I_b\right)^2 t_p t_b}{\left(t_p + t_b\right)^2}\right\} \end{aligned} \tag{5.9}$$

where for simplicity:

I_p = current EP peak (I_{EPP})
I_b = current EP background (I_{EPB})
t_p = time at EP peak current (t_{EPP})
t_b = time at EP background current (t_{EPB}).

This equation ignores the effects of slew rate, which decreases the resistive heating efficiency of the pulse waveform. Modern power supplies use slew rate to soften the arc and reduce noise. The VP-GMAW power supplies used in this investigation used a trapezoidal waveform for the EP polarity. The effects of EP slew rate (Figure 5.2) were characterised by Richardson et al (Ref 75). His work was performed to better characterise power supply dynamics. The waveform shown in Figure 5.2 was divided

into discrete time-based components that describe a trapezoidal waveform. The current in the trapezoidal waveform can be divided into four pulse periods as follows:

$$I_1 = I_b + \frac{(I_p - I_b)}{t_1} t \tag{5.10}$$

$$I_2 = I_p \tag{5.11}$$

$$I_3 = I_p - \frac{(I_p - I_b)}{t_3} t \tag{5.12}$$

$$I_4 = I_b \tag{5.13}$$

On the rising edge of the pulse, the response rate is given by:

$$\frac{dI}{dt} = \frac{(I_p - I_b)}{t_1} \tag{5.14}$$

and on the trailing edge, the response rate is given by:

$$\frac{dI}{dt} = \frac{(I_p - I_b)}{t_3} \tag{5.15}$$

Richardson, et al assumed that the rise and fall rates of the peak current pulse were equal so $t_1 = t_3$. The time period for t_p was equal to t_1 plus t_2 and the time period for t_b was t_3 plus t_4. Unequal slew rates led to a larger resultant equation although the basic mathematical behaviour remains unaltered. Performing the integral over one pulse cycle, and rearranging the equation to the form like Equation (5.9) yields:

$$MR_{pdc} = \frac{1}{t_{\substack{one\ pulse \\ cycle}}} \int MR_b(t)dt \tag{5.16}$$

$$MR_{pdc} = \alpha \bar{I} + \beta L \left\{ \bar{I}^2 + \frac{(I_p - I_b)^2 t_p t_b}{(t_p + t_b)^2} - \frac{(I_p - I_b)^3}{3(t_p + t_b) dI/dt} \right\} \tag{5.17}$$

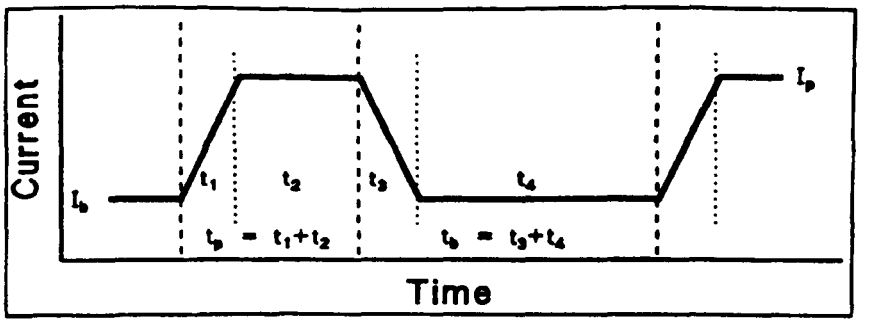

Figure 5.2 Trapezoidal Waveform and Pulse Parameters (Ref. 75)

5.3.2 Square Wave AC-GMAW Melting Rate

A modified form of the melting rate equation can be derived for square wave AC-GMAW. Here the waveform subscripts simply designate EP as (+) and EN as (-). The melting rate equation can be solved ignoring slew rate as follows:

$$MR_{ac} = \frac{1}{t_- + t_+} \int_{\substack{one\ pulse \\ cycle}} MR_b(t)dt$$

$$= \frac{\left(\alpha_- I_- t_- + \beta_- L_- I_-^2 t_-\right) + \left(\alpha_+ I_+ t_+ + \beta_+ L_+ I_+^2 t_+\right)}{t_- + t_+} \tag{5.18}$$

$$MR_{ac} = \frac{\alpha_- |I_-| t_- + \alpha_+ I_+ t_+}{t_+ + t_-} + \beta L \left\{ \frac{I_+^2 t_+ + I_-^2 t_-}{t_+ + t_-} \right\}$$

Assuming:

$$\beta_- = \beta_+ = \beta$$
$$L_- = L_+ = L$$

$$MR_{ac} = \left(\frac{\alpha_+ I_+ t_+ + \alpha_- |I_-| t_-}{(t_+ + t_-)} \right) + \beta L \left\{ \bar{I}^{*2} + \frac{(I_+ - |I_-|)^2 t_+ t_-}{(t_+ + t_-)^2} \right\} \tag{5.19}$$

Where:

$$\bar{I}^* = \left(\frac{I_+ t_+ + |I_-| t_-}{t_+ + t_-} \right) \tag{5.20}$$

Equation (5.19) is a simple equation making the fundamental assumption that the arc heating coefficient for each polarity is different. However, it also assumes that the resistive heating coefficient is constant. Square AC waveforms were not evaluated in

this project. The VP-GMAW waveform tests found that the resistive heating coefficient was affected by the rapid electrode extension burnoff during the EN period. Likewise behaviour could be expected in AC-GMAW. Therefore, this equation may need further modification to be experimentally applied but is provided as a building block to derive the melting rate equation for VP-GMAW.

5.3.3 VP-GMAW Melting Rate Equation with EP Slew Rate

The majority of melting rate measurements performed in this investigation were taken using the AC/MIG 200 power supply. This VP-GMAW waveform (Figure 5.3) uses a trapezoidal EP pulse with a small post-pulse EPB period. This small background period was believed to help minimize spatter after the ramp-down by permitting drop transfer before switching to EN current. This small period was included in the total EPB time. The peak, t_p and background, t_b time included one slew rate period, based on the approach by Richardson, to balance the melting rate contribution from a EP trapezoidal pulse waveform.

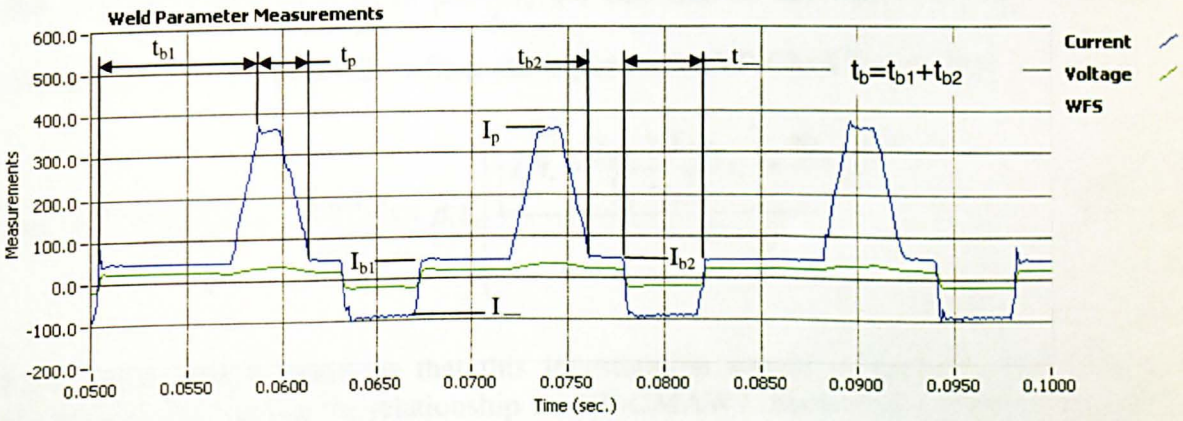

Figure 5.3 VP-GMAW Waveform from OTC AC/MIG 200

The melting rate equation for this power supply can be determined by combining the above equations over time and assuming the ramp-up and ramp-down slew rates are equal. This was the case with the AC/MIG 200 power supply. The resultant equation is the following:

$$MR_{vp} = \frac{1}{t}\int_{\substack{one\ pulse\\ cycle}} MR(t)dt \tag{5.21}$$

$$MR_{vp} = \frac{\alpha_-|I_-|t_- + \alpha_+\bar{I}_+t_+}{t_- + t_+} + \beta L\left\{\frac{I_-^{\,2}t_-}{t} + \frac{\left[\bar{I}_+^{\,2}t_+ + \frac{(I_p - I_b)^2 t_p t_b}{(t_p + t_b)^2} - \frac{(I_p - I_b)^3 t_+}{3(t_p t_b)dI/dt}\right]t_+}{t}\right\} \tag{5.22}$$

Where $t_+ = t_b + t_p$ (with equal slew rate time in t_b and t_p) as per Equations (5.14) and (5.15),

$t = t_- + t_+$

Results in this project showed that the resistive heating term was dependent on the polarity. This was because of the rapid electrode extension burnoff that occurred in the EN period. To consider the effects of electrode extension burnoff experimentally, L_+ and L_- were calculated using Equation (5.4), and β_+ and β_- were the slope of the lines calculated from the burnoff diagram for each period. These can be incorporated into Equation (5.22) to predict the relationship between welding parameters and melting rate. The DBR method was required to calculate these parameters and the arc heating coefficients, α for each period. In addition the DBR method permitted direct measurement of the slew rate time, t_s. The melting rate lost due to I^2R slew rate effects can be expressed by a simple integral for the slope ($I = \frac{I_s}{t_s} t$) of the pulse which equals

$$MR_s = \beta L \int_0^{t_s} \frac{I_s^2}{t_s^2} t^2 dt = \beta L \frac{I_s^2}{3t_s^2} t_s^3 = \beta L \frac{I_s^2}{3} t_s$$ for one rise or fall where the slew current rise, $I_s = I_p - I_b$. The preferred melting rate equation for VP-GMAW was then:

$$MR_{vp} = \frac{\alpha_- |\bar{I}_-| t_- + \alpha_+ \bar{I}_+ t_+}{t_- + t_+} + \frac{\beta_- L_- \bar{I}_-^2 t_-}{t} + \beta_+ L_+ \left(\frac{\left[\bar{I}_+^2 t_+ + \frac{(I_p - I_b)^2 t_p t_b}{(t_p + t_b)^2} t_+ \right] + \frac{2(I_p - I_b)^2}{3} t_s}{t} \right) \quad (5.23)$$

There were several questions that this investigation sought to answer. First, does Equation (5.23) explain the relationship for VP-GMAW? Second, does EN arc heating dominate the melting rate or does the electrode extension resistive heating (I^2R) dominate? Third, what are the relative strengths of the arc heating coefficient for EN and EP periods?

These questions were analysed systematically by developing the relationships between electrode melting rate and size, arc behaviour, and waveform shape. The electrode melting rate for each waveform period was determined using the DBR method that was developed in this investigation. The arc and resistive heating coefficients were empirically determined using the BDT and compared for each waveform period. These coefficients were applied in Equation (5.23) to predict melting rate, compare the contribution from each waveform period, and evaluate the accuracy of this equation.

5.4 Process Capability Measurements

The ARCWISE method for process characterisation was used to assess the potential of the VP-GMAW process on sheet metal welding applications. The ARCWISE method has been used at Edison Welding Institute since 1996 to assess arc welding process applications (Ref. 116-118). This method is straightforward and provides a data set that

relates functional welding parameters (V, I, WFS, and TS) to productivity and weld quality. This data set provides a foundation for selecting welding parameters and permits benchmarking of welding processes. In addition, because tests are performed under carefully controlled conditions, the data can be stored for future use on similar applications and compared to alternative processes.

The definition of an application is a set of fixed design factors such as base materials, joint type, position, weld size, bead shape, and mechanical properties requirements. The operational windows developed with the ARCWISE method are for a specific process-consumable combination that was evaluated on an application.

A major reason for the effectiveness of the method is that all test welds involve a constant ratio of deposition rate to weld travel speed (i.e., the WFS/TS ratio). In this manner, the deposit area is kept constant while variations in CTWD distance, arc length, shielding gas, and other factors like waveform effects are evaluated. Another unique aspect of the ARCWISE method is constant arc length testing. Arc length is adjusted for each test to a preferred distance using various techniques like the HSV calibration method used here. It is well known amongst welders, that arc length is critical to proper weld pool performance, yet this important aspect of parameter development is consistently overlooked.

5.4.1 ARCWISE Method

The 5 elements of the ARCWISE method are as follows:

	Planning	Testing	Analysis
Step	1. Weld size & acceptance criteria	2. Constant deposit area test matrix 3. Constant arc length testing 4. Bead cross-section measurements	5. - Parameter relationship graphs - Operational windows - Weld macrosection maps

5.4.2 VP-GMAW ARCWISE Characterisation

A constant deposit area test matrix (Table 5.2) was used to characterise systematically the potential of each power supply on the lap joint application. As shown in this table, a constant wire feed speed to travel speed ratio (WFS/TS) of 10 was maintained. This deposit area was based on preliminary weld sizing tests that optimised gap weldability and bead shape for this application. Travel speed was incrementally increased from 4.2 to 25.3 mm/s in 4.2 mm/s increments. At each travel and wire feed speed condition, a series of tests was performed to evaluate the full range of %EN balance offered by the power supply. This matrix covered the entire potential of each power supply from low currents, where lack-of-fusion was a problem, to high currents meeting the capacity or waveform stability of the power supply. The arc length was fixed at 3 mm for all tests based on preliminary trials that showed this arc length gave a good bead shape and can be used for process characterisation.

Table 5.2 WFS/TS Test Matrix for Lap Joint Applications

Travel Speed (mm/s)	Wire Feed Speed (mm/s)
4.2	42
8.4	84
12.7	127
16.9	169
21.2	212
25.3	253

The range of acceptable parameters for each power supply was first determined by visually examining the bead shape of each test. Each lap joint test was then cross sectioned to examine soundness. An acceptable bead shape had no lack-of-fusion or burnthrough. Graphs were created plotting the relationships between V_{RMS} versus I_{RMS}, V_{RMS} versus WFS, I_{RMS} versus WFS, power (AIP and RMS) versus WFS, and heat input (AIP) versus deposition rate. The maximum WFS that was tested was related to the power supply and its output capability. Table 5.3 outlines the range of constant deposit area tests for each electrode, CTWD, and power supply combination. For each electrode and power supply, the ARCWISE test matrix was repeated at two CTWDs. The AC/MIG 200 power supply was limited to 200 amps at 100% duty cycle so the maximum wire feed speed that was stable for the full range of %EN was 127 mm/s. Tests were performed at 169 mm/s but the metal transfer was unstable for most of the tests. The PC350 power supply was rated at 350 amps so the maximum WFS tested was 253 mm/s. Most of the tests performed at this WFS and at 212 mm/s were unstable. Unstable tests were plotted with hollow data points and not used for line plotting.

Table 5.3 Lap Joint Test Conditions for VP-GMAW Power Supplies

Power Supply	Electrode/Gas	WFS (mm/s)	Pendant Settings
AC/MIG 200	1.2-mm ER70S-6 90Ar-10CO_2 19-mm CTWD	42 84 127	-150 -75 0 75 150
AC/MIG 200	1.2-mm ER70S-6 90Ar-10CO_2 16-mm CTWD	42 84 127	-150 -75 0 75 150
AC/MIG 200	1.2-mm ER308L 95Ar-5CO_2 16-mm CTWD	42 84 127	-150 -75 0 75 150
AC/MIG 200	1.2-mm ER308L 95Ar-5CO_2 19-mm CTWD	42 84 127	-150 -75 0 75 150
PC350	1.2-mm ER70S-6 90Ar-10CO_2 16-mm CTWD	42 84 127 169 212 253	0 25 50 75 100

The productivity of the VP-GMAW processes was compared with GMAW-P to benchmark the capability of this process for the lap joint applications. The GMAW-P waveform was achieved by setting the %EN to zero, which correlated to pendant settings of -150 for the AC/MIG 200, and 0 for the PC350.

6.0 RESULTS

The AC/MIG 200 power supply was used for detailed analysis of VP-GMAW metal transfer. The basic VP-GMAW waveform cycle evaluated here had three parts; an EN period, an EPB period, and an EPP period (Figure 5.3). The droplet formation process began with the EN period and was completed during the EPP period. It was observed through HSV that the droplets were mostly formed during the EN polarity period. Here, the droplets grew rapidly as the arc climbed the tip of the electrode. The droplets were typically 1.5 to 2 times the wire diameter, or larger. The arc then switched polarity, becoming dim as the current passed through zero. The EPB current period was used to maintain the arc and droplet size that was created during the EN pulse. The droplet responded quickly to the high current EP pulse where it gained some additional size before being transferred to the weld pool. Based on the drop diameter, the drop transfer mode can be characterised as "pulse-globular" for the VP-GMAW process. This differs from conventional EP polarity GMAW-P waveforms, which typically transfer drops using the "drop-spray mode", where the primary drop size transferred during each pulse is equal to or slightly greater than the wire diameter. The transfer is also different from projected globular since the EP pulse accelerated the drop to higher speeds than what is achieved in CV projected transfer.

This power supply comes equipped with pre-programmed waveform algorithms for mild and stainless steel using several electrode diameters and shielding gas combinations. The pendant permitted precise adjustment of the waveform to control the arc length via pulse frequency. The quality of the pre-programmed pulse parameters for each wire feed speed setting varied depending on the %EN. Some VP pulse parameter settings produced spatter-free welds. Other VP pulse parameters produced some spatter. Lap joint spatter was observed to be due to the shape of the weld pool where, if the heat input was too low, the weld pool crowned and forced unplanned short circuits. Spatter also occurred when high percentages of EN were used, due to large droplets forming on the electrode and subsequently breaking apart during the crossover from EN to EP.

The metal transfer behaviour of this power supply for steel at 16 mm CTWD process was systematically characterised by evaluating the effects of WFS, %EN polarity, and EN current. The effects of %EN were evaluated by using constant EN current tests at each wire feed speed. At each wire feed speed, the pendant penetration adjust knob was varied to evaluate six %EN levels. The arc length was controlled at 3 mm at drop detachment, so the electrode extension, L starting in the EN period would be constant at 13 mm based on the arc position in the leading edge of the weld pool. The tests were bead-on-plate as described earlier. Arc length was controlled using a trim knob, which varied the waveform frequency. High speed DAQ and video were synchronized to develop the DBR measurement method. Electrical and video measurements were critical to the accuracy of these measurements. Preliminary tests were performed to determine the best measurement methods.

6.1 Electrical Measurements

A number of current, voltage, and power measurements were made to characterise the VP-GMAW process. RMS current and voltage measurements were made during this study to capture all the energy that was developed by the waveforms. RMS measurements are typically used to capture the resistive heating potential of a process or for AC type processes. This is a common practice in the welding industry since meters used on power supplies are either mean or RMS. Mean measurements of voltage and current were taken since these are commonly used to characterise EP GMAW-P. The VP-GMAW waveform had alternating current, so the net result of mean measurements was very low voltage and currents that do not represent the power in the arc. Mean measurements were not reported based on this reason. Power measurements (Table 4.1) were made by taking the product of the RMS current and voltage, and by averaging the instantaneous product of the current and voltage waveform; herein referred to as the AIP. The RMS power was compared with the AIP to evaluate the error that occurs when using conventional DAQ instruments. Research by Joseph (Ref. 92) and Bosworth (Ref. 93, 94) has proved that AIP is more representative of the power in the arc. The author was involved in Joseph's study (Ref. 92), which performed liquid nitrogen calorimetry to determine the best method for heat input and power measurements. The liquid nitrogen calorimeter measurements were reviewed in Section 2.7 where the process efficiency of the GMAW-P was 70.2% using AIP. These measurements agreed with the work performed by Bosworth for bead-on-plate welds. Based on these results, heat input graphs made in this study are based on using the AIP divided by the test travel speed and assuming 100% process efficiency since the process efficiency for lap joints was not determined here.

These results do open some questions concerning how voltage and current are measured for waveform processes. Today, most researchers still believe GMAW-P measurements of V and I are best characterised by mean measurements. RMS measurements are always higher than mean and AIP measurements for GMAW-P (Ref. 92). Mean power measurements are be lower than AIP for GMAW-P where the error is 14 to 30% (Table 2.5). The losses in power based on mean measurements are based on the higher power that develops in pulse waveforms when the current and voltage are in phase (Ref. 92). The current and voltage were found to be in phase for VP-GMAW waveforms.

True arc process measurements of V and I for the VP-GMAW process may be better characterised with an average absolute measurement, which is analogous to a true mean, since RMS values tend to give higher power levels than determined by calorimetry. Absolute measurements are the basis of AIP over time. Meters that read absolute voltage and current have not been employed on AC processes by the welding industry. This is an area of future work since the arc is a non-linear resister and heat generated in the arc is not affected by RMS energy.

The ARCWISE method was used to evaluate the potential of VP-GMAW power supplies on a lap joint application. The lap joints were made using a constant deposit area (WFS/TS ratio = 10). Arc length was held constant to the top edge of the lap joint, Figure 4.7. Tests were performed to evaluate incremental productivity levels (travel

speeds) and the effects of %EN. Graphs for RMS voltage versus current, RMS voltage versus wire feed speed, RMS current versus wire feed speed, RMS power versus AIP and heat input (AIP) versus deposition rate were plotted to map out the ARCWISE data set. The bead shape taken from weld cross sections was mapped and compared to the graphs. Weld quality was assessed by the fusion of the lap joint pieces and burnthrough. Maximum travel speed (productivity) was determined by the window which bounds acceptable fusion and burnthrough for each %EN setting. The RMS measurements were plotted so process setting could be related to the meters on the power supply. This permits the use of the graphs developed here for procedure parameter selection for the lap joint application.

6.2 Functional Process Relationships

The ARCWISE method was used to determine the functional relationships for each power supply over the full capability of the VP waveforms for each electrode and CTWD combination. For each process combination characterised on lap joints, the test waveforms were captured to evaluate waveform strategy, and determine the parameters for each waveform. Parameter relationships were determined for both the AC/MIG 200 and PC350 power supplies for the settings described in Table 5.3. Graphs were plotted for V_{RMS} versus I_{RMS}, V_{RMS} versus WFS, I_{RMS} versus WFS, P (both AIP and RMS) versus WFS, heat input (H_{AIP}) versus deposition rate. The burnoff rate diagram was also plotted for each process combination even though the arc heating and resistive heating coefficients using this approach are considered invalid. The burnoff diagram plotted the WFS/I against the electrode extension heating factor, F_L.

The pendant of each power supply was used to vary the %EN for each test WFS. The wire feed speed was varied in increments proportional to the travel speed by the WFS/TS ratio of 10. For the AC/MIG 200 power supply, the pendant settings were -150, -75, 0, 75 and 150. These settings changed the %EN from 0% at -150 setting to up to 80% for the 150 setting depending on the electrode and shielding gas that was used with the pre-programmed waveform. Zero percent EN, which was basically a GMAW-P waveform, was observed at -150 pendant setting and many of the -75 pendant settings for this power supply. The AC/MIG 200 power supply was limited to 200 amps at 100% duty cycle so the maximum wire feed speed that was stable for the full range of %EN was 127 mm/s. Tests were performed at 169 mm/s, but the metal transfer was unstable for most of the tests since the power output of the power supply was exceeded.

The PC350 power supply was rated at 350 amps so the maximum WFS tested was 253 mm/s. The pendant settings for this power supply were presented in %EN, however, the pendant settings were not a measure of the true %EN based on waveform measurements. In fact, the %EN varies during welding based on fuzzy logic for the short circuit anticipation control. Based on the fuzzy behaviour, no attempts were made to characterise the melting rate behaviour and detailed waveform parameters. The PC350 was only used to benchmark the productivity potential of this power supply.

The results of the ARCWISE characterisation were six graphs being plotted for each process combination. Since six combinations were evaluated, the data generated was

considerable, 40 pages of data. The complete ARCWISE data sets for the lap joint capability study are provided in Appendix A for the 16 mm CTWD tests and Appendix B for the 19 mm CTWD tests. The 16 mm CTWD results for steel are discussed in detail. The example was selected since bead-on-plate tests using the same parameter settings were used for metal transfer study. Benchmark comparisons using the bead shape maps for the lap joint application are described later.

6.2.1 V_{RMS} versus I_{RMS}

The voltage versus current relationship described the arc characteristic of the process combination for a 3 mm arc length at drop detachment. For steel with the AC/MIG 200 power supply, the RMS voltage increased as the RMS current increased (Figure 6.1). The trend was nearly linear with two points falling outside the line. These tests both had high %EN and were unstable settings for this power supply. Unstable settings produced random short circuits and irregular metal transfer even though the weld cross section appeared acceptable. The test results were grouped by the %EN as other electrical measurements were dependent on the waveform and the pendant settings. The RMS voltage ranged from 19 to 24 volts from 120 to 260 amps, respectively.

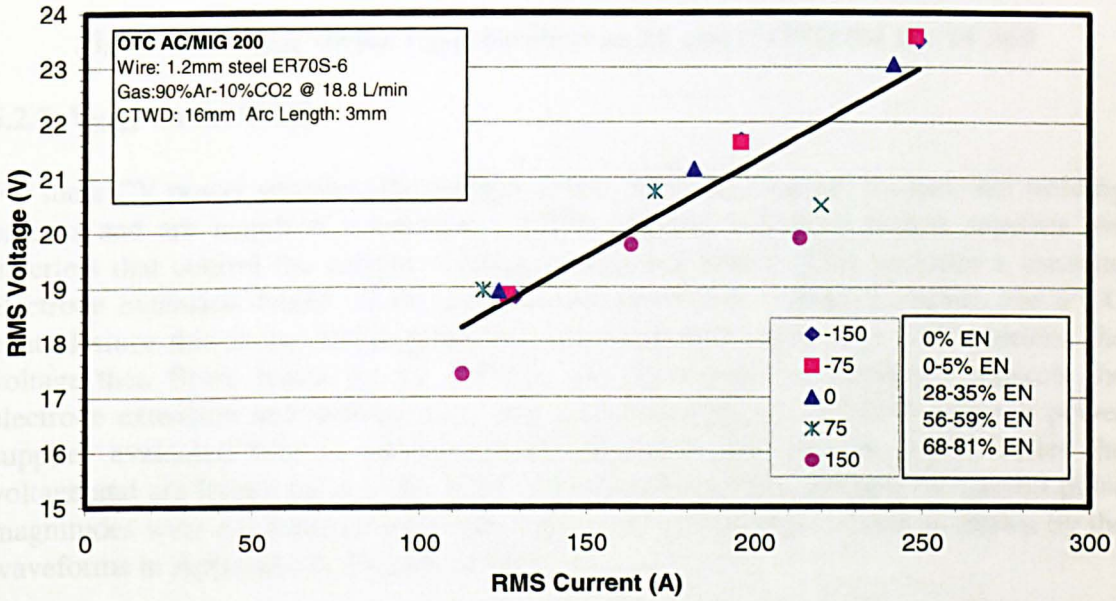

Figure 6.1 V_{RMS} versus I_{RMS} for Steel at 16 mm CTWD for the AC/MIG 200

The V-I behaviour of the PC350 power supply was totally different (Figure 6.2). The waveform produced intentional short circuit induced metal transfer. At each short circuit, the voltage in the waveform approached zero until the arc re-ignited This resulted in a larger voltage range as the current increased for the %EN range at each test WFS. This behaviour was attributed to the short circuit metal transfer, which reduced the RMS voltage depending on the short circuit frequency. The voltage range was 2 to 3 volts. Hollow points were used on these graphs if the metal transfer was unstable producing considerable spatter. This was the case at the highest wire feed speeds where

waveform improvements were needed to minimize the short circuit current, which exploded the droplets.

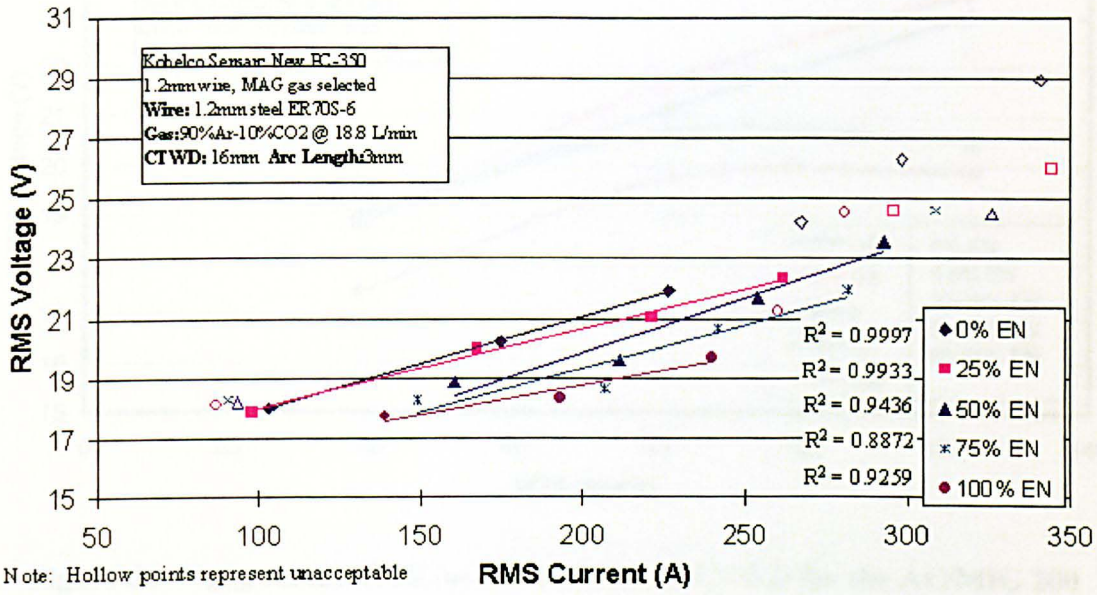

Figure 6.2 V_{RMS} versus I_{RMS} for Steel at 16 mm CTWD for the PC350

6.2.2 V_{RMS} versus WFS

For most CV power supplies, the voltage versus WFS relationship controls the welding process and arc length at a constant CTWD. Pulsed waveform power supplies use inverters that control the current waveform with transistors. This provides a constant electrode extension based on the melting rate behaviour. Many inverters use a CC control since this is the design parameter for using transistors. For CC inverters, the voltage then floats based on the CTWD, and the waveform frequency controls the electrode extension and melting rate. The pulse frequency is adjusted with the power supplies evaluated here to provide control of power and current, which varies the voltage and arc length for a given %EN pendant setting. The EN and EP current pulse magnitudes were constant for each wire feed speed and pendant setting as shown by the waveforms in Appendix A, Figures A7-A9.

The tests performed here used a constant CTWD, so pulse frequency was trimmed to get a constant arc length and electrode extension at drop detachment. The V_{RMS} range was approximately 2 volts at 42 and 84 mm/s WFS and it increased to almost 4 volts at the 127 mm/s WFS (Figure 6.3). Note the lower two points at 127 mm/s were considered unstable tests and the larger voltage range was attributed to unplanned short circuits at high %EN where the large droplets bridged the arc gap. The RMS voltage decreased as the %EN increased because less power was supplied to the process for the constant melting rate (mm/sec). The relationship between V_{RMS} and WFS was fit with lines for each pendant setting that provide a %EN range depending on the WFS.

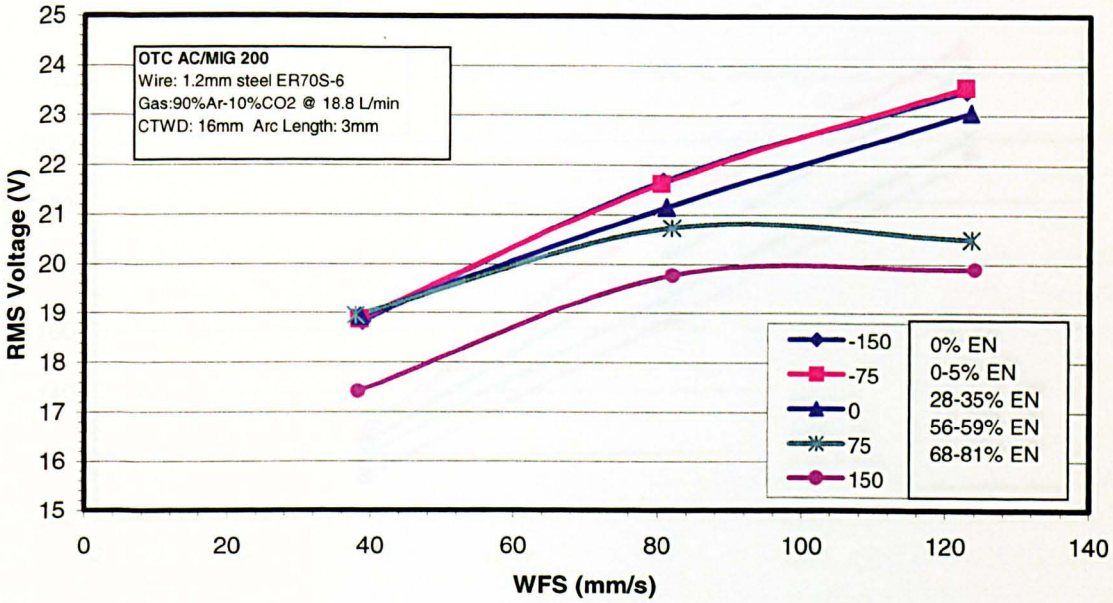

Figure 6.3 V_{RMS} versus WFS for Steel at 16 mm CTWD for the AC/MIG 200

The relationship between voltage and WFS for CV GMAW using 1.14 mm steel electrodes has been found to have a more non-linear behaviour. Here, the CV voltage required for constant arc length increases faster at lower WFSs. The rate of CV voltage increase decreases significantly at higher WFSs due to improved arc efficiency (i.e., at higher currents the arc produces more metal vapour, which decreases the cathode voltage drop). The VP processes characterised here did not examine the large range of WFS that is typically used to characterise CV processes so the effect was not as obvious. The behaviour of the V_{RMS} versus WFS was similar on the other process applications.

6.2.3 I_{RMS} versus WFS

The relationship between current and WFS is very important for determining the melting rate behaviour of CV GMAW process. As mentioned earlier, the melting rate behaviour is dependent on waveform, so this diagram cannot be used for determining the melting rate of VP-GMAW. For VP-GMAW, the DBR method was developed to evaluate the electrode melting rate, which included the change in electrode extension during each period. The data provided in Figure 6.4 may only be used to evaluate meter indications provided by the power supply. In general, the RMS current increased with increasing WFS and decreasing %EN. The EN heating decreased the current as expected since it significantly improves melting rate and lowers the current demand. The RMS relationship between current and WFS was linear as a function of %EN. For the steel application at 16 mm CTWD, RMS current varied from approximately 110 amps at 42 mm/sec to 250 amps at 127 mm/sec.

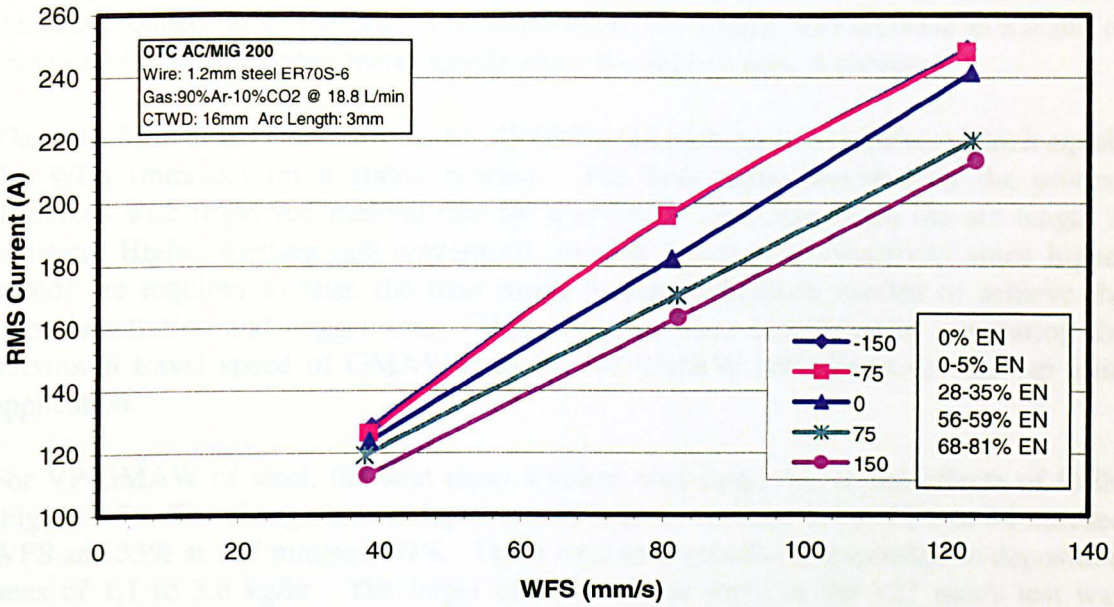

Figure 6.4 I_{RMS} versus WFS for Steel at 16 mm CTWD for the AC/MIG 200

The melting rate equation basically shows that WFS is proportional to I^2R. Therefore, this diagram is usually fitted by a second order polynomial where the rate of WFS change increases as current increases due to the I^2R effect. For the range of currents evaluated here, basically 100 to 200 amps, the I2R effect was not obvious. Tests performed using the 19 mm CTWD (Appendix B) had the same relationships except the current was slightly lower at each test WFS. This was expected since longer electrode extensions provide more I^2R heating. For stainless steel, the range of current at each WFS was even larger due to the higher resistance of this material.

6.2.4 Heat Input versus Deposition Rate

Heat input based on AIP was plotted versus the deposition rate, which is directly proportional to the WFS. In ARCWISE, this diagram is used to characterise the productivity potential of a process on a given welding application. This characterisation is based on shading a window where the bead shape is acceptable over capability range of the power supply and process combination. Typically, the effects of arc length are evaluated to determine the heat input range as a function of productivity, which is usually either measured in travel speed for sheet metal or by deposition rate for multipass applications. In this study, the effects of %EN at constant arc length were used to assess the travel speed potential of the VP-GMAW process. This approach was used so the focus could be studying the effects VP-GMAW waveforms. The 3 mm arc length selected was considered nominal for most applications using free flight drop transfer.

It has been the experience of the author (Ref. 116-118,, 128) that heat input stays constant (or slightly decreases) for constant arc length and weld deposit size as the test travel speed increases for a process combination (wire type, CTWD, shielding gas, and waveform). Higher travel speeds provide increased base metal melting efficiency. As

travel speed increases, there is less time for heat conduction losses to the base metal so the heat produces more melting. The penetration and nugget area increase as a result of increased melting at higher travel speeds since the deposit area is constant.

The waveform affects the burnoff rate (WFS/I), and melting rate (mm/sec) which equals the WFS (mm/sec) for a stable process. The heat input provided by the process decreases with improved melting rate for a constant weld size when the arc length is constant. Higher melting rate waveforms provide increased productivity since higher speeds are required to raise the base metal melting efficiency needed to achieve the same penetration and nugget area. These benefits were quantified by comparing the maximum travel speed of GMAW-P to the VP-GMAW waveforms for the lap joint application.

For VP-GMAW of steel, the heat input window was large due to the effects of %EN (Figure 6.5). The change in heat input was 19% at 42 mm/sec WFS, 22% at 84 mm/sec WFS and 33% at 127 mm/sec WFS. These wire feed speeds corresponded to deposition rates of 1.1 to 3.6 kg/hr. The larger change in heat input at the 127 mm/s test was related to the random short circuits that remove significant power from the process.

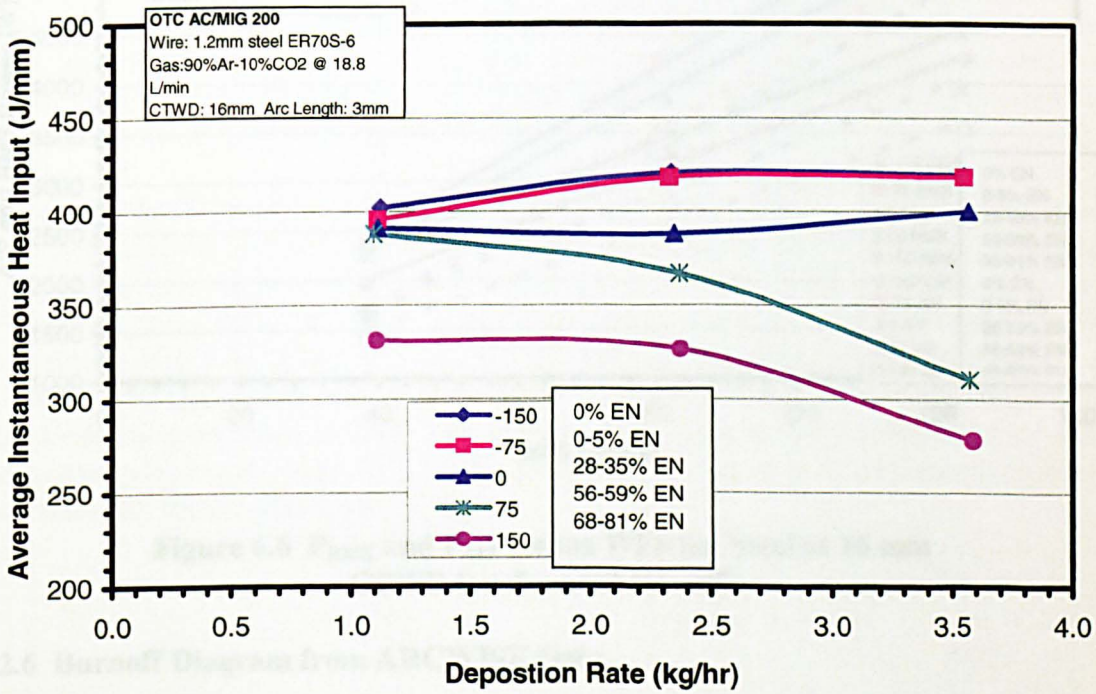

Figure 6.5 HI_{AIP} versus DR for Steel at 16 mm CTWD for the AC/MIG 200

Short circuit metal transfer was strategically used with the PC350 to further improve productivity capability of VP-GMAW process (Appendix A). The bead shape results and productivity process comparison are described later in Section 6.5. As it will be shown, both VP-GMAW power supplies offers higher welding travel speeds compared to GMAW-P and CV processes when achieving the same level of penetration and fusion quality.

6.2.5 Power (AIP, RMS) versus WFS

Heat input was calculated based on AIP as mentioned above. AIP was calculated using the high-speed DAQ software and graphed as shown in Figure 6.6. The RMS power was calculated using the product of V_{RMS} and I_{RMS} measurements. Power decreased as the %EN increased at each WFS. For the AC/MIG 200 power supply, the trend was the same for all applications. RMS power was always higher than AIP as a function of WFS at each %EN. The difference between RMS and AIP was approximately 800 watts at the 40 mm/sec WFS and decreased to 500 to 600 watts at the higher WFS's. The potential error in power measurements ranged from 40 to 11% as the WFS was increased from 42.3 to 127 mm/s, respectively. Therefore, RMS measurements should not be used to determine power for heat input calculations. V_{RMS} and I_{RMS} measurements should be used only for process settings relative to the power supply meter readings.

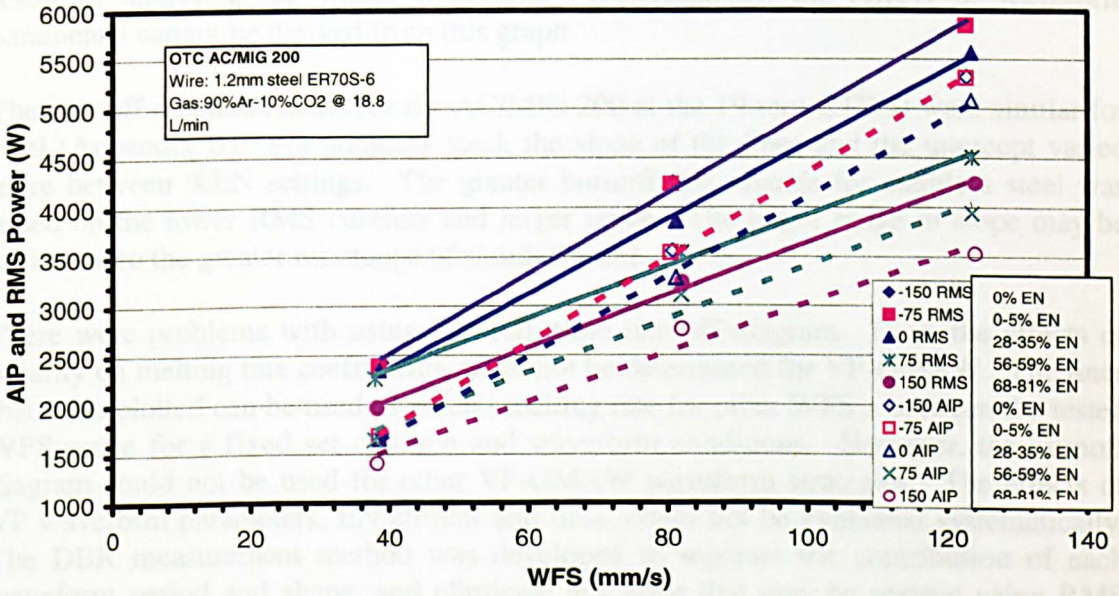

Figure 6.6 P_{RMS} and P_{AIP} versus WFS for Steel at 16 mm CTWD for the AC/MIG 200

6.2.6 Burnoff Diagram from ARCWISE Data

The WFS, I_{RMS}, and electrode extension, L were used to plot the burnoff diagram (Figure 6.7) by plotting burnoff rate, BR versus electrode extension heating factor, F_L. This burnoff diagram was for the whole waveform not separating the effects of the EN and EP periods. This evaluated the traditional way for characterization of melting rate using the BDT as applied by Allum (Ref. 63) and Richardson (Ref. 75). Lines were plotted on this figure for constant %EN based on the pendant setting of the power supply. As noted earlier, the actual EN time varied slightly for the same setting depending on the WFS. The burnoff rate increased and the electrode extension heating

factor decreased as the %EN increased at each wire feed speed. This was expected since EN polarity was found to decrease RMS current for a given WFS.

The lines were fitted with linear lines so the melting rate coefficients for arc heating, α and resistive heating, β could be determined by the resulting equations. The slope, β varied from 1.0 to 1.5 x 10^{-4} $amp^{-2}sec^{-1}$ as the waveform changed from 0% EN (GMAW-P) up to 81% EN, respectively. CV processes using the same 1.2 mm electrode in the spray mode typically yield a beta value of 0.7 to1.0 x $10^{-4}amp^{-2}sec^{-1}$ (Ref. 12, 19). Likewise, the arc heating coefficient averaged approximately from 0.08 to 0.11 $mm\text{-}amp^{-1}sec^{-1}$; based on ignoring the higher slope and low intercept for the tests made at pendant setting 75. The arc heating coefficient for spray GMAW using the same process combination is approximately 0.25 to 0.27 mm $amp^{-1}sec^{-1}$. The burnoff diagram here would indicate that resistive heating coefficients were higher and the arc heating coefficients were lower compared with CV processes. However, as explained in Section 2.0 there is no theory to explain these data other than these errors were a direct result of analysing the whole waveform. Unfortunately, the effects of waveform parameters cannot be derived from this graph.

The burnoff diagram results for the AC/MIG 200 at the 19 mm CTWD were similar for steel (Appendix B). For stainless steel, the slope of the lines and the intercept varied more between %EN settings. The greater burnoff rate change for stainless steel was based on the lower RMS currents and larger range. The larger range in slope may be attributed to the greater resistance of stainless steel.

There were problems with using this full-wave burnoff diagram. First, the effects of polarity on melting rate coefficients could not be determined for VP-GMAW. The lines that were plotted can be used to predict melting rate for other WFS's between the tested WFS range for a fixed set of torch and waveform conditions. However, the burnoff diagram could not be used for other VP-GMAW waveform strategies. The effects of VP waveform parameters, EN current and time, could not be evaluated systematically. The DBR measurement method was developed to separate the contribution of each waveform period and shape, and eliminate any error that may be present using RMS measurements on arc processes.

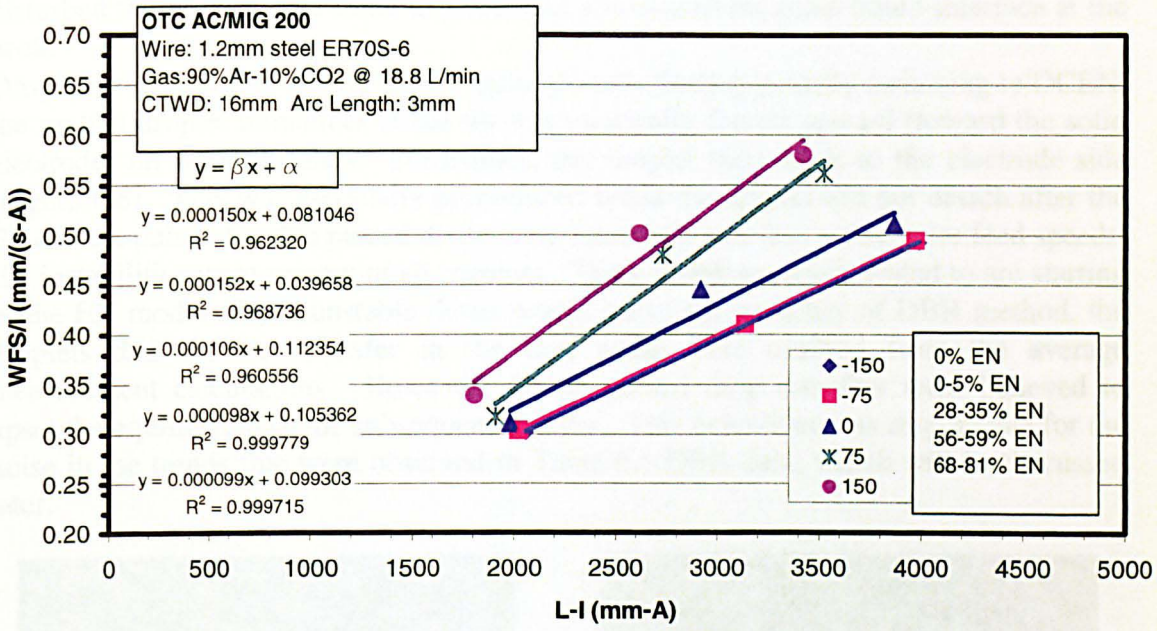

Figure 6.7 Burnoff Diagram Which Plots Burnoff Rate (WFS/I_{RMS}) versus Electrode Extension Heating Factor F_L, ($L*I_{RMS}$) for Steel at 16 mm CTWD for the AC/MIG 200

6.3 HSV Observations of Droplets and VP Arc Behaviour

The DBR method for measuring melting rate properties was based on synchronized HSV and DAQ. The main benefit of this method was including the effects of electrode extension burnoff into melting rate measurements. Prior researchers (Ref. 32, 50-52, 61-72) assumed a stationary electrode extension, and did not have the measurement capability that was applied in this investigation. The electrode extension burnback was often 50% of the droplet volume, especially at high wire feed speeds that used high EN current and low %EN (EN time); and during the EP pulse when the pre-pulse droplet volume was small.

Bead on plate tests were used so the arc length and electrode extension could be precisely measured in each period. The HSV image was optimised for the waveform period that was being characterised. The EP period was significantly brighter than the EN period. The EP arc used higher currents and the arc is constricted at the anode (electrode). The EN period used lower currents and the arc climbed over the electrode tip in the multi-spot cathode mode, as described by Norrish (Ref. 29). This produced concentrated melting until the droplet formed based on the EN current level. Therefore, each period was characterised using separate DBR tests.

The DAQ was used to determine when a waveform period started and the time was correlated to the HSV timer. The electrode extension neck position was marked at the beginning and end of each period. Special droplet conditions had to be evaluated during the HSV analysis. Arc stability was problematic during polarity changes which

disturbed the droplet, and some droplets had a non-uniform solid-liquid interface at the neck.
Drop transfer occurred during the EP pulse period. During polarity switching to DCEN, the molten droplet remainder at the tip was erratically forced upward (toward the solid electrode) on some droplets. Sometimes, the droplet then stuck to the electrode side (Figure 6.8). This was especially pronounced when the droplet did not detach after the EP current pulse. Double pulsed drops were more of a problem at low wire feed speeds. EN instabilities were present at all currents. These problems were related to arc starting in the EN mode. Since unstable drops would affect the accuracy of DBR method, the droplets that did not transfer in the first pulse were omitted from the average measurement calculations. However, double pulsed drop transfers were believed to upset the equilibrium of the subsequent transfer. This behaviour was responsible for the noise in the trends that were observed in Table 6.1 DBR data, which will be discussed later.

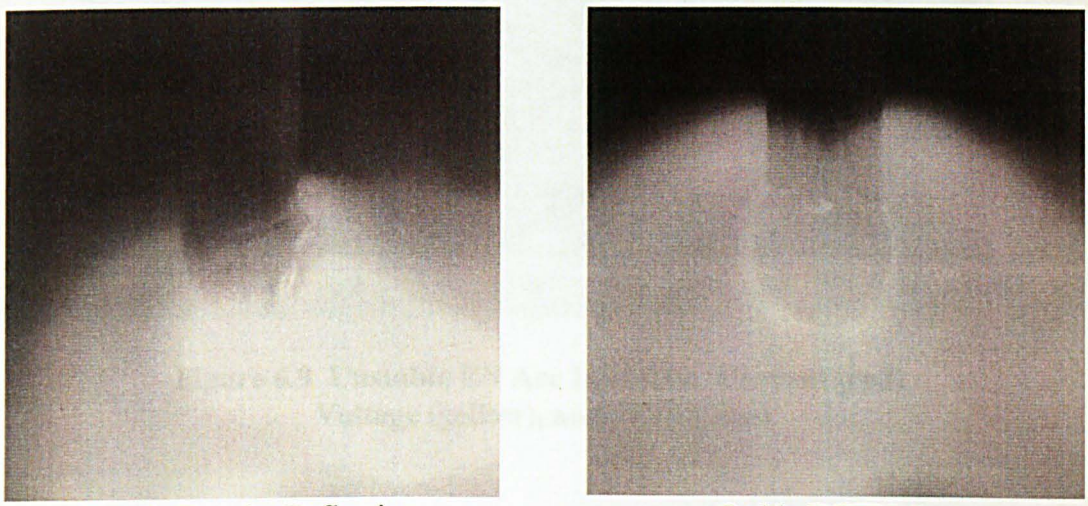

Erratic Droplet Deflection Stable DCEN Arc

Figure 6.8 Erratic and Stable EN Arc Initiation

Unstable arc ignition from EP to EN observed in the HSV data was related to the noise in the DAQ waveform for the EN period, Figure 6.9. After drop transfer and just prior to switching polarities, the EP arc spot moved to the side of the wire. The hot plasma cloud from EP arc remained off centre of the wire as the current went through zero. The low EPB current in the waveform may have promoted this arc wander. Note, prior researchers (Ref. 79-81) have noted that 40 amps is the minimum background current that should be used to maintain arc stability. The waveform here used a background current of 42 amps. A detailed sequence showing polarity switching from DCEP to DCEN was taken to document this phenomena and corresponding waveform (Figure 6.10).

After drop transfer and at the transition, the EP arc was observed to concentrate on the bottom of the droplet (Figure 6.10a). As the current was decreased the arc would start to wander on the bottom of the droplet. When the current passed through zero, the hot plasma from the EP period was still present as the EN current was applied. The EN arc

was softer and it climbed the electrode extension as the current was increased. Once into the EN period, the hot plasma cloud from the EP period disappeared. The EN arc rapidly grew the droplet and at higher EN currents caused significant electrode extension burnoff. The EN arc was stable during the main EN period. At the end of the EN period (Figure 6.11), the diffused EN arc shrank as the current approached zero. The new EP arc that started at background current (t = 0.5201 to 0.5228s) was focused on the bottom of the droplet when the droplet was large. The arc appeared to lift the droplet and little melting occurred before entering the EP peak current period. The peak current expanded the arc on the droplet and forced metal transfer.

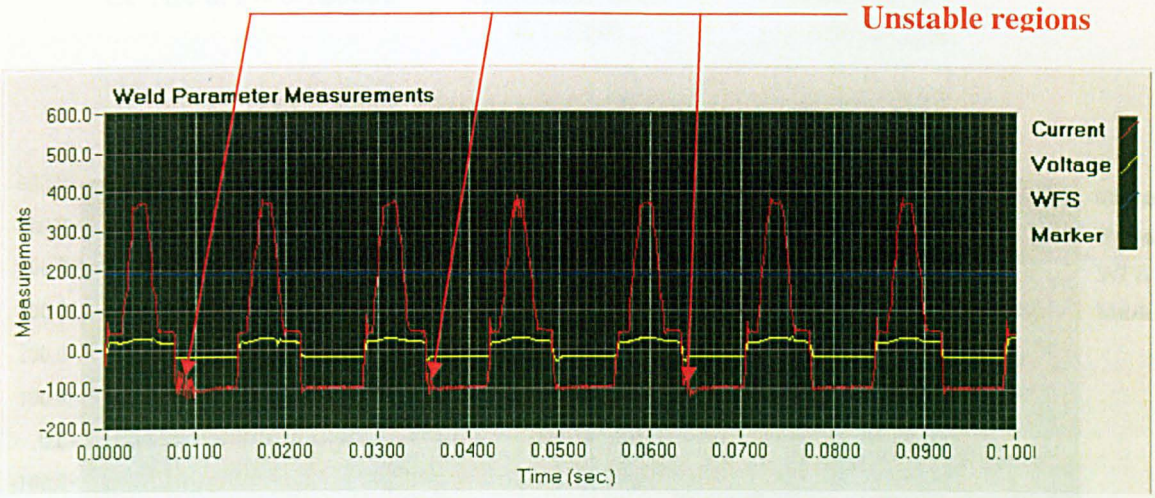

Figure 6.9 Unstable EN Arc Initiation, Current (red), Voltage (yellow), and WFS (blue)

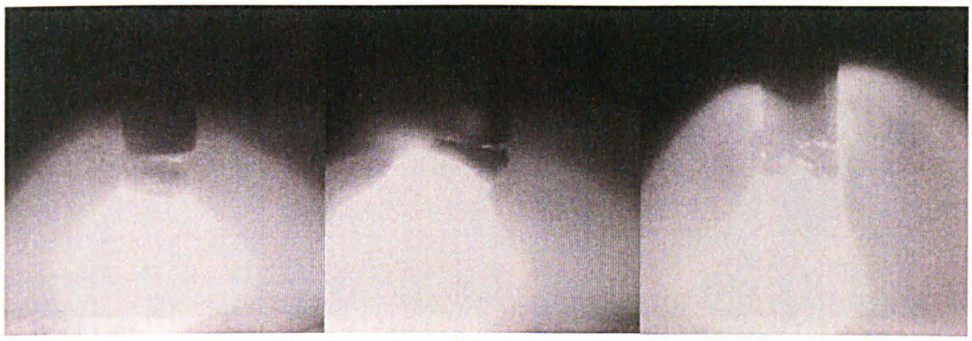

EP Arc at t = 0.12069s | Transition at t = 0.12096 | EN Arc at t = 0.12123s

(a) HSV Images Showing Polarity Change from EP to EN

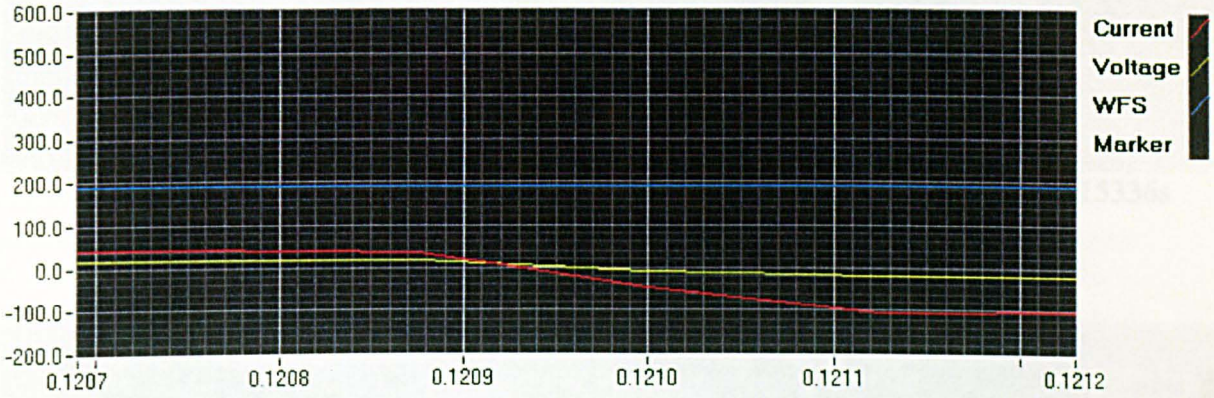

(b) DAQ of Change in Polarity

Figure 6.10 Detailed Analysis Showing Polarity Switching from EP to EN

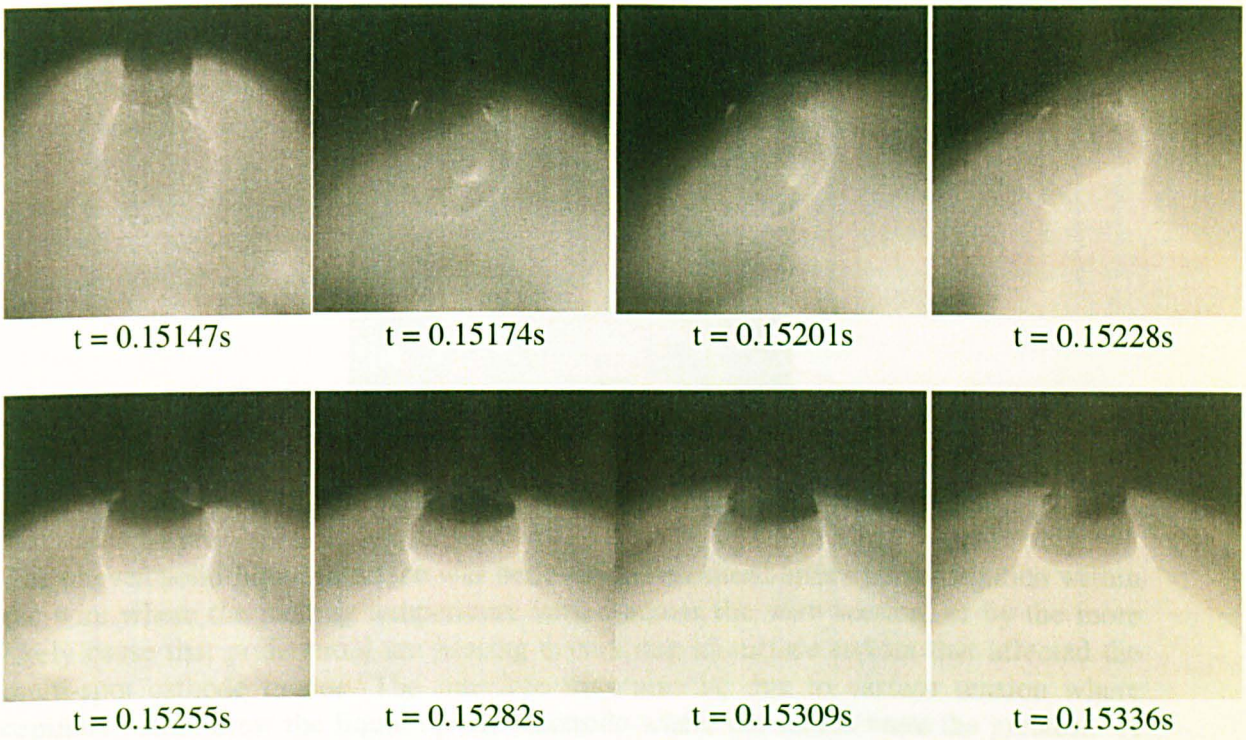

(a) HSV Images Showing Polarity Change from EN to EP

(b) Waveform Switching from EN to EP

Figure 6.11 Sequence of Photos Switching from EN to EP and Corresponding Waveform

The border between the wire and the droplet was not always a straight line (Figure 6.12). The advancing solid-liquid (burnoff) interface advanced up the electrode extension faster in some areas than others. This produced an uneven interface. If the interface was uneven at the point of measurement, an average level across the electrode droplet interface was used to determine the electrode extension burnoff, Δx.

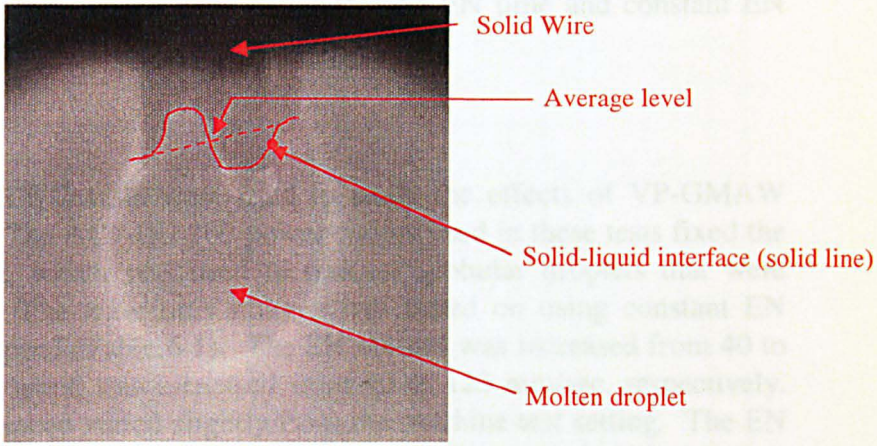

Figure 6.12 Uneven Solid-Liquid Interface at Electrode Neck

The uneven solid-liquid interface was believed to be caused either by segregation within the wire where the melting temperature varied across the wire section, or by the more likely cause that preferential arc heating occurs due to surface oxides that affected the multi-spot cathode mode. The interface may also be due to surface tension where capillary action drew the liquid up the electrode where the forces were the greatest. A second phase liquid appeared to segregate at the interface of some droplets (Figure 6.13). This material was assumed to be a slag since the steel electrode was ER70S-6, which is double deoxidised. This slag was observed floating on the surface but was always attached to the interface. If it was slag, it probably precipitated by reactions with the oxidizing shielding or was a remnant of the wire manufacturing process. The slag was believed to have interfered with the droplet growth process and cause the uneven solid-liquid interface on some droplets.

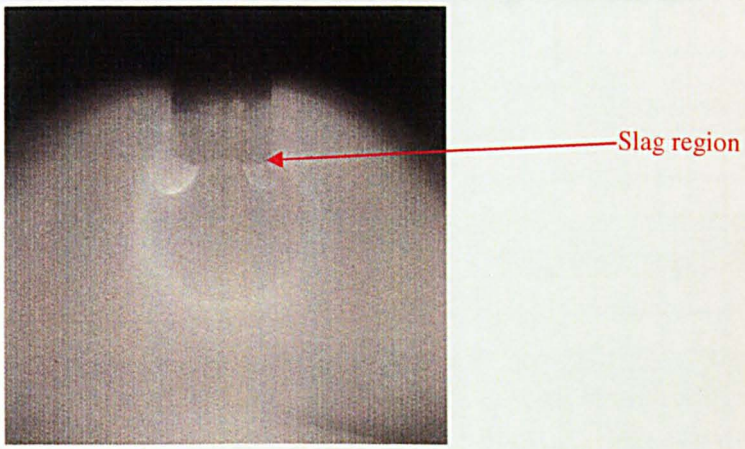

Figure 6.13 Molten Slag Floating on the Surface of Droplet Interface

As shown above, there were many sources for variation in metal transfer. These include the arc position during polarity cross-over, the melting interface of the growing droplets, impurities (or slag) in the wire, and poor waveform that inhibits a one drop per pulse regulation. These variations produced some noise in the data trends shown in Table 6.1

and promoted the detailed study of droplets that had good growth behaviour. The growth rates of droplets in each period were dependent on EN time and constant EN current, and EP pre-pulse droplet volume, respectively.

6.4 Melting Rate Results

Constant arc length and CTWD tests were used to study the effects of VP-GMAW waveform on melting rate. The AC/MIG 200 power supply used in these tests fixed the EP pulse period waveform, which was used to transfer globular droplets that were formed in the EN period. The waveform strategy was based on using constant EN current for each wire feed speed (Table 6.1). The EN current was increased from 40 to 133 amps as the wire feed speed was increased from 40 to 123 mm/sec, respectively. The actual DAQ wire feed speed varied slightly from the machine test setting. The EN current strategy was almost linear over this wire feed range. It was approximately 1 to 1.1 amp EN to each mm/sec of wire feed speed over this range, respectively. The power transferred to the work was controlled by setting the %EN which changed the pulse frequency and the EN time. The %EN settings ranged from -150 to 150. However, most of the waveforms generated using %EN setting from 0 to -150 were GMAW-P type waveforms, therefore, these settings were not studied. EN period waveform was consistently added to the waveform strategy at a pendant setting of 0 to 150. The EN period time increased as the pendant setting increased to the maximum of 150. The arc length trim feature varied pulse frequency by varying EPB time, to control arc length.

The DBR method was used to measure the melting rate properties of each waveform period. The main focus was EN heating and waveform effects. Many measurements were taken to capture the relationship between EN current and time on the melting rate. DBR measurements were also taken for the EP period which used a constant pulse waveform. Here, separate DBR measurements were taken during the peak of the trapezoidal waveform (constant peak current) and at constant background current.

Table 6.1 DBR Measurements for EN Waveform Parameters

Weld No.	WFS_{DAQ} (mm/s)	Δx (mm)	t_{EN} (s)	$\Delta x/t_{EN}$ (mm/s)	MR_{EN} (mm/s)	V_d (mm^3)	V_D (mm^3/s)	I_{EN} (A)	BR (mm/(s A))	F_L (mm A)	f (Hz)	%EN (%)
0-42	39.32	-0.074	0.0083	-8.896	30.42	0.258	31.22	40.03	0.761	513.92	41.75	34.57
30-42	39.01	-0.005	0.0113	-0.451	38.56	0.446	39.57	39.81	0.968	512.48	44.04	49.63
60-42	38.26	0.020	0.0143	1.423	39.68	0.581	40.71	39.68	1.001	511.26	45.31	64.70
90-42	38.52	-0.097	0.0173	-5.582	32.93	0.584	33.79	39.56	0.833	507.45	39.51	68.31
120-42	38.96	-0.010	0.0202	-0.503	38.45	0.797	39.45	39.55	0.972	509.01	39.01	78.76
150-42	38.95	-0.041	0.0232	-1.752	37.20	0.885	38.17	39.55	0.941	508.40	34.72	80.52
0-63	59.28	0.076	0.0056	13.553	72.83	0.420	74.73	60.72	1.201	784.08	66.94	37.64
30-63	59.28	0.127	0.0086	14.767	74.04	0.653	75.97	62.30	1.189	806.07	66.07	56.82
60-63	59.28	0.157	0.0116	13.623	72.90	0.865	74.80	62.33	1.169	807.41	57.80	66.82
90-63	59.28	0.155	0.0145	10.663	69.94	1.043	71.76	62.39	1.121	808.10	50.03	72.69
120-63	59.28	0.366	0.0175	20.877	80.15	1.441	82.24	62.49	1.283	815.99	42.98	75.30
150-63	59.28	0.152	0.0205	7.423	66.70	1.405	68.44	62.33	1.070	807.25	36.90	75.76
0-85	80.34	0.276	0.0040	68.415	148.76	0.616	152.64	97.20	1.528	1264.92	74.03	29.89
30-85	83.01	0.502	0.0070	71.409	154.42	1.113	158.46	96.24	1.603	1263.26	71.78	50.43
60-85	81.65	0.592	0.0100	58.946	140.60	1.448	144.27	95.36	1.474	1255.96	61.51	61.76
90-85	81.83	0.528	0.0130	40.703	122.54	1.632	125.73	95.07	1.289	1249.17	51.00	66.20
120-85	81.96	0.478	0.0159	30.014	111.98	1.828	114.90	95.05	1.178	1246.48	43.99	69.99
150-85	81.25	0.546	0.0189	28.833	110.08	2.139	112.95	94.91	1.160	1247.83	38.90	73.68
0-106	102.24	0.218	0.0032	68.476	170.72	0.559	175.17	110.61	1.546	1436.18	91.04	29.04
30-106	102.24	0.650	0.0062	105.217	207.46	1.316	212.87	112.90	1.837	1490.29	74.98	46.34
60-106	102.24	0.737	0.0092	80.503	182.74	1.716	187.51	115.19	1.587	1525.50	60.99	55.81
90-106	102.24	0.785	0.0121	64.864	167.10	2.075	171.46	115.64	1.445	1534.25	51.00	61.71
120-106	102.24	0.897	0.0151	59.300	161.54	2.506	165.75	115.60	1.397	1540.17	42.19	63.79
150-106	102.24	0.970	0.0181	53.666	155.91	2.892	159.97	115.67	1.348	1545.37	37.12	67.11
0-127	123.28	0.426	0.0031	136.979	260.26	0.831	267.05	133.60	1.948	1748.63	91.09	28.34
30-127	123.49	0.754	0.0061	123.265	246.76	1.550	253.20	133.30	1.851	1766.52	71.83	43.96
60-127	123.55	0.813	0.0091	89.319	212.87	1.988	218.43	132.00	1.613	1753.14	58.06	52.83
90-127	123.31	0.914	0.0121	75.695	199.01	2.467	204.20	131.37	1.515	1751.45	49.68	60.01
120-127	123.21	0.554	0.0150	36.964	160.17	2.462	164.35	131.88	1.214	1734.47	43.60	65.31
150-127	123.94	0.777	0.0181	42.989	166.93	3.097	171.29	131.63	1.268	1745.89	38.06	68.81

The DBR method measured the total melting rate, MR by adding the electrode extension burnoff rate $\Delta x/t$ to the data acquisition wire feed speed, WFS_{DAQ} measured by the tachometer in that period. Hence, near steady-state conditions were established permitting the use of the BDT for solving the melting rate equation coefficients for each period and different waveforms. The synchronised DAQ and HSV measurements were also used to measure droplet volume, V_d and growth rate, V_D. These measurements provided important insight into variations in melting rate measurements as a function of EN waveform.

6.4.1 EN Time Effects on Droplet Volume Growth Rate

HSV was used to measure the droplet volume as a function of time at each wire feed speed. The average EN droplet volume measurement for all DBR tests (Table 6.1) was taken from 0.5 sec of image data at 3700 fps frame speed. The raw data for all the DBR measurements are included in Appendix C. Typically ten droplets per condition were used for DBR measurements depending on the stability of the waveform and metal transfer. The frequency range was small, only 35 to 42 Hz, at the low wire feed speed of 40 mm/sec. At 123 mm/sec wire feed speed, the pulse frequency ranged from 38 to 91 Hz. Pulse frequency at each wire feed speed decreased as the %EN decreased. The number of droplets available for measurement for each EN waveform condition, therefore, varied from 17 to 45 droplets (1/2 the frequency) since only 0.5 sec of data was taken.

Table 6.1 shows that five EN current and wire feed speed combinations were studied to assess the effects of EN time and current. The EN current was constant for each wire feed speed. The five different wire feed speeds (42, 63, 84, 106, and 127 mm/s) were characterised at low %EN, which ranged from a minimum of 28 to 38%, to the highest %EN ranging from 67 to 81%. The EN time increased as the %EN increased for each constant current test. Pendant settings for these times corresponded to 0 for low EN time and 150 for the maximum EN time offered by the AC/MIG 200 power supply. The low EN times varied between 3.1 to 8.3 msec at a 0 setting for wire feed speeds ranging from 127 and 42 mm/s, respectively. The high EN times ranged 18 to 23 msec at the 150 setting for the same wire feed speeds. Slightly longer EN times were used at the lower wire feed speeds, but the EN current and frequency were much lower.

From the data in Table 6.1, there appeared to be a non-linear relationship in electrode extension burnoff, Δx and droplet volume, V_d, as a function of EN time. At long EN times, the electrode extension burnoff saturated on average at about 10 msec of EN time for wire feed speeds greater than 63 mm/s. The droplet volume continued to grow but at a slower rate once the electrode burnoff saturated. The change in droplet volume was related by evaluating the droplet volume growth rate.

The droplet volume growth rate, V_D was typically higher at short EN time for constant EN current. This was especially true for the higher wire feed speed tests. The total wire feed speed was heavily dependent on the electrode extension burnoff, Δx. Observation of the burnoff distance for each group of tests gave insight to the variation in electrode

melting rate as a function of time. Here, the electrode extension burnoff was a larger part of the total wire feed speed at short EN time.

Since there was a non-linear relationship between EN current and melting rate, which was a function of EN time, additional image analysis was performed on three droplets from the low and high time from each wire feed speed test group. The droplets that were selected had uniform arc initiation and were considered ideal. Note, that many of the droplets observed in the full 0.5 sec of HSV data had unstable arc initiation entering the EN period. This provided one source of error as discussed earlier.

The droplet volume was graphed during the whole EN period by continuously accounting for the wire feed speed and electrode extension burnoff in each HSV frame as a function of time. The graphs (Figures 6.14) were plotted to (1) evaluate how the EN droplet volume, V_d grows with time, (2) determine the magnitude of growth rate, V_D from the slope of the line and (3) compare the effects of EN pulse time at constant EN current. These results were plotted in Figures 6.14a through 6.14e for each wire feed speed and EN current combination.

The line fitted in each graph was for droplet volume based on the melting rate over time. The slope of the line equalled the droplet volume growth rate, V_D. At a wire feed speed of 42 mm/s, V_D was 38.7 and 25 mm^3/sec for low and high time, respectively as shown in Figure 6.14a. The EN current for this wire feed speed was 40 amps. The V_D increased to 276.7 and 192.6 mm^3/sec at low and high EN time, respectively for 123 mm/s wire feed speed (EN current = 133 amps) as shown in Figure 6.14e. In all these tests, the low EN time produced a higher V_D compared to long EN times. The lines fitted in these graphs were linear. From observation of the data in each graph, it appeared that the droplet volume growth rate was constant for both low and high EN time near the origin. However, the linear lines fitted to the long EN time tests showed that the overall droplet volume growth rate was less for each WFS test condition at long EN time. A 2^{nd} order polynomial may have provide a better data fit for the long EN time tests, but for EN time comparison the linear data was easier to compare between the short and long EN time tests. These measurements were based on the best droplets from the HSV data. In general, this data agreed with the average trend measured for all the droplets over the 0.5 sec of HSV data shown in Table 6.1, especially for the higher wire feed speed test groups.

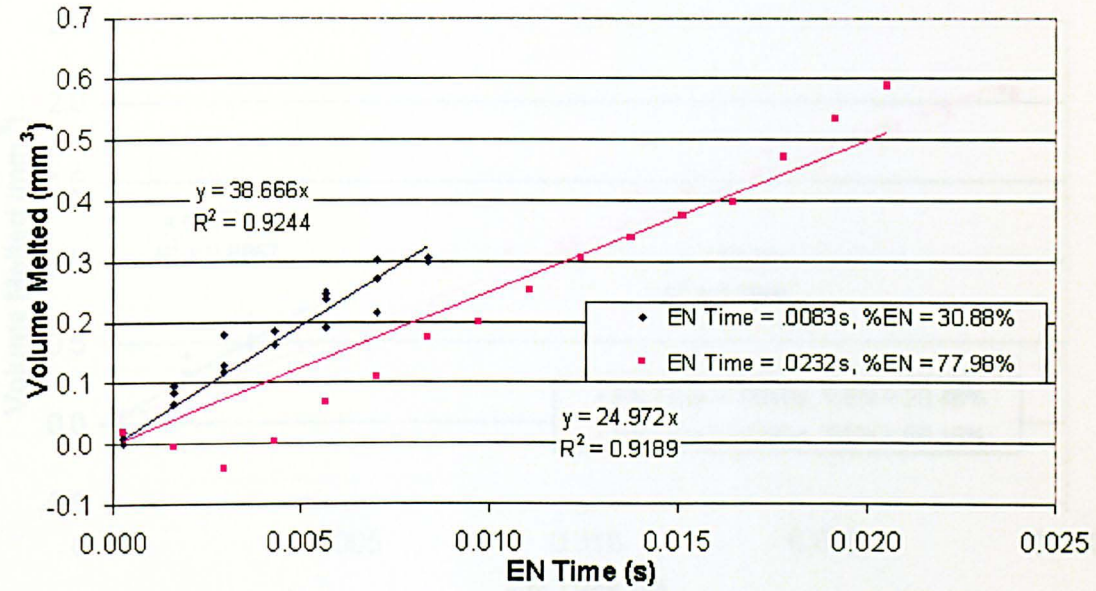

Figure 6.14(a) Volume Melted vs. EN Time (42 mm/s) for Three Droplets at 40 amps

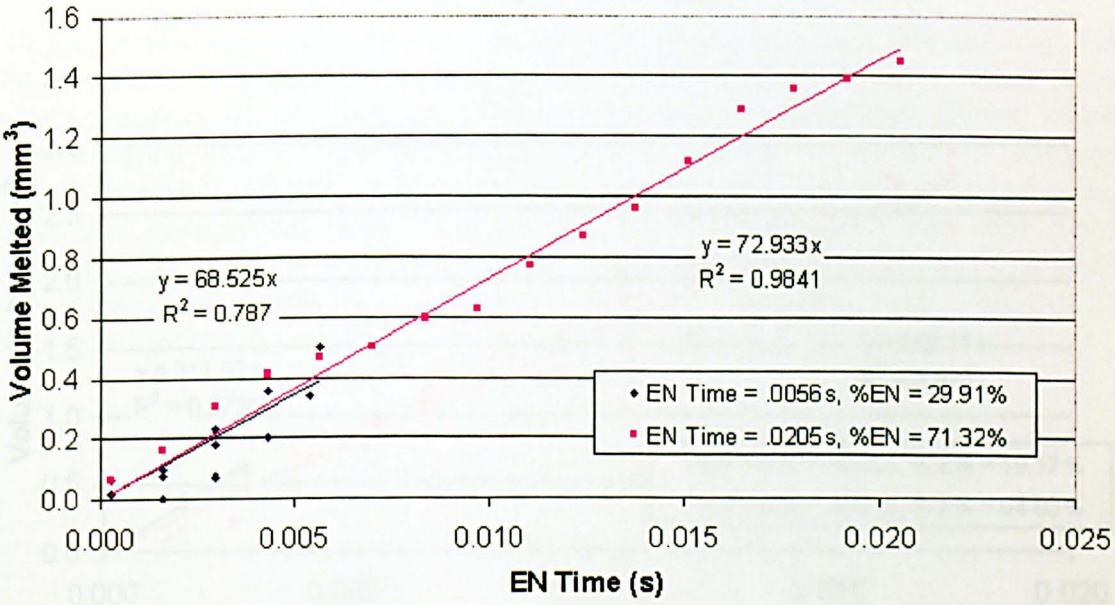

Figure 6.14(b) Volume Melted vs. EN Time (63 mm/s) for Three Droplets at 62 amps

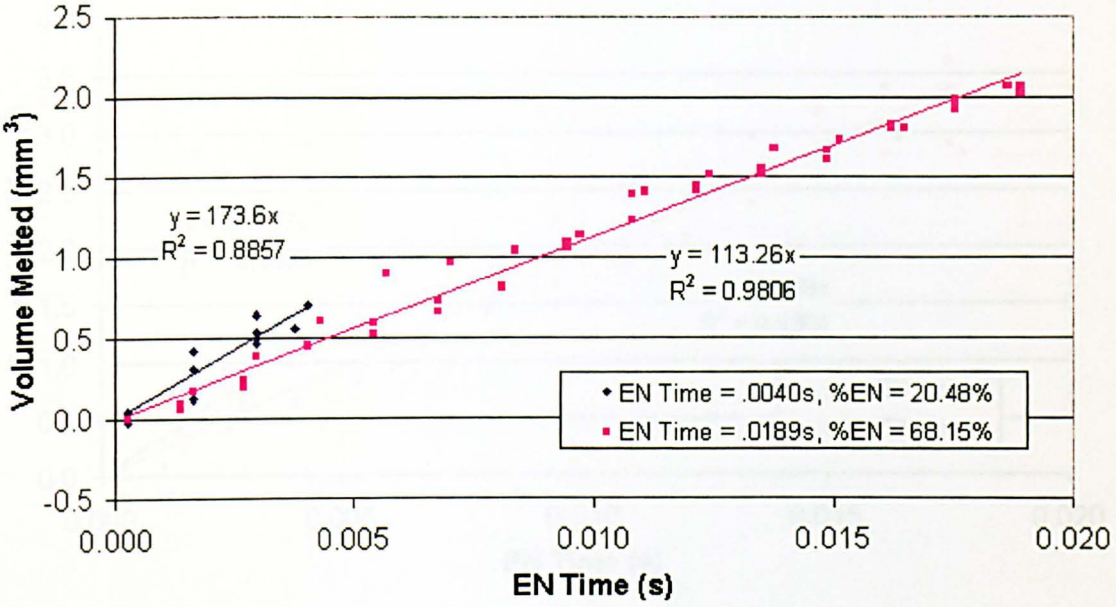

Figure 6.14(c) Volume Melted vs. EN Time (85 mm/s) for Three Droplets at 95 amps

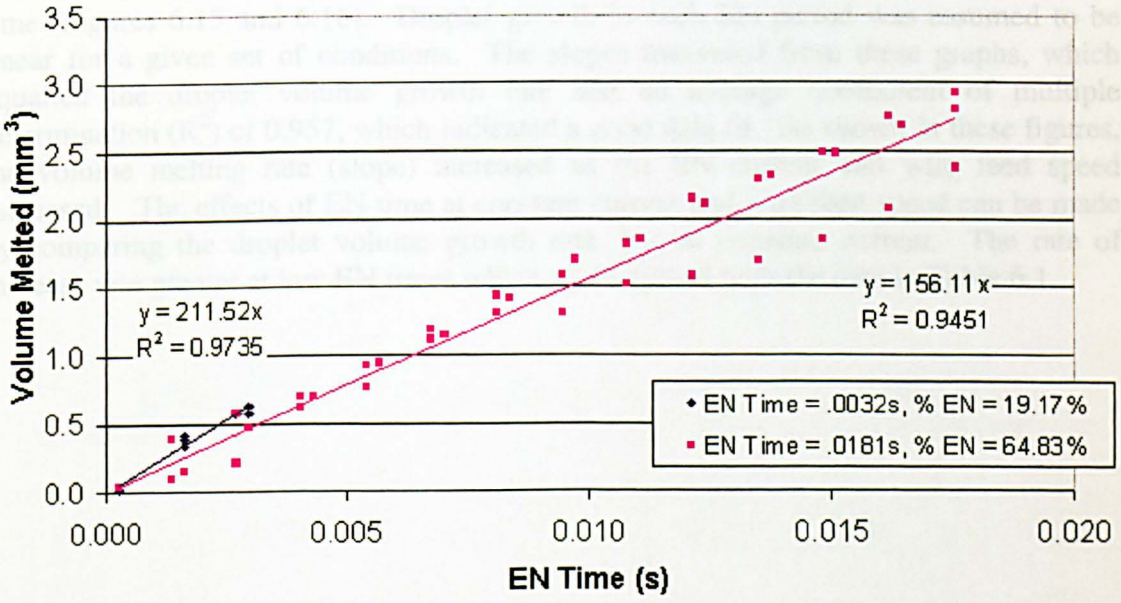

Figure 6.14(d) Volume Melted vs. EN Time (106 mm/s) for Three Droplets at 115 amps

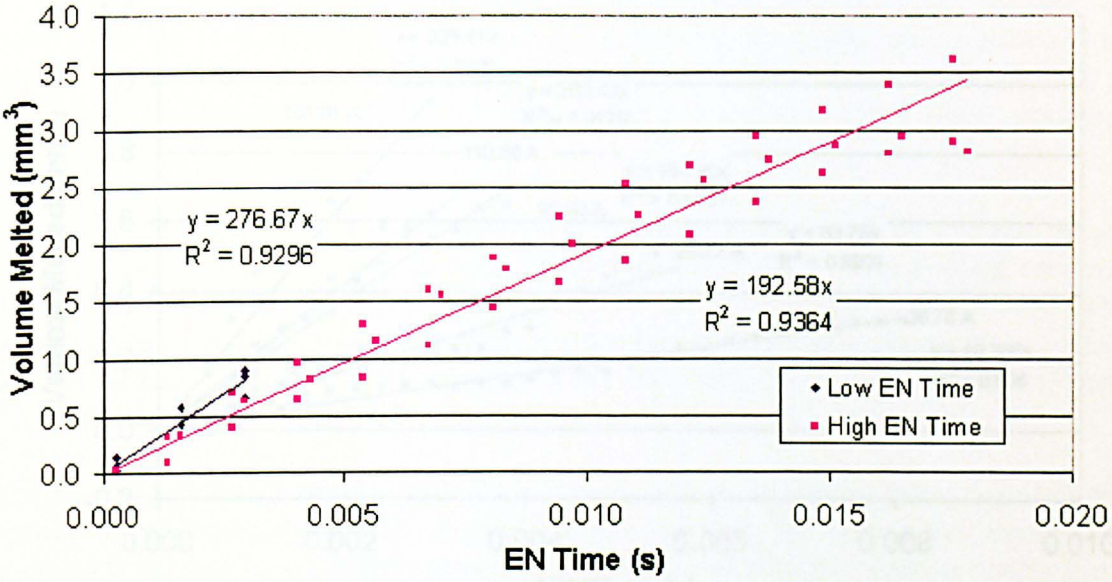

Figure 6.14(e) Volume Melted vs. EN Time (127 mm/s) for Three Droplets at 133 amps

A summary of these droplet growth rate tests was graphed for both low and high EN time (Figures 6.15 and 6.16). Droplet growth in each EN period was assumed to be linear for a given set of conditions. The slopes measured from these graphs, which equalled the droplet volume growth rate had an average coefficient of multiple determination (R^2) of 0.957, which indicated a good data fit. As shown in these figures, the volume melting rate (slope) increased as the EN current and wire feed speed increased. The effects of EN time at constant current and wire feed speed can be made by comparing the droplet volume growth rate, V_D, at constant current. The rate of increase was greater at low EN times which again agreed with the data in Table 6.1.

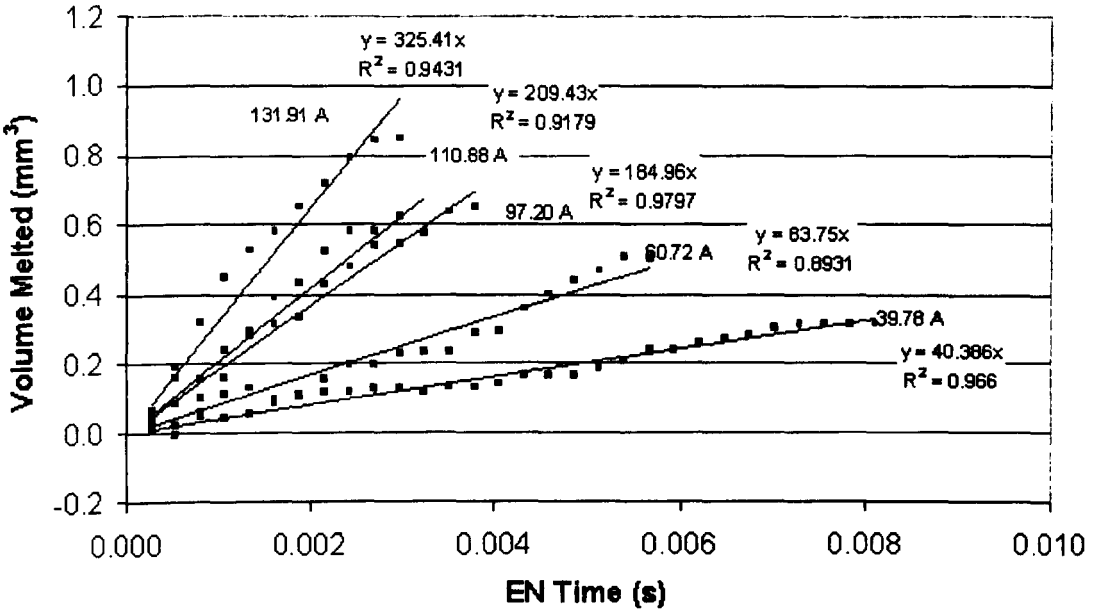

Figure 6.15 Volume Melted vs. EN Time (All WFS/Low EN Time)

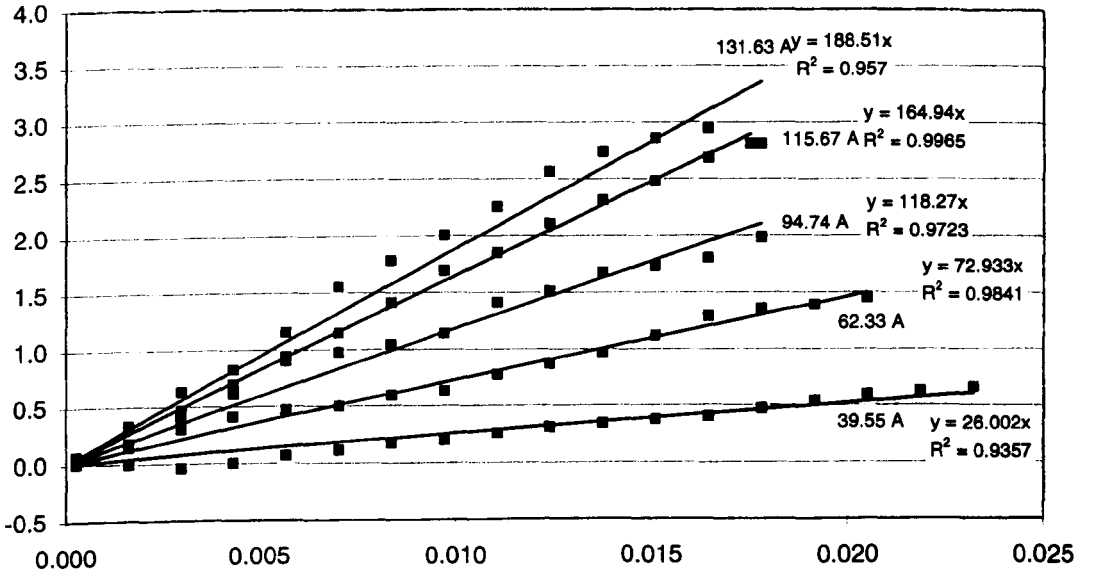

Figure 6.16. Volume Melted vs. EN Time (All WFS/High EN Time)

6.4.2 DBR Measurements for the EN Period

The DBR method described in Section 5.2 was used to study metal transfer and determined the melting rate for each period in the VP-GMAW waveform. Most of these measurements were focused on the EN period. The melting rates, MR's which account for the electrode extension burnoff were determined for five different wire feed speeds (42, 63, 84, 106, and 127 mm/s) using six different %EN levels that varied from 0 to

75% (Table 6.1). Again, the corresponding pendant settings were 0, 30, 60, 90, 120, and 150. Since the melting rates were sensitive to EN time, the results were separated into groups for plotting. The EN time groups were 3 to 5.9, 6.0 to 8.9, 9.0 to 11.9, 12.0 to 14.8, 14.9 to 17.9, and 18.0 to 23.2 msec. These were basically 3 msec groupings except for the last.

The synchronised HSV and DAQ data were averaged to determine an average MR_{EN}, L_{EN}, and EN current and time at each condition (Table 6.1). The burnoff rate was determined by dividing the total melting rate by the EN current for each test. The heating factor was determined by multiplying the average electrode extension, L_{EN} times the EN current. These results were plotted to construct the burnoff diagram (Figure 6.17), which was used to solve for the melting rate coefficients.

The burnoff rate was plotted against the electrode extension heating factor based on the burnoff diagram technique, BDT. Again, Richardson (Ref. 75) showed this approach to be an accurate way to solve experimentally for the arc and resistive heating coefficients. The y-axis intercept was equal to the arc heating coefficient, α and the slope of each line was equal to the resistive heating coefficient, β. The overall shape of this graph showed that the burnoff rate range increased as the heating factor increased, so these coefficients were not constant for EN heating.

This was the opposite of CV burnoff diagrams where a single line should be produced describing the melting rate behaviour of a GMAW consumable set. The lines in Figure 6.17 were fitted to the data and were based on the 3 msec EN time increment. This approach was used based on the dependency on droplet growth rate to EN time that was established earlier. The highest burnoff rates as a function of heating factor, F_L were achieved at the lowest EN times. Likewise, long EN times showed a decrease in burnoff rate. The line fit was satisfactory considering the effects of EN time was grouped into increments to show these trends.

There appeared to be distinct variation in burnoff behaviour with EN time. The EN waveforms were found to produce higher burnoff rates with shorter EN time at each current and wire feed speed combination. Comparing the equations that were solved for each line shows that the slope, which equals the resistive heating coefficient (β) varied from 2.9 to 6.0 x 10^{-4}, $A^{-2}s^{-1}$. These units were large for the resistive heating coefficients. This was not expected since polarity should not affect the resistivity of the electrode.

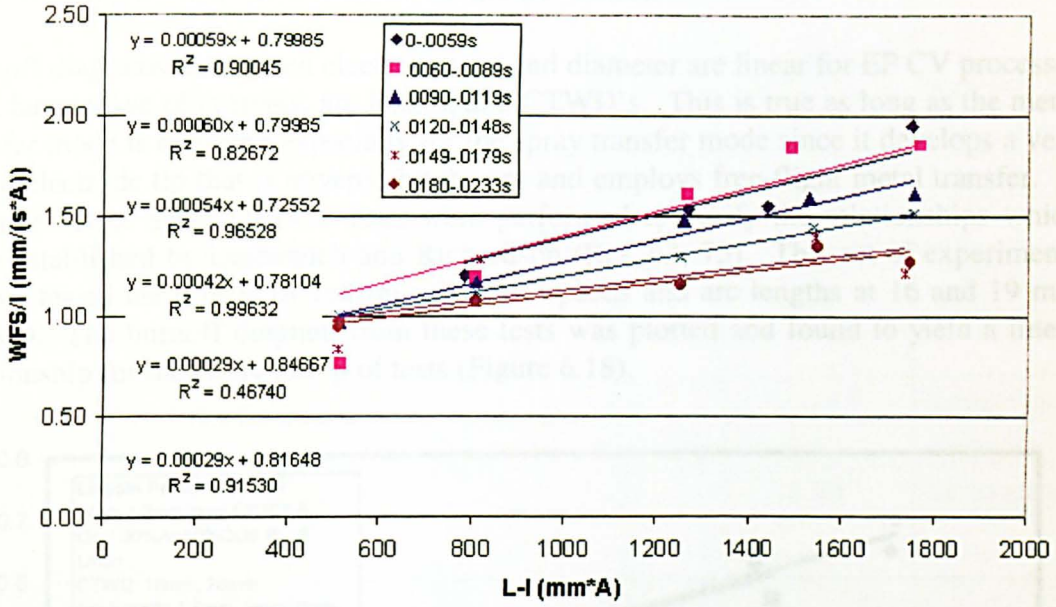

Figure 6.17 Burnoff Diagram for EN Waveforms for 1.2 mm Steel Electrode at 3 mm Arc Length and 16 mm CTWD Using AC/MIG 200 Power Supply

A theory was developed to explain why β was dependent on EN time. The increase in melting rate at short EN times was believed to be due to a concentrated melting effect. Careful observation of the HSV data showed that the EN arc rapidly climbed the electrode tip; the extent depended on the current level. The electrode tip that was covered by the EN arc rapidly melted and promoted higher droplet growth rates in the initial part of the EN period. The electrode extension burnoff, Δx, saturated as the EN time increased at constant current and wire feed speed. The large droplet that was formed decreased the melting effect of cathode heating at long EN time since the arc concentrated on it heating the droplet. Plus, the charge distribution carrying current may be affected as boiling metal vapour releases free electrons, which can promote thermionic emission lowering arc heating. This theory is supported by the Norrish (Ref. 29) who observed that a constant voltage EN arc can oscillate between a multi-spot and single spot cathode as the droplets form and detach, respectively.

The burnoff rate in Figure 6.17 was heavily dependent on the electrode extension burnoff based on the measurements in Table 6.1. The electrode extension burnoff rate was up to 50% of the total melting rate at low EN time, especially at the higher currents and wire feeds speeds. Since higher burnoff rate results in large changes in line slope, the effect is measured by the resistive heating coefficient. The average electrode length was used in determining the electrode extension heating factor. Since the electrode extension became shorter when including the burnoff effect, the heating factor decreased. This would increase the slope of the lines too. Therefore, electrode extension burnoff acts to increase the slope of the burnoff diagram based on its affect on both graph parameters, BR and F_L. Prior researchers did not include the effects of electrode extension changes with waveform which can be a significant contribution to electrode melting.

6.4.3 Melting Rate Measurements for the EP Period

Burnoff diagrams for a given electrode type and diameter are linear for EP CV processes for a large range of currents, arc length, and CTWD's. This is true as long as the metal transfer mode is constant; especially for the spray transfer mode since it develops a very stable electrode tip that is covered by the arc and employs free-flight metal transfer. A separate set of spray GMAW tests were performed to verify the relationships which were established by Lesnewich and Richardson (Ref. 63, 75). This set of experiments simply tested the effects of several wire feed speeds and arc lengths at 16 and 19 mm CTWD. The burnoff diagram from these tests was plotted and found to yield a linear relationship for the entire group of tests (Figure 6.18).

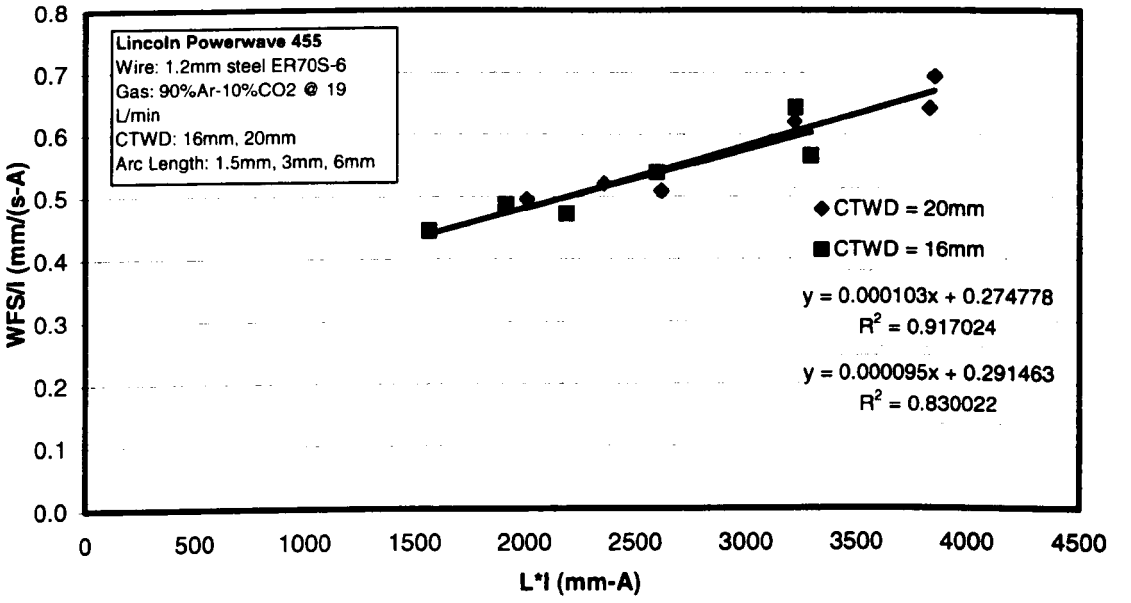

Figure 6.18 Burnoff Diagram for Spray Metal Transfer using a EP CV Power Supply for 1.2 mm Steel Electrode at Various Arc Lengths and 16 and 19 mm CTWD

Here, the arc heating coefficient was 0.28 mm-$A^{-1}s^{-1}$ and the resistive heating coefficient was 0.9 to 1.0 x 10^{-4}, $A^{-2}s^{-1}$. This simple set of tests reinforced the use of the BDT for solving melting rate relationships. The arc heating and resistive heating coefficients were in good agreement with the measurements provided by Lesnewich and Halmoy for CV spray as shown in Table 6.2.

Table 6.2 Summary of Melting Rate Coefficients for Steel Electrodes

Process	Electrode Diameter (mm)	Polarity	EN Time (msec)	α (mm* $A^{-1}s^{-1}$)	β (10^{-4}, $A^{-2}s^{-1}$)	Reference
CV Spray	0.8	EP		0.56	2.9	Lesnewich
CV Spray	1.14	EP		0.25	0.7	Lesnewich
CV Spray	0.8	EP		0.47	0.9	Halmoy
CV Spray	1.0	EP		0.47	0.9	Halmoy
GMAW-P	0.8	EP		0.55	3.5-3.7	Richardson
GMAW-P	1.0	EP		0.47	0.91	Richardson
GMAW-P	1.2	EP		0.27	0.59	Richardson
VP-GMAW	1.14	EN	0.0-5.9	0.80	5.9	Sect. 6.4.2
			6.0-8.0	0.80	6.0	
			9.0-11.9	0.72	5.4	
			12.0-14.8	0.78	4.2	
			14.9-17.9	0.85	2.9	
			18.0-23.3	0.82	2.9	
CV Spray	1.14	EP		0.28	0.9 - 1.0	Sect. 6.4.3
VP-GMAW	1.14	EP		-0.35 - 0.55	0.7 – 1.2	Sect. 6.4.3.1

6.4.3.1 DBR Measurements for EP Pulse

Measurements made on the EP period of the VP-GMAW waveforms were found to be difficult. The major challenge was accommodating the wide range in light intensity during the current while following the position of the electrode extension neck. The image analysis software helped filter the light intensity of recorded images, but the contrast was too great during the full peak current to locate the solid - liquid interface if the arc expanded over the droplet. Even though improvement can still be made to the HSV equipment, enough good images were obtained at several waveforms to study the EP pulse melting process in VP-GMAW.

Visual observation of the melting process yielded some important results. First, like EN period, the arc in the EP pulse rapidly climbed the electrode tip above the droplet, when the droplet was small as the current was ramped to high values. As the arc covered the electrode, rapid melting occurred. An entire column of electrode above the droplet was observed to melt and mix with the droplet on pulses where the arc grew on the electrode extension. The droplet started to neck in most cases before finishing the pulse peak or

during the downslope. Different arc behaviour was observed when the droplet size was large. Here, the EP pulse arc rooted on the bottom of large droplets. This behaviour was found to influence the electrode melting rate (Table 6.3).

Once the neck started for droplet detachment, the peak current arc would follow the detaching drop towards the weld pool. This resulted in some solidification at the electrode tip as the neck broke and before the arc re-attached itself to the electrode tip. Therefore, the melting efficiency of the EP period was related to the droplet formation process and size, but here the driving mechanism which controlled melting was largely related to the pre-pulse droplet size.

Detailed DBR measurements for EP pulse GMAW were performed on 10 different conditions shown in Table 6.3. These conditions represented the range of EP pulse conditions that were observed with the VP-GMAW waveforms. The droplet volume immediately after detachment was measured to be 0.391 mm^3 for most waveforms. The droplet was approximately equal to a half hemisphere based on the wire diameter immediately after detachment and starting into a new period. The EN pendant settings of 0, 90, and 150 resulted in %EN range of 34 to 81% for 42 mm/s and 28 to 69% for 127 mm/s tests. Electrode positive background was only measured on four of the waveforms. At both wire feed speeds, the 150 pendant setting resulted in a waveform that had no background time and alternated between EP and EN pulses.

The DBR measurements were calculated for each EP period based on the steady state time for the arc, t_p or t_b. The time used for EP background t_b was equal to the time for that period. For the EP peak period, the time t_p was from the period beginning until drop detachment of the first drop. This was factored to accommodate the large change in electrode melting rate that occurred at drop detachment.

These EP pulse parameters were used to calculate the burnoff rate, BR, and the electrode extension heating factor, F_L. The BDT was then used to plot the data in Table 6.3 and solve for the arc and resistive heating coefficients (Figure 6.19). Lines were fitted on the DBR measurements that had both background and peak periods for that waveform. The points on the left side of this figure were from background measurements and the right side were from peak measurements. From these lines it was obvious that EP melting rate coefficients were not constant.

The change in arc heating coefficients was related to the pre-pulse droplet volume, Figure 6.20. This relationship was made to account for the arc behaviour observed in the HSV images. As the pre-pulse droplet volume increased with increasing %EN, both the arc and resistive heating coefficient decreased. The effect was the greatest on the arc heating coefficient.

Table 6.3 BDR Measurements for EP Waveforms

Weld No.	WFS_{DAQ} (mm/s)	Δx (mm)	t_p or t_b (s)	$\Delta x/t_p$ or $\Delta x/t_b$ (mm/s)	MR (mm/s)	V_d (mm^3)	V_D (mm^3/s)	I_p or I_b (A)	BR (mm/(s A))	F_L (mm A)	f (Hz)	EPP or EPB Period (%)	V_{pp}-(pre-pulse) (mm^3)
B-0-42	39.09	-0.273	0.0119	-22.890	16.20	0.198	16.62	25.19	0.430	320.88	41.75	49.81	0.39
B-90-42	38.94	-0.057	0.0015	-37.708	1.23	0.002	1.27	24.81	0.028	318.72	39.51	5.97	0.39
B-0-127	123.28	-0.115	0.0009	-125.521	-2.24	-0.002	-2.30	46.46	-0.051	595.50	91.09	8.36	0.39
B-90-127	123.31	-0.221	0.0016	-141.286	-17.97	-0.029	-18.44	46.12	-0.315	588.69	49.68	7.78	0.39
P-0-42	39.09	0.500	0.0016	303.535	342.63	0.579	351.56	362.08	0.980	4752.26	41.75	6.87	0.78
P-90-42	38.94	0.424	0.0030	142.661	181.60	0.553	186.34	365.32	0.497	4780.87	39.51	11.73	1.05
P-150-42	38.84	0.184	0.0023	81.325	120.17	0.280	123.30	365.39	0.407	4738.09	34.72	7.87	1.38
P-0-127	123.28	-0.130	0.0053	-24.338	98.95	0.541	101.53	373.14	0.267	4779.97	91.09	48.56	1.11
P-90-127	123.31	-0.556	0.0044	-125.595	-2.28	-0.010	-2.34	381.48	-0.008	4805.50	49.68	21.99	2.86
P-150-127	123.97	-0.617	0.0047	-132.507	-8.56	-0.041	-8.79	382.26	-0.022	4803.67	38.20	17.79	3.78

Notes:

1) Weld No. code defines EP period - pendant setting – wire feed speed (mm/s)
2) For EP period: B indicates background period and P indicates peak period from that test
3) The pendant setting of 150 had no background period to measure
4) Pre-pulse droplet volume, V_{pp} was measured from high speed video DBR plus post-pulse remainder of 0.39 mm^3

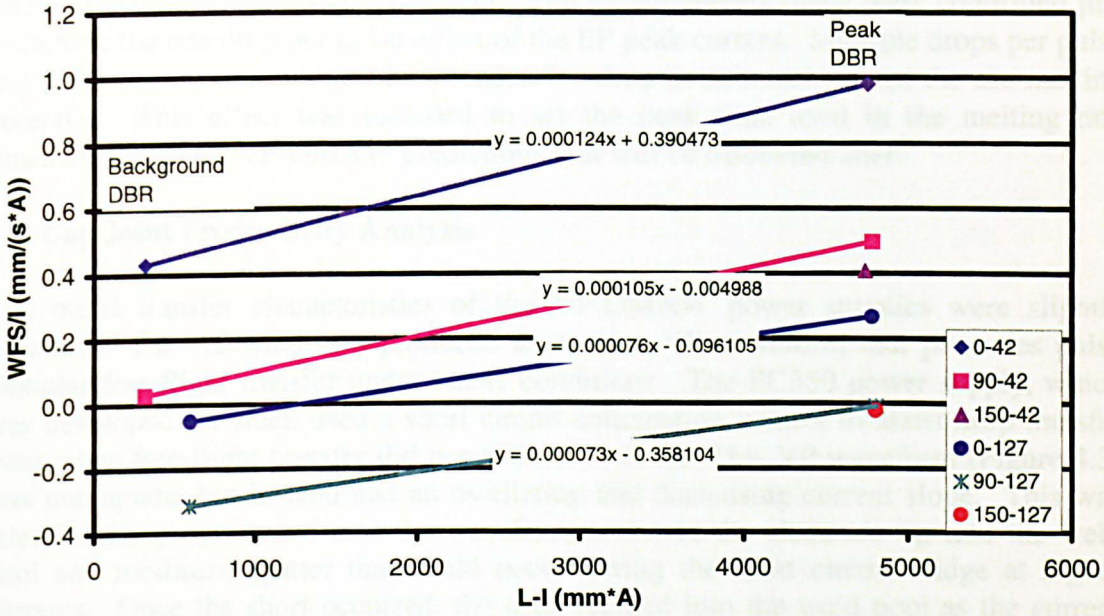

Figure 6.19 Burnoff Diagram for EP Waveforms for 1.2 mm Steel Electrode at 3 mm Arc Length and 16 mm CTWD Using AC/MIG 200 Power Supply

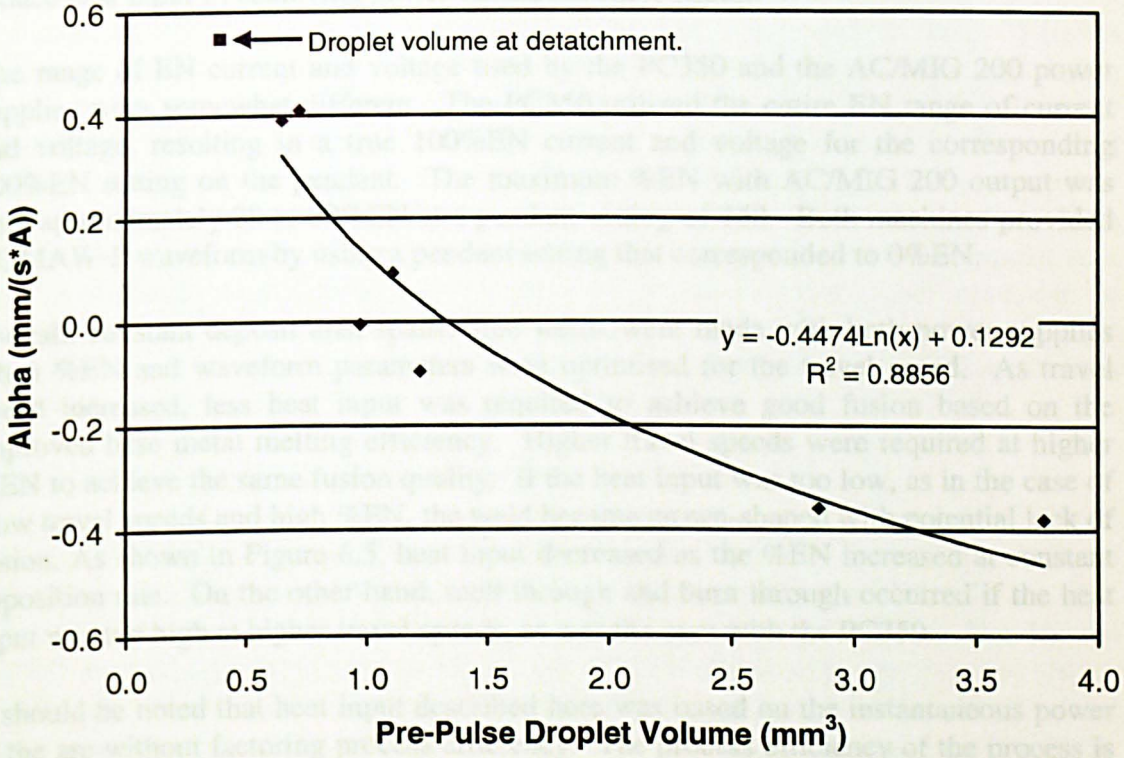

Figure 6.20 EPP Pre-pulse Droplet Volume Effects on Arc Heating Coefficient

As shown above, the droplet formation process had a large effect on the burnoff rate (WFS/I) and the arc heating coefficient. The measurements made were controlled just to capture the one drop per pulse effect of the EP peak current. Multiple drops per pulse and peak current time longer than needed for drop detachment reduce the arc melting potential. This effect was included to set the peak time used in the melting rate Equation (5.22) for VP-GMAW predictions that will be discussed later.

6.5 Lap Joint Productivity Analysis

The metal transfer characteristics of the VP-GMAW power supplies were slightly different. The AC/MIG 200 produced a constant VP waveform that promotes pulse globular free-flight transfer under stable conditions. The PC350 power supply, which was developed for steel, used a short circuit anticipation control to assist drop transfer even when free-flight transfer did occur (Ref. 1, 2, 8). This VP waveform (Figure 4.3) was not square, but instead had an oscillating and decreasing current slope. This was intentionally programmed into the waveform to lower the electrode tip into the weld pool and minimize spatter that could occur during the short circuit bridge at higher currents. Once the short occurred, the drop merged into the weld pool as the current increased rapidly back to peak level to melt the electrode and restrike the arc. If the short circuit occurred too early in the peak period of either polarity, the short circuit anticipation control would add peak time to the pulse as it went through its pre-programmed cycle. The current is then reduced again to promote another lower current short circuit assuring droplet transfer. The short circuit transfer mechanism also helped reduce heat input by removing power during the short circuit.

The range of EN current and voltage used by the PC350 and the AC/MIG 200 power supplies were somewhat different. The PC350 utilized the entire EN range of current and voltage, resulting in a true 100%EN current and voltage for the corresponding 100%EN setting on the pendant. The maximum %EN with AC/MIG 200 output was only approximately 28 to 80%EN at a pendant setting of 150. Both machines provided a GMAW-P waveform by using a pendant setting that corresponded to 0%EN.

Overall, constant deposit area spatter-free welds were made with both power supplies when %EN and waveform parameters were optimised for the travel speed. As travel speed increased, less heat input was required to achieve good fusion based on the improved base metal melting efficiency. Higher travel speeds were required at higher %EN to achieve the same fusion quality. If the heat input was too low, as in the case of slow travel speeds and high %EN, the weld became crown-shaped with potential lack of fusion. As shown in Figure 6.5, heat input decreased as the %EN increased at constant deposition rate. On the other hand, melt through and burn through occurred if the heat input was too high at higher travel speeds, as was the case with the PC350.

It should be noted that heat input described here was based on the instantaneous power in the arc without factoring process efficiency. The process efficiency of the process is sensitive to joint design (Ref. 93, 94) where bead-on-plate typically has the lowest efficiency (~70%) and groove welds the highest (~80%). Since calorimeter measurements were not taken, the heat input discussion here is based on arc power. The

process efficiency for lap is probably between bead on plate and groove welds, but may be slightly higher due to the efficiency of VP-GMAW melting rate.

Lap joint tests were performed on both steel and stainless steel with the AC/MIG 200 and with steel on the PC350. The lap joint for each material used equal thickness sheet, which was 1.8 mm. The weld size was based on a WFS/TS ratio of 10 and assured ample filler material for bridging the 1t gap if the heat input was optimised for the travel speed. A gap was used since a major claimed benefit of VP-GMAW is gap filling on sheet metal welds. Arc length was held constant at approximately 3 mm, which is a preferred arc length for easy benchmarking GMAW processes. On sheet metal, shorter arc lengths, probably near 1 mm offer higher possible welding speeds. The 3 mm arc length was slightly long but was found necessary with the large droplets formed with this process. In addition, waveforms and drop transfer tend to be more erratic at shorter arc lengths since short circuits are more common. Shorter arc lengths require much better metal transfer otherwise spatter levels will be unacceptable.

The ARCWISE test matrix required up to 30 tests depending on the capacity of the power supply. The PC350 offered 350 amps so it required the greatest number of tests to evaluate the power supply capability. The results of these tests were used to characterise travel speed (productivity) potential of each power supply versus standard GMAW-P, the 0%EN tests. The travel speed of each application was determined by shading the area for acceptable bead shape on the heat input versus deposition rate graph. An acceptable weld had no lack of fusion or melt through.

For constant deposit area welding applications, the heat input required for good fusion decreased with increasing travel speed and deposition rate (Figures 6.21 through 6.25). Heat input was controlled for the constant weld deposit area by the %EN in the waveform test matrix. Higher travel speeds were required to increase the base metal melting efficiency with lower heat input. As travel speed increases, there was a lower heat input loss by base metal conduction, so the heat was used more efficiently for base metal melting. The ARCWISE approach is based on comparing constant deposit area weld applications so the benefits of advanced processes, like lower heat input, can be compared for an application. The shaded area on these graphs represented acceptable weld beads based on visual analysis of the bead shape maps, which are discussed in the following.

6.5.1 AC/MIG 200 Productivity Analysis on Steel

The AC/MIG 200 power supply was evaluated on the lap joint application at both 16 and 19 mm contact tip to work distance, CTWD as shown in Figures 6.21 and 6.22. The ARCWISE data sets showed little difference between the two CTWD's. The 16 mm CTWD showed a slightly larger window. The GMAW-P tests that used pendant setting of -75, and -150 were all acceptable across the full range of the power supply. The heat input was almost constant for both the -75 and -150 pendants setting at each CTWD. Here, the heat input was 440 J/mm at 16 mm CTWD and 400 J/mm at the 19 mm CTWD, respectively. The longer CTWD provide a 10% reduction in heat input.

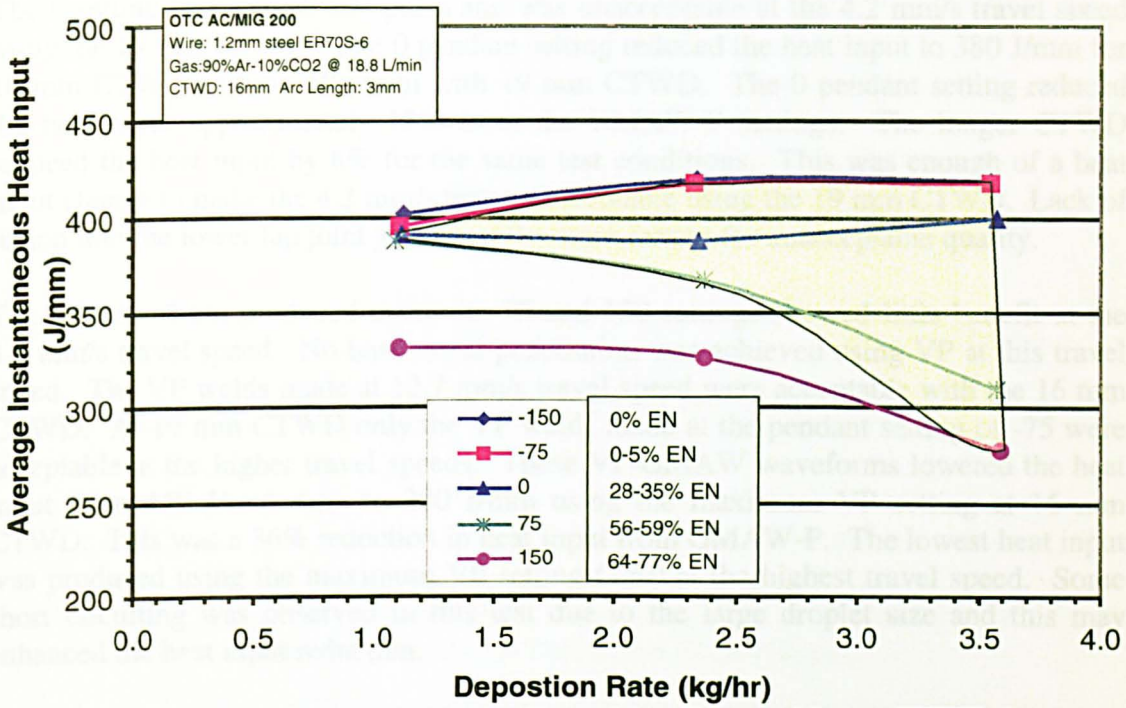

Figure 6.21(a) Heat Input versus Deposition Rate at 16 mm CTWD for Steel Using the AC/MIG 200 Power Supply

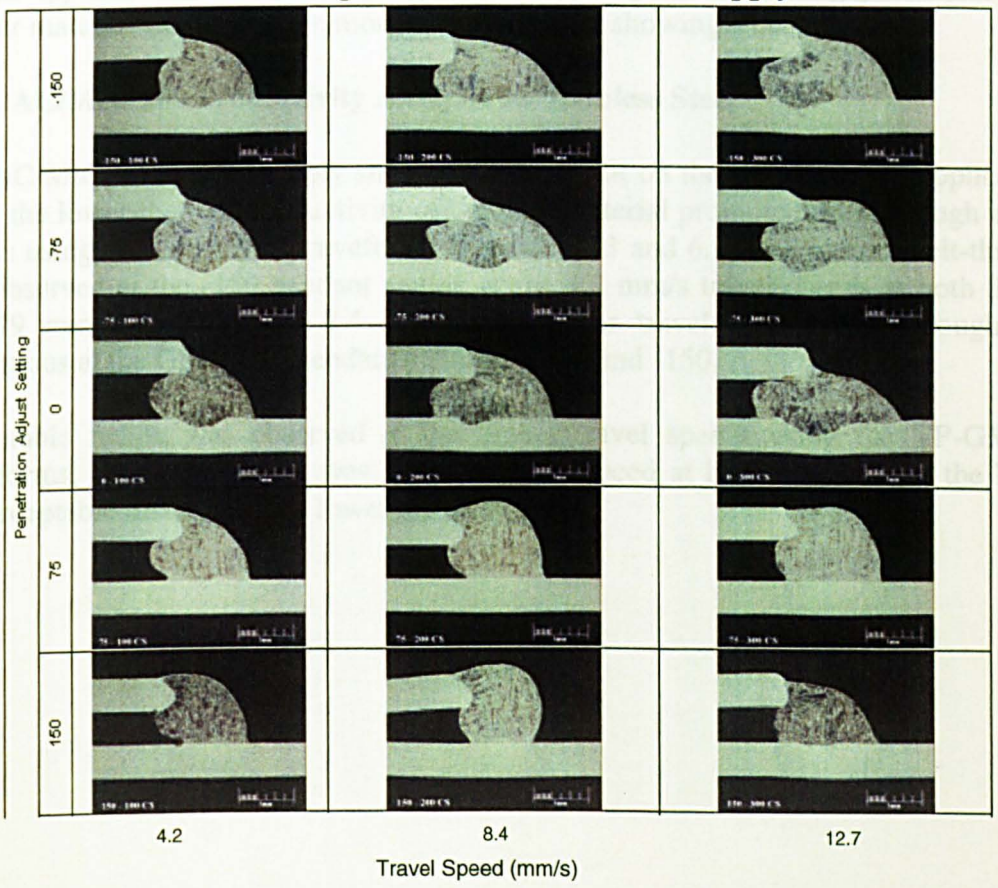

Figure 6.21(b) Macrosection Map for Steel Lap Joint Application at 16 mm CTWD Using AC/MIG 200 Power Supply

The 0 setting had a small EN pulse and was unacceptable at the 4.2 mm/s travel speed using the 19 mm CTWD. The 0 pendant setting reduced the heat input to 380 J/mm for 16 mm CTWD and to 350 J/mm with 19 mm CTWD. The 0 pendant setting reduced the heat input approximately 13% from the GMAW-P settings. The longer CTWD reduced the heat input by 8% for the same test conditions. This was enough of a heat input change to make the 4.2 mm/s tests unacceptable using the 19 mm CTWD. Lack of fusion into the lower lap joint piece was the main reason for unacceptable quality.

The VP waveform produced using the 75 and 150 settings showed little benefit at the 4.2 mm/s travel speed. No base metal penetration was achieved using VP at this travel speed. The VP welds made at 12.7 mm/s travel speed were acceptable with the 16 mm CTWD. At 19 mm CTWD only the VP welds made at the pendant setting of -75 were acceptable at the higher travel speeds. These VP-GMAW waveforms lowered the heat input from 440 J/mm min. to 280 J/mm using the maximum VP setting at 16 mm CTWD. This was a 36% reduction in heat input from GMAW-P. The lowest heat input was produced using the maximum VP setting (150) at the highest travel speed. Some short circuiting was observed in this test due to the large droplet size and this may enhanced the heat input reduction.

Overall, the current capacity of the AC/MIG 200 limited the benefit of VP waveforms on this application. Smaller weld deposits made on joints with no gap or made from thinner material would provide more opportunity for showing a benefit.

6.5.2 AC/MIG 200 Productivity Analysis on Stainless Steel

The AC/MIG 200 power supply showed more benefit on the stainless steel application. Here, the lower thermal conductivity of the base material promoted melt-through at low speeds using the GMAW-P waveforms (Figures 6.23 and 6.24). Random melt-through was observed at the -150 pendant setting at the 4.2 mm/s travel speeds at both the 16 and 19 mm CTWD's. At 8.4 mm/s and higher travel speeds melt-through was continuous at the GMAW-P pendant settings of -75 and -150.

Acceptable fusion was observed at the higher travel speeds using the VP-GMAW waveforms. The penetration was significantly reduced at higher %EN, but the beads had acceptable fusion into the lower lap joint piece.

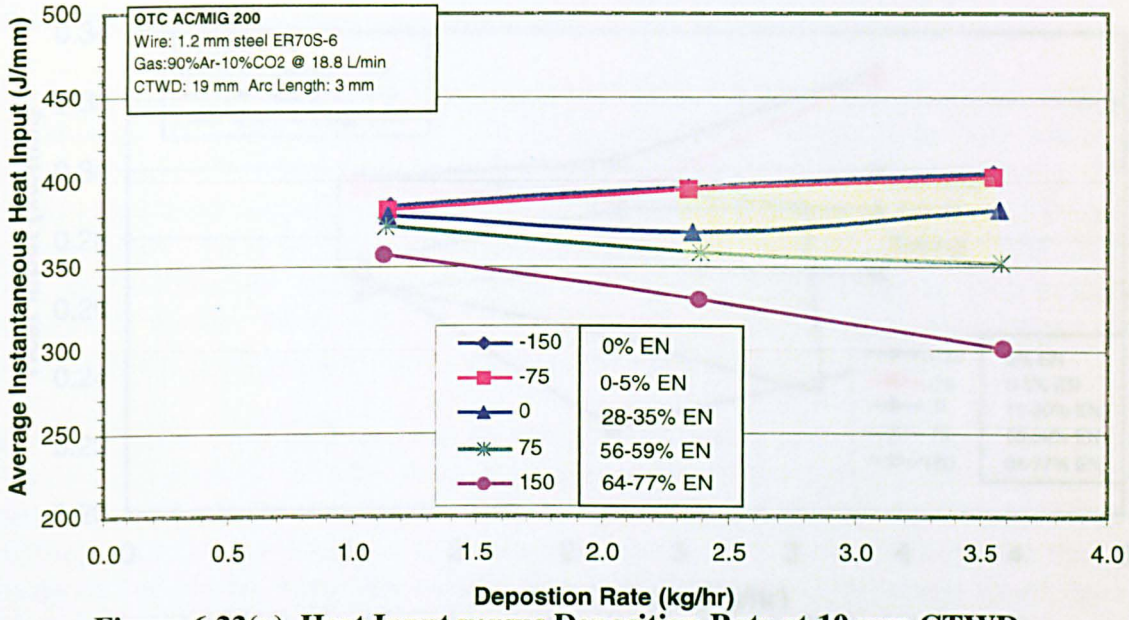

Figure 6.22(a) Heat Input versus Deposition Rate at 19 mm CTWD for Steel Using the AC/MIG 200 Power Supply

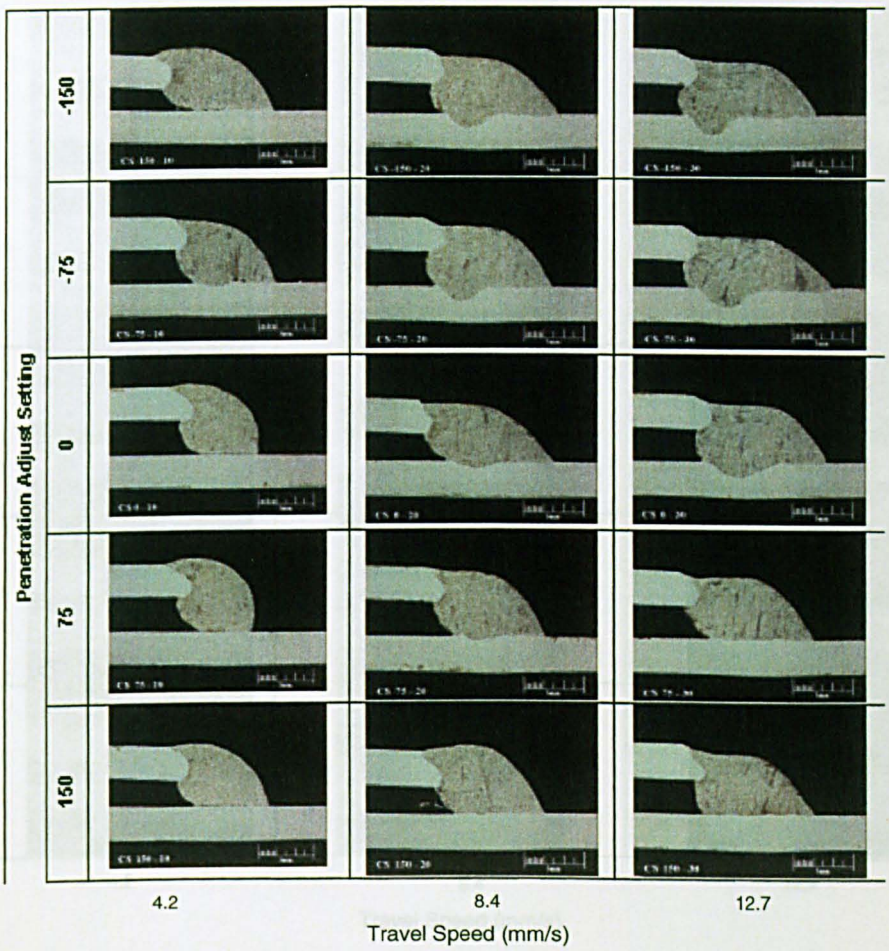

Figure 6.22(b) Macrosection Map for Steel Lap Joint Application at 19 mm CTWD Using AC/MIG 200 Power Supply

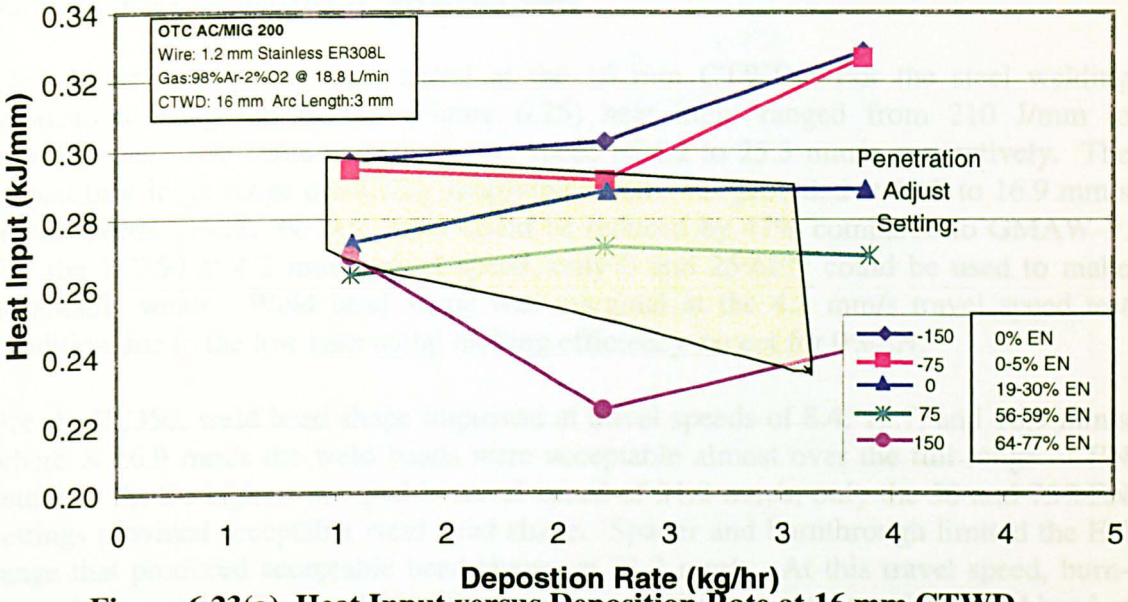

Figure 6.23(a) Heat Input versus Deposition Rate at 16 mm CTWD for Stainless Steel Using the AC/MIG 200 Power Supply

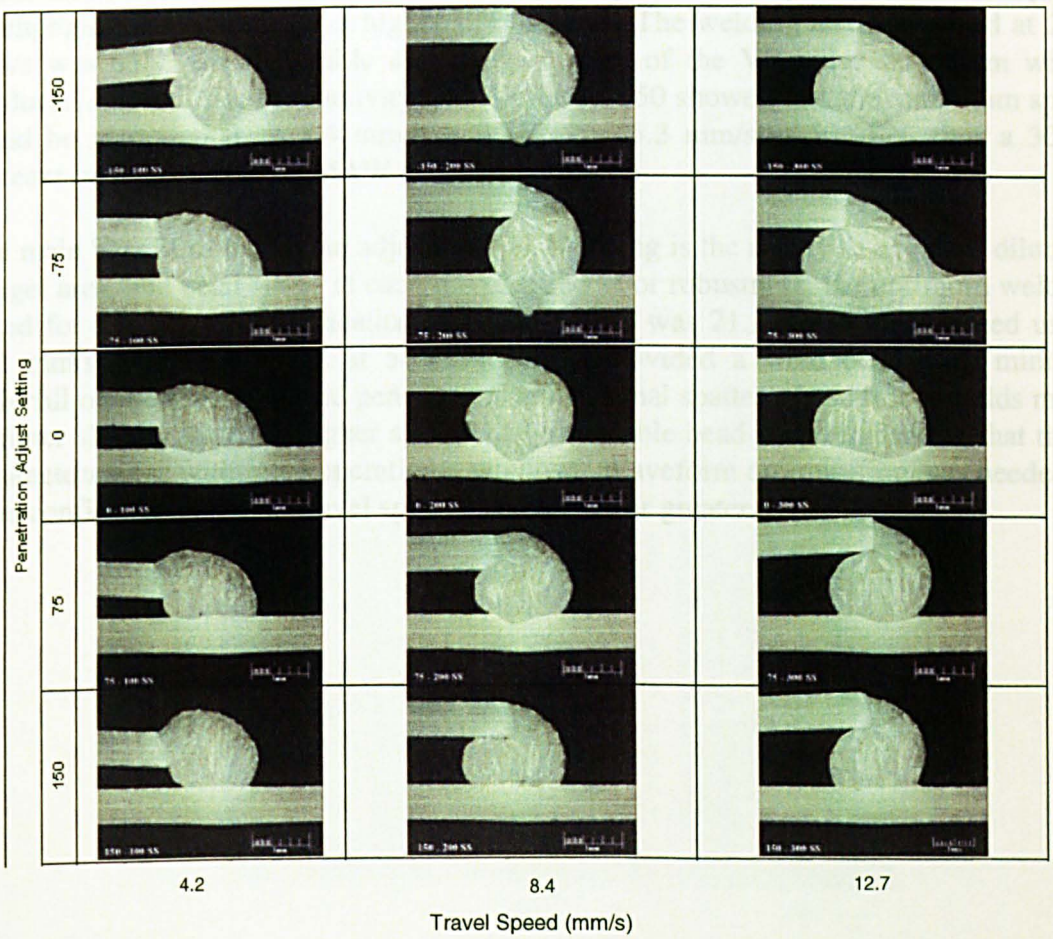

Figure 6.23(b) Macrosection Map for Stainless Steel Lap Joint Application at 16 mm CTWD Using AC/MIG 200 Power Supply

6.5.3 PC350 Productivity Analysis on Steel

This power supply was only tested at the 16 mm CTWD. For the steel welding application using the PC350 (Figure 6.25) heat input ranged from 210 J/mm to approximately 370 J/mm over the travel speed of 4.2 to 25.3 mm/s, respectively. The largest heat input range producing acceptable welds was provided at 12.7 to 16.9 mm/s travel speeds. Here, the heat input could be reduced by 47% compared to GMAW-P. For the PC350 at 4.2 mm/s travel speed, only 0 and 25%EN could be used to make acceptable welds. Weld bead shape was marginal at the 4.2 mm/s travel speed test condition due to the low base metal melting efficiency except for 0%EN.

For the PC350, weld bead shape improved at travel speeds of 8.4, 12.7, and 16.9 mm/s where at 16.9 mm/s the weld beads were acceptable almost over the full range of EN settings. At the highest acceptable travel speed of 21.2 mm/s, only the 50 and 75%EN settings provided acceptable weld bead shape. Spatter and burnthrough limited the EN range that produced acceptable bead shapes at 21.2 mm/s. At this travel speed, burn-through occurred at the 0 and 25%EN and spatter limited the quality of the weld bead at 100%EN. It was believed that higher welding speeds would be possible based on the welds made at 25.3 mm/sec at 50%EN, but pulse parameter improvements are required to improve metal transfer at a higher EN balance. The welding test performed at 25.3 mm/s was only partially stable due to the quality of the VP pulse waveform which produced spatter. The productivity data for the PC350 showed that the maximum speed could be increased from 8.4 mm/s at 0%EN to 25.3 mm/s at 50%EN, thus a 300% increase by using the VP-GMAW process.

The main benefit of having an adjustable %EN setting is the ability to engineer dilution, nugget area, and bead shape at each travel speed. For robustness, the optimum welding speed for this lap joint application with the PC350 was 21.2 mm/s travel speed using 212 mm/s wire feed speed at 50%EN. This provided a weld bead with minimal underfill on the top leg, sound penetration and minimal spatter. In addition, welds made at either slightly lower or higher speeds had acceptable bead shape indicating that these parameters were within the operational window. Waveform optimisation was needed to have confidence in higher travel speeds, 25.3 mm/s or greater.

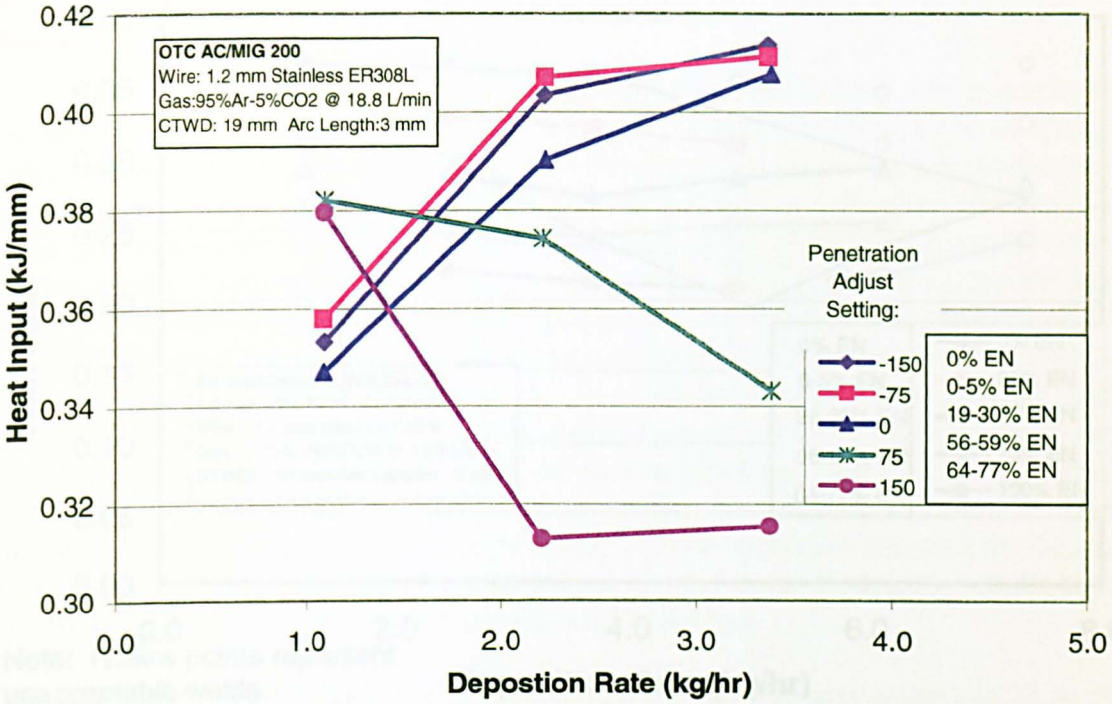

Figure 6.24(a) Heat Input versus Deposition Rate at 19 mm CTWD for Stainless Steel Using the AC/MIG 200 Power Supply

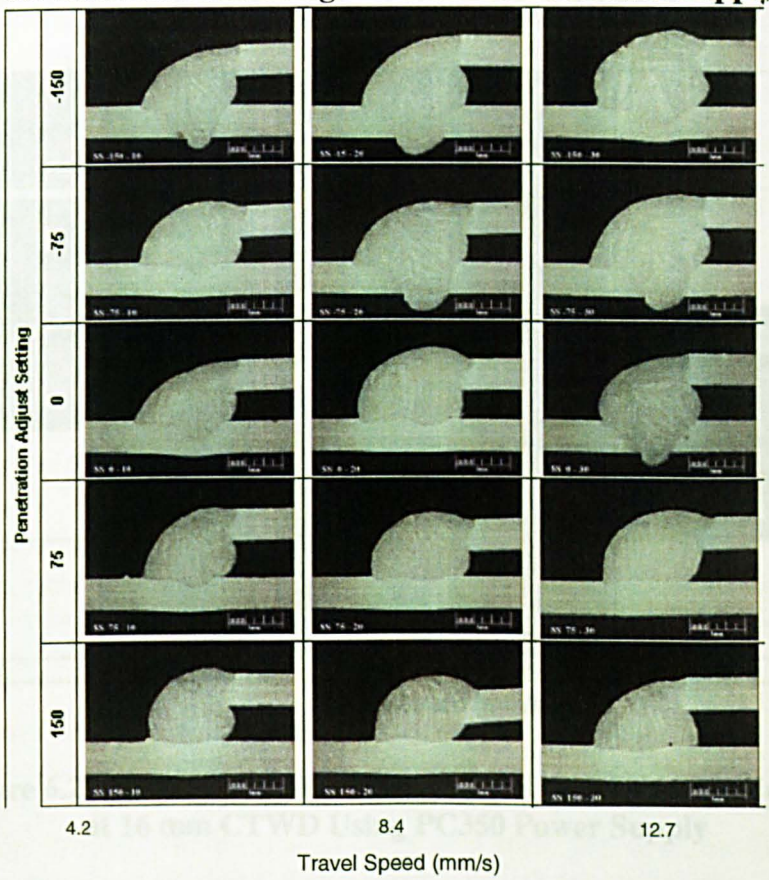

Figure 6.24(b) Macrosection Map for Stainless Steel Lap Joint Application at 19 mm CTWD Using AC/MIG 200 Power Supply

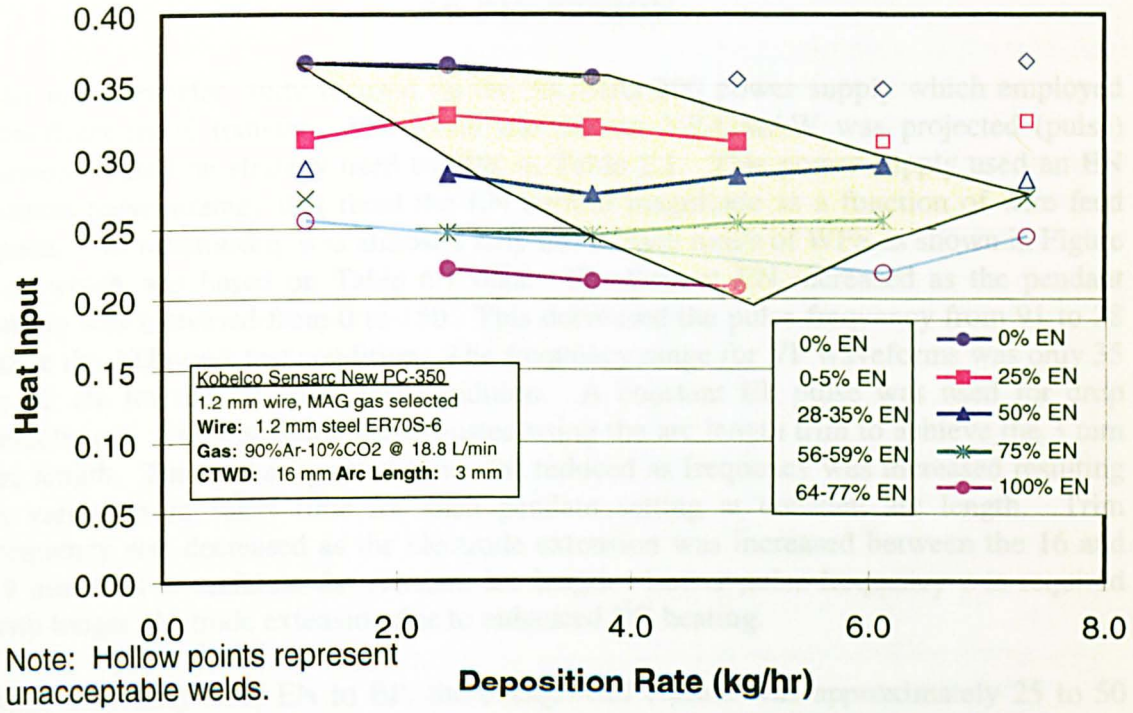

Figure 6.25(a) Heat Input versus Deposition Rate at 16 mm CTWD for Steel Using the PC350 Power Supply

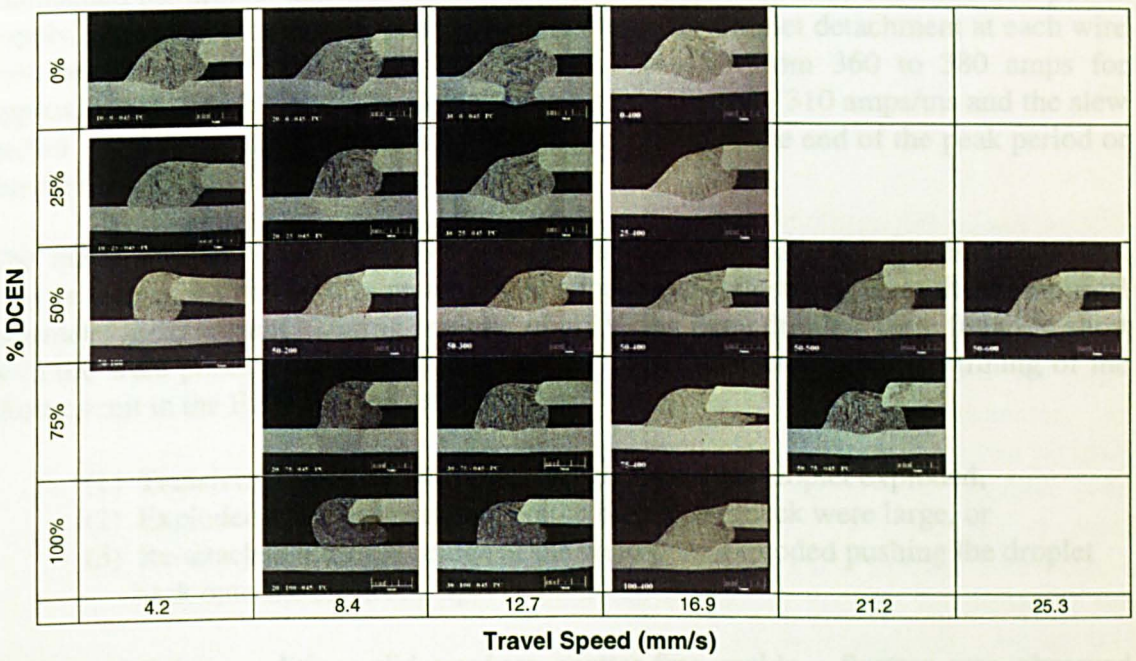

Figure 6.25(b) Macrosection Map for Steel Lap Joint Application at 16 mm CTWD Using PC350 Power Supply

7.0 DISCUSSION

The metal transfer study focused on the AC/MIG 200 power supply which employed free-flight metal transfer. The metal transfer for VP-GMAW was projected (pulse) globular based on strategy used by IIW in Table 2.1. This power supply used an EN current pulse strategy that fixed the EN current magnitude as a function of wire feed speed. The relationship was almost 1 amp EN to each mm/s of WFS as shown in Figure 7.1, which was based on Table 6.1 data. The time at EN increased as the pendant setting was increased from 0 to 150. This decreased the pulse frequency from 91 to 38 Hz at the 123 mm/s test condition. The frequency range for VP waveforms was only 35 to 42 Hz for the 40 mm/s test condition. A constant EP pulse was used for drop detachment. The frequency was adjusted using the arc length trim to achieve the 3 mm arc length. The EP background time was reduced as frequency was increased resulting in variations in %EN time for each pendant setting at constant arc length. Trim frequency was decreased as the electrode extension was increased between the 16 and 19 mm tests to maintain the constant arc length. Lower pulse frequency was required with longer electrode extension due to enhanced I^2R heating.

After switching from EN to EP, the background current was approximately 25 to 50 amps; except the -150 setting (pure GMAW-P) where it approached 80 amps. At higher wire feed speeds and %EN, the EP background period was omitted and the waveform basically switched from EN to EP pulse. When used, the background current maintained the droplet that was created during the EN period. The AC/MIG 200 power supply had an almost constant peak pulse waveform for droplet detachment at each wire feed speed setting. The trapezoidal EP pulse peaked from 360 to 380 amps for approximately 2 to 3.5 ms. The slew rate was approximately 310 amps/ms and the slew period was 1.2 ms. Drop detachment typically occurred at the end of the peak period or during the pulse downslope.

The metal transfer produced by VP waveforms was not stable for all test conditions. This is a common problem in many power supplies in industry as a result of empirical parameter development. During analysis of HSV, the large droplets were found to short with the weld pool on occasion during the EP pulse. Depending on the timing of the short circuit in the EP pulse, the droplet either:

(1) Transferred in cases where the bridge above the droplet exploded,
(2) Exploded creating spatter when the bridge and neck were large, or
(3) Re-attached after the bridge at the weld pool exploded pushing the droplet back onto the electrode tip.

Some waveform conditions did produce spatter-free welds. Spatter was observed typically in waveforms and welding parameter combinations that produced large droplets. This was more a problem at the high wire feed speed tests that used long EN time. Here, the droplet volume was as large as 4 mm^3 just after the EN period. The droplets typically gained another 0.9 to 1.0 mm^3 of volume during the EP pulse. These large droplets inhibit the use of shorter arc lengths with these waveforms.

VP-GMAW waveform optimisation is an area for future work. One way to correct this problem at high %EN would have been to increase the EN current more as the wire feed speed was increased so that higher pulse frequencies could be used. This would require a reduction in EP pulse energy to maintain the melting rate and provide the same range of arc power. A theory is that these larger droplets do not need as much EP pulse energy to achieve droplet transfer since the surface tension force is reduced by the larger droplet. The gravitational force on the droplet should aid detachment when the droplets become this large (Ref. 32, 65). Note, a 4 mm^3 droplet has an equivalent drop diameter of 2 mm. The AC/MIG 200 power supply did not permit the evaluation of this theory.

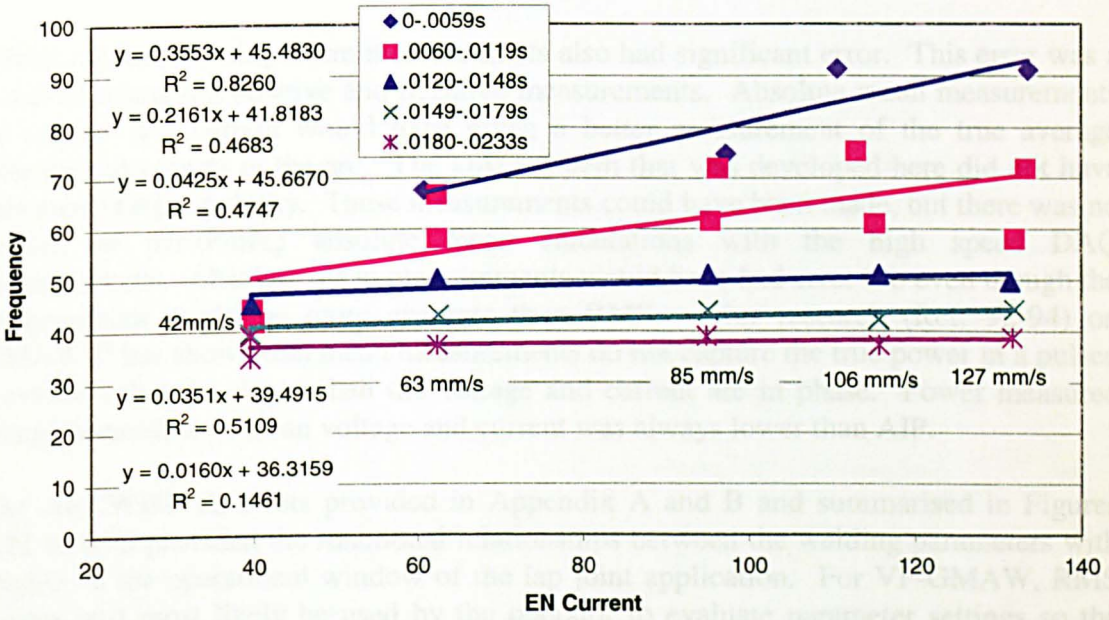

Figure 7.1 EN Waveform Strategy for 1.2 mm Steel on AC/MIG 200 Based on EN Time for a Range of Five Wire Feed Speeds

A goal of this investigation was to develop an analytical relationship that could be used to predict melting rate for different waveform strategies. At the same time, the pulse strategy needs to provide a synergic control that provides smooth metal transfer. As discussed in the literature review, there are many waveform strategies that can be used to achieve good metal transfer. For VP power supplies, an underlying objective is to provide a range of heat input (arc power) for each melting rate (WFS) so higher travel speeds can be achieved on welding applications, especially sheet metal. Therefore, a concurrent model should be used to predict the power in the arc by knowing the relationship to arc voltage and current for each portion of the waveform. Again, this requires the use of high speed DAQ to calculate the average instantaneous power, AIP.

7.1 Electrical Measurements

A key aspect of the data in this investigation is the quality of electrical measurements. As discussed earlier, the VP-GMAW process was characterised using RMS measurements for current and voltage. This was required because the process used an

alternating polarity waveform. However, RMS measurements of power were found to give inaccurate relationships. The root cause of RMS errors is due to the non-linear resistive properties of the arc (Ref. 92). Power measured using RMS was always higher than AIP. As current increases, the voltage drops at the cathode and in the arc can change due to the presence of metal vapour, and the avalanche effect of arc ionisation where the rate of voltage change decreases with increasing current. The avalanche effect becomes important, above say 50 amps (Ref. 15). Below this current the voltage can significantly increase as current is decreased to maintain the potential required for arc ionisation. Therefore, the arc does not act like a perfect resistor where power can be represented by the product of RMS voltage and current.

Power calculated using mean measurements also had significant error. This error was a result of averaging positive and negative measurements. Absolute mean measurements of voltage and current would have given a better measurement of the true average voltage and current in the arc. The DAQ system that was developed here did not have this measuring capability. These measurements could have been made, but there was no benefit of performing absolute mean calculations with the high speed DAQ measurements. Absolute mean measurements would have had error too even though the measurement might be more accurate than RMS. Prior research (Ref. 92-94) on GMAW-P has shown that mean measurements do not capture the true power in a pulsed waveform that develops when the voltage and current are in phase. Power measured using the product of mean voltage and current was always lower than AIP.

The ARCWISE data sets provided in Appendix A and B and summarised in Figures 6.21 to 6.25 provided the functional relationships between the welding parameters with respect to the operational window of the lap joint application. For VP-GMAW, RMS meters will most likely be used by the operator to evaluate parameter settings so the ARCWISE graphs used this current and voltage measurement. Using the ARCWISE graphs, operators can determine optimum welding parameters by relating the RMS measurements on the power supply to the operational window that was graphically determined for each application and pre-set power supply waveform. RMS values are considered readings not measurements and should be used for indication only.

The electrode extension does respond to RMS heating. The melting rate equations developed for arc welding processes capture this effect by separating the melting contribution of the arc from the electrode extension. The only true way of determining the relationship between the electrical measurements and metal transfer is to understand the analytical effect of waveform parameters and to know the melting rate coefficients, α and β.

The DBR method characterised the detailed electrode melting behaviour of each waveform period. The BDT permitted experimental determination of the arc and resistive heating coefficients for each waveform period; EN, EPB, and EPP. This provided a method for measuring how waveform affected metal transfer. The current and voltage measured for each period was determined by measuring waveform. This was the best method for the AC/MIG 200 power supply since the current in each period was constant.

The actual relationship between arc voltage and current for each polarity at the 16 mm CTWD and 3 mm arc length was determined from the waveforms (Figure 7.2). This diagram was for a 13 mm electrode extension and 3 mm arc length. The voltage – current relationship based on the line equation was almost the same. Electrode negative arcs had a slightly higher slope and lower intercept. The intercept is normally used to characterize the voltage drop sum for the anode, cathode and electrode extension. Additional tests are required to separate the voltage drop in the electrode extension, which is typically near 2 volts, and the anode is 4 to 5 volts. Based on these assumptions, the cathode voltage drop was approximately 10 volts.

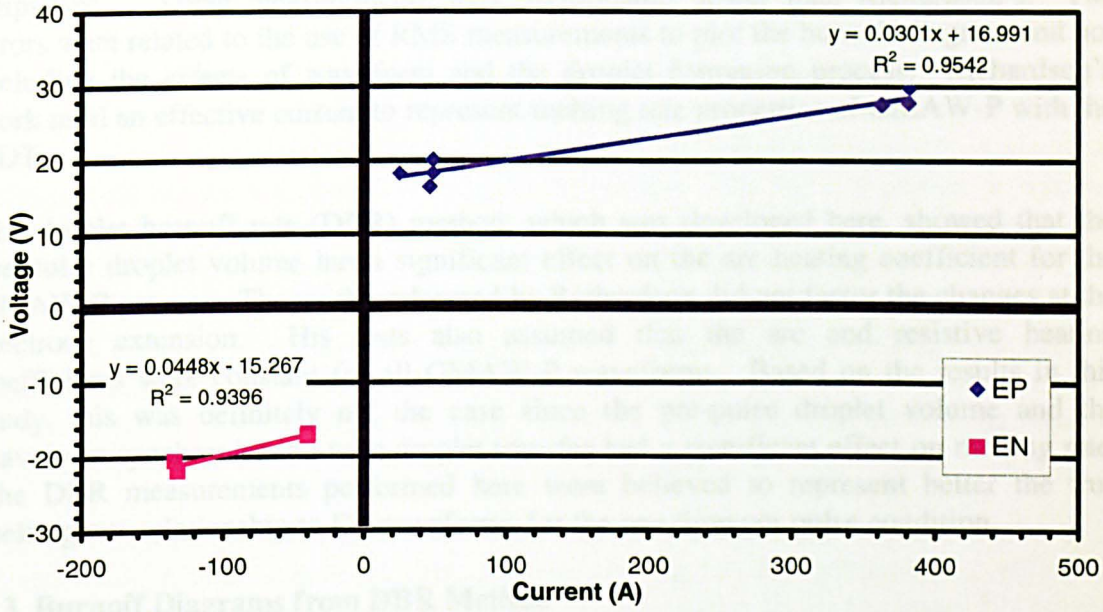

Figure 7.2 True V-I Curve for VP-GMAW Arc Periods in 90Ar-10CO_2

The PC350 used a fuzzy logic control that oscillated the current waveform in each period to help assist in metal transfer. The design of this waveform was very advanced and could not be simply represented using graphs. This waveform varied the EN and EP periods as it lowered the current using a superimposed oscillating wave. Once it detected a short circuit, it either switched polarity or repeated the waveform for that polarity. The ability to relate these waveforms to melting rate properties is an area for future work.

7.2 Burnoff Diagrams from ARCWISE Characterisation

The burnoff diagram (Figure 6.7) for the whole waveform (EN and EP) was plotted using I_{RMS} assuming constant electrode extension and WFS. This diagram did not provide accurate measurements for the melting rate coefficients. This burnoff diagram did show the benefit of EN heating on melting rate and can be used to indicate melting rate for different %EN using a waveform that is similar to the AC/MIG 200. For Figure 5.7, the lines for 1.2 mm steel using 16 mm CTWD had similar slope, β but larger differences in the intercept, α. At each wire feed speed the burnoff rate increased and

the electrode extension factor ($L \cdot I$) decreased as the %EN increased. This was expected since EN polarity was found to decrease RMS current for a given WFS.

In theory, the 0% EN tests should provide good correlation with melting rate measurements made by other researchers since this was a GMAW-P waveform. The melting rate coefficients determined from these lines can be compared to prior research since there was no switching of polarity. Richardson (Table 6.2) measured melting rate coefficients for GMAW-P where the resistive heating coefficient, β was 3.5 to 3.74 x 10^{-4} $amps^{-2}sec^{-1}$ and the arc heating coefficients, α was 0.55 $amps^{-1}sec^{-1}$ (Ref. 75). For the 0%EN tests (pendant setting -150), β was 2 x 10^{-4} $amps^{-2}sec^{-1}$ and α was 0.01 $amps^{-1}sec^{-1}$. These measurements were significantly lower than Richardson's. The errors were related to the use of RMS measurements to plot the burnoff diagram and not including the effects of waveform and the droplet formation process. Richardson's work used an effective current to represent melting rate properties of GMAW-P with the BDT.

The droplet burnoff rate (DBR) method, which was developed here, showed that the pre-pulse droplet volume has a significant effect on the arc heating coefficient for the GMAW-P process. The work performed by Richardson did not factor the changes at the electrode extension. His tests also assumed that the arc and resistive heating coefficients were constant for all GMAW-P waveforms. Based on the results in this study, this was definitely not the case since the pre-pulse droplet volume and the waveform synchronisation with droplet transfer had a significant effect on melting rate. The DBR measurements performed here were believed to represent better the true melting rate relationship to EP waveforms for the one drop per pulse condition.

7.3 Burnoff Diagrams from DBR Method

As shown in Figure 6.18, EP constant voltage welding produced a linear burnoff relationship for a wide range of electrode extensions, wire feed speeds, and current conditions. The second order melting rate relationship described by Equation (5.7), which was developed by Lesnewich and verified by Richardson, was verified here too. Based on this data, the burnoff diagram technique (BDT) can be used to measure melting rate coefficients for GMAW processes that have a stable mode of transfer; like spray transfer.

The DBR method evaluated the direct relationship between the arc current waveform and electrode melting rate by using synchronised HSV and DAQ. Best fit lines were used to trend the data on the BDT for EN heating as a function of EN time (Figure 6.17), and EP background and pulse heating for different pre-pulse droplet volumes (Figures 6.19 and 6.20). This was performed to explain the variation in electrode melting rate with VP-GMAW.

A summary of arc and resistive heating coefficients was prepared for comparison, Table 6.2. Richardson found for EP GMAW-P, the resistive heating coefficient, β equalled 0.59 x 10^{-4}, $A^{-2}s^{-1}$ for 1.2 mm steel electrodes. For EP constant voltage spray, Lesnewich

found β to equal approximately 0.7 x 10^{-4}, $A^{-2}s^{-1}$ for steel at this wire diameter. The resistive heating coefficient is dependent on electrode cross section and resistivity so different values would be expected if different size and types of electrodes were tested. However, it was expected that regardless of polarity, β values for EN and EP should be constant for a given set of electrode conditions.

At the very highest EN time group shown in Table 6.2, the β values for EN heating decreased enough that they were near the values measured by Richardson for GMAW-P for smaller electrodes. For the 1.14 mm wire diameter, the EN resistive heating coefficients were 3 to 6 times greater than the values reported by Lensewich and Halmoy for constant voltage GMAW.

The data from the burnoff diagram based on the DBR method was not as physically linked to arc and resistive heating as the fundamental equation developed by Lesnewich. Here, the BDT provided measurement of 2^{nd} order polynomial behaviour of electrode melting rate for each period as a function of current. For the EN period, it was not believed that the resistive heating was different than constant voltage EP heating. The slope of the lines in Figure 6.17, which equalled β, increased since the burnoff rate increased and the electrode extension factor decreased when EN time decreased for a given EN current. This behaviour was related to the concentrated melting theory that is based on the transient behaviour between the forming droplets and the arc. In reality, the arc heat used for melting is changing based on the conditions between the forming droplet and the arc, but the BDT measures these changes by slope changes.

The data fit was good except at the lower wire feed speeds and currents as shown in Figure 6.17. Linear lines were used to make solving for the melting rate coefficients easy. A higher order polynomial may have provided better fit for the lower EN current data. Ignoring the low EN current data, the intercept of the lines for the EN burnoff diagram varied little. The variation in data line fit was attributed to grouping the EN time into 3 msec groups. This data grouping was based on a best fit of the incremental pendant setting tests that produced a range of EN times at each wire feed speed.

The EN arc heating coefficients (intercepts in Figure 6.17) were significant and were almost constant for all the EN time groups. Average α was approximately 0.8 $mm\text{-}A^{-1}s^{-1}$ and ranged from 0.72 to 0.85 $mm\text{-}A^{-1}s^{-1}$ (Table 6.2). For comparison the arc heating coefficient for GMAW-P and CV spray were 0.27 and 0.25 $mm\text{-}A^{-1}s^{-1}$ according to Richardson and Lesnewich, respectively. The arc heating coefficient was more than 3 times greater than the measurements made by the prior researchers.

The EP resistive heating coefficients β_+ determined from the line slopes in Figure 6.19 did not vary too much from 0.7 to 1.2 x 10^{-4}, $A^{-2}s^{-1}$over the test conditions evaluated. As shown in Table 6.2, for CV spray, Lesnewich found β to equal approximately 0.7 x 10^{-4}, $A^{-2}s^{-1}$ for steel at this wire diameter. Independent CV spray measurements performed in this investigation found β equalled to 0.9 to 1.0. It appeared that the EP resistive heating coefficient did increase slightly with decreasing pre-pulse droplet volume but the range agreed well with CV steady state measurements.

The EP arc heating coefficients (intercepts in Figure 6.19) were significant and were both positive and negative; α varied from -0.35 to 0.35 mm-$A^{-1}s^{-1}$ for the different conditions. As shown in Table 6.2, the arc heating coefficient for GMAW-P and CV spray were 0.27 and 0.25 mm-$A^{-1}s^{-1}$ per Richardson and Lesnewich, respectively for 1.2 to 1.14 mm electrodes.

The droplet volumes plotted in Figure 6.20 were calculated from the HSV data just before entering the peak pulse period (Table 6.3). These measurements were scaled to include the droplet remainder immediately after detachment from the previous pulse. As mentioned earlier, the arc was found to climb rapidly as the current was pulsed. Concentrated electrode extension melting occurred when the arc covered the solid surface. However, large liquid droplets inhibit further melting of the electrode tip, and this effect is shown by these data. A logarithmic relationship was used between the arc heating coefficient, α and the pre-pulse droplet volume, V_{pp}. Large droplets significantly reduced arc melting because the arc was rooted on the droplet bottom; especially at low background current. A negative arc heating coefficient indicated that the electrode extension was increasing in length and the arc length was decreasing. Here, the heat from the arc was focused on the droplet which inhibited electrode melting. This resulted in a negative coefficient with large pre-pulse droplets.

The relationships in Figures 6.19 and 6.20 were for the one drop per pulse condition based on the DBR measurements up to drop detachment. The melting rate was observed to decrease during the necking process and after drop detachment until the arc re-attached to the electrode tip. The arc followed the pulse globular droplet as the neck formed. The electrode tip was observed to partially solidify in the absence of the arc immediately after neck rupture.

GMAW-P melting rate measurements have been difficult to make for researchers. Limitations in HSV optics and DAQ made metal transfer study difficult. In this project, the DBR method was used to study closely the melting on a droplet by droplet basis. Advanced HSV and DAQ equipment made this possible. This method was found to yield time dependent relationships for melting rate efficiency as a function of EN current. The melting process at the electrode tip was strongly related to the transient arc behaviour of the EN pulse. Melting was observed to occur quickly once the arc covered the electrode and decreased once the droplet formed. The droplet varied in size when entering the EP period depending on the EN waveform. The droplet size entering the EP peak periods also varied in GMAW-P when using long EP background periods. The pre-pulse droplet volume had a significant effect on the EP arc heating coefficient. Significant variation in electrode melting rate occurred between the periods using a range of GMAW-P and VP-GMAW waveforms. The variation in electrode melting rate caused by these complex waveforms was related to the concentrated melting theory.

7.3.1 Concentrated Melting Theory

A theory was developed to describe the dependency of electrode melting rate in VP-GMAW on (1) EN time at constant EN current, and (2) the pre-pulse droplet volume for

EP pulsing. The theory was named the "concentrated melting theory" and is defined as follows:

> "The melting potency of GMAW current waveforms is strongly dependent on arc concentration at the electrode tip above the droplet interface and the droplet size and growth process. Virgin electrode metal is consumed rapidly when the arc is permitted to climb over and concentrate on the electrode extension. Droplet growth is rapid in current transients when the arc climbs the electrode tip causing extension burnoff. During a waveform constant current period, the electrode melting rate decreases once the burnoff is complete and the droplet size inhibits further arc concentration and climb on the electrode. Once the arc is rooted on the droplet bottom, the electrode melting rate will continue to decrease as the droplet grows until drop detachment."

The concentrated melting theory applies to open-arc GMAW processes that employ current waveform that pulses the current and/or polarity to regulate metal transfer.

Droplet transfer in VP-GMAW occurred during the EP pulse. Observations made during HSV analysis found that the EN arc climbed over the electrode tip, which had a small droplet remainder, as soon as the current switched polarity and the EN arc was ignited as shown in Figure 6.10. The arc cathode was distributed over a large electrode tip area. This was quite different from the CV processes like spray transfer where the arc is stable and continuously covers a portion of the electrode tip. This EN arc behaviour was also observed by Norrish (Ref. 29). In steady state EN welding, Norrish observed that the gas metal arc formed a mulit-spot cathode that climbed the electrode after drop detachment. Once a droplet formed the arc switch to a single spot cathode mode and rooted on the droplet bottom. The observations by Norrish reinforce the concentrated melting theory for EN waveforms.

Higher EN currents promoted larger arc plasmas that covered more of the solid electrode extension tip. The electrode extension area that was enveloped by the EN arc melted early in the EN period. Once a large droplet formed, the electrode melting rate decreased because the arc concentrated the heat on the droplet. Therefore, high current waveforms that used low EN time had much larger droplet volume growth rates, V_D compared to long EN times as shown in Figures 6.15 and 6.16. Droplet growth rate was dependent on the concentrated melting based on the size of the arc plasma. Once the electrode extension burnoff saturated, the melting rate decreased since the arc was concentrated on the droplet instead of solid electrode. Analysis of the high speed image data showed that the electrode extension burnback was the greatest at the beginning of the EN period (Table 6.1). At EN times up to 20 ms, the change in electrode extension, Δx saturated at 9 to 11 msec into the period for EN currents that were 60 amps or higher.

High speed images showed the arc climb and concentrate on electrode extension during the EN period; an example can be seen in Figure 7.3. At the midrange WFS of 82 mm/s, the electrode extension burnoff was 0.276 mm after an EN time of 3.78 msec. The droplet was slightly larger than the diameter of the electrode. At high EN time, the

electrode extension burnoff increased to 0.546 mm, but this distance was typically achieved 10 msec into the 18.6 msec period (Table 6.1). The final droplet size was much larger than the diameter of the electrode. The volume melted ranged from 0.615 to 2.139 mm^3 for the low and high EN time tests at 95 amps, respectively. This corresponded to theoretical drop diameters melted of 1.04 and 1.35 mm. Obviously the droplets in Figure 7.3 appeared bigger than the volume melted since the electrode extension tip was molten at the beginning of the EN period.

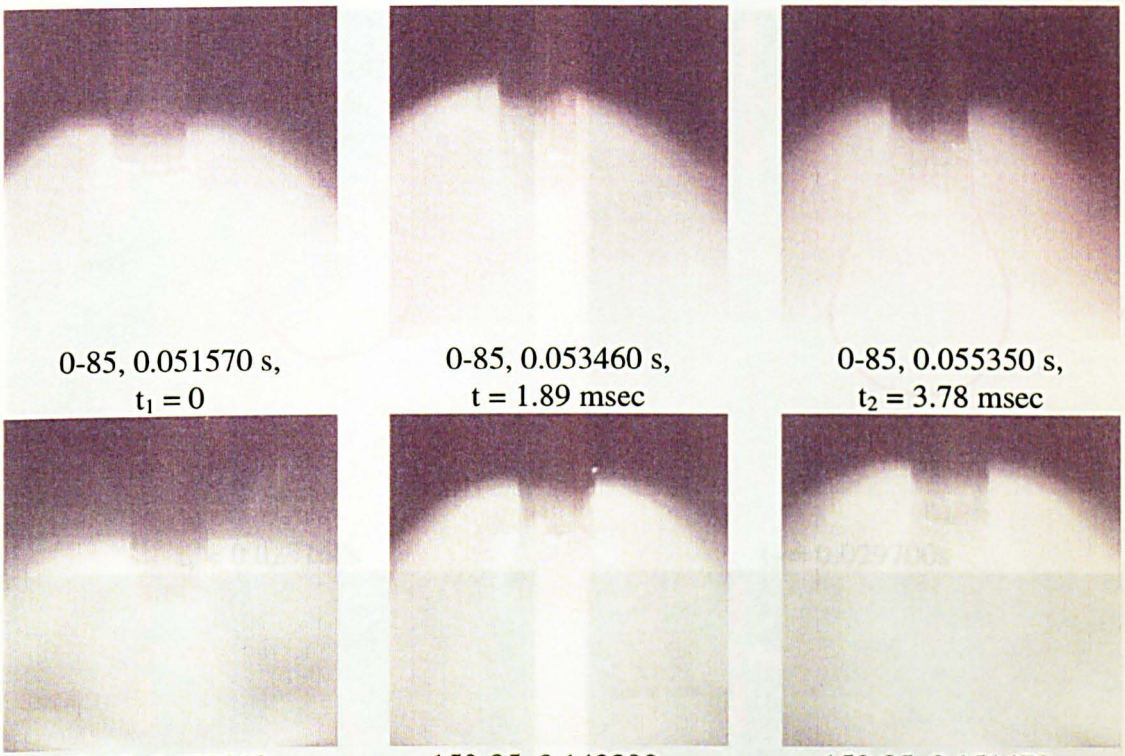

Figure 7.3 HSV Images of Droplet Growth at 95 amps EN and 85 mm/s WFS Showing Change in Electrode Extension with EN time

The minimum and maximum droplet volumes based on EN melting, not the image recorded in these tests, were 0.259 and 3.097 mm^3 for weld tests 0-42 and 150-127 (Table 6.1). These droplet volumes correspond to theoretical drop diameters of 0.79 and 1.8 mm, respectively. These droplet volumes are increased during the EP period by approximately 0.9 to 1.0mm^3 before drop transfer.

The concentrated melting theory also applied to EP pulse waveforms. The pre-pulse droplet volume had a significant effect on the arc heating coefficient. HSV images were taken to show how the pre-pulse droplet affected the electrode extension burnoff. When the pre-pulse droplet volume was small, the arc was observed to climb rapidly over the solid tip behind the droplet as the current increased as shown in Figure 7.4. A column of electrode would collapse and mix with the droplet. The arc became eventually rooted

on the droplet that grew from electrode melting and extension burnoff. Further electrode melting was limited when the detachment process started with the formation of a neck. The arc followed the droplet through the detachment process. A decrease in melting rate was observed during the necking process where the electrode tip was observed to solidify after the droplet bridge ruptured, and at the same time the arc length shortened. The arc would then jump to the electrode tip after drop detachment to maintain the circuit where a new droplet was initiated.

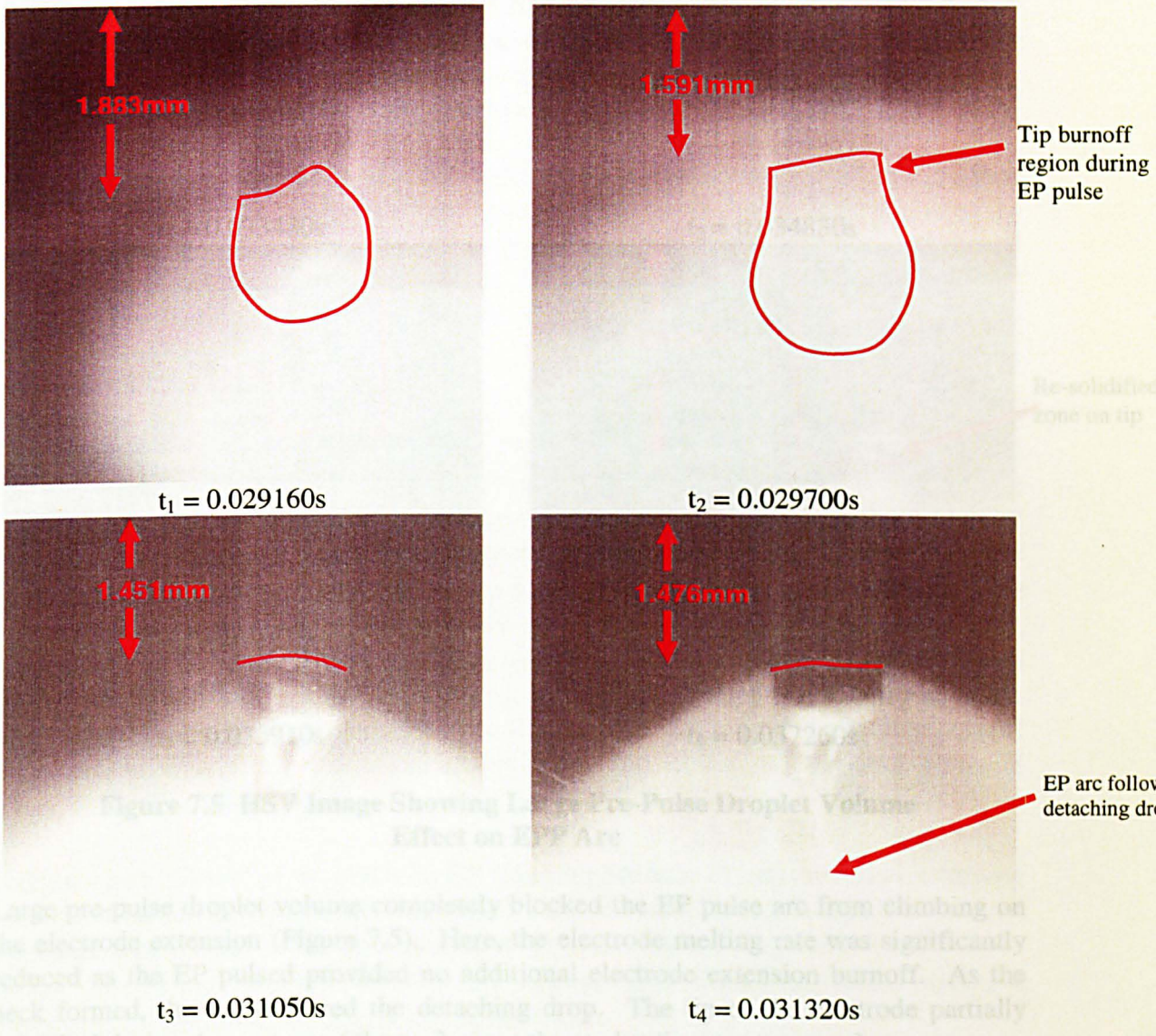

Figure 7.4 HSV Image Showing Small Pre-Pulse Droplet Volume Effect on EPP Arc

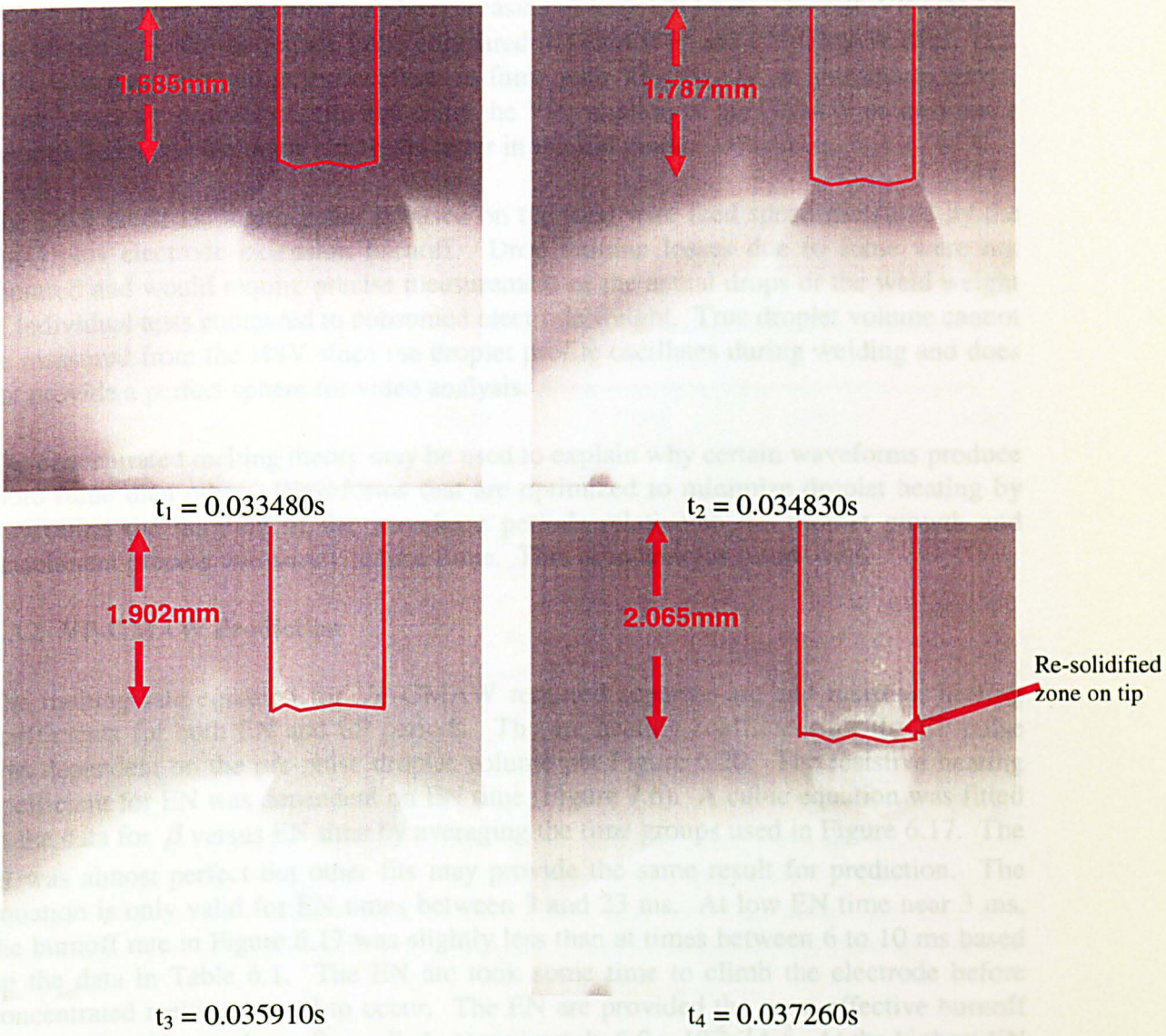

Figure 7.5 HSV Image Showing Large Pre-Pulse Droplet Volume Effect on EPP Arc

Large pre-pulse droplet volume completely blocked the EP pulse arc from climbing on the electrode extension (Figure 7.5). Here, the electrode melting rate was significantly reduced as the EP pulsed provided no additional electrode extension burnoff. As the neck formed, the arc followed the detaching drop. The tip of the electrode partially solidified during the rupture of the neck since the arc heating was removed.

These visual observations together with the DBR data show that the melting rate of GMAW waveforms is strongly dependent on the transient behaviour between the arc in each period and the droplet formation process. A new arc that climbs and concentrates on solid electrode is more effective in melting than an arc rooted on a liquid droplet, hence, the concentrated melting theory. The prediction of VP-GMAW melting rate required detailed understanding of these mechanisms.

A source of melting rate loss was droplet heating once the droplet formed and the arc rooted on it. Here metal fume may be increasing at long EN times. Overall, VP-GMAW was shown by Ushio to reduce fume compared to GMAW-P and CV GMAW (Ref. 112, 113). His work showed large decreases in fume with VP-GMAW on aluminium alloys. Fume losses are probably optimised using the VP variation of the GMAW process since the arc climbs and melts the electrode better in the EN mode.

The DBR electrode melting rate is based on the total wire feed speed measured by the DAQ plus electrode extension burnoff. Drop volume losses due to fume were not captured and would require precise measurement of the actual drops or the weld weight of individual tests compared to consumed electrode weight. True droplet volume cannot be measured from the HSV since the droplet profile oscillates during welding and does not provide a perfect sphere for video analysis.

The concentrated melting theory may be used to explain why certain waveforms produce more fume than other. Waveforms that are optimized to minimize droplet heating by controlling the duration of the waveform periods relative to the droplet growth and detachment process will surely reduce fume. This is an area for future work

7.3.2 VP-GMAW Prediction

The melting rate equation for VP-GMAW required separate arc and resistive heating coefficients for both EN and EP periods. The arc heating coefficient for the EP pulse was dependent on the pre-pulse droplet volume per Figure 6.20. The resistive heating coefficient for EN was dependent on EN time (Figure 7.6). A cubic equation was fitted to the data for β versus EN time by averaging the time groups used in Figure 6.17. The fit was almost perfect but other fits may provide the same result for prediction. The equation is only valid for EN times between 3 and 23 ms. At low EN time near 3 ms, the burnoff rate in Figure 6.17 was slightly less than at times between 6 to 10 ms based on the data in Table 6.1. The EN arc took some time to climb the electrode before concentrated melting started to occur. The EN arc provided the most effective burnoff between 6 to 10 ms where β equalled approximately $6.0 \times 10^{-4} s^{-1} A^{-2}$. At the highest EN times, β appeared to saturate.

If Equation (5.23) was to be used with EN times higher than 17 ms, the resistive heating coefficient should be considered constant at $3.0 \times 10^{-4} s^{-1} A^{-2}$ even though this was not evaluated past 23 ms. The cubic equation predicts higher β values for EN times greater than 20 ms. Melting rate saturates with the large droplet that forms making it impossible for improved melting at higher EN times.

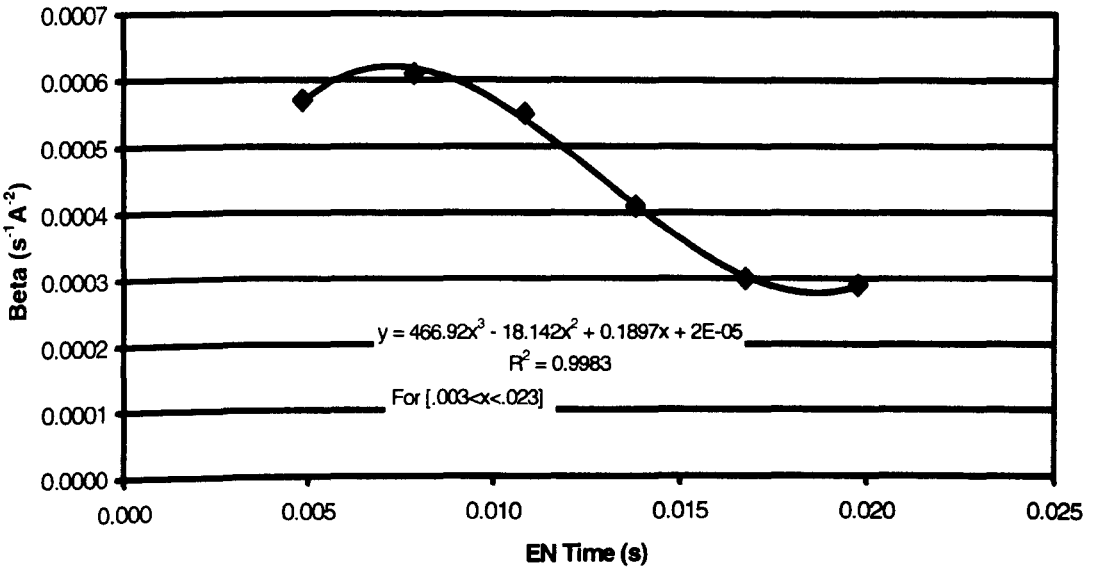

Figure 7.6 Resistive Heating Coefficient versus EN Time for 1.2 mm Steel Electrode in 90Ar-10CO_2 Shielding Gas

It should also be noted that Figure 7.6 was for 90Ar-10CO_2 shielding gas. The oxidation potential of the shielding gas affects the activation of the electrode during EN welding. Electrode activation increases as the concentrations of oxygen or CO_2 increases in the shielding gas. The melting rate coefficients can be expected to change slightly with the use of different shielding gases, electrodes, and electrodes that have surface activation. As the activation of the electrode increases, EN heating should decrease since thermionic electron emission promotes reduced cathode heating (Ref. 12). Some electrode suppliers have incorporated small quantities of surface active elements into copper coatings used on steel electrodes; the exact details are kept as a trade secret. The electrode used here was a bare steel wire and did not have any surface activation.

The analytical relationship developed in Equation (5.23) that relates melting rate to VP waveform parameters was used for prediction. The predicted melting rate used the waveform parameters defined in Tables 6.1 and 6.3 for EN and EP heating, respectively. Pure GMAW-P waveforms from the -150 pendant setting were also characterized and used for predictions even though detailed DBR measurements were not performed on waveforms that had no EN heating. The arc and resistive heating coefficients, determined here, were used in this equation but since these coefficients were not constant, the series of calculations was required to solve for the melting rate of each waveform. A spreadsheet in Excel™ was used to perform the calculations using five steps:

Step 1 – Identify waveform parameters, $I_-, t_-, I_b, t_b, I_p, t_p, dI/dt$

Step 2 – Determine β_- based on EN time, t_- as per Figure 7.6

Step 3 – Determine the EP pre-pulse droplet volume, V_{pp} based on EN pulse melting rate or (EP background melting rate for GMAW-P)

Step 4 – Solve for α_+ using V_{pp} as per Figure 6.20

Step 5 – Calculate VP-GMAW melting rate

The time used for EP pulse, t_p and EP background, t_b periods included one half of the total ramp-up time as per Figure 5.3. The peak time averaged approximately 3 ms including one ramp time, which was 1.2 ms. The remaining waveform parameters were measured off the high speed DAQ profiles. The actual background time was found to vary from wave to wave due to power supply regulation at each setting, so the average frequency was used to determine the background time by subtracting the EN and EP pulse time from the total period.

The resistive heating coefficient for EN melting can be determined by using the cubic equation from Figure 7.6 as follows.

$$\beta_- = 466.92t_-^3 - 18.14t_-^2 + 0.19t_- + 2.0x10^{-5} \tag{7.1}$$

The pre-pulse droplet volume, V_{pp} can be approximated by using the melting rate due to EN heating based on the β_- relationship to EN time and using the average resistive heating coefficient, α_- from Table 6.2 as follows:

$$V_{pp} = (\alpha_- I_- + \beta_- L I_-^2) A_w t_- + 0.391 \tag{7.2}$$

where: $\alpha_- = 0.795 mm A^{-1} s^{-1}$

t_- = EN time from 3 to 23 msec

A_w = wire area, 1.02 mm^2

L = electrode extension, 13 mm

0.391 mm^3 = droplet remainder after detachment

From Figure 6.20, the EP arc heating coefficient is:

$$\alpha_+ = -0.4474 \ln V_{pp} + 0.1292 \tag{7.3}$$

The pre-pulse droplet volume created by the EN pulse was not affected by the EP background period for most tests. The droplets were large enough that the EP background arc concentrated on the droplet bottom producing negligible size increase. Therefore, the effects of any background time can be ignored for the pre-pulse droplet volume calculation on VP waveforms. This observation was supported by Figure 6.19, which showed that burnoff rate was negative at background for the VP-GMAW waveforms. A negative burnoff rate meant the electrode extension is increasing and arc length is decreasing during that period.

The prediction of GMAW-P melting rates required a pre-pulse droplet volume calculation using the EP background period melting rate as follows:

$$V_{pp} = (\alpha_b I + \beta_b L I^2) A_w t_b \tag{7.4}$$

where:

$$\beta_b = 1.2x10^{-4}$$

as taken from Figure 6.19 based on the burnoff rate at minimum pre-pulse droplet volume. The EP pre-pulse droplet volume made in the EP background period can be used to determine the arc heating coefficient for the EP peak period using Equation 7.3 for GMAW-P predictions.

For pre-pulse droplet volume calculations, the electrode extension can now be assumed constant since the effects of extension burnoffs are less than 7% when L equals 13 mm. The largest electrode extension burnoff, Δx in Table 6.1, was 0.91 mm. The resistive heating contribution to the pre-pulse droplet volume was less than half for most EN waveforms. The effects of average L was not included into Equations (7.2) and (7.4) since it accounted for less than a few percent of the predicted pre-pulse droplet volume, which is used solve for α_+.

Overall, the need to factor the average electrode extension into melting rate equation was not required either. The burnoff, Δx could be determined by developing an equation between EN time and current for the EN period, and the pre-pulse droplet volume for the EP period. This would just add more complexity with limited improvement in melting rate prediction for VP-GMAW. Average $L_{EN.EPB.EPP}$ for each period of the melting rate equation could be determined using Equation (5.4). The electrode extension burnoff was important for determining the DBR electrode melting rates of each period and these effects were captured in the arc and resistive heating coefficients.

The average EP resistive heating coefficient from Table 6.2 was used for VP-GMAW predictions where β_+ equals $1.0 \times 10^{-4} s^{-1} A^{-2}$. This was the average of the 0.8 to $1.2 \times 10^{-4} s^{-1} A^{-2}$ range. It decreased slightly with increasing pre-pulse droplet volume. The resistive heating coefficient was assumed constant for VP and GMAW-P predictions since the range was small. The pre-pulse droplet volume had a larger effect on the arc heating coefficient. The melting rate Equation (5.23) developed here in the experimental approach was based on the theory created by Allum (Ref. 63) and Richardson (Ref. 75) as follows:

$$MR_{vp} = \frac{\alpha_- |I_-| t_- + \alpha_+ \bar{I}_+ t_+}{t_- + t_+} + \frac{\beta_- L_- I_-^2 t_-}{t} + \beta_+ L_+ \left(\frac{\left[\bar{I}_+^2 t_+ + \frac{(I_p - I_b)^2 t_p t_b}{(t_p + t_b)^2} t_+ \right] - \frac{2(I_p - I_b)^2}{3} t_s}{t} \right) \tag{7.5}$$

This equation assumed the arc heating coefficient was constant in the EP waveform. Since α_+ was dependent on the pre-pulse droplet volume, separate terms were needed for arc heating in the EPB and EPP periods. This results in the following Equation (7.6):

$$MR_{vp} = \frac{\alpha_-|I_-|t_- + \alpha_b I_b t_b + \alpha_p I_p t_p}{t} + \frac{\beta_- L_- I_-^2 t_-}{t} + \beta_+ L_+ \left(\frac{\left[\bar{I}_+^2 t_+ + \frac{(I_p - I_b)^2 t_p t_b}{(t_p + t_b)^2} t_+ \right] - \frac{2(I_p - I_b)^2}{3} t_s}{t} \right)$$

A spreadsheet was set up so the magnitude of each waveform period could be compared while summing the melting rate (Table 7.1). Waveform parameters were characterised for three wire feed speeds. Pendant settings of -150, 0 and 150 were characterised to provide the largest range of current and time for each period, EN, EPB, and EPP. Additional pendant settings of 30, 60, 90, and 120 were also characterised for the 42 mm/s wire feed speed. Predictions were made and are summarized on the right side of the second part of Table 7.1. The terms in Equation (7.6) were separated to evaluate the melting rate contribution from each period and slew rate. These terms can be summarised as follows:

$$term1 = \alpha_- I_- t_- / t$$

$$term2 = \alpha_b I_b t_b / t$$

$$term3 = \alpha_p I_p t_p / t$$

$$term4 = \beta_- L I^2 t_- / t$$

$$term5 = \beta_+ L \bar{I}^2 t_+ / t$$

$$term6 = \beta_+ L \frac{(I_p - I_b)^2 t_p t_b t_+}{(t_p + t_b)^2 t}$$

$$term7 = -\beta_+ L \frac{2(I_p - I_b)^2 t_s}{3t}$$

Terms 1, 2, and 3 are for arc heating and terms 4, 5, 6, and 7 are for resistive heating. For the GMAW pulse, terms 5, 6, and 7 are used to separate the contributions from mean current, the pulse resistive heating, and the negative influence of slew rate, respectively.

Predictions using Equation (7.6) were found to yield acceptable results as shown in Table 7.1, which is shown in two parts. The waveform parameters were measured from the DAQ and are listed in the first table. The second table shows the melting rate coefficients used for calculating the pre-pulse droplet volume and the melting rate for each term in Equation (7.6).

The predicted melting rate, MR_T was found to have good agreement with the data acquisition wire feed speed, WFS_{DAQ}. For VP-GMAW waveforms, the error ranged from -8.14 to 7.53%. For the three GMAW-P waveforms, the error ranged from -13.64 to 8.07%. No DBR measurements were actually performed on pure GMAW-P waveforms. The higher error was attributed to calculating the pre-pulse droplet volume, which was not experimentally measured and used to improve the Equation (7.3). The results were plotted to show the predicted WFS (melting rate) versus the wire feed speed taken from the DAQ (Figure 7.7). The overall prediction was good.

Other sources of error in this data could be attributed to the pulse frequency used to set the test arc length. These predictions were for a 13 mm electrode extension and 3 mm arc length. The error in arc length measurement is attributed to the weld pool shape which did vary depending on the arc power in each constant deposit area test.

The relationship between EN time and the resistive heating was not ideal. Experimental work using a power supply that permits precise study of EN waveform settings would help improve Figure 6.17. This figure, which was used to generate Figure 7.6, used EN time ranges at constant current. Close study of the data fit in Figure 6.17 shows that better correlation is needed at the lower burnoff rates and currents.

Table 7.1 VP-GMAW and GMAW-P Melting Rate Predictions for a Range of Waveforms

Weld Number	WFS_{DAQ} (mm/s)	I_- (A)	t_- (s)	I_b (A)	t_b (s)	I_p (A)	t_p (s)	t_+ (s)	t (s)	I_m (A)	t_s (s)	$^{dI}/_{dt}$ (A/s)
-150-42	38.85	0.00	0.0000	30.38	0.0168	365.00	0.0022	0.0191	0.0191	69.57	0.0011	308880.00
0-42	39.09	40.43	0.0083	24.97	0.0133	364.18	0.0023	0.0157	0.0240	75.54	0.0012	294962.32
30-42	38.97	39.47	0.0113	24.81	0.0091	363.86	0.0023	0.0114	0.0227	92.38	0.0011	312969.23
60-42	38.86	39.28	0.0142	25.48	0.0055	361.01	0.0024	0.0078	0.0221	126.81	0.0011	305030.30
90-42	38.94	39.42	0.0172	24.88	0.0059	365.48	0.0022	0.0081	0.0253	116.90	0.0010	346369.49
120-42	38.88	39.45	0.0202	47.45	0.0013	361.17	0.0021	0.0034	0.0236	244.29	0.0012	254367.57
150-42	38.84	39.51	0.0233	46.35	0.0030	365.08	0.0025	0.0055	0.0288	191.18	0.0012	261964.38
-150-85	80.68	0.00	0.0000	50.05	0.0072	365.00	0.0029	0.0101	0.0101	139.56	0.0014	222317.65
0-85	81.14	97.00	0.0041	49.55	0.0060	365.00	0.0027	0.0087	0.0128	147.54	0.0014	228038.55
150-85	81.99	95.00	0.0201	50.80	0.0012	365.00	0.0026	0.0038	0.0239	266.64	0.0014	227132.53
-150-127	122.72	0.00	0.0000	81.54	0.0060	412.98	0.0041	0.0101	0.0101	215.48	0.0019	175985.84
0-127	123.37	142.35	0.0030	51.28	0.0012	412.61	0.0038	0.0050	0.0081	326.46	0.0017	212543.14
150-127	124.01	140.24	0.0180	52.60	0.0012	412.65	0.0038	0.0050	0.0231	326.81	0.0018	198190.83

Table 7.1 (Cont.) VP-GMAW and GMAW-P Melting Rate Predictions for a Range of Waveforms

			Pre-Pulse					term1	term2	term3	term4	term5	term6	term7		
Weld Number	α_- (mm/s A)	β_- ($s^{-1}A^{-2}$)	α_b (mm/s A)	β_b ($s^{-1}A^{-2}$)	V_{pp} (mm^3)	α_p (mm/s A)	β_p ($s^{-1}A^{-2}$)	$MR_{(\alpha-)}$ (mm/s)	$MR_{(\alpha b)}$ (mm/s)	$MR_{(\alpha p)}$ (mm/s)	$MR_{(\beta-)}$ (mm/s)	$MR_{(\beta+)}$ (mm/s)	$MR_{(\beta+)}$ (mm/s)	MR_s (mm/s)	MR_T (mm/s)	Error (%)
-150-42	-	-	0.549000	0.000124	0.70	0.285749	0.000100	-	14.73	12.22	-	0.09	15.05	-0.1051	41.98	8.07%
0-42	0.795	0.000612			0.78	0.242983	0.000100	11.14	0.00	8.62	4.50	0.06	12.40	-0.1147	36.61	-6.35%
30-42	0.795	0.000519			0.88	0.187290	0.000100	15.66	0.00	6.80	5.25	0.06	11.94	-0.1079	39.61	1.65%
60-42	0.795	0.000391			0.96	0.146754	0.000100	20.14	0.00	5.68	5.06	0.06	10.95	-0.1073	41.78	7.53%
90-42	0.795	0.000300			1.05	0.107521	0.000100	21.25	0.00	3.42	4.11	0.05	9.57	-0.0989	38.30	-1.66%
120-42	0.795	0.000300			1.17	0.060214	0.000100	26.84	0.00	1.97	5.19	0.05	4.31	-0.1052	38.25	-1.62%
150-42	0.795	0.000300			1.29	0.016165	0.000100	25.41	0.00	0.51	4.93	0.05	6.25	-0.1071	37.04	-4.63%
-150-85	-	-	0.549000	0.000124	0.62	0.339866	0.000100	-	19.67	35.26	-	0.18	26.23	-0.1218	81.22	0.67%
0-85	0.795	0.000523			0.98	0.138431	0.000100	24.58	0.00	10.69	20.38	0.13	18.87	-0.1193	74.54	-8.14%
150-85	0.795	0.000300			2.67	-0.310282	0.000100	63.41	0.00	-12.48	29.55	0.06	4.43	-0.1184	84.85	3.49%
-150-127	-	-	0.549000	0.000124	0.73	0.268552	0.000100	-	26.68	44.82	-	0.28	34.39	-0.1793	105.98	-13.64%
0-127	0.795	0.000442			1.11	0.084466	0.000100	42.55	0.00	16.56	43.73	0.26	19.23	-0.1924	122.15	-0.99%
150-127	0.795	0.000300			3.87	-0.476578	0.000100	87.16	0.00	-32.68	59.96	0.09	6.68	-0.2041	121.01	-2.42%

MR_T = Total predicted MR_{VP} or MR_p

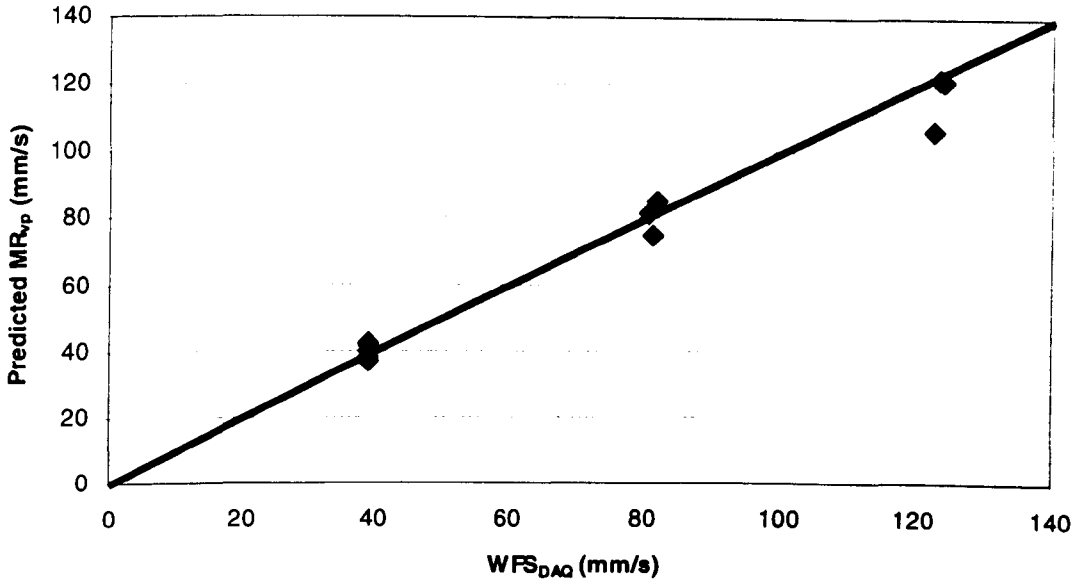

Figure 7.7 Predicted WFS for VP-GMAW and GMAW-P Waveform Parameters shown in Table 6.1

This project sought to compare the relative importance of arc and resistive heating for electrode melting rate with different VP-GMAW waveform designs. This analysis can be performed by combining the melting rate terms for EP arc and resistive heating (Table 7.2). The EN ratio was calculated per Equation (2.32) which is based on the ratio of product of current and time for each period to the sum of these products for the whole waveform. The EN ratio parameter was used since it is proportional to arc heating ($\alpha I t$) as compared to %EN which is based on the time ratio. The EN ratio varied from 0% for GMAW-P to 65% for the 150 pendant setting at 85 mm/s wire feed speed.

Bar charts were plotted to evaluate the magnitude of arc and resistive heating for each polarity (Figure 7.8). For VP-GMAW waveforms using the 0 setting, the melting contribution due to EN arc and resistive heating was over half the melting even though the EN ratio was only 21 to 24%. The EN melting contribution increased to 82% for test 150-42 which had an EN ratio of 47%.

The melting due to EP arc heating was negligible for test 150-42. The melting rate due to EP arc heating was negative on tests 150-85 and 150-127. Here, the melting rate was not actually negative. The electrode extension is increasing and arc length is decreasing during the EP periods that calculated a negative melting rate. This was due to the large pre-pulse droplet that was formed in the EN period. For these tests, the sum of EN melting rate terms was over 100% to balance the melting rate.

These charts show the importance of the droplet formation process on the melting rate potency for EP pulse heating. A large pre-pulse droplet inhibited further melting and resulted in a negative melting rate for that EP period. Here, the arc length was decreasing as the wire feed speed was greater than the melting rate. For pure GMAW-P

waveforms using the -150 setting, the melting rate due to arc heating was almost twice the resistive heating. Based on this comparison, it was not possible to simply establish the potency of each term. Overall, it was concluded that EN was more potent than EP for melting droplets and the contribution from arc heating was greater than resistive heating when the pre-pulse droplet volume was small.

Table 7.2 Relative Importance of MR Terms for Arc and Resistive Heating

Weld No.	EN Ratio (%)	term 1 α_- Contribution (%)	terms 2 & 3 α_+ Contribution (%)	term 4 β_- Contribution (%)	terms 5, 6 & 7 β_+ Contribution (%)
-150-42	0.00%	-	64.18%	-	35.82%
0-42	22.11%	30.42%	23.54%	12.30%	33.73%
150-42	46.67%	68.60%	1.38%	13.30%	16.72%
-150-85	0.00%	-	67.63%	-	32.37%
0-85	23.52%	32.98%	14.35%	27.35%	25.33%
150-85	65.10%	74.73%	-14.71%	34.83%	5.14%
-150-127	0.00%	-	67.46%	-	32.54%
0-127	20.81%	34.84%	13.56%	35.80%	15.80%
150-127	60.59%	72.03%	-27.01%	49.55%	5.43%

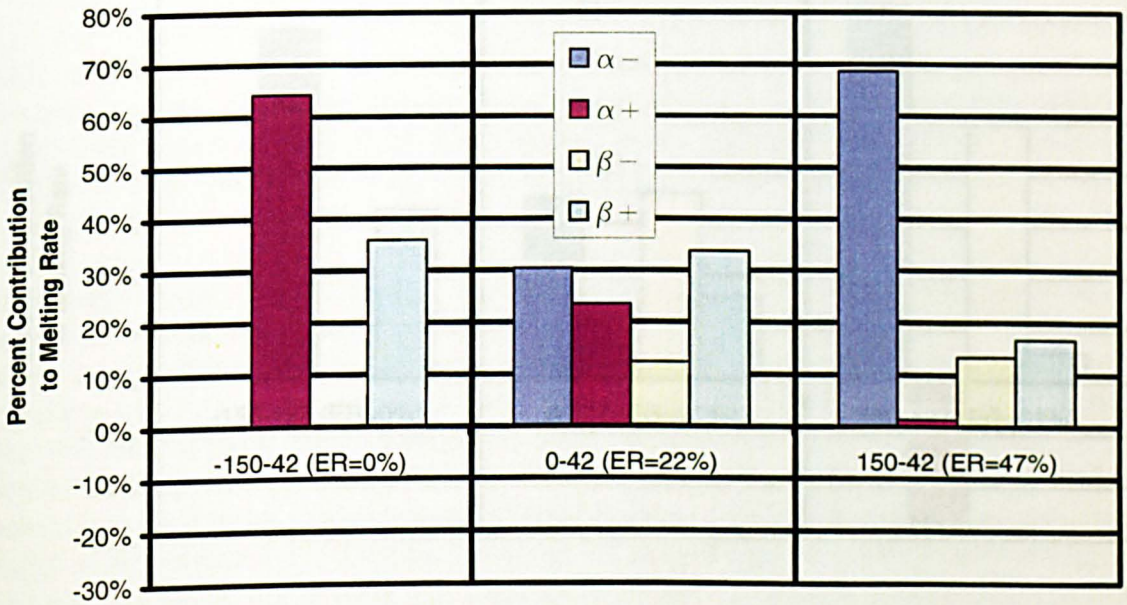

Figure 7.8(a) Melting Rate Contribution for Arc and Resistive Heating at 42 mm/s

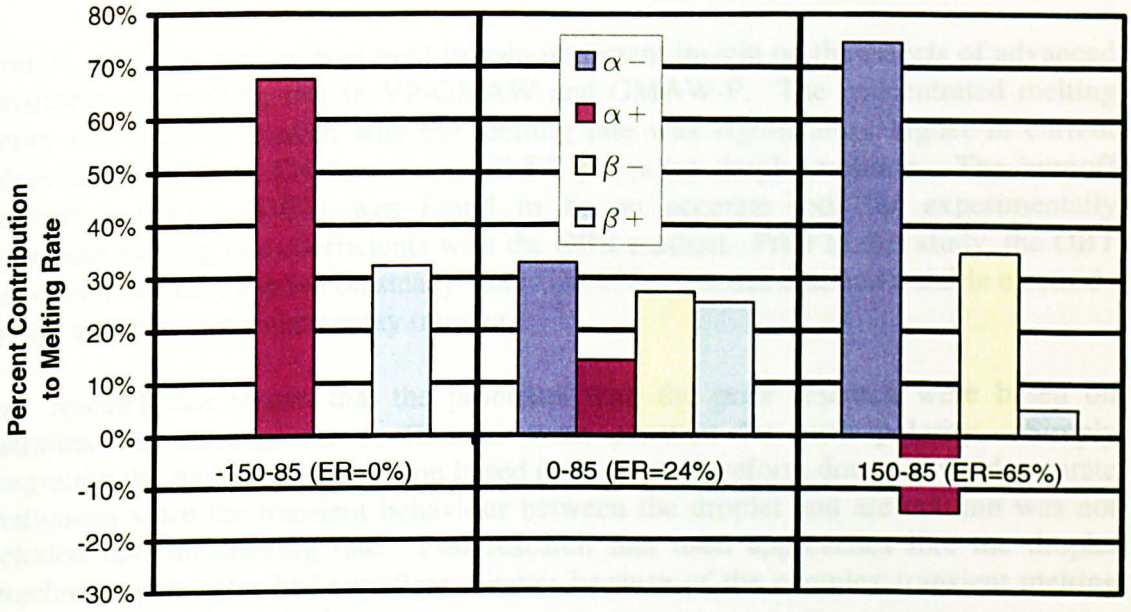

Figure 7.8(b) Melting Rate Contribution for Arc and Resistive Heating at 85 mm/s

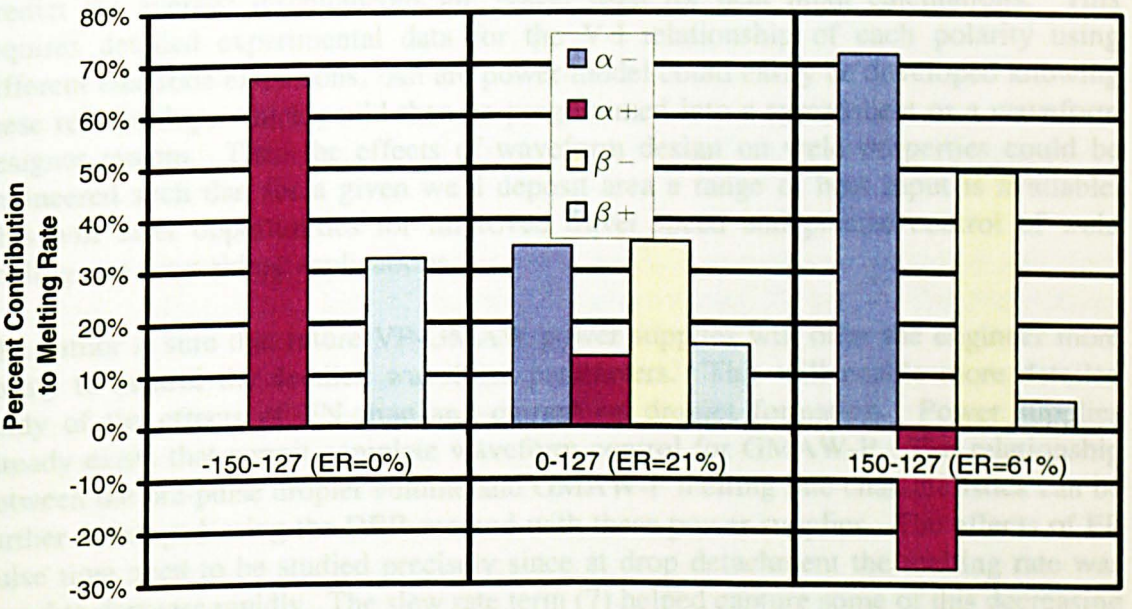

Figure 7.8(c) Melting Rate Contribution for Arc and Resistive Heating at 127 mm/s

7.3.2.1 Summary of DBR Method Predictions

Overall, the DBR method was used to gain important insight on the effects of advanced waveforms on melting rate in VP-GMAW and GMAW-P. The concentrated melting theory was used to explain why the melting rate was significantly higher in current pulses that had short EN time or small EP pre-pulse droplet volume. The burnoff diagram technique (DBT) was found to be an accurate tool for experimentally measuring melting rate coefficients with the DBR method. Prior to this study, the DBT was only accurately applied on steady-state GMAW processes that had a stable electrode tip and arc root, like stream spray transfer.

This research has shown that the problems with the prior research were based on assuming the melting rate coefficients were constant for each polarity. Simply integrating the melting rate equation based on current waveform does not yield accurate predictions since the transient behaviour between the droplet and arc column was not included into the melting rate. Past research that used approaches like the droplet detachment parameter had significant scatter because of the complex transient melting behaviour at the electrode tip.

This research yields opportunity to develop accurate analytical models for predicting the melting rate behaviour of advanced waveforms. Future work could evaluate the effects of different shielding gases, wire types and diameters, and the detailed mechanism at the electrode tip. The melting rate equation should be used with analytical models which predict the average instantaneous arc power used for heat input calculations. This requires detailed experimental data for the V-I relationship of each polarity using different electrode extensions. An arc power model could easily be developed knowing these relationships which could then be programmed into a spreadsheet or a waveform designer system. Then the effects of waveform design on weld properties could be engineered such that for a given weld deposit area a range of heat input is available. This will offer opportunities for improved travel speed and precise control of weld cooling rate for welding applications.

The author is sure that future VP-GMAW power supplies will offer the engineer more ability to control the detailed waveform parameters. This will enable more detailed study of the effects of EN time and current on droplet formation. Power supplies already exists that permit complete waveform control for GMAW-P. The relationship between the pre-pulse droplet volume and GMAW-P melting rate characteristics can be further developed using the DBR method with these power supplies. The effects of EP pulse time need to be studied precisely since at drop detachment the melting rate was found to decrease rapidly. The slew rate term (7) helped capture some of this decreasing melting rate effect, but in theory, it does not represent the change in melting rate since the droplet growth and detachment processes are more dominant. The term needs to be modified to relate the melting rate coefficients to the droplet formation process as a function of time and wave shape. Waveforms that yield multiple drops per pulse offer additional complexity as the arc is trying to transition into stream spray at normal EP pulse currents.

7.4 Process Capability Study

Two VP-GMAW power supplies were evaluated for welding 1.8 mm lap joints on steel and stainless steel with 1t gap. This evaluation used the ARCWISE method, which systematically developed the functional relationships between the welding parameters, weld bead quality, and productivity (measured in travel speed) for this application. ARCWISE provided a good method for benchmarking the capability of these power supplies since each test was made with a constant deposit area and arc length. Therefore, the effects of electrode melting rate, arc power, and metal transfer stability due to waveform quality that were provided by the VP-GMAW power supplies could be compared directly.

7.4.1 Productivity Analysis Summary

The VP-GMAW waveforms used in the PC350 used a fuzzy logic short circuit anticipation control. The use of short circuiting with these fuzzy VP waveforms resulted in lower heat inputs compared to the AC/MIG 200 power supply at each wire feed speed. The AC/MIG 200 power supply used a free flight pulsed globular transfer. The lowest heat input observed with an AC/MIG 200 test that did not have significant short circuiting was 325 J/mm. At the same travel speed of 8.4 mm/s, the PC350 produced a lower heat input of 225 J/mm. The short circuiting of the PC350 was able to reduce the heat input an additional 30% using 100% EN with short circuit controlled transfer. Higher travel speeds were required to achieve acceptable fusion at these low heat inputs.

Overall, the PC350 power supply offered higher travel speeds due to its higher current capacity. Both power supplies offered an increase in travel speed compared to GMAW-P. Even higher welds speeds were possible on this application with reduced gap that would permit the use of smaller weld deposits.

For the PC350, a larger range of %EN could be used to make acceptable welds since this power supply offered higher currents, 350 amps versus 200 amps. The productivity data for the PC350 showed that the maximum travel speed could be increased 300% by using the VP-GMAW process compared to GMAW-P. Even higher speeds were possible with higher %EN but the metal transfer provided by the PC350 at the higher wire feed speeds resulted in spatter. Waveform optimization is needed to improve metal transfer stability at higher currents with VP-GMAW.

The bead shape maps show that for this lap joint thickness the AC/MIG 200 power supply did not provide as much improved productivity where the travel speed was limited to 12.7 mm/s. This was directly related to the current capacity and duty cycle of this power supply which was designed for thinner materials. From these results, there appeared to be opportunity to further increase travel speed using either power supply by optimising the VP-GMAW waveform with higher currents (i.e., greater than 350 amps at 100% duty cycle).

Even though actual penetration and base metal dilution measurements are not presented in this report, some visual trends can be observed in Figures 6.21 through 6.25. The first trend in that penetration and base metal dilution (or nugget area) increased as the travel speed increased for these constant deposit area tests at each %EN setting. This occurs since less time was available for heat conduction into the base material even when the heat input was decreasing. The weld nugget area clearly gets larger as the travel speed increased from 4.3 mm/s to the maximum speed tested for each %EN. This of course is the driving force to use waveform processes, like VP-GMAW that significantly improve melting rate. The higher the melting rate of the process for a given amount of current and arc power, the higher the travel speed must be to achieve the same fusion quality for a given deposit size.

7.4.2 Weld Sizing Strategy

All tests performed on this application used a WFS/TS ratio of 10 which provided a deposited area of 10.26 mm^2. This was six times the area of a 1.8 mm fillet weld that is 1.6 mm^2 assuming uniform leg size. The later deposit area would be ideal assuming perfect fit-up and process control. Overwelding is required when welding sheet metal to account for variation in electrode extension cast and gap in the lap joint. These tests used a 1.8 mm gap to simulate a worst case production condition. Higher welding speeds could be achieved with either power supply if the fit-up was improved allowing a smaller deposit area weld. Smaller welds require less heat input so higher travel speeds would be required to achieve the same fusion quality.

Some backfilling of the gap was observed in the macrosections in Figures 6.21 and 6.25. Welding over a gap required enough weld metal to span the gap for proper weld size and to permit some gap backfilling. Short arc lengths directed at the top sheet were believed to minimize the amount of gap backfilling by focusing the drop stream into the weld pool. Wire electrode aimed at the gap and excessive push travel angle in preliminary tests appeared to promote gap backfilling. Tests in this investigation were performed with 10 degrees push travel angle while aiming the torch at the top piece corner of the lap joint. This controlled the backfilling to a minimum.

Based on the deposit area observed in these tests, a simple geometric relationship was determined for sizing welds for lap joints with gap. This equation assumes an equal amount of gap back-filling equivalent to the gap opening, G^2. A quarter ellipse deposit area (convex weld) was assumed because of the low heat input required to minimize burnthrough. For horizontal fillets the resulting equation would be the following:

$$A_{HF} = \frac{\pi a(bt)}{4} + G^2 \tag{7.7}$$

where: A = weld deposit area
t = sheet thickness
a = vertical leg = t + G
G = gap
b = lap leg factor

The lap leg factor, b, describes how much overwelding was required to assure the convex fillet was large enough to bridge the gap and make the weld. It is the only unknown based on the form of this equation and knowing the joint geometry. For lap joint applications, the lap leg factor would be the variable as a function of joint conditions. A small range of b needs to be defined to determine the minimum and maximum weld deposit size that could properly fill the joint using a GMAW process. The author believes that there is a deposit area range which is a property of arc welded sheet metal joint for each set of conditions. The vertical leg, a, was simply assumed to be equal to the thickness of the sheet plus the gap. Substitutions can be made resulting in the following equation:

$$A_{HF} = \frac{\pi(t+G)bt}{4} + G^2 \tag{7.8}$$

The weld deposit area equalled 10.26 mm^2 for the application studied here. Based on this deposit area, the lap leg factor could be solved for as follows:

$$10.26mm^2 = \frac{\pi(1.8mm + 1.8mm)b \cdot 1.8mm}{4} + (1.8)^2 mm^2 \tag{7.9}$$

Solving the equation yields a value of 1.4 for b. This was considered a nominal value for b and a range exists that would provide good weld fill for 1.8 mm lap joints with 1.8 mm gap. Future work should be performed to further develop the relationship between deposit area requirements and sheet metal joint conditions. Here, the effects of joint type, thickness, material type, position and fit-up tolerance (like gap and offset) should be related to the weld size range that provides the proper joint fill for the conditions. This information would provide for rapid optimisation of sheet metal arc welding applications using methods like ARCWISE or statistical design of experiments.

8.0 CONCLUSIONS

1. Melting rate was very dependent on current waveform, polarity, and droplet size, and metal transfer events if they occurred, during each waveform period. The transient conditions of current waveform and metal transfer produced rapid changes in arc behaviour, which strongly influenced the melting rate for each period of various VP-GMAW waveforms.

2. The concentrated melting theory was developed to explain the significant increase in electrode extension burnoff and droplet growth rate that occurred at short EN time as a function of current, and during EP peak pulse when the pre-pulse droplet volume was small. The highest electrode extension burnoff and droplet growth rate occurred when the arc was permitted to climb over the solid electrode tip producing rapid concentrated melting. Likewise, large molten droplets were found to promote a negative electrode extension burnoff and a decreased droplet growth rate. The arc rooted on large droplets providing additional heating but limited additional electrode melting.

3. The droplet burnoff rate (DBR) method was found to yield good experimental measurements for the arc and resistive heating coefficients used in melting rate equations for complex waveforms like used in VP-GMAW. The coefficients were not as physically linked to arc and resistive heating, like the prior research, but provided characterisation of second order behaviour for electrode melting rate in each period of the waveform.

4. EN time affected the melting rate as a function of EN current. The melting rate contribution from electrode extension burnoff increased as the EN time decreased in a range from 23 to 3 msec. This was measured by the change in the resistive heating coefficient. This change was related to the slope of the burnoff diagram, which increased when burnoff rate increased as a result of electrode extension burnoff. The change in the resistive heating coefficient was due to changes in the location of concentrated arc heating not resistive heating in the electrode extension.

5. The melting rate of the EP periods, both background and peak, were related to the pre-pulse droplet volume. Large pre-pulse droplets, which formed in the EN period, decreased the EP melting rate since the arc concentrated more on the droplet than above it on the un-melted electrode extension. The arc was observed to follow the droplet during detachment and some solidification of the molten tip occurred before the arc re-attached to the tip at drop transfer. This reduced the electrode melting rate of EP peak periods that had early or multiple drop transfers.

6. For EP pulse waveforms, the pre-pulse droplet volume effect on melting rate was measured by a change in the arc heating coefficient, which was negative for some DBR measurements that had large pre-pulse droplet volumes. The negative influence was not a result of reduced heating, but a result of preferential

heating of the droplet instead of melting the electrode tip. The electrode extension increased under these conditions resulting in a shorter arc length.

7. Overall, it was concluded that EN was more potent than EP for electrode melting by comparison of the arc and resistive heating coefficients used in the melting rate equation. The contribution from arc heating was greater than resistive heating when the pre-pulse droplet volume was small.

8. VP-GMAW power supplies offered stable operation for welding sheet structures on both carbon steel and stainless steel. Higher travel speeds were required as the %EN increased to produce the same constant deposit area weld quality. Welding speeds were up to 300% higher with VP-GMAW compared to the GMAW-P process when welding lap joints on 1.8 mm thick material with 1.8 mm gap. VP-GMAW heat input was up to 47% less than GMAW-P for the same melting rate.

9.0 FUTURE WORK

There is significant opportunity to build off the research developed in this dissertation. Future work can be performed to help further the understanding of metal transfer, melting rate and arc behaviour for both VP-GMAW and GMAW-P processes. This will help expand the use of these processes in industry and maximise the benefits of better metal transfer, lower heat inputs and higher travel speeds on welding applications. The following is a list of topic areas for future work;

1) Waveform Optimisation – VP-GMAW waveform parameters need to be developed that minimise spatter, and permit the use of shorter arc lengths, higher currents, and higher wire feed speeds. This will provide improved productivity on sheet metal and cladding applications that can take advantage of the low heat input of VP-GMAW.
2) Numerical Modelling – Most numerical models that characterise forces on droplets, melting rate and metal transfer, assume the electrode extension and the interface between the droplet and arc are constant. Future research should factor the concentrated melting theory and DBR electrode melting rate properties into their models and improve their accuracy.
3) Welding Fume – The fume reducing benefits of VP-GMAW metal transfer needs to be better characterised and related to the concentrated melting theory and waveform optimisation. These studies could be performed on a range of electrode types and shielding gases used by industry.
4) Droplet Burnoff Rate (DBR) Method Studies – The DBR method offers the ability to better characterise the true melting rate behaviour of advanced waveform processes. Future work using this method should evaluate other electrode types and sizes, shielding gases, and waveform strategies for both VP-GMAW and GMAW-P. A database of DBR melting rate properties will help optimize waveform metal transfer stability, melting rate, heat input and fume on welding applications using these processes.

10.0 REFERENCES

1. Ogasawara, T., Maruyama, T, Saito, T., Sato, M., and Hida, Y. 1987. A power source for gas shielded arc welding with new current waveforms. *Welding Journal*, March, pp. 57-63.
2. Maruyama, T., Okada, M., Hida, Y, Honma, M., and Minato, T. 1995. Current waveform control in gas shielded arc welding for robotic systems. Kobelco Technology Review, No. 18, April, pp. 10-14.
3. Nacey, T. 1995. The effect of dynamic variables on GMAW arc characteristics - Controlling the power supply response. *The Fabricator*, March, Vol. 25(2), pp. 18-20.
4. Nacey, T. and Pagano, K. 1995. Advancements in DC and AC low current pulse GMAW. *Proceedings from ICAWT 11th Annual Conference*, Columbus, Ohio, Paper No. 2-3(C).
5. Maruo, H. and Hirata, Y. 1988. MIG welding with rectangular wave AC. Technology Reports of the Osaka University. Vol. 38(1935), pp. 237-245.
6. Maruyama, T., et al. 1988. Polarity Ratio Control GMA Welding Power Source, Data for the JWS 118th Welding Method Research Committee.
7. Tanimoto, J., Minooka, M., Nishida, Y. 1988. Development of the AC pulsed MAG welding process. IIW Asian Pacific Regional Welding Congress, 36th Annual AWI Conference.
8. Okada, M. 1989. Sensarc PC350 EP/EN ratio-controllable GMA welding power source. Masashi OKADA, Welding Equipment Robot Department, Welding Division, Kobelco Technology Review, No. 6.
9. Okada, M. 1992. Sensarc AL350 penetration-controllable MIG welding power source for aluminum Alloy. Kobe Steel, Factory Automation and Robotics Group, New Business Division, Kobelco Technology Review, No. 6.
10. Harada, S., Ueyama, T., Mita, T., Innami, T., and Ushio, M. 1999. The state-of-the-art of AC-GMAW process in Japan. IIW Doc. XIII-1589-99, pp. 1-10.
11. Ueyama, T., Tong, H., Harada, S., and Ushio, M. 2000. Improve sheet metal welding quality and productivity with AC pulsed MIG welding system. IIW Doc. XII-1629-00, pp. 86-102.
12. Lesnewich, A. 1958. Control of melting rate and metal transfer in gas-shielded metal-arc welding - Part 1 - Control of electrode melting rate. *Welding Research Supplement*, August, pp. 343s-353s.
13. Lesnewich, A. 1958. Control of melting rate and metal transfer in gas-shielded metal-arc welding - Part 2 - Control of metal transfer. *Welding Research Supplement*, September, pp. 418s-425s.
14. The Welding Handbook, Volume 2 – Welding Processes, AWS, 8th edition.
15. Guile, A.E., 1986. The electric arc. Chapter 5 in The Physics of Welding by Lancaster, J.F., 2nd Edition, Pergamon Press.
16. Lancaster, J.F., 1986. The electric arc in welding. Chapter 6 in The Physics of Welding, 2nd Edition, Pergamon Press.
17. Lancaster, J.F., 1986. Metal transfer and mass flow in the weld pool. Chapter 7 in The Physics of Welding, 2nd Edition, Pergamon Press.
18. Halmoy, E. Electrode melting in arc welding. Physical Aspects of Arc Welding, pp. 81-93.

19. Halmoy, E., 1979. Wire melting rate, droplet temperature, and effective anode melting potential. Arc Physics and Weld Pool Behavior, TWI, Paper 29, pp. 49-57, May 1979.
20. Halmoy, E., 1986. Electrode wire heating in terms of welding parameters. Appendix A in The Physics of Welding by Lancaster, J.F, 2nd edition, Pergamon Press.
21. Jonsson, P.G., Szekely, J., Madigan, R.B., and Quinn, T.P. 1995. Power characteristics in GMAW: Experimental and numerical investigation. *Welding Research Supplement*, March, pp. 93s-101s.
22. Zhu, P., Lowke, J.J., and Morrow, R. 1992. A unified theory of free burning arcs, cathode sheaths, and cathodes. *J. Phys. D: Appl. Phys.* 25: 1221-1230.
23. Guile, A.E. 1971. Arc-electrode phenomena. Proc. IEE, IEE REV. 118(9R): 1131-1154.
24. Essers, W.G. and Walter, R. 1980. Some aspects of the penetration mechanisms in metal inert gas (MIG) welding. Int. Conf. of Arc Physics and Weld Pool Behavior, pp. 289-300, London, The Welding Institute.
25. Pintard, J. 1962. Some experimental data on short circuit transfer. Physics of the Welding Arc, pp. 92-97, London, The Institute of Welding.
26. Guile, A.E. 1970. Studies of short electric arcs in transverse magnetic fields with application to arc welding. *Welding in the World*, 8(1): 43-53.
27. Matsunawa, A., and Nishiguchi, K. 1979. Arc characteristics in high pressure argon atmospheres. Arc Physics and Weld Pool Behaviour, The Welding Institute, Cambridge.
28. Lesnewich, A. 1955. Electrode activation for inert-gas-shielded metal-arc welding. *The Welding Journal*, December, pp. 1167-1178.
29. Norrish, J. 1974. High deposition MIG-welding with electrode negative polarity. Proceedings from 3rd Intl. Conf. on Advances in Welding Processes, The Welding Institute, May 7-9, pp. 121-128.
30. Quintino, L. and Allum, C.J. 1984. Pulsed GMAW: Interactions between process parameters - Part 1. *Welding and Metal Fabrication*, March, pp. 85-89.
31. Quintino, L. and Allum, C.J. 1984. Pulsed GMAW: Interactions between process parameters - Part 2. *Welding and Metal Fabrication*, April, pp. 126-129.
32. Greene, W.J. 1960. An analysis of transfer in gas-shielded welding arcs. *Proceedings of AIEE Electric Welding Committee Winter Meeting*, Jan. 31-Feb. 5, 1960, New York, NY, pp. 194-202.
33. Kim, Y.-S., McEligot, D.M., and Eagar, T.W. 1991. Analysis of electrode heat transfer in gas metal arc welding. *Welding Research Supplement*, January, pp. 20s-31s.
34. Choi, S.K., Yoo, C.D., and Kim, Y.-S. 1998. Dynamic Simulation of metal transfer GMAW - Part 1: Globular and spray transfer modes. *Welding Research Supplement*, January, pp. 38s-44s.
35. Shepard, M.E. and Cook, G.E. 1992. A frequency-domain model of self-regulation in gas-metal arc welding. *Proceedings of International Trends in Welding Science and Technology*, ASM International.
36. Shepard, M.E. and Cook, G.E. 1992. A nonlinear time-domain simulation of self-regulation in gas-metal arc welding. *Proceedings of International Trends in Welding Science and Technology*, ASM International.

37. Haidar, J. 1998. An analysis of the formation of metal droplets in arc welding. Journal Physics D: Applied Physics, pp 1233-1244.
38. Quinn, T.P. 2002. Process sensitivity of GMAW: Aluminum vs. steel. *Welding Journal Research Supplement*, May. 55s-61s.
39. Huismann, G. and Hoffmeister, 1998. H. Sensing the MIG process by measuring the wire feed rate and the current. IIW Document 212-931-98.
40. Waszink, J.H. and van den Heuvel, G.J. 1982. Heat generation and heat flow in the filler metal in GMAW welding. *Welding Research Supplement*, August, pp. 269s-282s.
41. Boughton, P and MacGregor, G. 1972. Control of short circuiting in MIG-welding. The Welding Institute Research Report P57/72.
42. Cook, G.E., DeLapp, D.R., Barnett, R.J., and Strauss, A.M. 1995. Modeling and control parameters for GMAW, short-circuiting transfer. *Proceedings of 4th International Trends in Welding Research Conference*, June 5-8, 1995, Gatlinburg, TN, pp. 721-726.
43. Darwish, A.H. 1975. Penetration and bead contour in CO_2 welding of structural steel. IIW Doc. XII-B-179-75.
44. Dutra, J.C. 1990. Statistical analysis of arc stability in MIG-MAG welding with short-circuit transfer. IIW Doc. XII-1172-90.
45. Hermans, M.J.M. and den Ouden, G. 1995. Process stability and weld pool oscillation during short circuiting GMA welding. *Proceedings of 4th International Trends in Welding Research Conference*, June 5-8, 1995, Gatlinburg, TN, pp. 505-510.
46. Koves, A. 1985. Analysis of CO_2 welding process of thin plates. IIW Doc. XII-909-85.
47. Lebedev, A.V. 1990. Controlled metal transfer in CO_2 arc welding. IIW Doc. XII-1201-90.
48. Needham, J.C. and Percival, D.F. 1983. Parametric relationships in short-circuit MIG welding. The Welding Institute Research Report 214/1983.
49. Ushio, M. and Mao, W. 1997. Dynamic characteristics of arc sensor in GMA welding in dip transfer mode. pp. 272-280.
50. Waszink, J.H. and Graat, L.H.J. 1983. Experimental investigation of the forces acting on a drop of weld metal. *Welding Research Supplement*, April, pp. 108s-116s.
51. Jones, L.A., Eagar, T.W., and Lang, J.H. 1992. Investigations of drop detachment control in gas metal arc welding. *Proceedings of International Trends in Welding Science and Technology*, ASM International, pp. 1009-1013.
52. Jacobsen, N. 1992. Monopulse investigation of drop detachment in pulsed gas metal arc welding. *J. Phys. D: Appl. Phys.*, Vol. 25, pp. 783-797.
53. Kennedy, C.R. 1970. Gas mixtures in welding. *Australian Welding Journal*, pp. 38-52.
54. Salter, G. R., and Dye, S.A. 1971. Selecting gas mixtures for MIG welding. *Metal Construction and British Welding Journal*. pp. 230-233.
55. Modenesi, P.J., and Nixon, J.H. 1994. Arc instability phenomena in GMA welding. *Welding Journal Research Supplement*, pp. 219s-224s.
56. Boughton, P., and Amin Mian, M. 1972. Aspects of the arc root behavior in welding. Second International Conf. on Gas Discharges, IEE, pp 130-131.

57. Hilton, D.E., and McKeown, D. 1986. Improvement in mild steel weld properties by changing the shielding gas – theory and practice. *Metal Construction*, pp 617-619.
58. Agusa, K., Nishiyama, N., and Tsuboi, J. 1981. MIG welding with pure argon shielding - arc stabilization by rare earth additions to electrode wires. *Metal Construction*, September, pp. 570-574.
59. Ushio, M. 1990. Materials sensitive phenomena in gas-shielded arc welding process. *Transactions of JWRI*, Vol. 19(1), pp. 31-36.
60. Plasma_MIG Handbook, The Phillips Electric Company.
61. Ma, J. and Apps, R.L. 1982. MIG transfer discovery of importance to industry. *Welding and Metal Fabrication*, September, pp. 307-316.
62. Ma, J. and Apps, R.L. 1983. Analyzing metal transfer during MIG welding. *Welding and Metal Fabrication*, April, pp. 119-128.
63. Allum, C.J. 1983. MIG welding- time for a reassessment. *Metal Construction*, pp. 347-353.
64. French, I., Ogilvie, G., Ramakrishnan, S., Ogilvy, M., and Bosworth, M. 1988. Droplet transfer from gas shielded solid and flux cored electrodes. Proc. of Annual Welding Conf. for Australian Welding Association, Hobart, pp. 72-84.
65. Norrish, J. and Richardson, I.F. 1988. Metal transfer mechanisms. *Welding & Metal Fabrication*, January/February, pp. 17-22.
66. Ueguri, S., Hara, K., and Komura, H. 1985. Study of metal transfer in pulsed GMA welding. *Welding Research Supplement*, August, pp. 242s-250s.
67. Jones, L.A., Eagar, T.W., and Lang, J.H. 1992. Investigations of drop detachment control in gas metal arc welding. *Proceedings of International Trends in Welding Science and Technology*, ASM International, pp. 1009-1013.
68. Jones, L.A., Eagar, T.W., and Lang, J.H. 1998. Images of a steel electrode in Ar-2%O_2 shielding during constant current gas metal arc welding. *Welding Research Supplement*, April, pp. 135s-141s.
69. Choi, S.K., Lee, K.H., Yoo, C.D., Lee, T.S. 1996. Analysis of metal transfer through equilibrium shape of pendent drop in GMAW. *Journal of Japan Welding Society*, Vol. 14(2), pp. 243-247.
70. Allum, C.J. 1985. Metal transfer in arc welding as a varicose instability: 1. Varicose instability in current carrying liquid cylinder with surface charge. Journal Physics D: Applied Physics,18, pp. 1431-1446.
71. Allum, C.J. 1985. Metal transfer in arc welding as a varicose instability: II. 1.Development of model for arc welding. Journal Physics D: Applied Physics, 18, pp. 1447-1468.
72. Kim, Y.K., and Eager T.W. 1993. Analysis of metal transfer in gas metal arc welding. *Welding Research Supplement*, Vol. 71, pp. 269s-278s.
73. Lawrence, B.D. and Jackson, C.E. 1969. Variable frequency gas shielded pulsed current arc welding. *Welding Research Supplement*, March, pp. 97s-104s.
74. Smati, Z. 1986. Automatic pulsed MIG welding. *Metal Construction*. January, pp. 38-44.
75. Richardson, I.M., Bucknall, P.W., and Stares, I. 1994. The influence of power source dynamics on wire melting rate in pulsed GMA welding. *Welding Research Supplement*, February, pp. 32s-37s.

76. Kim, Y.S., and Eager, T.W. 1993. Metal transfer in pulsed current gas metal arc welding. *Welding Journal Research Supplement*, July. pp. 279s -287s.
77. Amin, M. 1981. Synergic pulse MIG welding. *Metal Construction*, June, pp. 349-353.
78. Amin, M. 1983. Pulse current parameters for arc stability and controlled metal transfer in arc welding. *Metal Construction*, May, pp. 272-278.
79. Welz, W. and Knoch, R. 1989. Setting and classifying pulsed arc for active-gas metal arc welding. *Welding and Cutting*, Vol. 12, pp. 17-19.
80. Welz, W. and Knoch, R. 1990. Setting parameters for pulsed welding. *Welding Design & Fabrication*, July, pp. 16.
81. Nixon, J.H. and Norrish, J. Determination of pulsed MIG process parameters. *Synergic MIG Supplement*, pp. 4-7, Pulse Parameters for XMT 300 CC/CV.
82. Kohn, G. and Siewert, T.A. The effect of power supply response characteristics on droplet transfer of GMA welds. *Proceedings of Advances in Welding Science and Technology*, ASM International, pp. 299-302.
83. Trindade, E. 1981. MSc Thesis, School of Industrial Science, Cranfield University.
84. Matsuda, F., Ushio, M., Tanaka, Y., Itonaga, K., and Yokoo, T. 1984. Pulsed GMAW: One-drop-transfer and process parameter. *Transactions of JWRI*, Vol. 13(2), pp. 15-20.
85. Matsuda, F., Ushio, M., and Tanaka, Y. 1983. Metal transfer characteristics in pulsed GMA welding. *Transactions of JWRI*, Vol. 12(1), pp. 9-17.
86. Richardson, I.M. and Nixon, J.H. 1985. Open arc pulsed current GMAW - Application to hyperbaric welding operations. *Proceedings of the JDC University Research Symposium*, 1985 International Welding Congress, Toronto, Ontario, Canada, October 15-17, 1985, pp. 153-163.
87. Hansen, H.R., Rasmussen, A., and Richardson, I.M. 1991. Hyperbaric GMA process control and properties at pressures 1 to 60 bar. OMAE - Volume III-A, Materials Engineering, ASME, pp. 181-187.
88. Dilthey, U., Reisgen, U., Bachem, H., and Gollnick, J. 1998. Two-wire processes for higher deposition rate and higher welding speed. IIW Doc. XII-1549-98.
89. Kodama, M., Kawano, T., Iwabuchi, H. 1997. Development of high speed horizontal fillet welding process in GMAW process. IIW Doc. XII-1489-97.
90. Rippl, P. 1998. Improved performance in MIG/MAG welding due to the two-wire technique. IIW Doc. XII-1528-98.
91. Shinoda, T., Nakata, J., and Miyauchi, H. 1998. Double wire MIG welding process and its applications. IIW Doc. XII-1543-98.
92. Joseph, A, 2001. Assessing the effects of GMAW pulse parameters on arc power and weld heat input. Masters Thesis, The Ohio State University.
93. Bosworth, M.R. 1991. Effective heat input in pulsed current gas metal arc welding with solid wire electrodes. *Welding Research Supplement*, May, pp. 111s-117s.
94. Bosworth, M.R. 1993. Finding the correct heat input values for pulsed current welding. *Australasian Welding Journal*, pp. 20-24.
95. Street, J.A., Burr, A., and Newling, R.G. 1980. Instrumentation in gas metal arc welding. The Welding Institute Research Report 113/1980.

96. Rehfeldt, D. and Wittkopf, R. 1998. A fast and economical calibration system for welding power sources. IIW Doc. XII-1559-98.
97. Dilthey, U. and Killing, R. 1990. Heat input for pulsed GMAW. *Welding Design and Fabrication*, September, pp. 51-53.
98. Melton, G.B. 1994. Measurement of arc welding parameters and validation of equipment. *Proceedings of EUROJOIN 2 - Second European Conference on Joining Technology*, Florence Italy, May 16-18, 1984.
99. Melton, G.B. 1998. Requirements for arc monitoring and equipment calibration. IIW Doc. XII-1525-98.
100. Needham, J.C. 1985. What do you mean by current? *The Welding Institute Research Bulletin*, August, pp. 273-277.
101. Needham, J.C. 1985. What do you mean by voltage? *The Welding Institute Research Bulletin*, September, pp. 311-316.
102. Lucas, W. and Needham, J.C. 1975. Why not AC MIG-welding? The Welding Institute Research Bulletin, March, pp. 63-67.
103. Lucas, W. 1978. Solid wire AC MIG welding. Welding Research International, Vol. 8(2), pp. 102-127.
104. Dymenko, V.V. and Zaruba, I.I. 1979. Stabilizing the arc discharge during welding with AC. Automatic Welding, Vol. 31(3), pp. 25-29.
105. Nakanishi, M., Katsumoto, N., Komizo, Y., Hasunuma, S, and Seta, I. 1983. Development of AC MIG arc welding. The Sumitomo Search, No. 28, October, pp. 73-86.
106. Tsushima, S. and Fujita, H. 1992. Pulse generator for high-current AC-MIG welding process - Development of AC-MIG welding process (Report 2).
107. Tsushima, S., Ohkita, S., and Horii, Y. 1992. Effects of oxygen on the toughness of Ti B containing AC MIG weld metal - Development of AC MIG welding process (Report 3). pp. 56-63.
108. Tsushima, S. and Kitamura, M. 1994. Tandem electrode AC-MIG welding - Development of AC-MIG welding process (Report 4). Welding International, Vol. 8(8), pp. 599-605.
109. Tsushima, S., Horii, Y., and Yurioka, N. 1994. Application of AC-MIG narrow-gap welding to butt joints in 980 MPa high-strength steels (5th Report) - Development of AC-MIG welding. *Welding International*, Vol. 8(7), pp. 525-531.
110. Talkington, J.E. 1998. Variable polarity gas metal arc welding. The Ohio State University, Thesis.
112. Ushio, M., Nakata, K., Tanaka, M. 2000. AC pulsed GMA welding of Al-Mg alloy - Fume and welding arc phenomena. Productivity Beyond 2000, IIW Asian Pacific Welding Congress, The WTIA 43rd National Welding Congress, pp. 859-873.
113. Ushio, M., Nakata, K., Tanaka, Tong, H., and Mita, T. 1994. Fume generation in Al-Mg alloy welding with AC-pulsed GMAW welding method. *Trans. of JWRI*, Vol. 23(1).
114. Harwig, D.D., Joseph, A., and Dierksheide, J. 2992. Capability of variable polarity GMAW for automotive applications. AWS Sheet Metal Welding Conference X, Detroit, MI, May 15-17th.
115. Harwig, D. D., Joseph, A., Anderson, C., and Moore, J. 2000. Characteristics of

variable polarity (AC) GMAW power supplies. Proceedings from ICAWT 2000, AWS, Orlando, FL, December 6-8th.

116. Harwig, D.D. 1996. Weld parameter development of robot welding. SME Technical Paper RP96-291.
117. Harwig, D.D. 1997. The ARCWISE™ technique for increasing productivity in arc welding. International Conference on Advances in Welding Technology. Sept. 17-19, Columbus, OH.
118. Harwig, D.D. 2000. A wise method for assessing arc welding performance and quality. *Welding Journal*, 79(12):35-39.
119. Synergic control in MIG welding 1 - Parametric relationships for steady DC open arc and short circuiting arc operation. *Metal Construction*, January 1987, Vol. 19(1), pp. 22-28.
120. Kennedy, N.A. 1988. The development of tolerant MIG fillet welding procedures - preliminary report. The Welding Institute Research Report 384/1988.
121. Hardesty, J. 1995. Tolerance and optimisation of weld procedures for high speed welding of steel sheet. Master's Thesis, The Ohio State University, Columbus, OH.
122. Reilly, R., Xu, X., and Jones, J.E.. 1992. Neural network application to acoustic emission signal processing. International Conference on Computerisation of Welding Information IV Proceedings, Orlando, FL, pp. 146-s to 160-s.
123. McConnell, I.A. and McPherson, N.A. 1997. The application of statistical process design to a FCAW process. *Welding Journal*, 76(10):412-s to 416-s.
124. Noruk, J.S. 1997. Gas metal arc penetration welding development utilising neural nets. Robotic Arc Welding Conference Proceedings, Orlando, FL.
125. Ribardo, C. 2000. Desirability functions for comparing arc welding parameter optimisation methods and for addressing process variability under six sigma assumptions. Ph.D Dissertation, The Ohio State University, Columbus, OH.
126. Allen, T.T., Ittiwattana, W., and Bernshteyn, M. 2000. A method for robust machine design applied to arc welding. Third International Symposium on Tools and Methods of Competitive Engineering, Delft, Netherlands.
127. Allen, T.T., Richardson, R.W., Tagliabue, D.P., and Maul, G.P. 2002. Statistical process design for robotic GMA welding of sheet metal. *Welding Journal*, pp. 69-s to 77-s.
128. Harwig, D.D., Zheng, B., Reichert, C., Huang, T., Joseph, A., and Baughman, A. 2002. Semi-adaptive synergic-fill welding tractor for ship unit erection. Proceedings of 2002 Ship Production Symposium, Boston, MA, September 25.

Appendix A

ARCWISE Data Sets for 16 mm CTWD

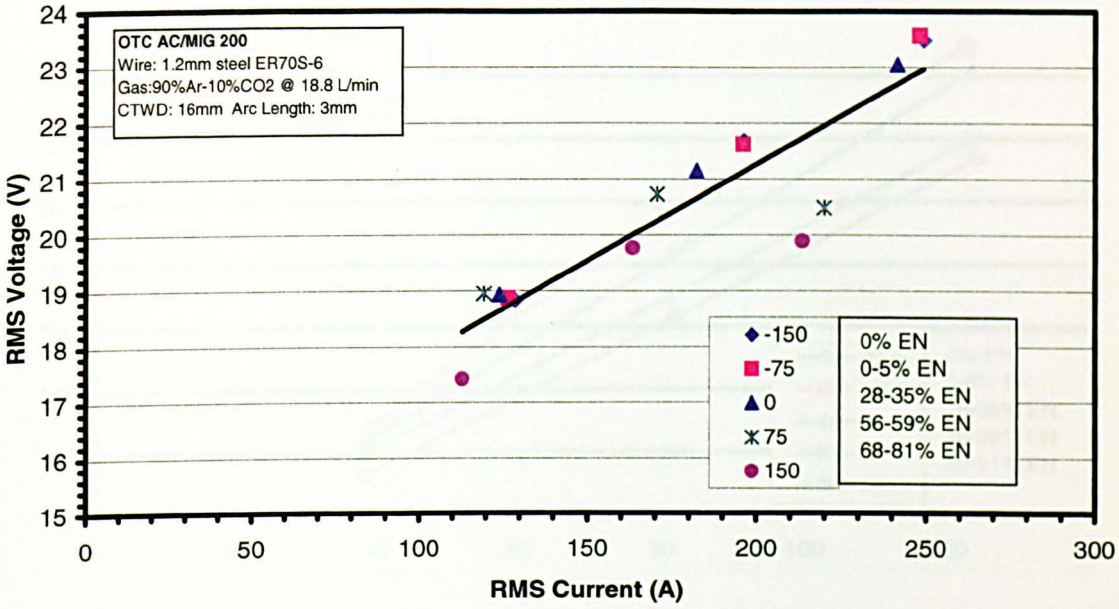

Figure A-1 RMS Voltage versus Current at 16 mm CTWD for Steel Using the AC/MIG 200 Power Supply

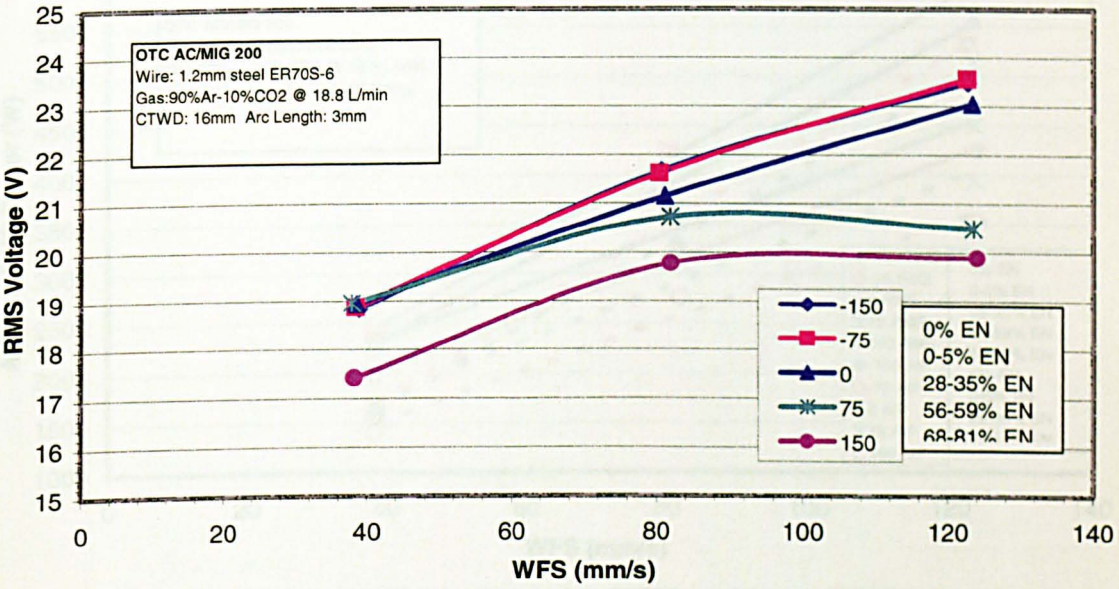

Figure A-2 RMS Voltage versus WFS at 16 mm CTWD for Steel Using the AC/MIG 200 Power Supply

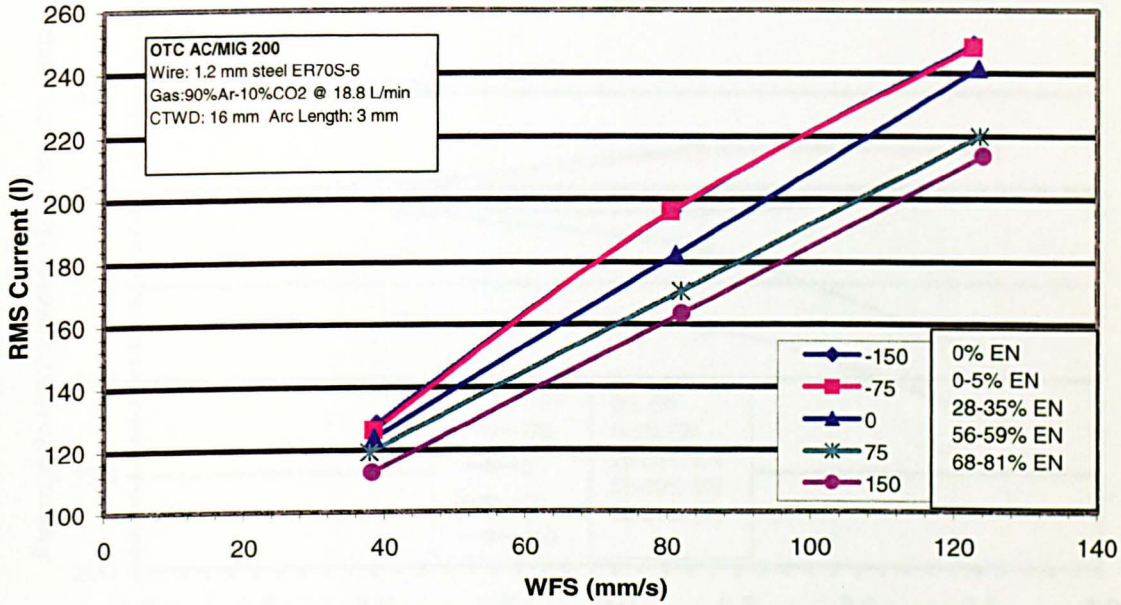

Figure A-3 RMS Current versus WFS at 16 mm CTWD for Steel Using the AC/MIG 200 Power Supply

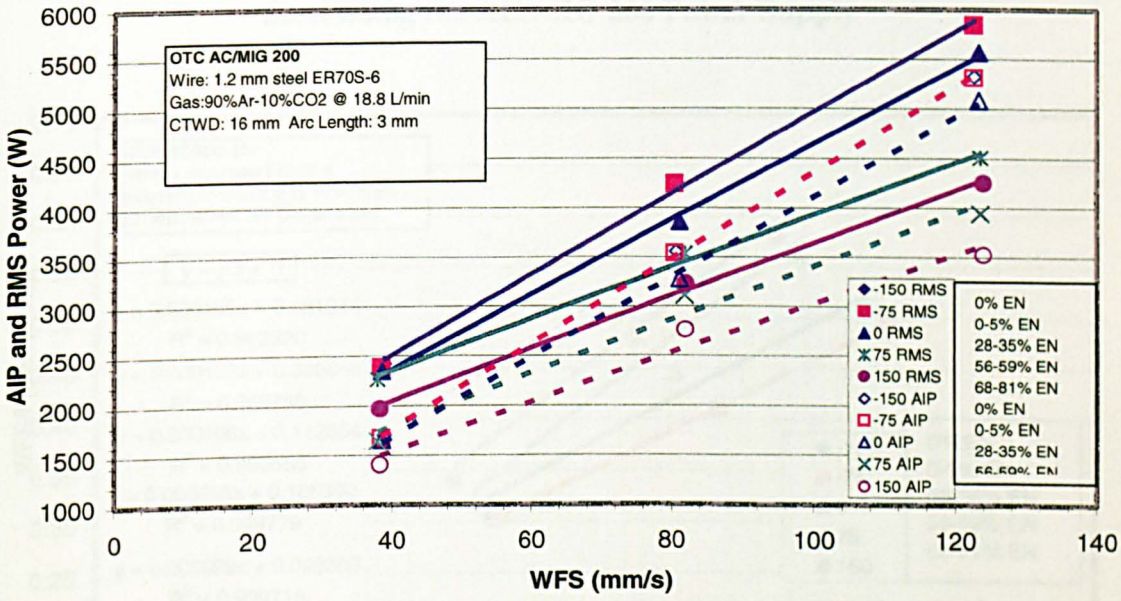

Figure A-4 AIP and RMS Power versus WFS at 16 mm CTWD for Steel Using the AC/MIG 200 Power Supply

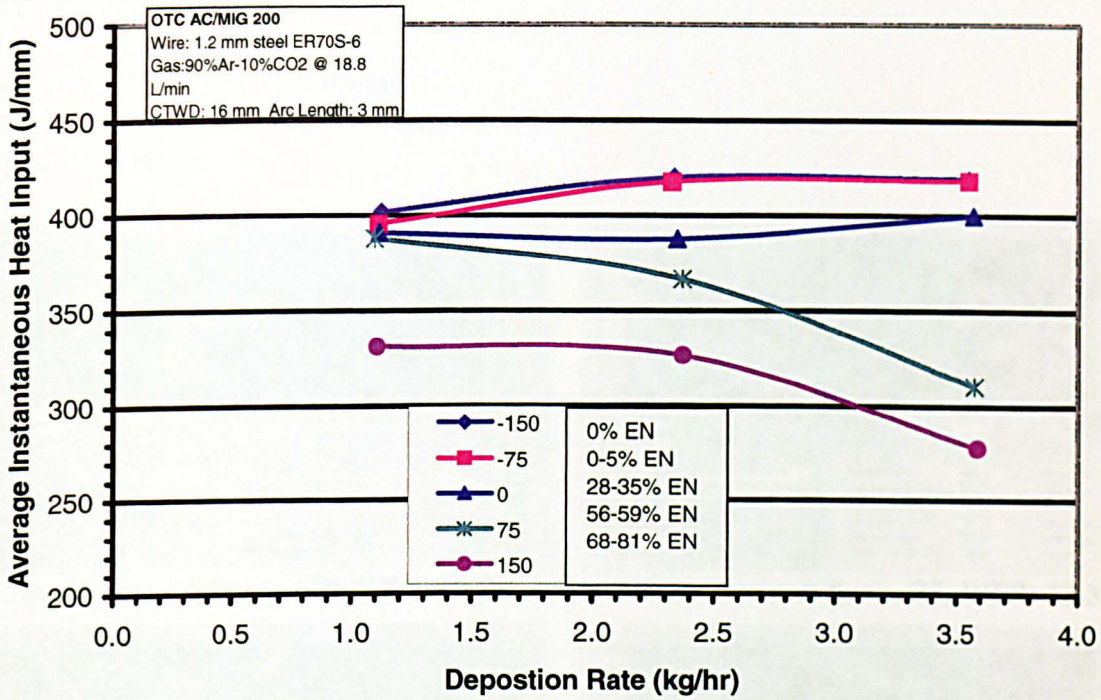

Figure A-5 Heat Input versus Deposition Rate at 16 mm CTWD for Steel Using the AC/MIG 200 Power Supply

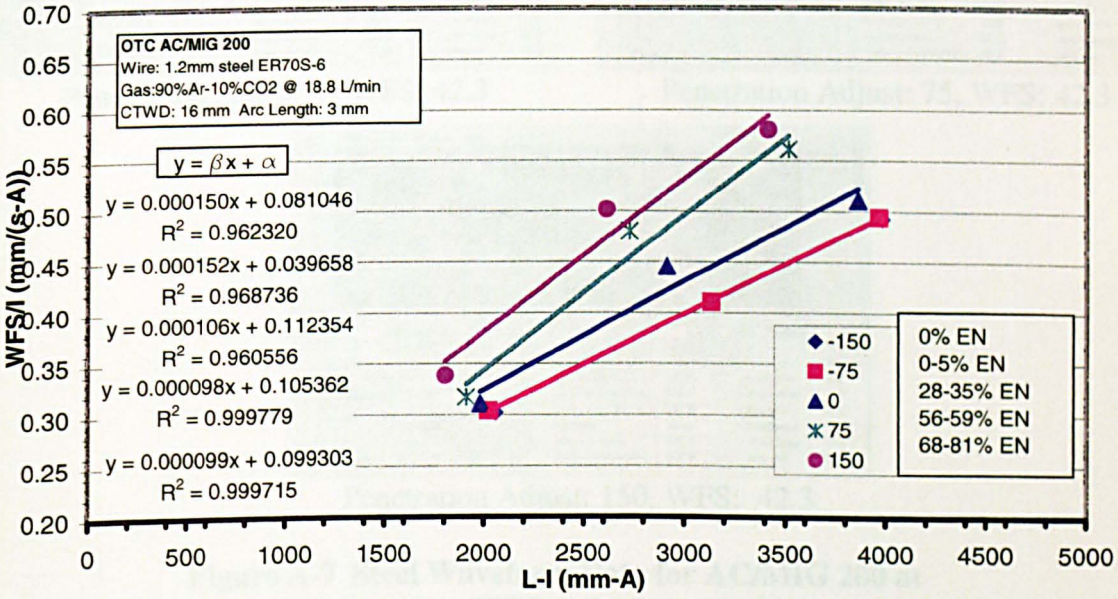

Figure A-6 Burnoff Rate versus Heating Factor for Steel Using the AC/MIG 200 Power Supply

OTC AC/MIG 200
Wire: 1.2 mm. Steel ER70S-6
Gas: 90Ar-10CO_2 at 18.8 l/min
CTWD: 16 mm, Arc Length: 3 mm
WFS: 42.3 mm/s

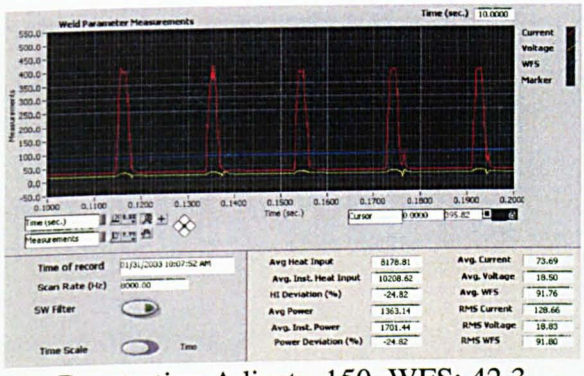

Penetration Adjust: -150, WFS: 42.3

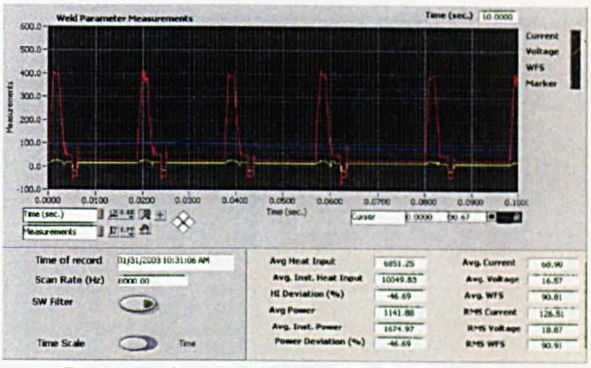

Penetration Adjust: -75, WFS: 42.3

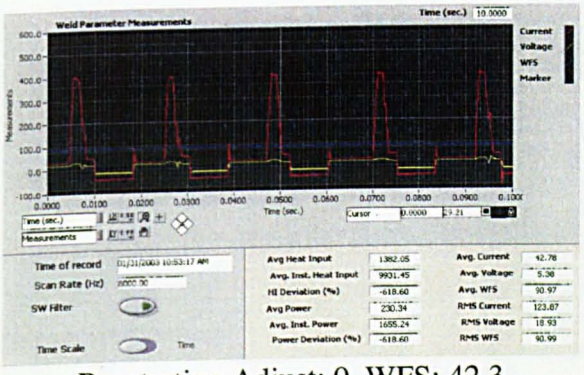

Penetration Adjust: 0, WFS: 42.3

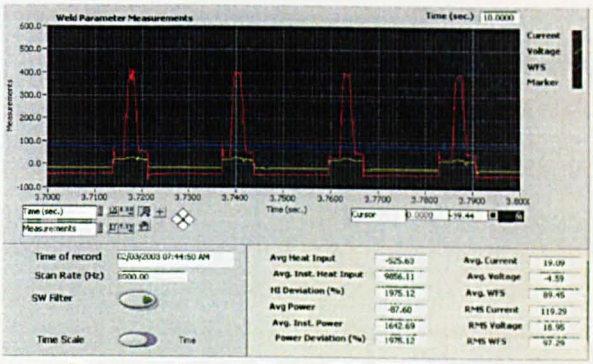

Penetration Adjust: 75, WFS: 42.3

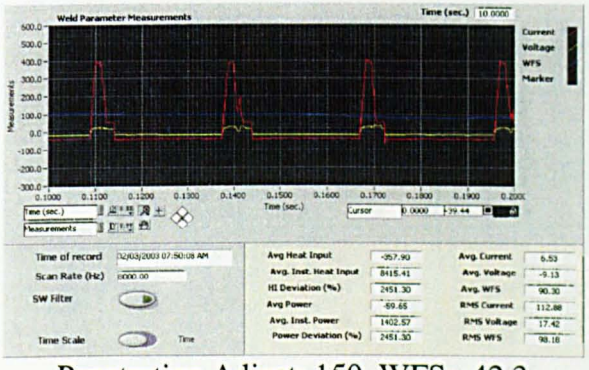

Penetration Adjust: 150, WFS: 42.3

Figure A-7 Steel Waveform Data for AC/MIG 200 at 42.3 mm/sec WFS and 16 mm CTWD

OTC AC/MIG 200
Wire: 1.2 mm Steel, ER70S-6
Gas: 90Ar-10CO_2 at 40 18.8 l/min
CTWD: 16 mm, Arc Length: 3 mm
WFS: 84.6 mm/s

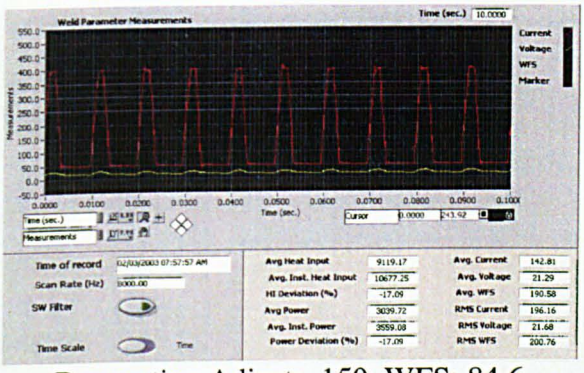

Penetration Adjust: -150, WFS: 84.6

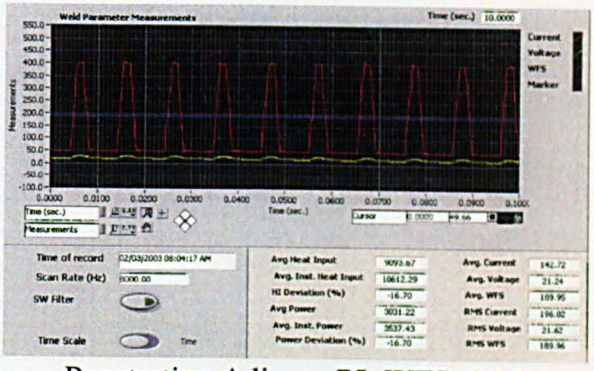

Penetration Adjust: -75, WFS: 84.6

Penetration Adjust: 0, WFS: 84.6

Penetration Adjust: 75, WFS: 84.6

Penetration Adjust: 150, WFS: 84.6

Figure A-8 Steel Waveform Data for AC/MIG 200 at 84.6 mm/sec WFS and 16 mm CTWD

OTC AC/MIG 200
Wire: 1.2 mm Steel ER70S-6
Gas: 90Ar-10CO_2 at 18.8 l/min
CTWD: 16 mm, Arc Length: 3 mm
WFS: 127 mm/s

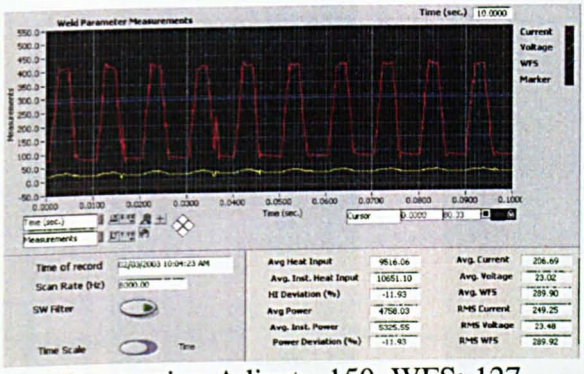

Penetration Adjust: -150, WFS: 127

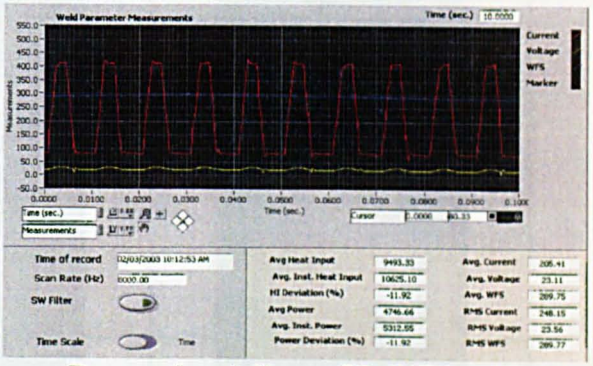

Penetration Adjust: -75, WFS: 127

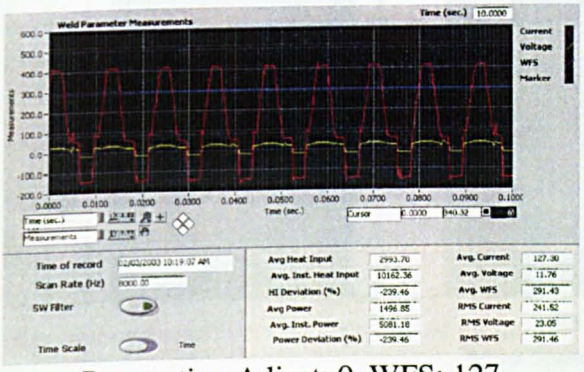

Penetration Adjust: 0, WFS: 127

Penetration Adjust: 75, WFS: 127

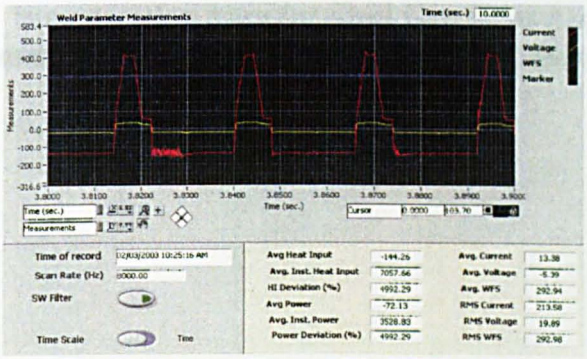

Penetration Adjust: 150, WFS: 127

Figure A-9 Steel Waveform Data for AC/MIG 200 at 127 mm/sec WFS and 16 mm CTWD

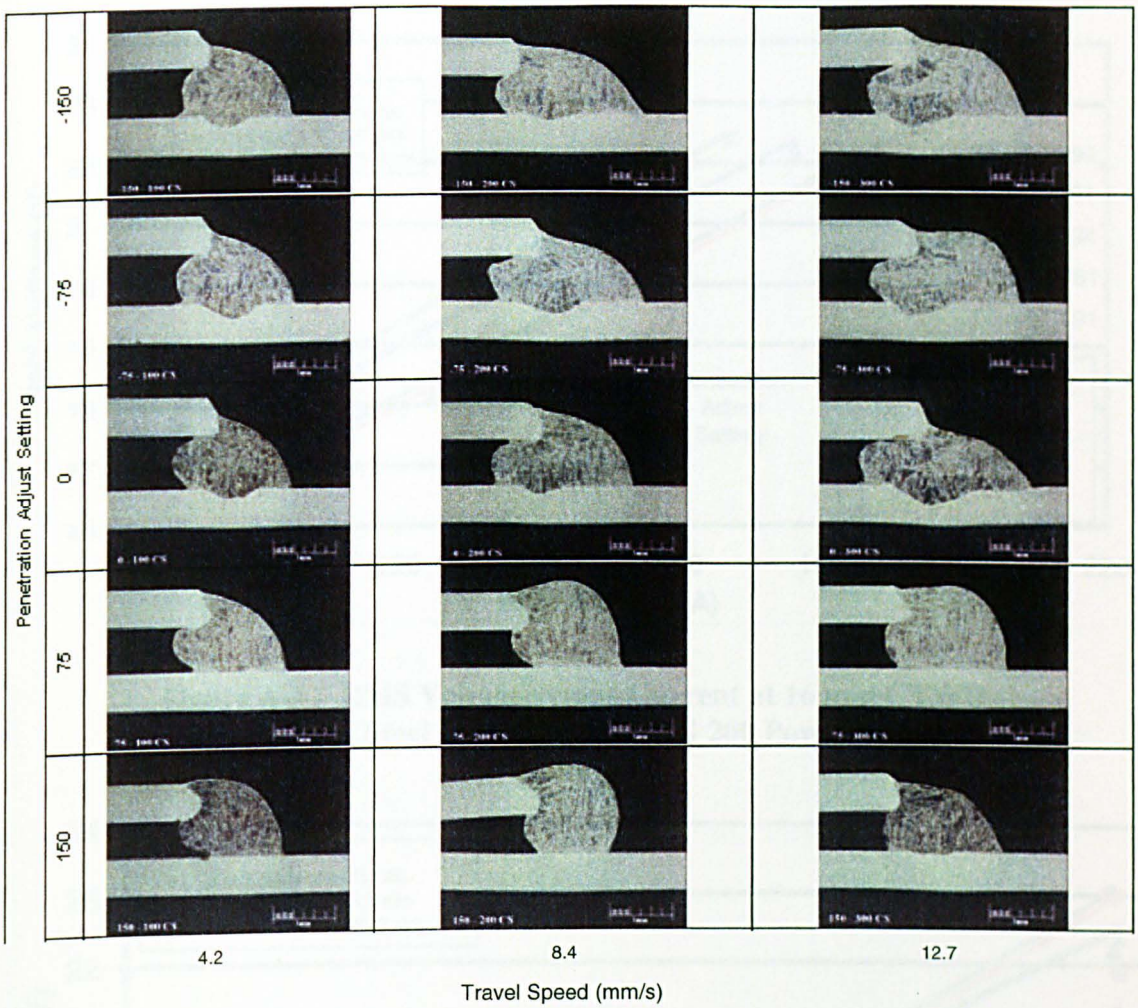

Figure A-10 Macrosection Map for Steel Lap Joint Application at 16 mm CTWD Using AC/MIG 200 Power Supply

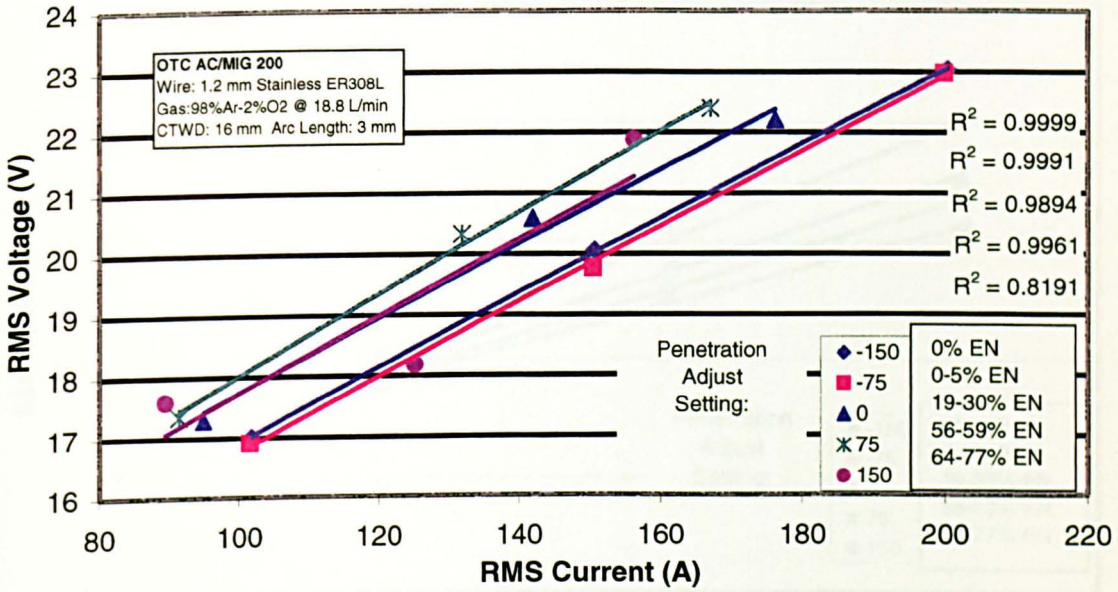

Figure A-11 RMS Voltage versus Current at 16 mm CTWD for Stainless Steel Using the AC/MIG 200 Power Supply

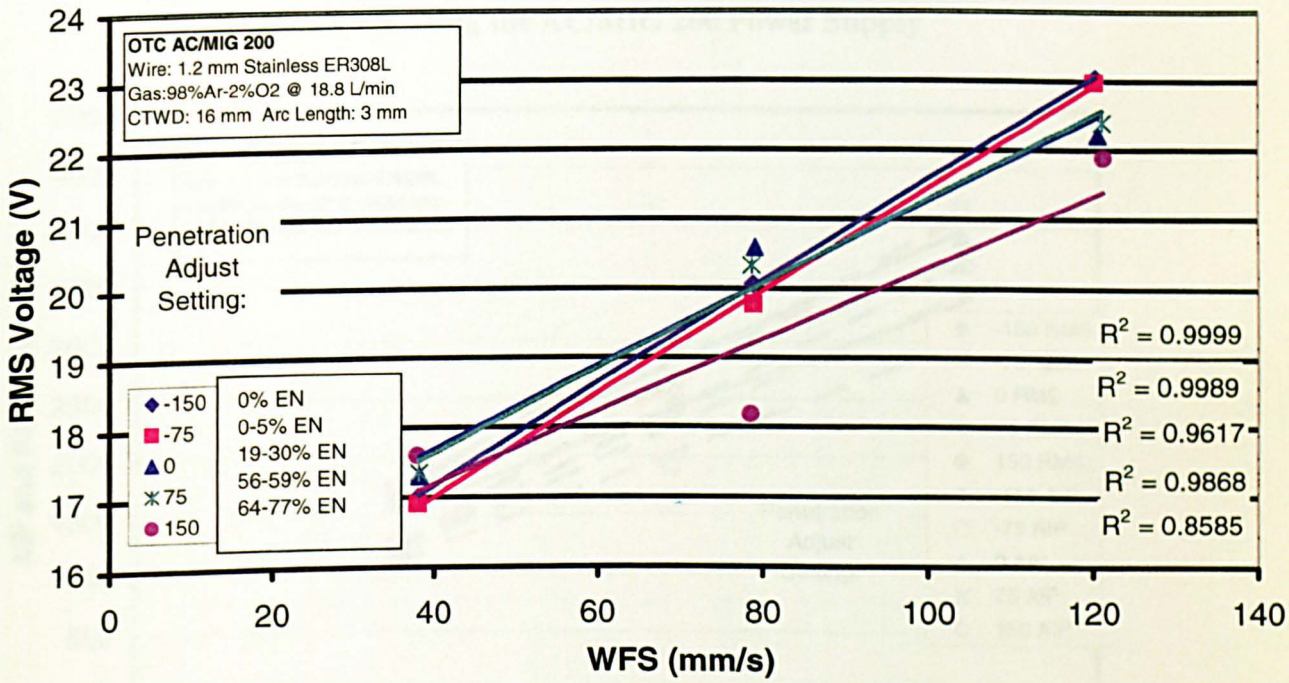

Figure A-12 RMS Voltage versus WFS at 16 mm CTWD for Stainless Steel Using the AC/MIG 200 Power Supply

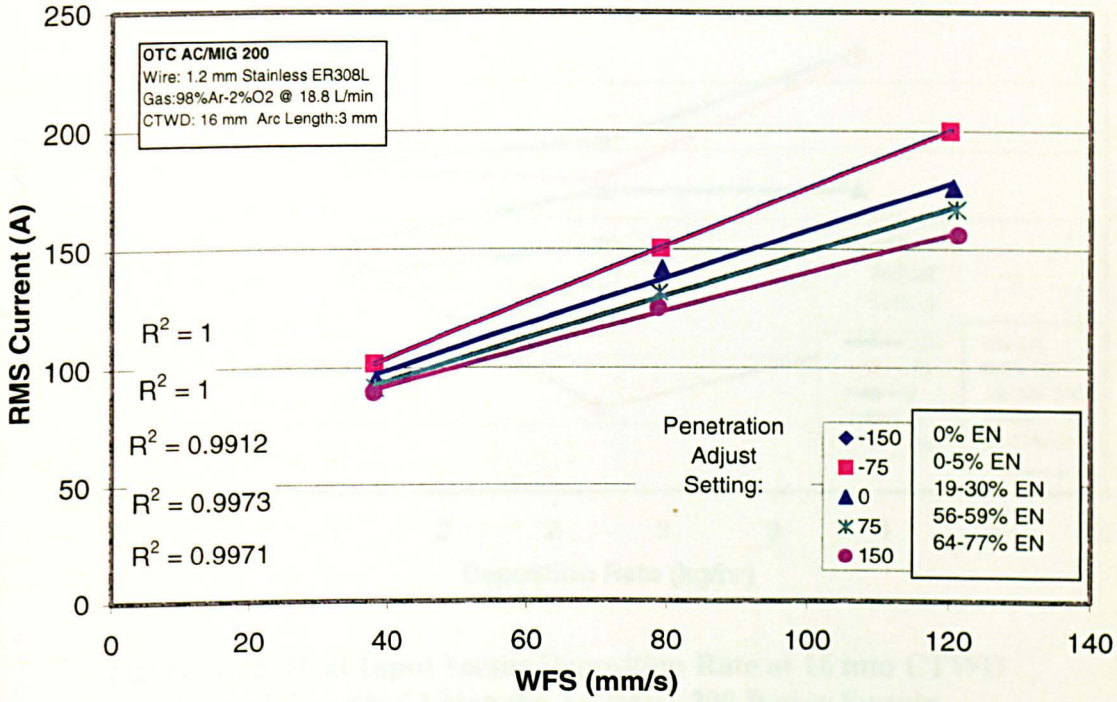

Figure A-13 RMS Current versus WFS at 16 mm CTWD for Stainless Steel Using the AC/MIG 200 Power Supply

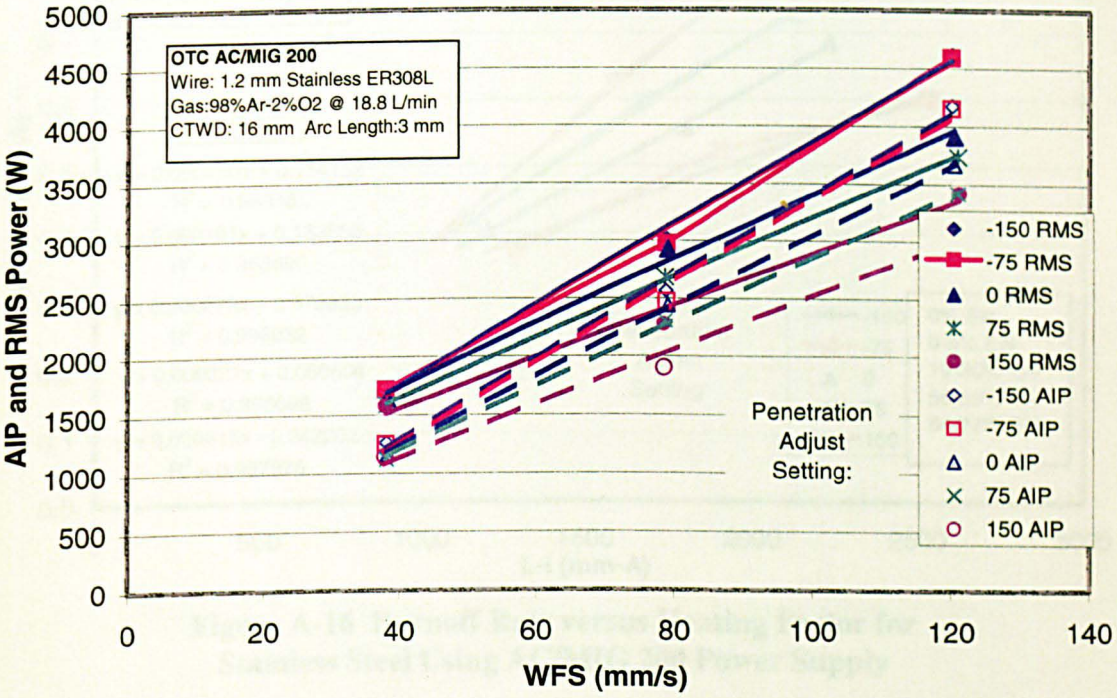

Figure A-14 – AIP and RMS Power versus WFS at 16 mm CTWD for Stainless Steel Using the AC/MIG 200 Power Supply

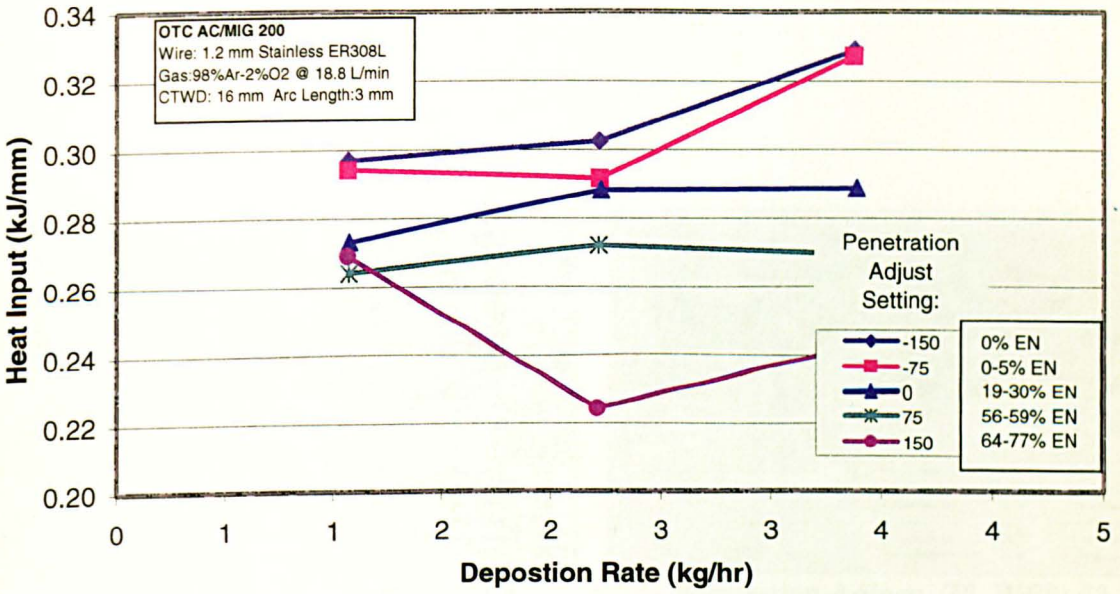

Figure A-15 Heat Input versus Deposition Rate at 16 mm CTWD for Stainless Steel Using the AC/MIG 200 Power Supply

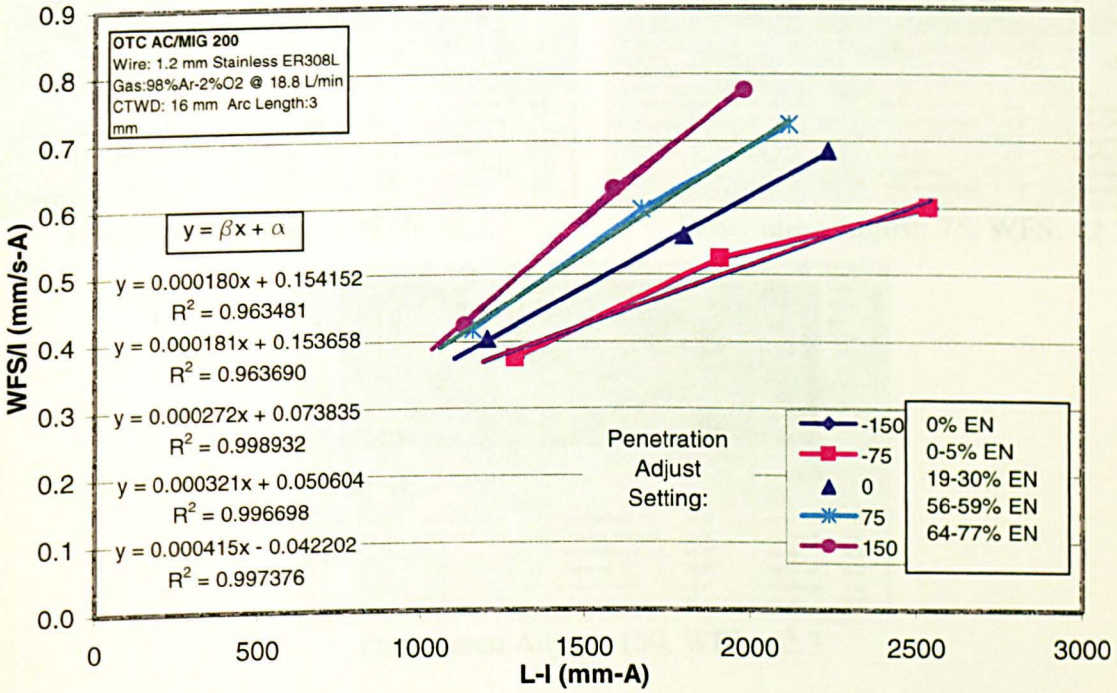

Figure A-16 Burnoff Rate versus Heating Factor for Stainless Steel Using AC/MIG 200 Power Supply

OTC AC/MIG 200
Wire: 1.2 mm Stainless ER308L
Gas: 98Ar-2O_2 at 18.8 l/min
CTWD: 16 mm, Arc Length: 3 mm
WFS: 42.3 mm/s

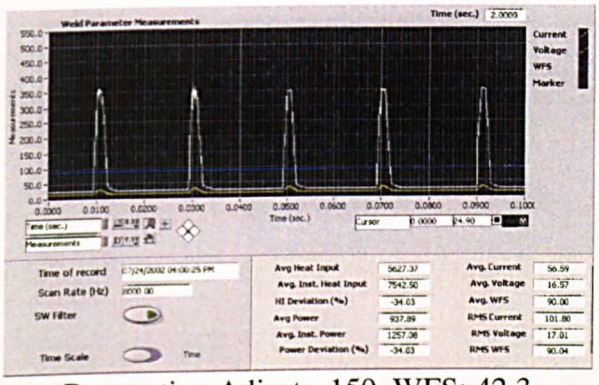

Penetration Adjust: -150, WFS: 42.3

Penetration Adjust: -75, WFS: 42.3

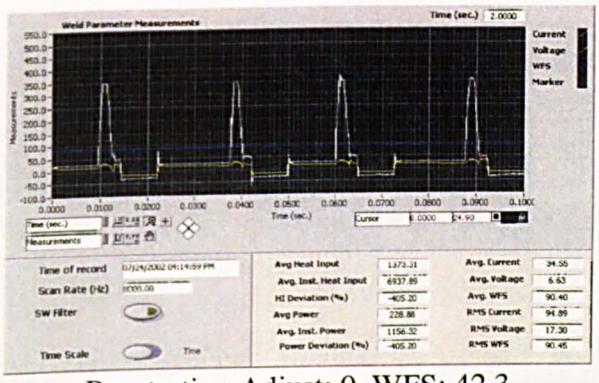

Penetration Adjust: 0, WFS: 42.3

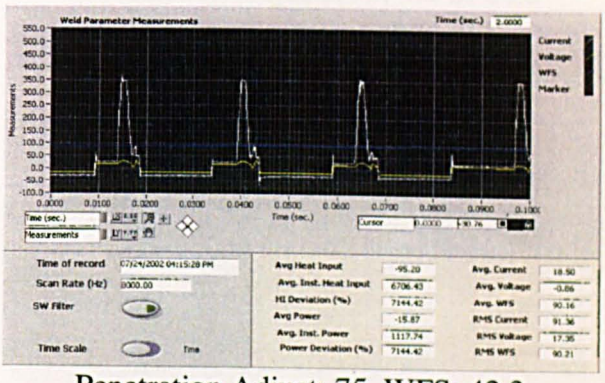

Penetration Adjust: 75, WFS: 42.3

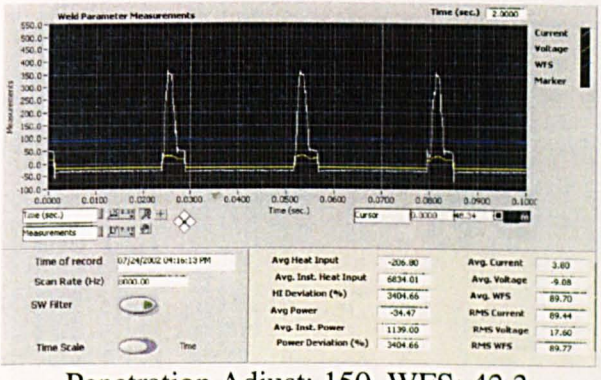

Penetration Adjust: 150, WFS: 42.3

Figure A-17 Stainless Steel Waveform Data for AC/MIG 200 at 42.3 mm/sec WFS and 16 mm CTWD

OTC AC/MIG 200
Wire: 1.2 mm Stainless ER308L
Gas: 98Ar-2O_2 at 18.8 l/min
CTWD: 16 mm, Arc Length: 3 mm
WFS: 84.6 mm/s

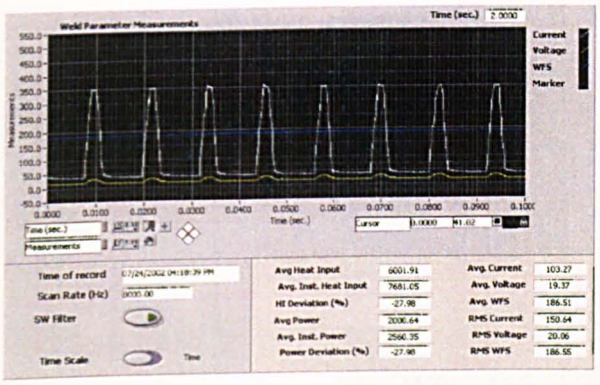

Penetration Adjust: -150, WFS: 84.6

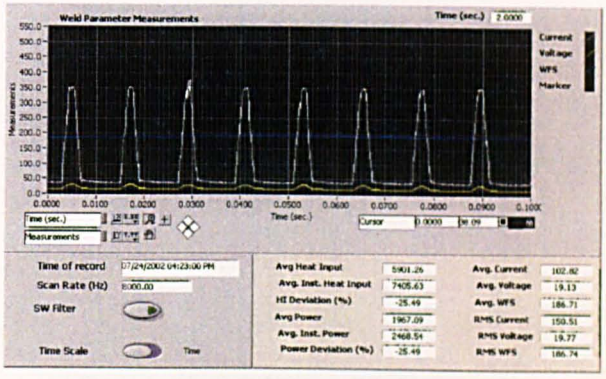

Penetration Adjust: -75, WFS: 84.6

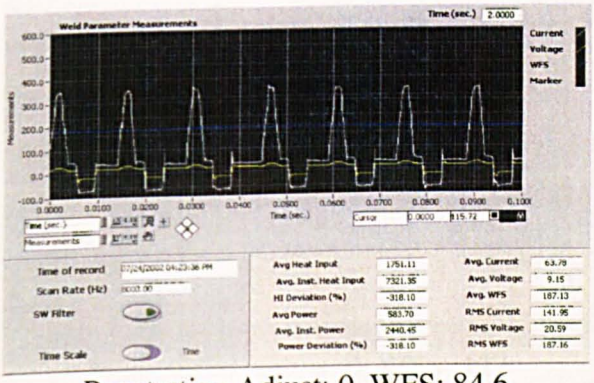

Penetration Adjust: 0, WFS: 84.6

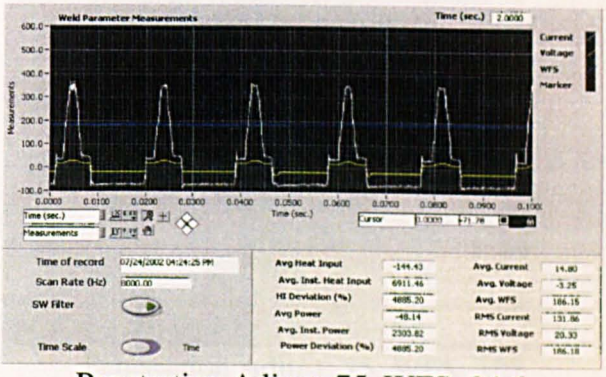

Penetration Adjust: 75, WFS: 84.6

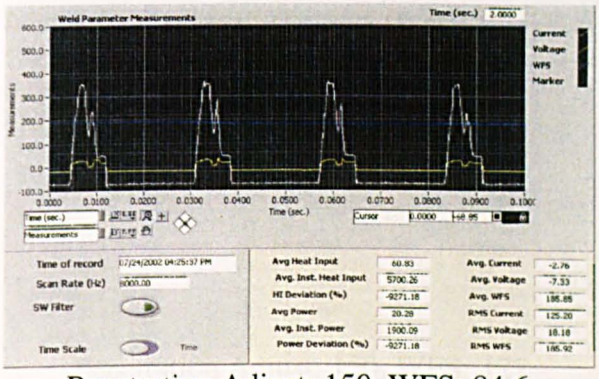

Penetration Adjust: 150, WFS: 84.6

Figure A-18 Stainless Steel Waveform Data for AC/MIG 200 at 84.6 mm/sec WFS and 16 mm CTWD

OTC AC/MIG 200
Wire: 1.2 mm Stainless ER308L
Gas: 98Ar-2O_2 at 18.8 l/min
CTWD: 16 mm, Arc Length: 3 mm
WFS: 127 mm/s

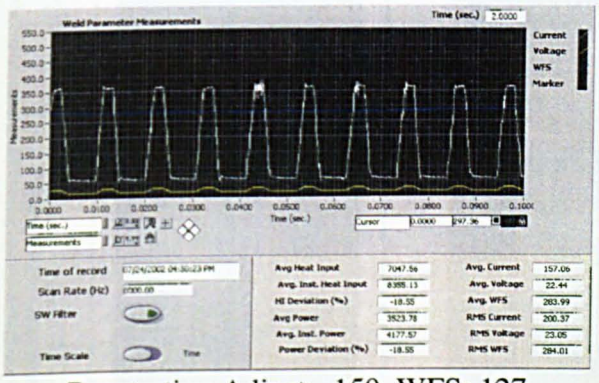

Penetration Adjust: -150, WFS: 127

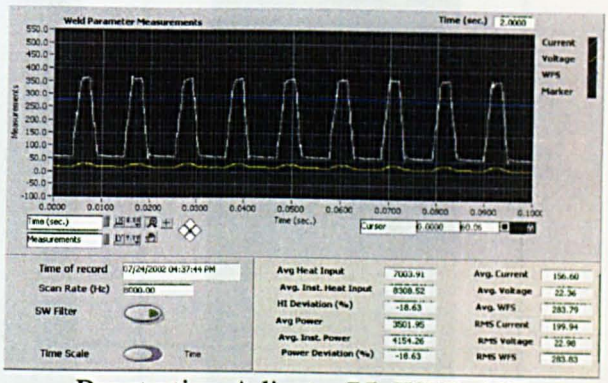

Penetration Adjust: -75, WFS: 127

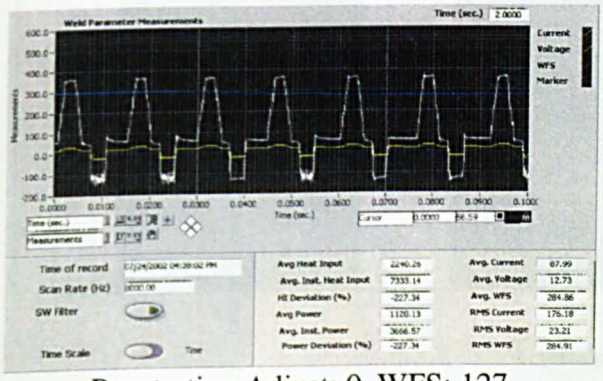

Penetration Adjust: 0, WFS: 127

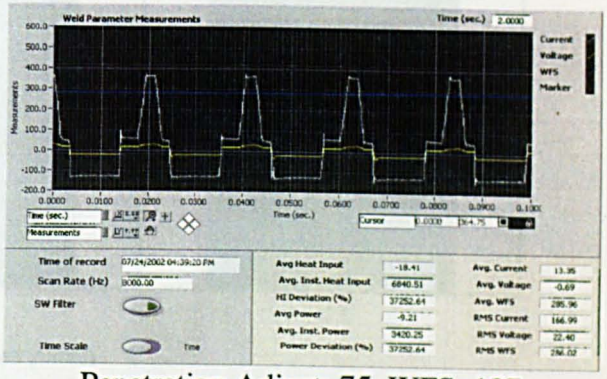

Penetration Adjust: 75, WFS: 127

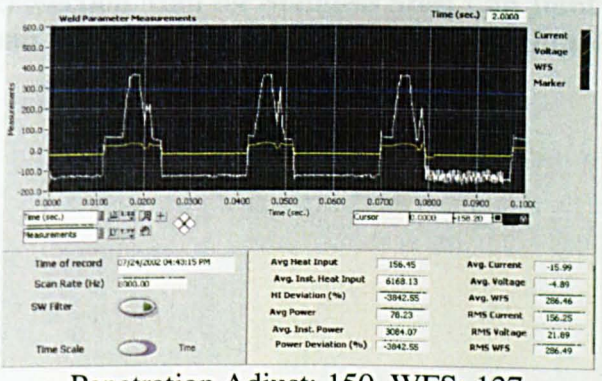

Penetration Adjust: 150, WFS: 127

Figure A-19 Stainless Steel Waveform Data for AC/MIG 200 at 127 mm/sec WFS and 16 mm CTWD

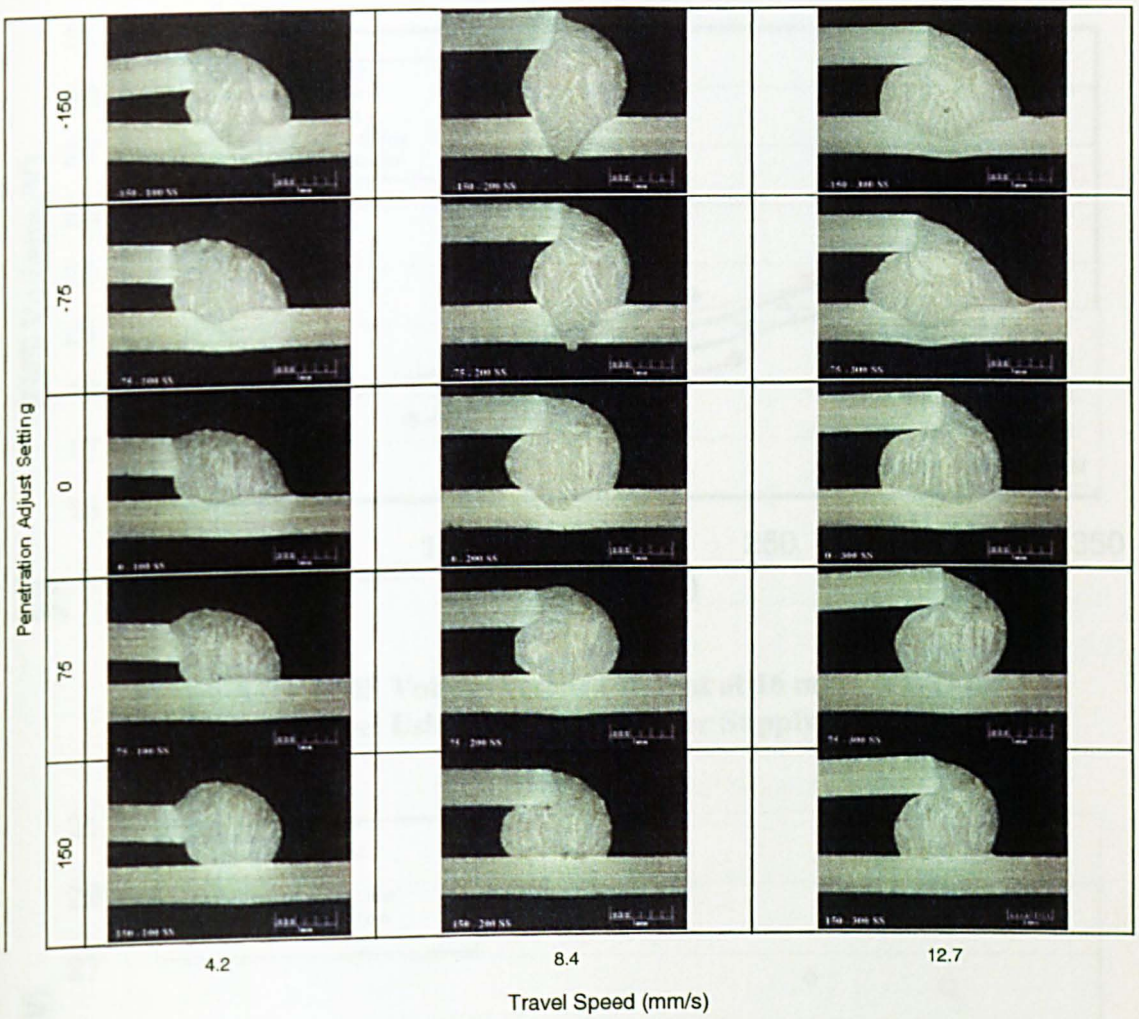

Figure A-20 Macrosection Map for Stainless Steel Lap Joint Application at 16 mm CTWD Using AC/MIG 200 Power Supply

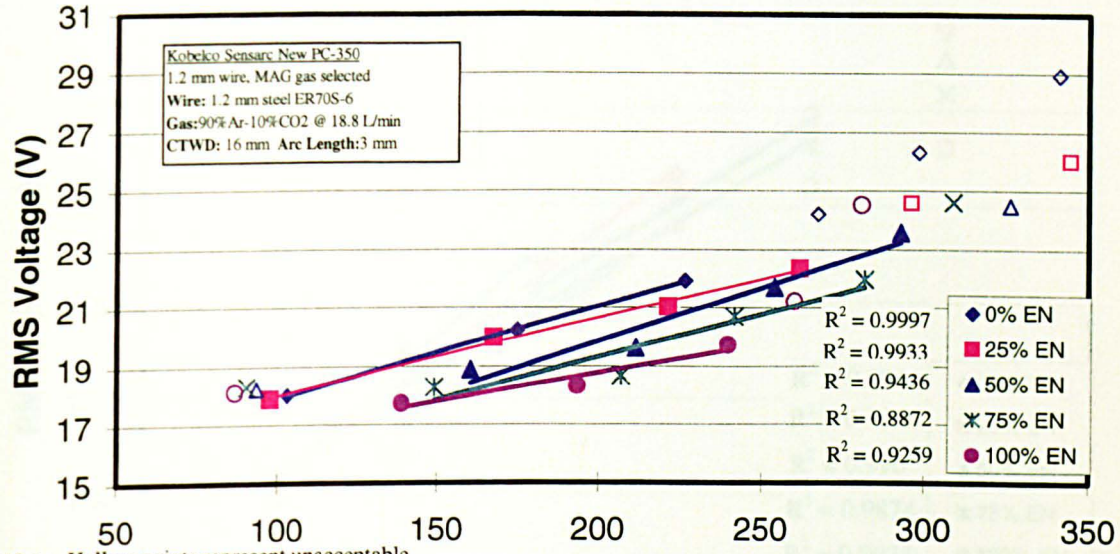

Note: Hollow points represent unacceptable welds.

Figure A-21 RMS Voltage versus Current at 16 mm CTWD for Steel Using the PC350 Power Supply

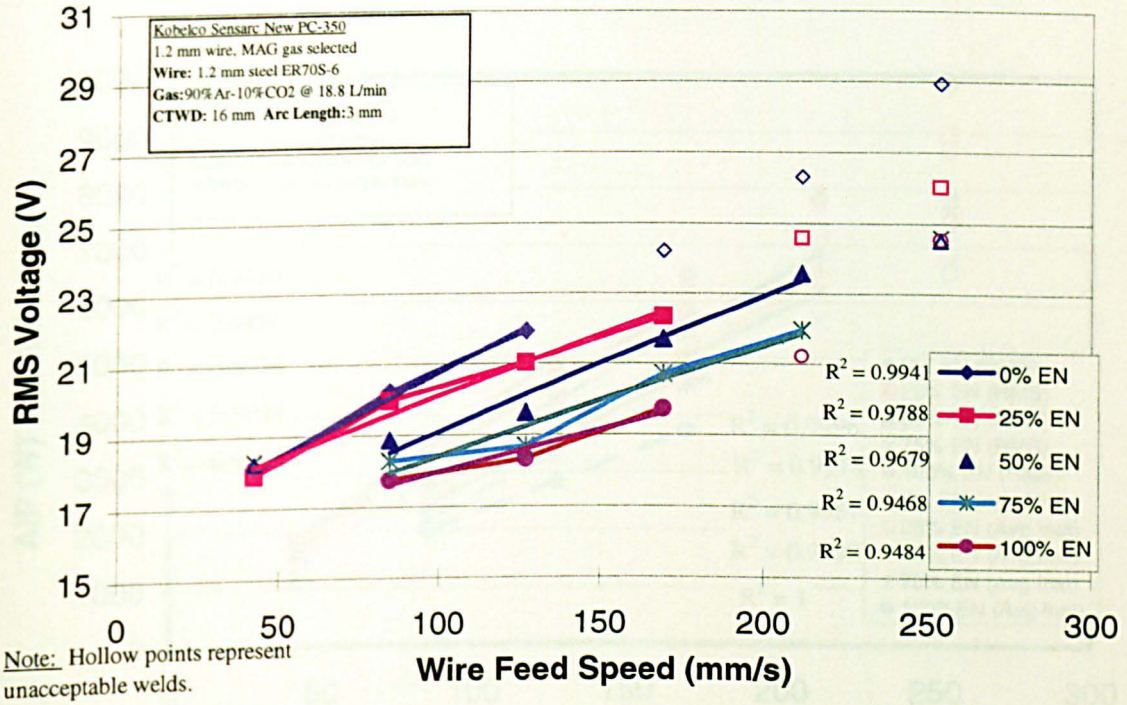

Note: Hollow points represent unacceptable welds.

Figure A-22 RMS Voltage versus WFS at 16 mm CTWD for Steel Using the PC350 Power Supply

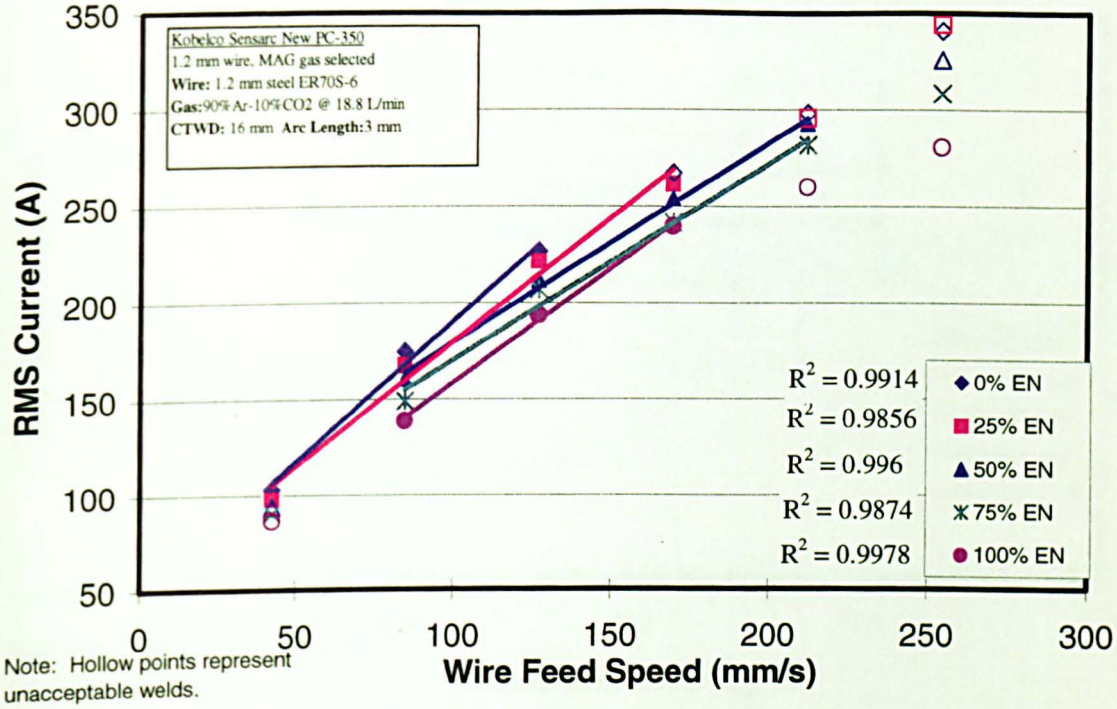

Figure A-23 RMS Current versus WFS at 16 mm CTWD for Steel Using the PC350 Power Supply

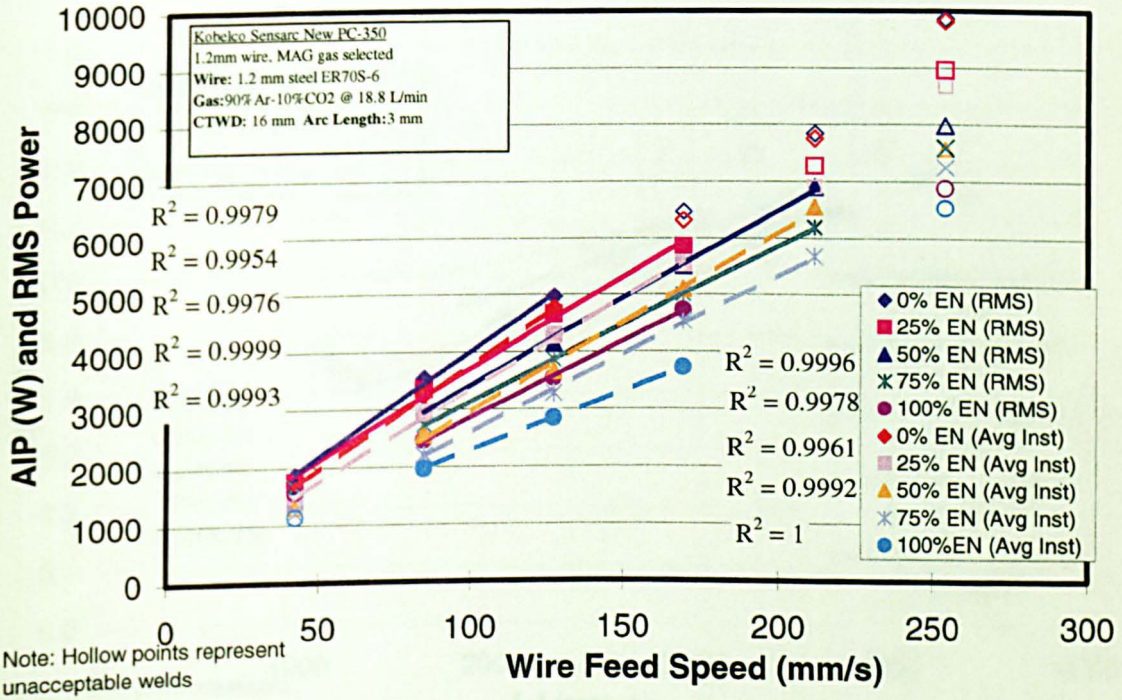

Figure A-24 AIP and RMS Power versus WFS at 16 mm CTWD for Steel Using the PC350 Power Supply

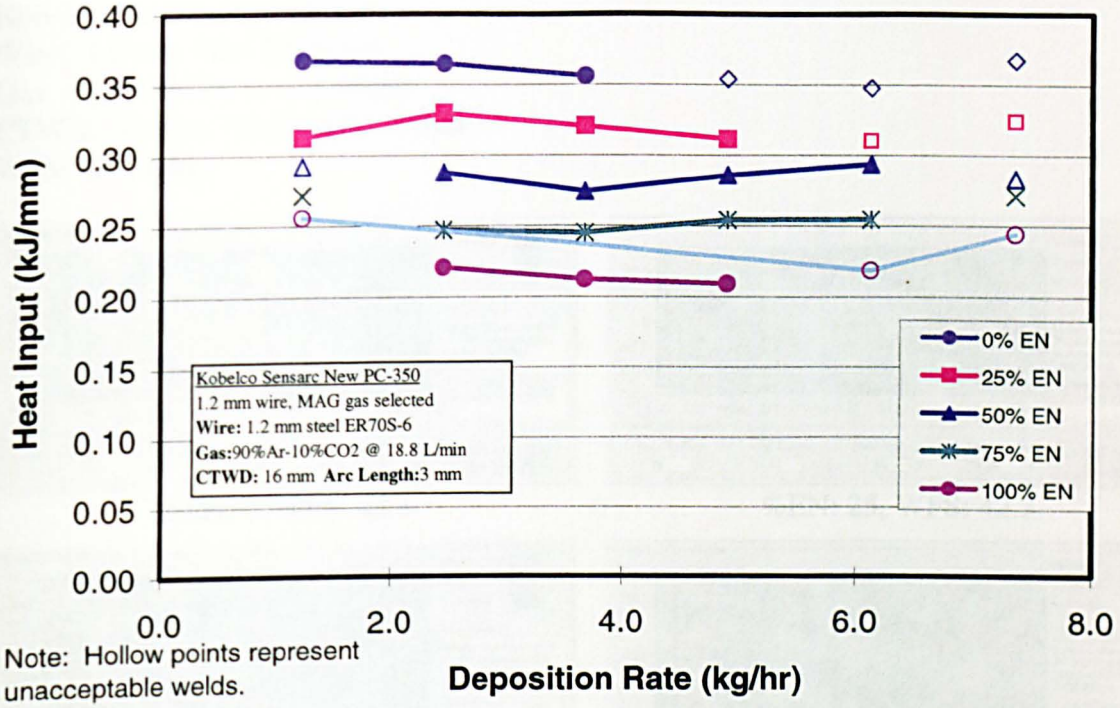

Figure A-25 Heat Input versus Deposition Rate at 16 mm CTWD for Steel Using the PC350 Power Supply

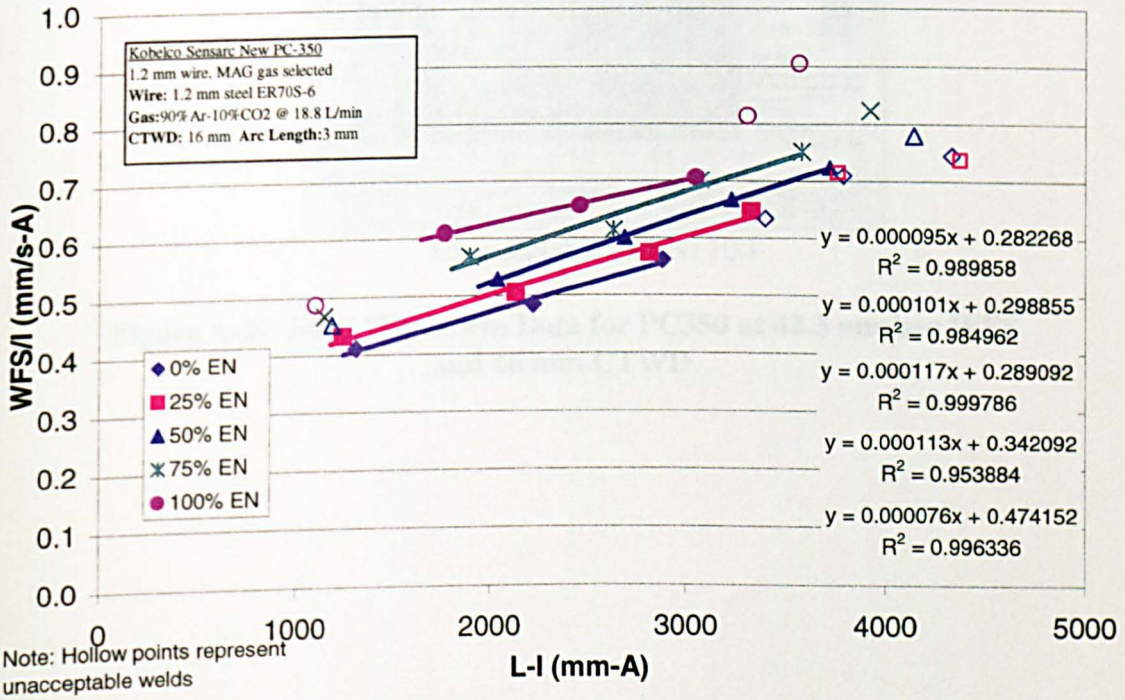

Figure A-26 Burnoff Rate versus Heating Factor for Steel Using PC350 Power Supply

Kobelco Sensarc New PC350
Wire: 1.2 mm Steel ER70S-6
Gas: 90Ar-10CO_2 at 18.8 l/min
CTWD: 16 mm, Arc Length: 3 mm
WFS: 42.3 mm/s

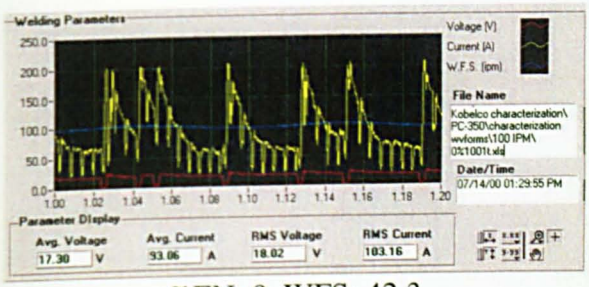

%EN: 0, WFS: 42.3

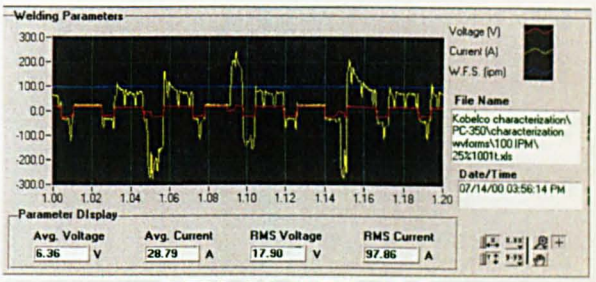

%EN: 25, WFS: 42.3

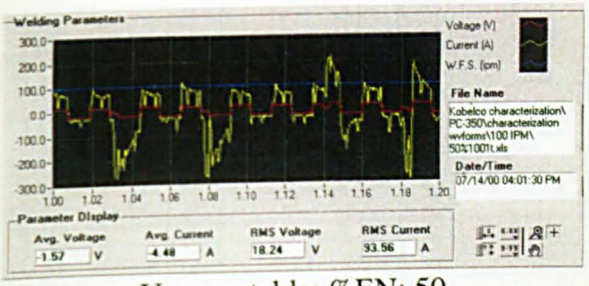

Unacceptable; %EN: 50

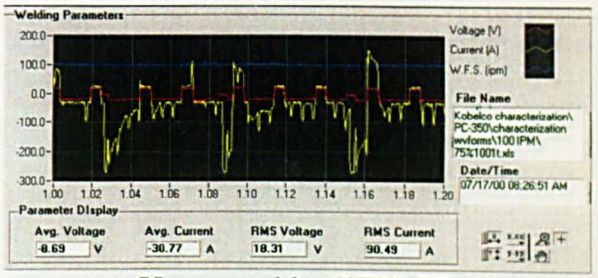

Unacceptable; %EN: 75

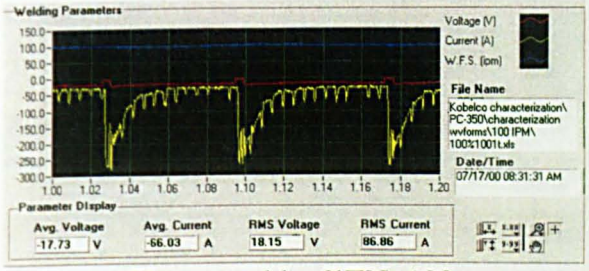

Unacceptable: %EN: 100

Figure A-27 Steel Waveform Data for PC350 at 42.3 mm/sec WFS and 16 mm CTWD

Kobelco Sensarc New PC350
Wire: 1.2 mm Steel ER70S-6
Gas: 90Ar-10CO_2 at 18.8 l/min
CTWD: 16 mm, Arc Length: 3 mm
WFS: 84.6 mm/s

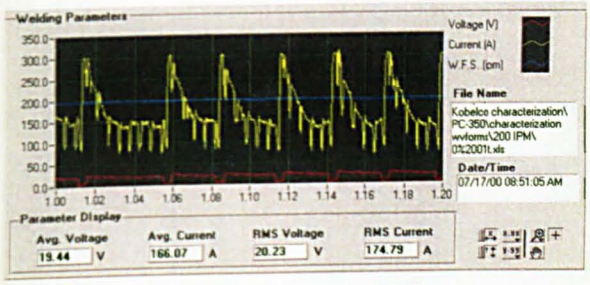

%EN: 0, WFS: 84.6

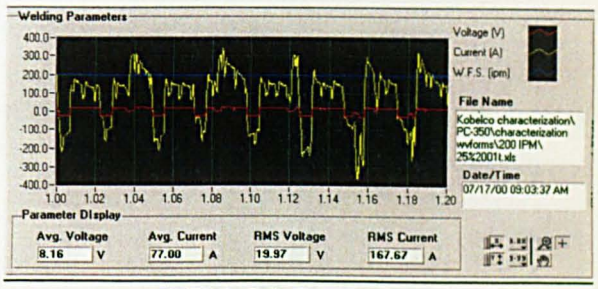

%EN: 25, WFS: 84.6

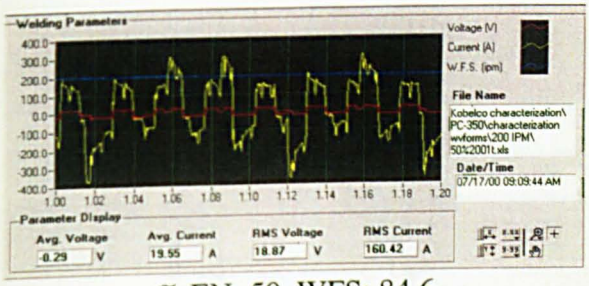

% EN: 50, WFS: 84.6

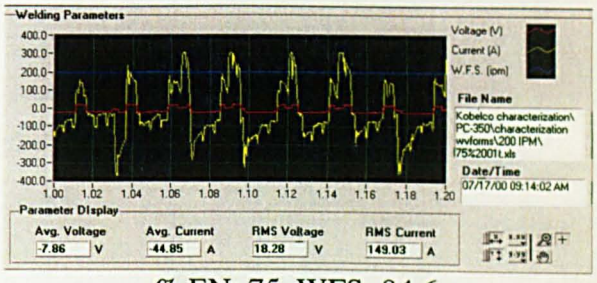

% EN: 75, WFS: 84.6

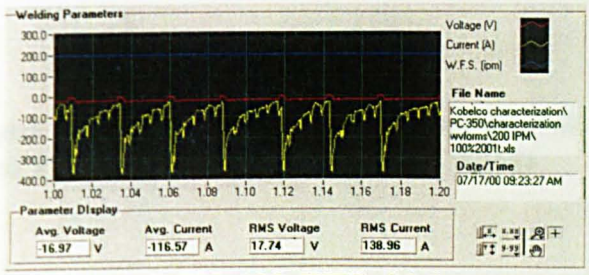

% EN: 100, WFS: 84.6

Figure A-28 Steel Waveform Data for PC350 at 84.6 mm/sec WFS and 16 mm CTWD

Kobelco Sensarc New PC350
Wire: 1.2 mm Steel ER70S-6
Gas: 90Ar-10CO_2 at 18.8 l/min
CTWD: 16 mm, Arc Length: 3 mm
WFS: 127 mm/s

%EN: 0, WFS: 127

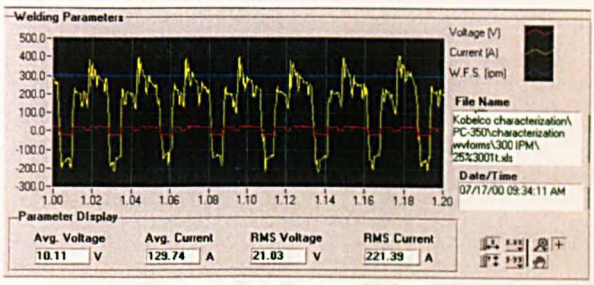

%EN: 25, WFS: 127

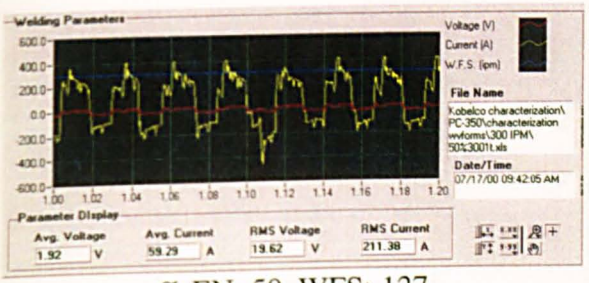

% EN: 50, WFS: 127

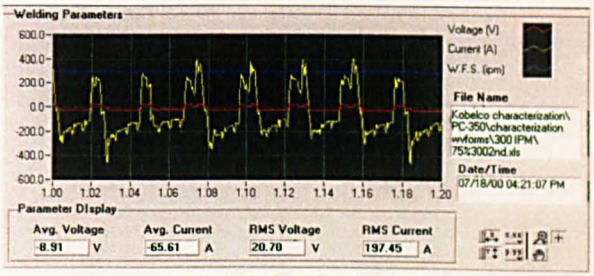

%EN: 75, WFS: 127

% EN: 100, WFS: 127

Figure A-29 Steel Waveform Data for PC350 at 127 mm/sec WFS and 16 mm CTWD

Kobelco Sensarc New PC350
Wire: 1.2 mm Steel ER70S-6
Gas: 90Ar-10CO_2 at 18.8 l/min
CTWD: 16 mm, Arc Length: 3 mm
WFS: 169.2 mm/s

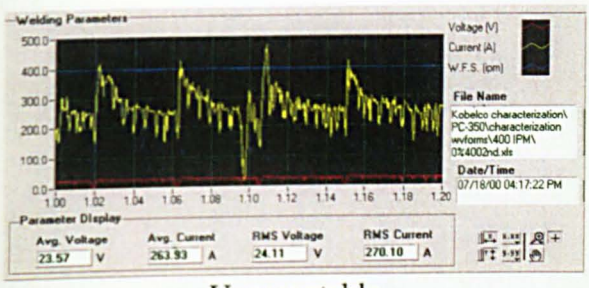

Unacceptable

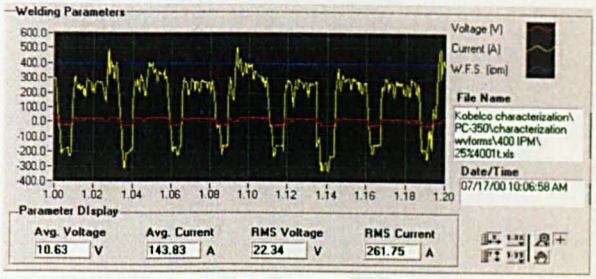

%EN: 25, WFS: 169.2

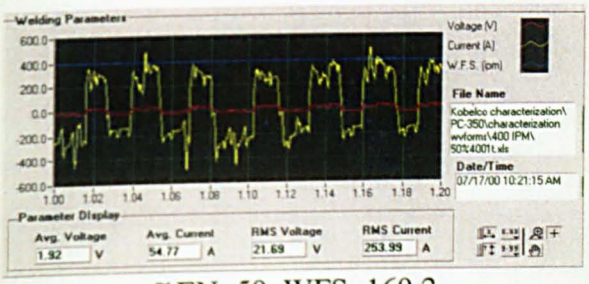

%EN: 50, WFS: 169.2

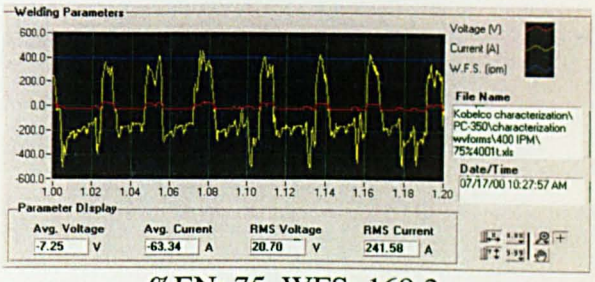

%EN: 75, WFS: 169.2

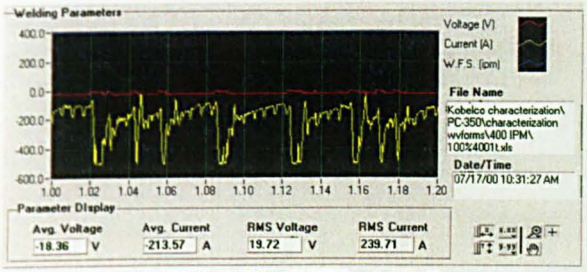

%EN: 100, WFS: 169.2

Figure A-30 Steel Waveform Data for PC350 at 169.2 mm/sec WFS and 16 mm CTWD

Kobelco Sensarc New PC350
Wire: 1.2 mm Steel ER70S-6
Gas: 90Ar-10CO_2 at 18.8 l/min
CTWD: 16 mm Arc Length: 3 mm
WFS: 211.5 mm/s

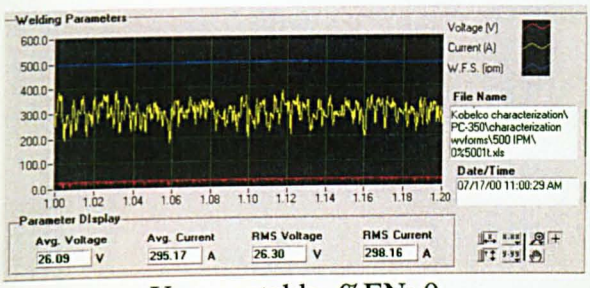

Unacceptable, %EN: 0

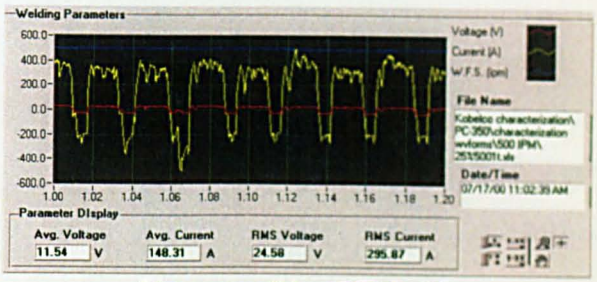

Unacceptable, %EN: 25

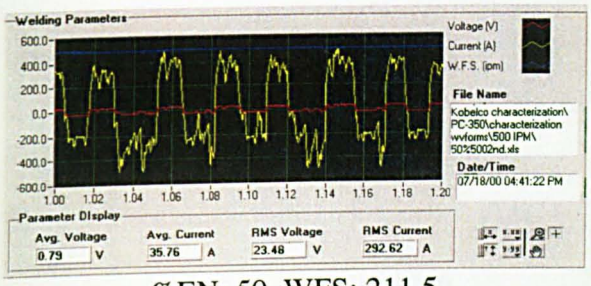

%EN: 50, WFS: 211.5

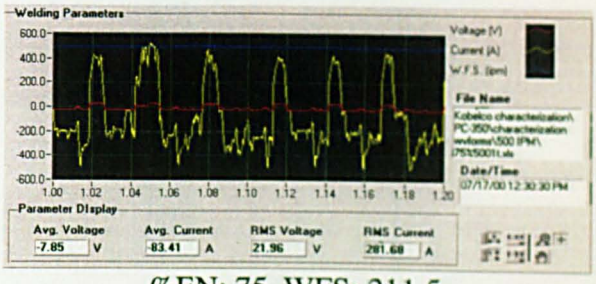

%EN: 75, WFS: 211.5

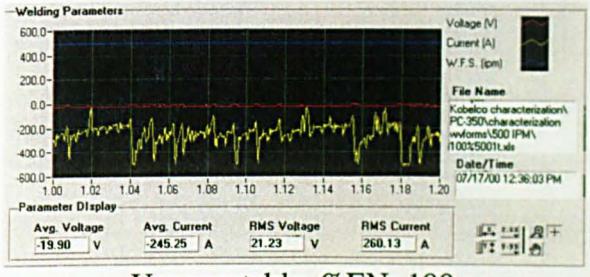

Unacceptable, %EN: 100

Figure A-31 Steel Waveform Data for PC350 at 211.5 mm/sec WFS and 16 mm CTWD

Kobelco Sensarc New PC
Wire: 1.2mm Steel ER70S-6
Gas: 90Ar-10CO_2 at 18.8 l/min
CTWD: 16 mm, Arc Length: 3mm
WFS: 253.8 mm/s

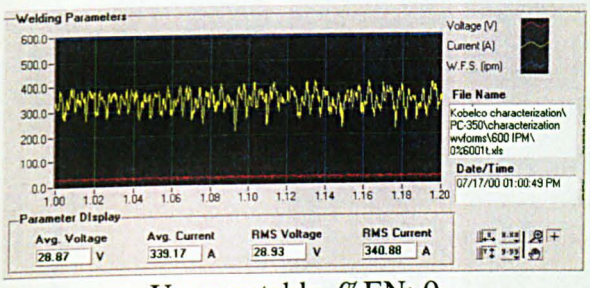

Unacceptable, %EN: 0

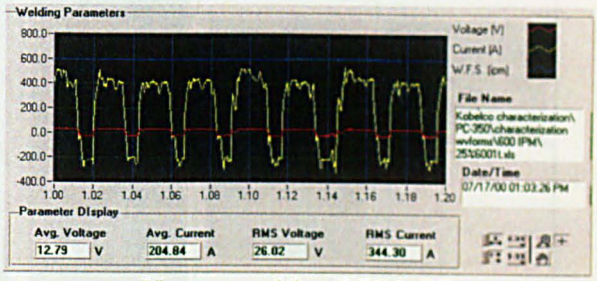

Unacceptable, %EN: 25

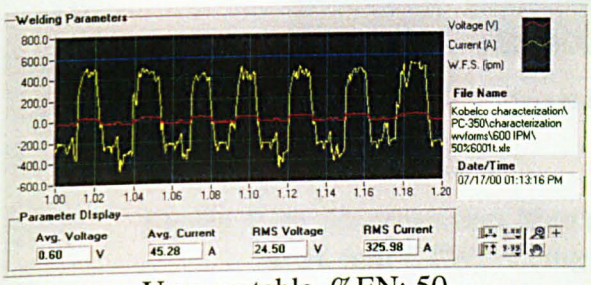

Unacceptable, %EN: 50

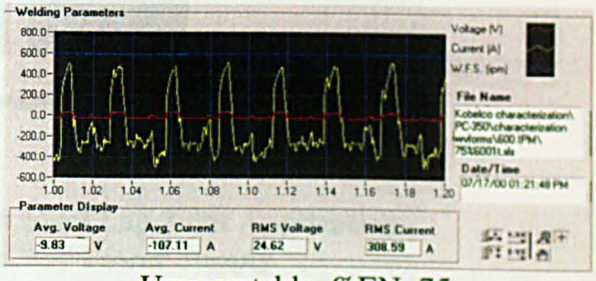

Unacceptable, %EN: 75

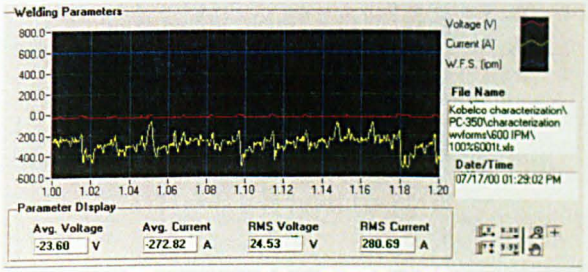

Unacceptable, %EN: 100

Figure A-32 Steel Waveform Data for PC350 at 253.8 mm/sec WFS and 16 mm CTWD

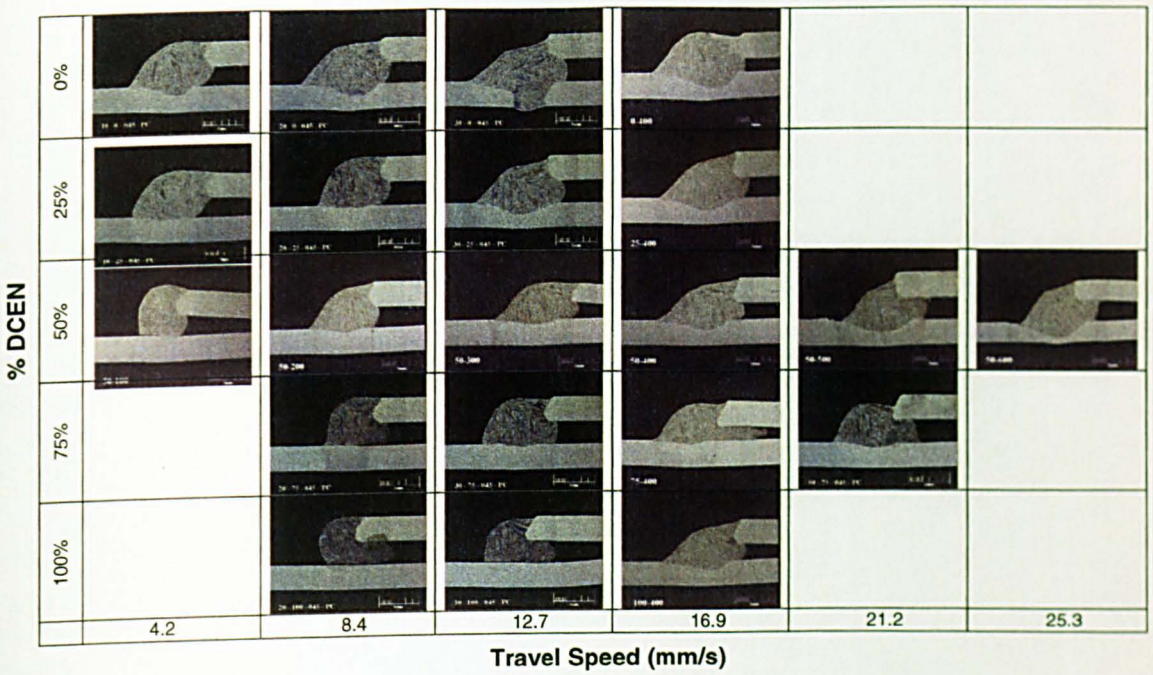

Figure A-33 Macrosection Map for Steel Lap Joint Application at 16 mm CTWD Using PC350 Power Supply

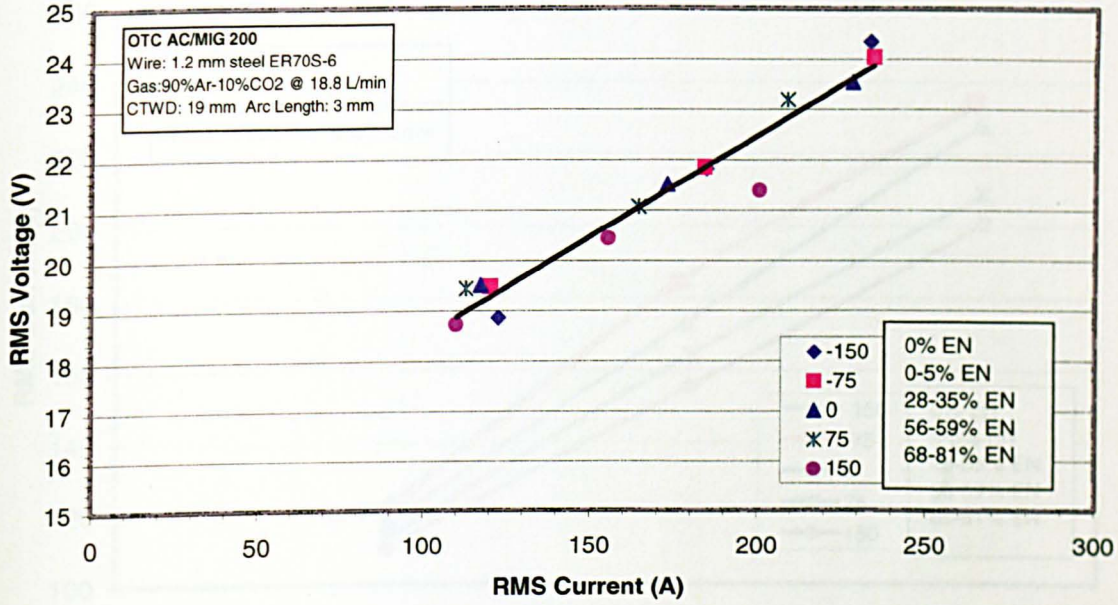

Figure B-1 RMS Voltage versus Current at 19 mm CTWD for Steel Using the AC/MIG 200 Power Supply

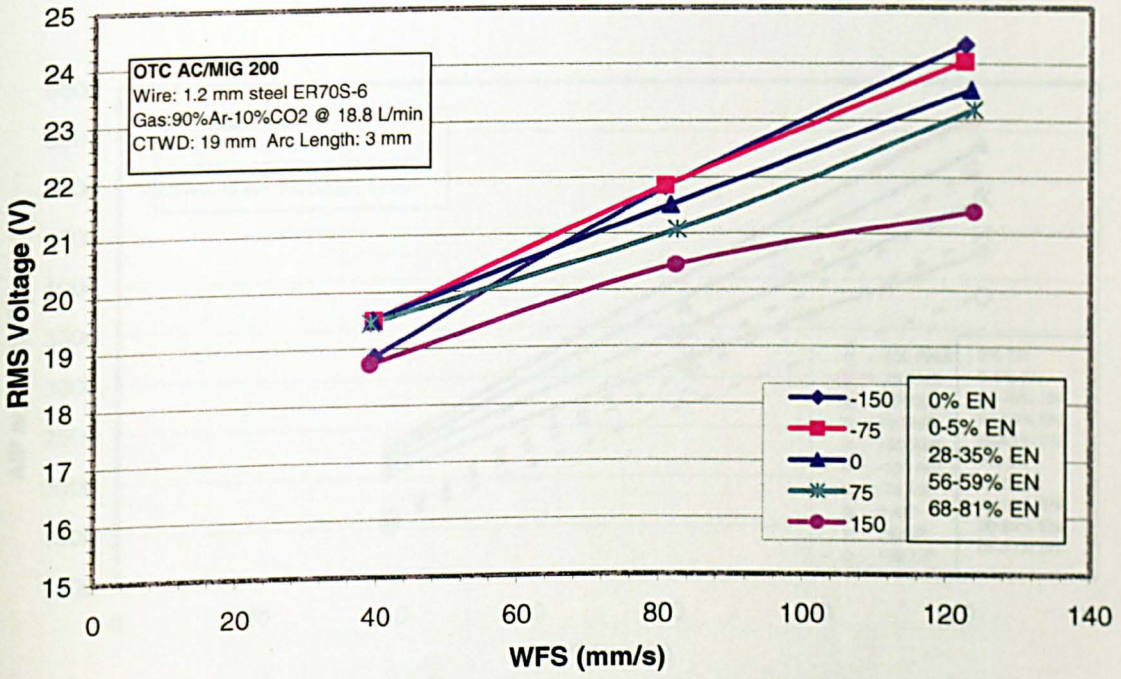

Figure B-2 RMS Voltage versus WFS at 19 mm CTWD for Steel Using the AC/MIG 200 Power Supply

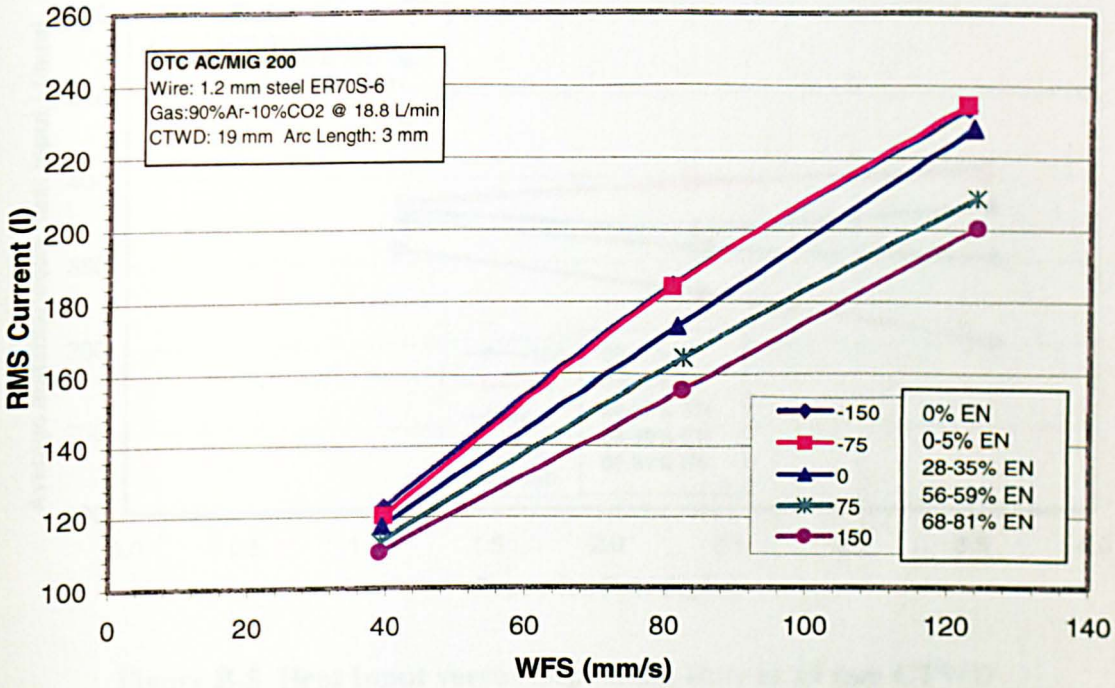

Figure B-3 RMS Current versus WFS at 19 mm CTWD for Steel Using the AC/MIG 200 Power Supply

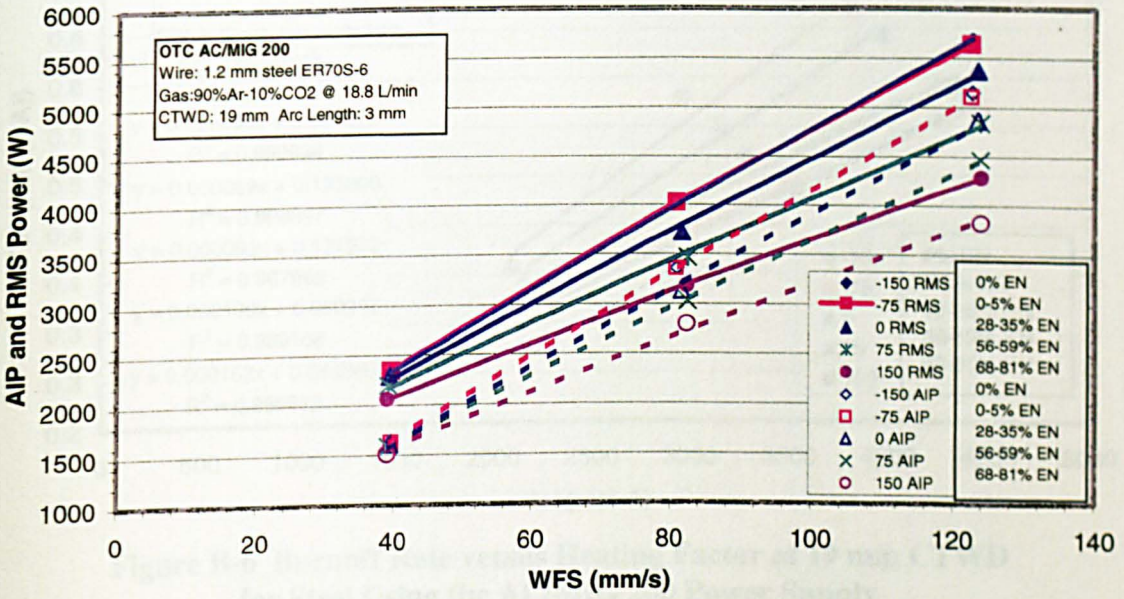

Figure B-4 AIP and RMS Power versus WFS at 19 mm CTWD for Steel Using the AC/MIG 200 Power Supply

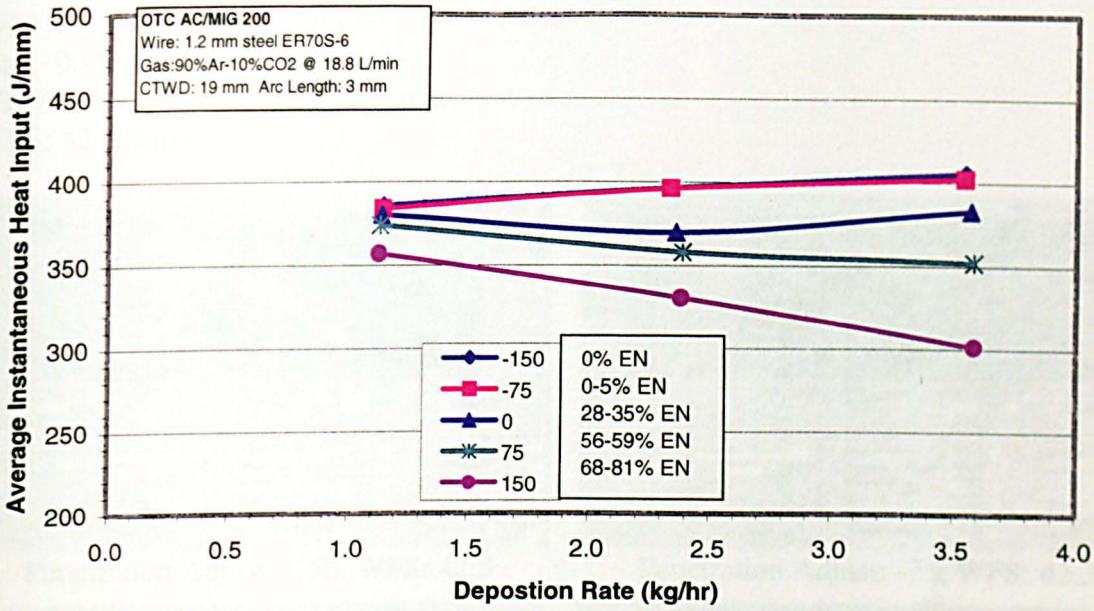

Figure B-5 Heat Input versus Deposition Rate at 19 mm CTWD for Steel Using the AC/MIG 200 Power Supply

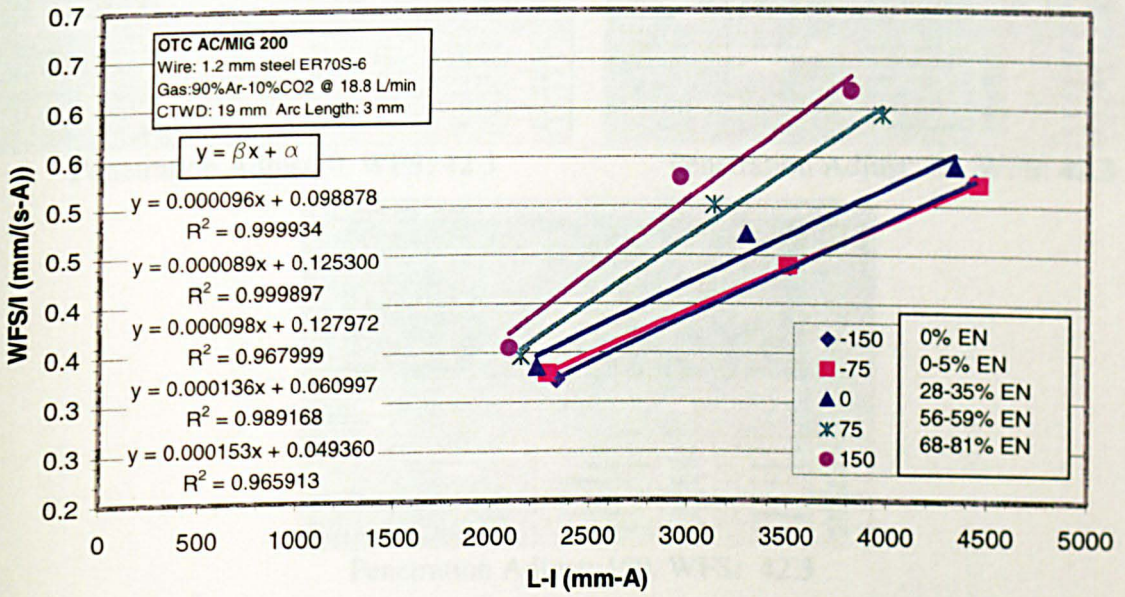

Figure B-6 Burnoff Rate versus Heating Factor at 19 mm CTWD for Steel Using the AC/MIG 200 Power Supply

OTC AC/MIG 200
Wire: 1.2 mm. Steel ER70S-6
Gas: 90Ar-10CO_2 at 18.8 l/min
CTWD: 19 mm, Arc Length: 3 mm
WFS: 42.3 mm/s

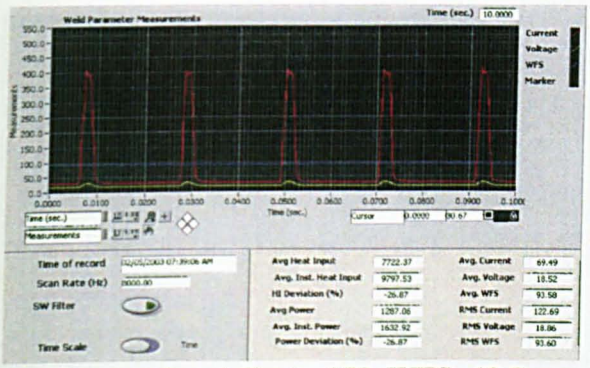

Penetration Adjust: -150, WFS: 42.3

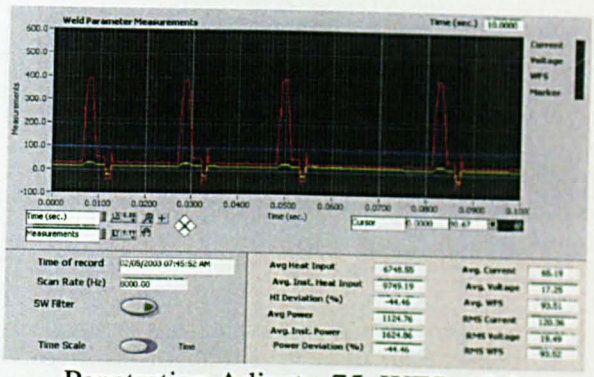

Penetration Adjust: -75, WFS: 42.3

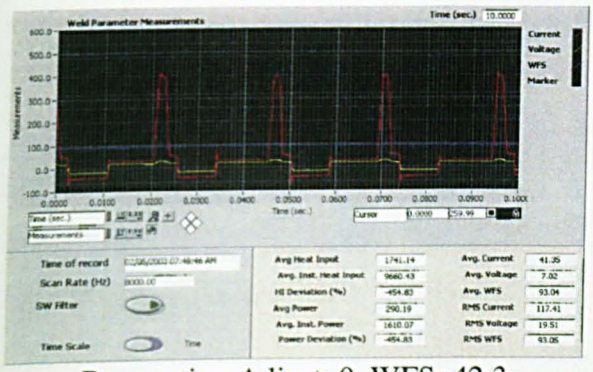

Penetration Adjust: 0, WFS: 42.3

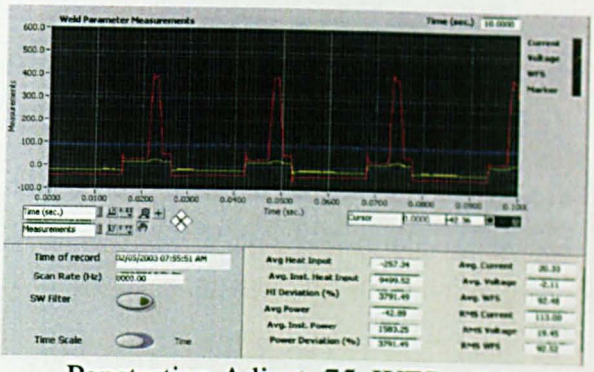

Penetration Adjust: 75, WFS: 42.3

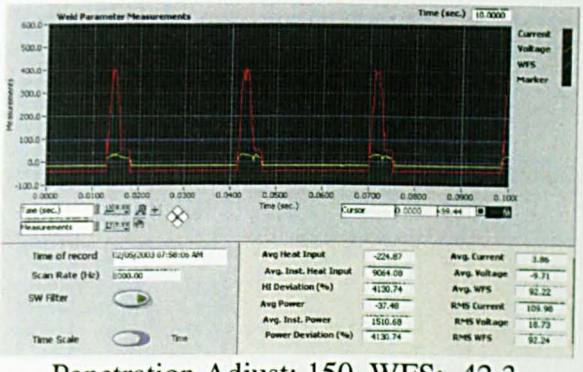

Penetration Adjust: 150, WFS: 42.3

Figure B-7 Steel Waveform Data for AC/MIG 200 at 42.3 mm/sec WFS and 19 mm CTWD

OTC AC/MIG 200
Wire: 1.2 mm Steel, ER70S-6
Gas: 90Ar-10CO_2 at 40 18.8 l/min
CTWD: 19 mm, Arc Length: 3 mm
WFS: 84.6 mm/s

Penetration Adjust: -150, WFS: 84.6

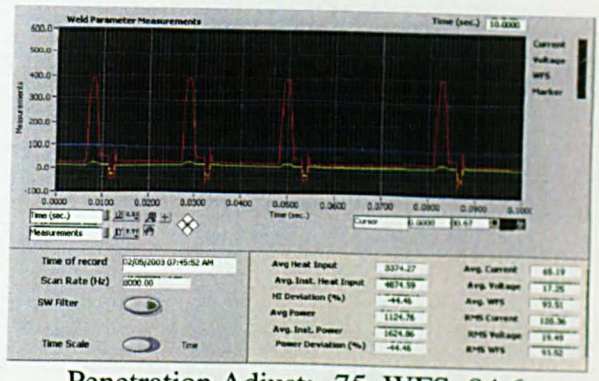

Penetration Adjust: -75, WFS: 84.6

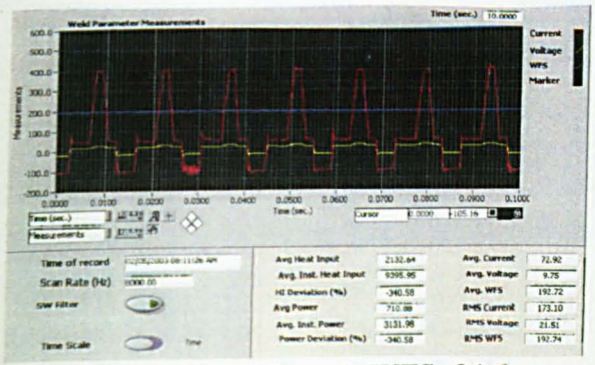

Penetration Adjust: 0, WFS: 84.6

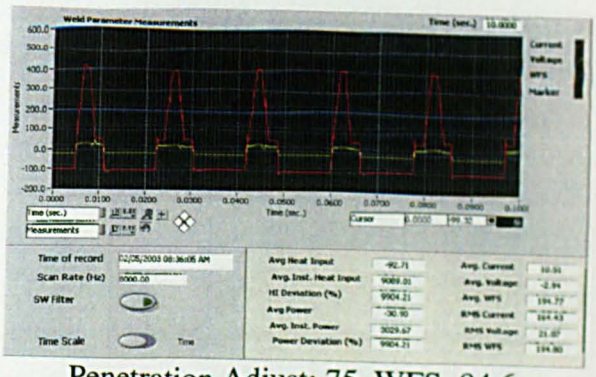

Penetration Adjust: 75, WFS: 84.6

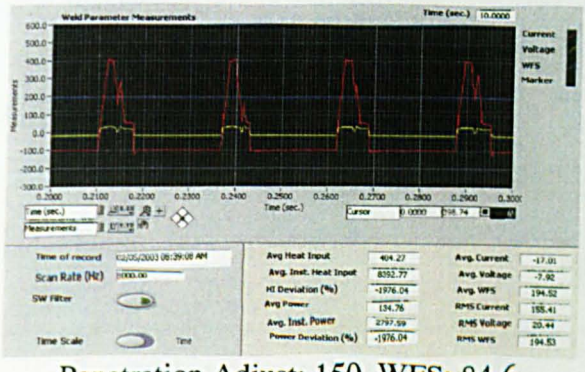

Penetration Adjust: 150, WFS: 84.6

Figure B-8 Steel Waveform Data for AC/MIG 200 at 84.6 mm/sec WFS and 19 mm CTWD

OTC AC/MIG 200
Wire: 1.2 mm Steel ER70S-6
Gas: 90Ar-10CO_2 at 18.8 l/min
CTWD: 19 mm, Arc Length: 3 mm
WFS: 127 mm/s

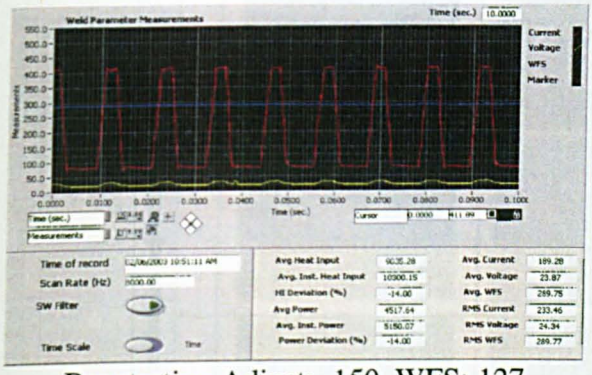

Penetration Adjust: -150, WFS: 127

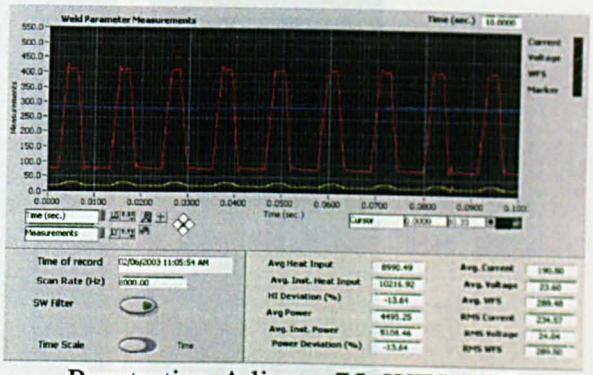

Penetration Adjust: -75, WFS: 127

Penetration Adjust: 0, WFS: 127

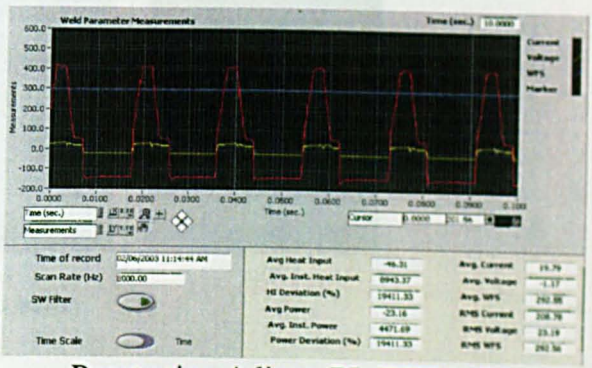

Penetration Adjust: 75, WFS: 127

Penetration Adjust: 150, WFS: 127

Figure B-9 Steel Waveform Data for AC/MIG 200 at 127 mm/sec WFS and 19 mm CTWD

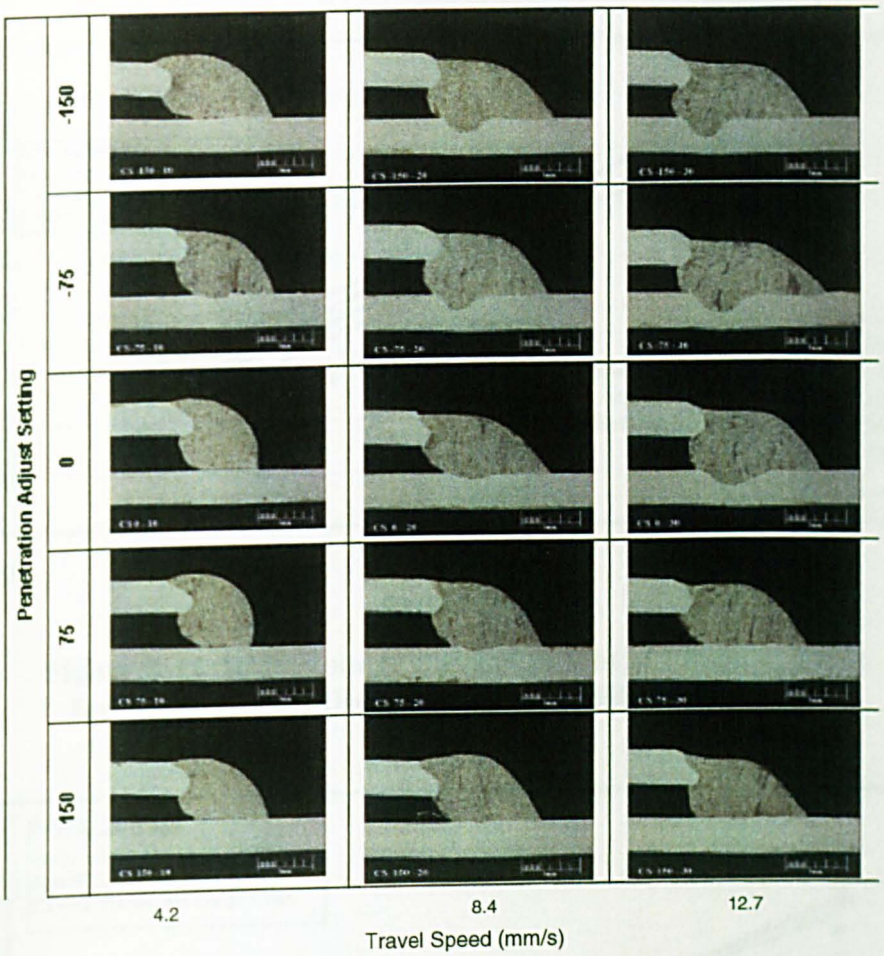

Figure B-10 Macrosection Map for Steel Lap Joint Application at 19 mm CTWD Using AC/MIG 200 Power Supply

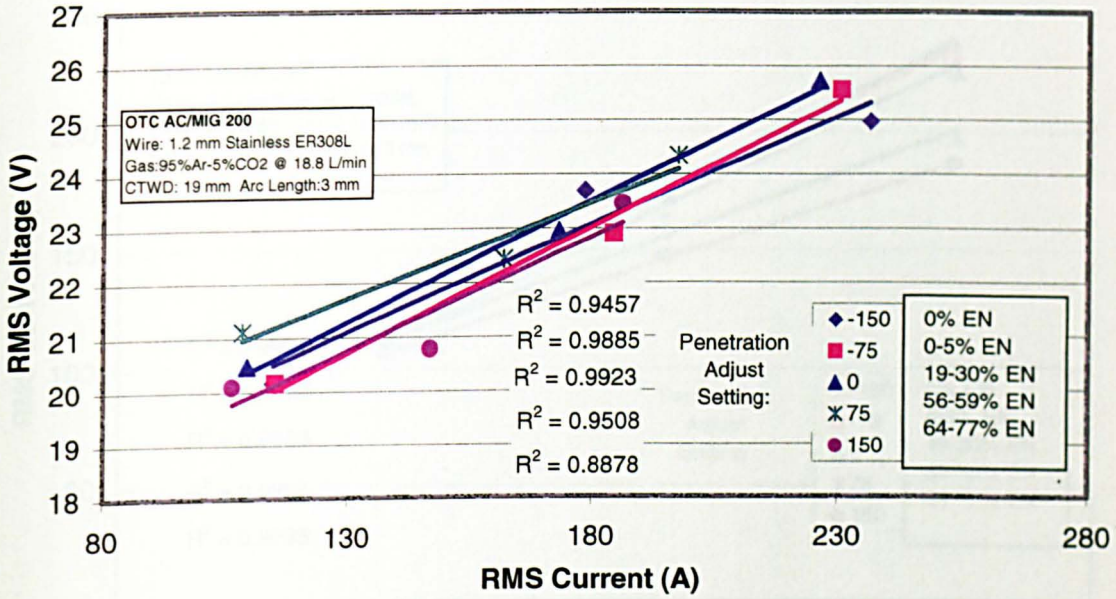

Figure B-11 RMS Voltage versus Current at 19 mm CTWD for Stainless Steel Using the AC/MIG 200 Power Supply

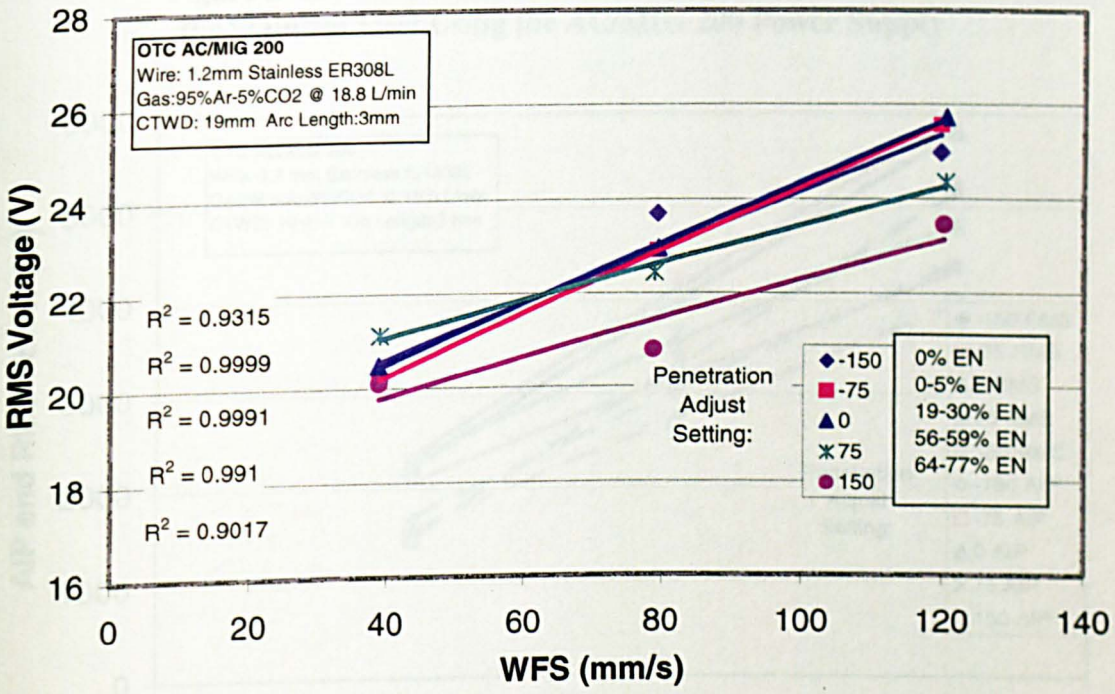

Figure B-12 RMS Voltage versus WFS at 19 mm CTWD for Stainless Steel Using the AC/MIG 200 Power Supply

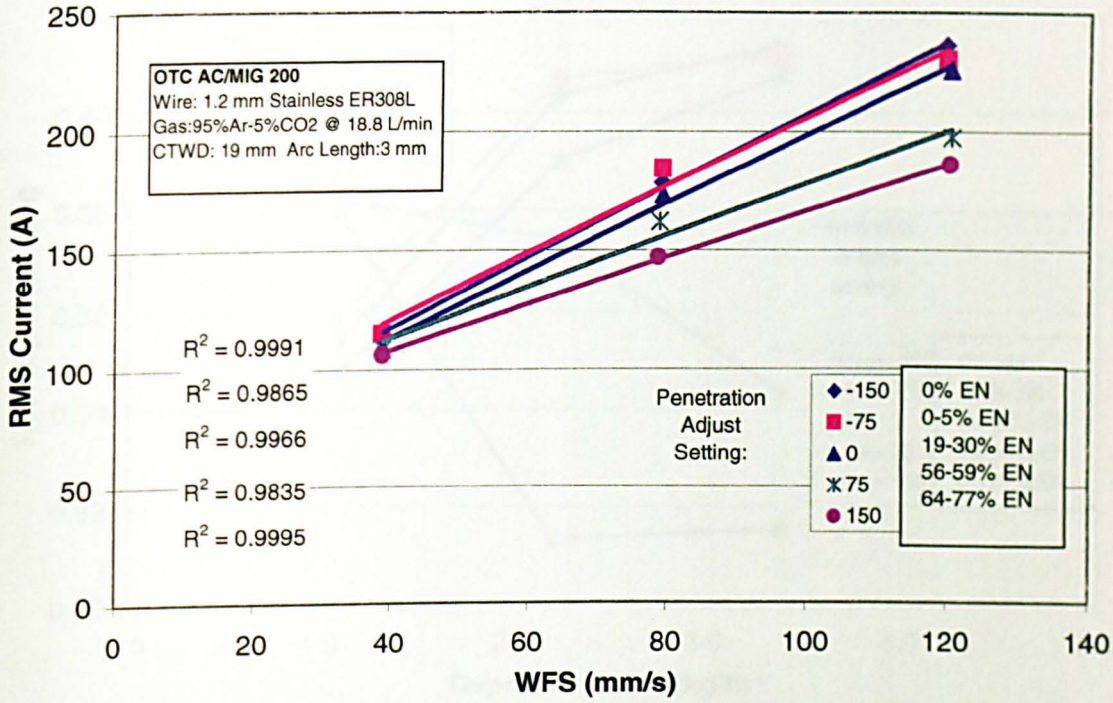

Figure B-13 - RMS Current versus WFS at 19 mm CTWD for Stainless Steel Using the AC/MIG 200 Power Supply

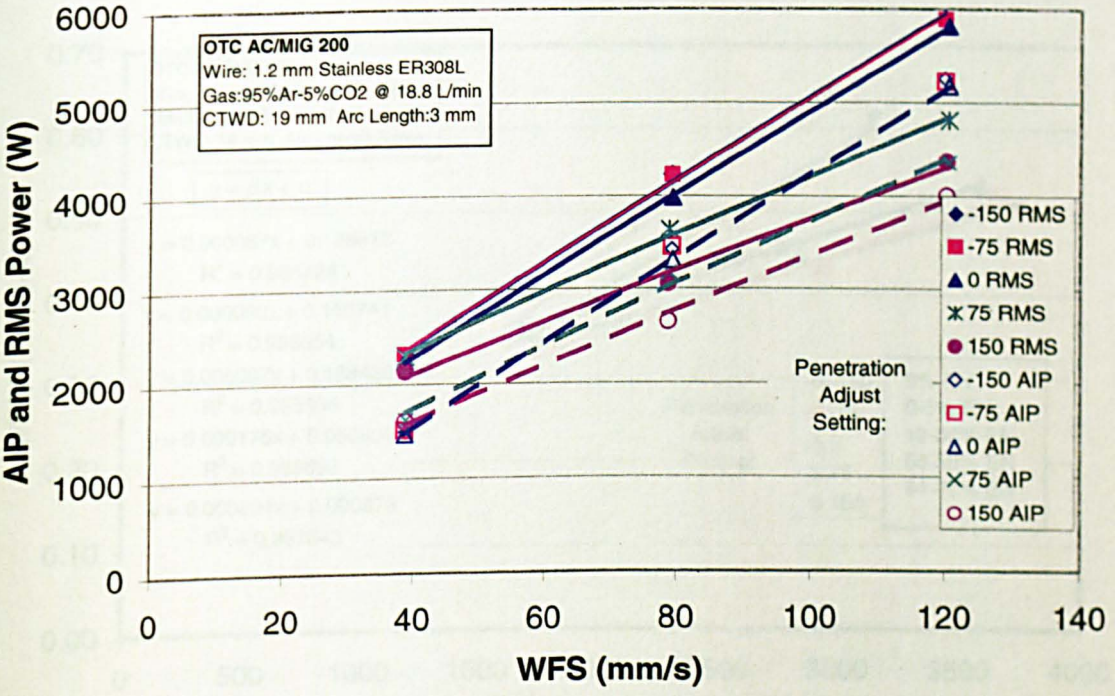

Figure B-14 AIP and RMS Power versus WFS at 19 mm CTWD for Stainless Steel Using the AC/MIG 200 Power Supply

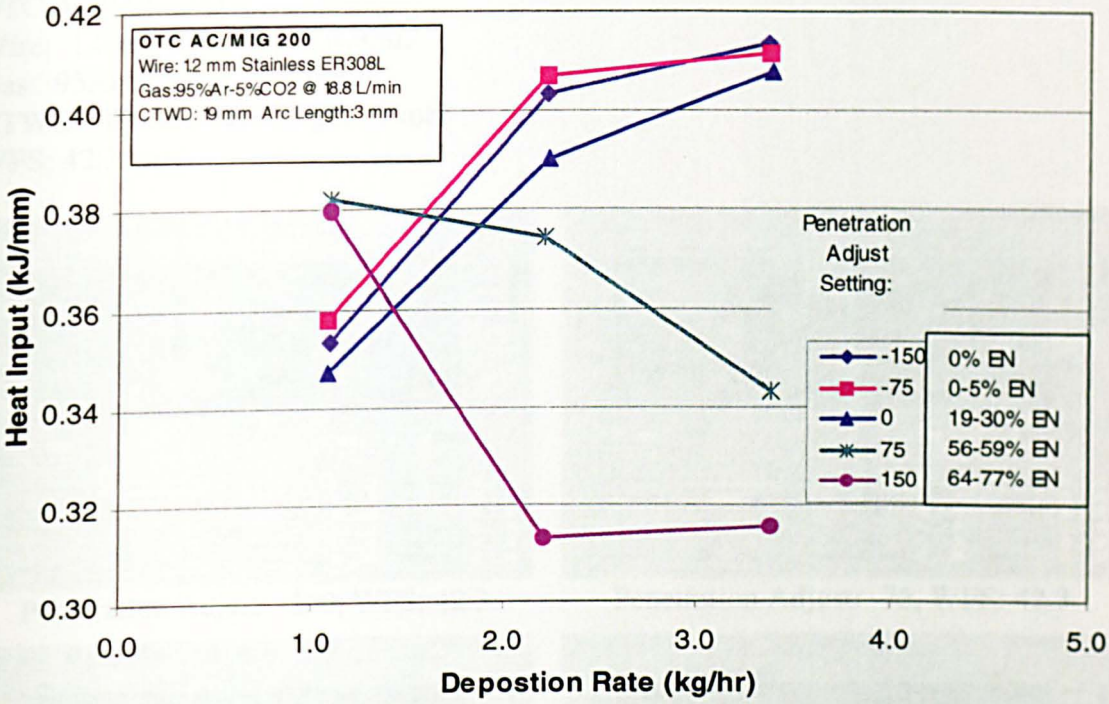

Figure B-15 Heat Input versus Deposition Rate at 19 mm CTWD for Stainless Steel Using the AC/MIG 200 Power Supply

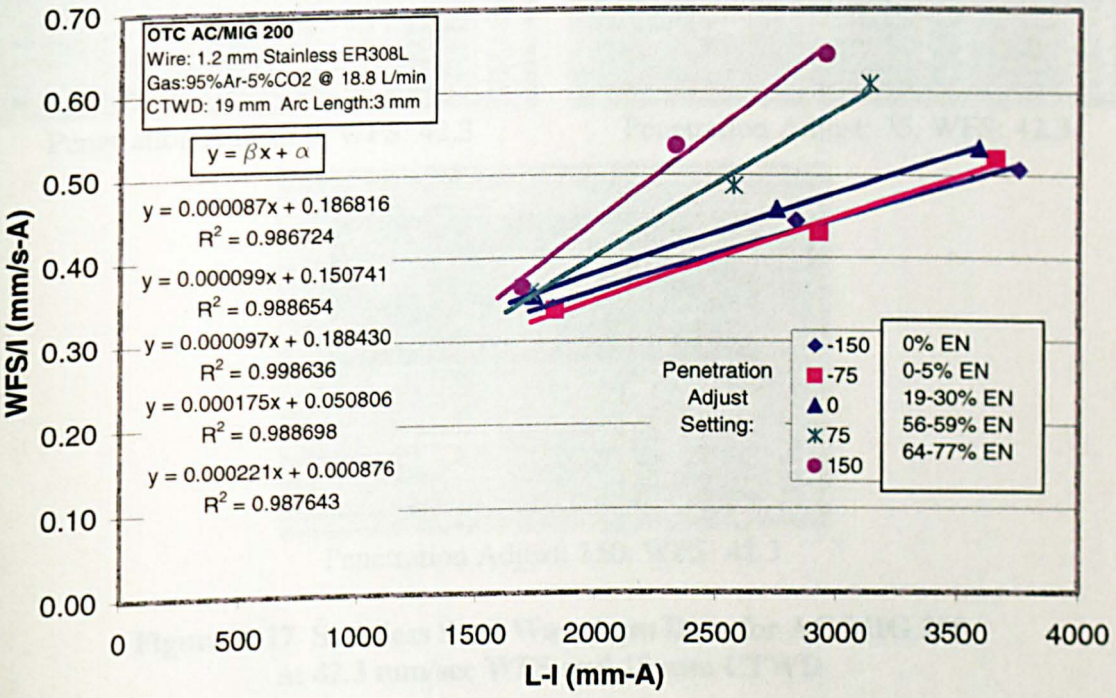

Figure B-16 Burnoff Rate versus Heating Factor at 19 mm CTWD for Stainless Steel Using the AC/MIG 200 Power Supply

OTC AC/MIG 200
Wire: 1.2 mm Stainless ER308L
Gas: 95Ar-5CO_2 at 18.8 l/min
CTWD: 19 mm, Arc Length: 3 mm
WFS: 42.3 mm/s

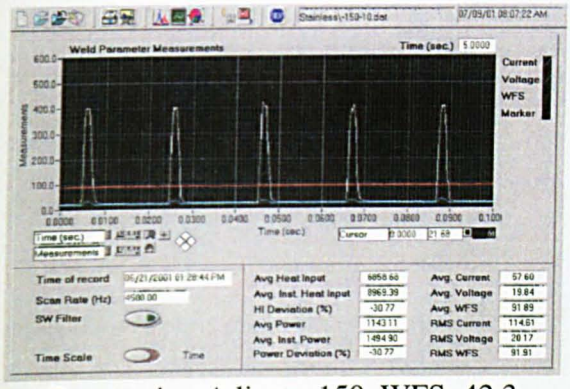

Penetration Adjust: -150, WFS: 42.3

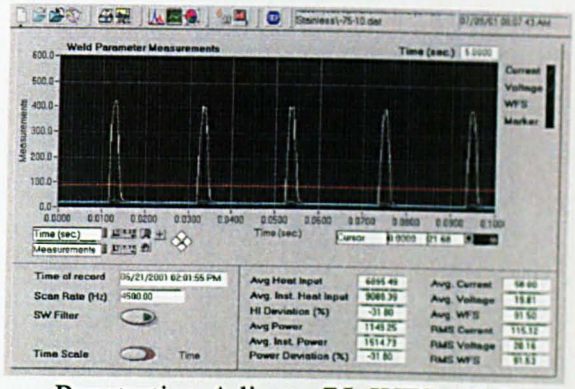

Penetration Adjust: -75, WFS: 42.3

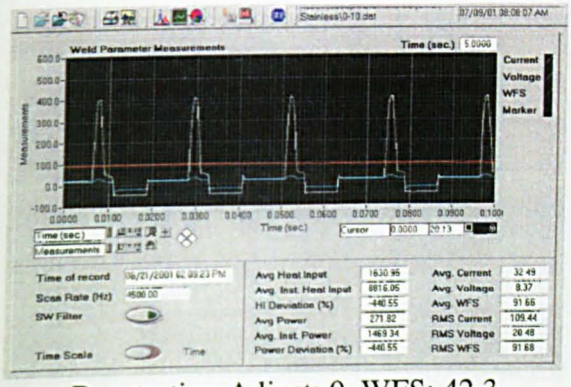

Penetration Adjust: 0, WFS: 42.3

Penetration Adjust: 75, WFS: 42.3

Penetration Adjust: 150, WFS: 42.3

Figure B-17 Stainless Steel Waveform Data for AC/MIG 200 at 42.3 mm/sec WFS and 19 mm CTWD

OTC AC/MIG 200
Wire: 1.2 mm Stainless ER308L
Gas: 95Ar-5CO_2 at 18.8 l/min
CTWD: 19 mm, Arc Length: 3 mm
WFS: 84.6 mm/s

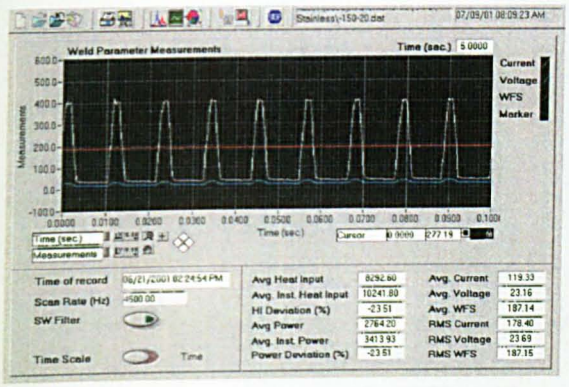

Penetration Adjust: -150, WFS: 84.6

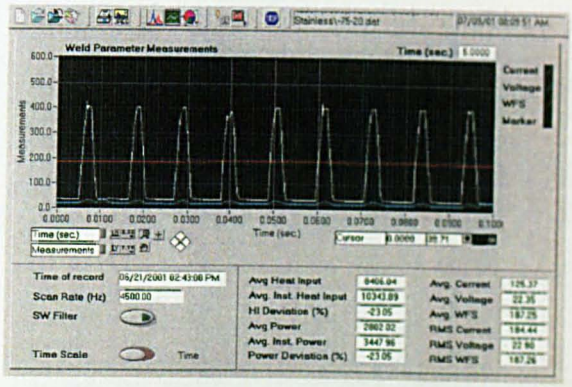

Penetration Adjust: -75, WFS: 84.6

Penetration Adjust: 0, WFS: 84.6

Penetration Adjust: 75, WFS: 84.6

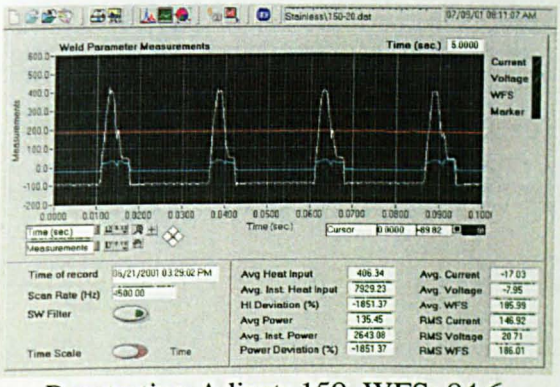

Penetration Adjust: 150, WFS: 84.6

Figure B-18 Stainless Steel Waveform Data for AC/MIG 200 at 84.6 mm/sec WFS and 19 mm CTWD

OTC AC/MIG 200
Wire: 1.2 mm Stainless ER308L
Gas: 95Ar-5CO_2 at 18.8 l/min
CTWD: 19 mm, Arc Length: 3 mm
WFS: 127 mm/s

Penetration Adjust: -150, WFS: 127

Penetration Adjust: -75, WFS: 127

Penetration Adjust: 0, WFS: 127

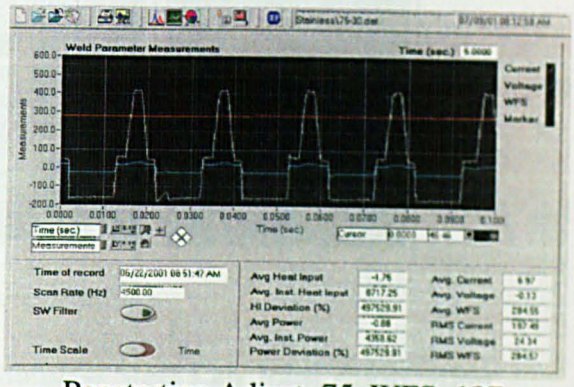

Penetration Adjust: 75, WFS: 127

Penetration Adjust: 150, WFS: 127

Figure B-19 Stainless Steel Waveform Data for AC/MIG 200 at 127 mm/sec WFS and 19 mm CTWD

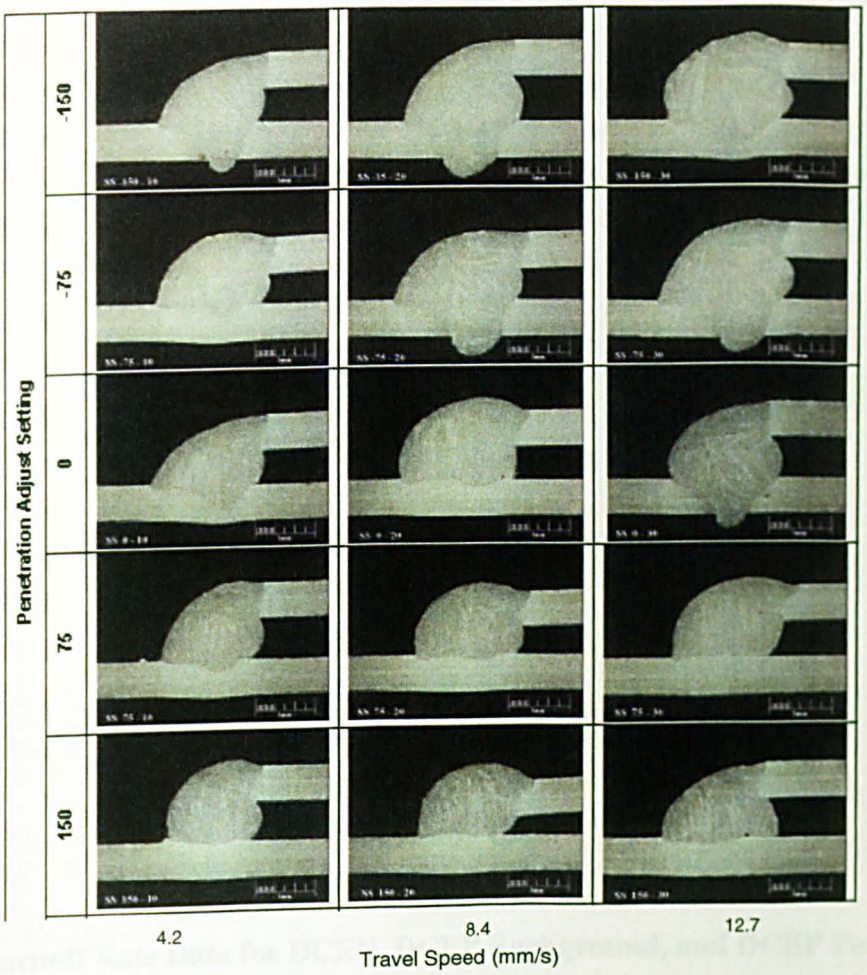

Figure B-20 Macrosection Map for Stainless Steel Lap Joint Application at 19 mm CTWD Using AC/MIG 200 Power Supply

Appendix C

Droplet Burnoff Rate Data for DCEN, DCEP Background, and DCEP Peak Cycles

Weld No.	Droplet No.	WFS_{DAQ} (mm/s)	Δx (mm)	t_{EN} (s)	$\Delta x/t_{EN}$ (mm/s)	MR (mm/s)	V_d (mm^3)	V_D (mm^3/s)	I_{EN} (A)	BR (mm/(s A))	L_{AVG} (mm)	F_L (mm A)	f (Hz)	%EN (%)
0-42	1	39.65	0.000	0.0082	0.000	39.65	0.334	40.68	39.98	0.992	12.875	514.74	41.75	34.24%
0-42	2	39.69	-0.102	0.0082	-12.390	27.30	0.230	28.01	39.91	0.684	12.824	511.81	41.75	34.24%
0-42	3	38.66	0.000	0.0082	0.000	38.66	0.325	39.67	39.88	0.969	12.875	513.46	41.75	34.24%
0-42	4	39.57	-0.076	0.0085	-8.965	30.60	0.267	31.40	39.78	0.769	12.837	510.65	41.75	35.49%
0-42	5	39.42	0.000	0.0083	0.000	39.42	0.336	40.45	39.97	0.986	12.875	514.61	41.75	34.65%
0-42	6	38.68	-0.152	0.0082	-18.585	20.09	0.169	20.62	40.16	0.500	12.799	514.00	41.75	34.24%
0-42	7	39.67	-0.178	0.0083	-21.422	18.25	0.155	18.72	40.04	0.456	12.786	511.96	41.75	34.65%
0-42	8	39.34	-0.152	0.0084	-18.143	21.20	0.183	21.75	40.81	0.519	12.799	522.32	41.75	35.07%
0-42	9	39.32	0.000	0.0083	0.000	39.32	0.335	40.35	39.63	0.992	12.875	510.24	41.75	34.65%
0-42	10	39.16	-0.076	0.0082	-9.293	29.87	0.251	30.64	40.15	0.744	12.837	515.40	41.75	34.24%
0-42	AVG	39.32	-0.074	0.0083	-8.896	30.42	0.258	31.21	40.03	0.761	12.838	513.92	41.75	34.57%
0-42	STDEV	0.38	0.071	0.0001	8.597	8.58	0.072	8.81	0.32	0.218	0.036	3.44	0.00	0.43%
30-42	1	38.09	0.076	0.0112	6.804	44.89	0.516	46.06	39.96	1.123	12.913	516.01	44.04	49.32%
30-42	2	38.43	-0.076	0.0114	-6.684	31.75	0.371	32.58	39.71	0.800	12.837	509.75	44.04	50.21%
30-42	3	38.63	-0.076	0.0112	-6.804	31.83	0.366	32.66	39.72	0.801	12.837	509.88	44.04	49.32%
30-42	4	40.96	0.076	0.0113	6.743	47.70	0.553	48.95	39.70	1.202	12.913	512.65	44.04	49.77%
30-42	5	39.96	-0.076	0.0113	-6.743	33.22	0.385	34.08	39.87	0.833	12.837	511.81	44.04	49.77%
30-42	6	36.80	0.076	0.0113	6.743	43.55	0.505	44.68	39.93	1.091	12.913	515.62	44.04	49.77%
30-42	7	37.33	-0.178	0.0112	-15.875	21.46	0.247	22.01	39.94	0.537	12.786	510.68	45.04	50.44%
30-42	8	39.35	0.127	0.0113	11.239	50.59	0.587	51.91	39.90	1.268	12.939	516.25	46.04	52.03%
30-42	9	40.55	0.000	0.0113	0.000	40.55	0.470	41.61	39.72	1.021	12.875	511.40	44.04	49.77%
30-42	10	40.04	0.000	0.0112	0.000	40.04	0.460	41.09	39.67	1.009	12.875	510.75	44.04	49.32%
30-42	AVG	39.01	-0.005	0.0113	-0.451	38.56	0.446	39.57	39.81	0.968	12.872	512.48	44.34	49.97%
30-42	STDEV	1.38486	0.09564	0.00007	8.498	8.89564	0.103	9.13	0.11708	0.223	0.048	2.55108	0.67495	0.00811
60-42	1	38.22	-0.127	0.0143	-8.881	29.34	0.431	30.11	39.95	0.734	12.812	511.82	45.31	64.79%
60-42	2	37.66	-0.102	0.0142	-7.155	30.50	0.444	31.30	39.74	0.768	12.824	509.63	45.31	64.34%
60-42	3	38.40	0.051	0.0143	3.552	41.95	0.616	43.05	39.33	1.067	12.900	507.37	45.31	64.79%
60-42	4	37.03	-0.076	0.0145	-5.255	31.78	0.473	32.61	39.55	0.803	12.837	507.70	45.31	65.70%

Weld No.	Droplet No.	WFS_{DAQ} (mm/s)	Δx (mm)	t_{EN} (s)	$\Delta x/t_{EN}$ (mm/s)	MR (mm/s)	V_d (mm^3)	V_D (mm^3/s)	I_{EN} (A)	BR (mm/(s A))	L_{AVG} (mm)	F_L (mm A)	f (Hz)	%EN (%)
60-42	5	37.77	0.025	0.0143	1.776	39.55	0.580	40.58	39.71	0.996	12.888	511.77	45.31	64.79%
60-42	6	37.91	-0.076	0.0143	-5.329	32.58	0.478	33.43	39.66	0.821	12.837	509.11	45.31	64.79%
60-42	7	39.67	0.127	0.0142	8.944	48.62	0.708	49.89	39.85	1.220	12.939	515.60	45.31	64.34%
60-42	8	38.54	0.102	0.0143	7.105	45.65	0.670	46.84	39.65	1.151	12.926	512.51	45.31	64.79%
60-42	9	37.73	0.229	0.0142	16.099	53.83	0.784	55.23	39.64	1.358	12.989	514.90	46.31	65.76%
60-42	10	39.65	0.051	0.0142	3.577	43.23	0.630	44.36	39.70	1.089	12.900	512.15	45.31	64.34%
60-42	AVG	38.26	0.020	0.0143	1.423	39.68	0.581	40.72	39.68	1.001	12.885	511.26	45.41	64.84%
60-42	STDEV	0.85	0.115	0.0001	8.052	8.42	0.121	8.64	0.17	0.213	0.057	2.79	0.32	0.51%
90-42	1	39.56	-0.127	0.0174	-7.299	32.26	0.576	33.10	39.65	0.814	12.812	507.98	39.51	68.75%
90-42	2	38.15	0.025	0.0173	1.468	39.62	0.703	40.65	39.42	1.005	12.888	508.03	39.51	68.35%
90-42	3	38.15	-0.229	0.0173	-13.214	24.94	0.443	25.59	39.42	0.633	12.761	503.03	39.51	68.35%
90-42	4	39.47	0.025	0.0172	1.477	40.95	0.723	42.02	39.59	1.034	12.888	510.22	39.51	67.96%
90-42	5	39.67	0.025	0.0172	1.477	41.15	0.726	42.22	39.71	1.036	12.888	511.77	39.51	67.96%
90-42	6	38.52	0.000	0.0173	0.000	38.52	0.684	39.53	39.49	0.976	12.875	508.43	39.51	68.35%
90-42	7	37.72	-0.102	0.0173	-5.873	31.85	0.565	32.68	39.54	0.806	12.824	507.07	39.51	68.35%
90-42	8	37.78	-0.127	0.0174	-7.299	30.48	0.544	31.27	39.61	0.769	12.812	507.46	39.51	68.75%
90-42	9	37.81	-0.432	0.0173	-24.960	12.85	0.228	13.19	39.55	0.325	12.659	500.67	40.51	70.08%
90-42	10	38.34	-0.025	0.0172	-1.477	36.86	0.651	37.83	39.64	0.930	12.862	509.86	39.51	67.96%
90-42	AVG	38.52	-0.097	0.0173	-5.582	32.94	0.584	33.79	39.56	0.833	12.827	507.45	39.61	68.49%
90-42	STDEV	0.77	0.146	0.0001	8.413	8.81	0.155	9.04	0.10	0.222	0.073	3.32	0.32	0.63%
120-42	1	38.96	-0.025	0.0198	-1.283	37.67	0.765	38.65	39.55	0.953	12.862	508.70	39.01	77.24%
120-42	2	38.96	-0.102	0.0201	-5.055	33.90	0.699	34.78	39.55	0.857	12.824	507.20	39.01	78.41%
120-42	3	38.96	0.051	0.0203	2.502	41.46	0.864	42.54	39.55	1.048	12.900	510.21	39.01	79.19%
120-42	4	38.96	0.051	0.0202	2.515	41.47	0.860	42.55	39.55	1.049	12.900	510.21	39.01	78.80%
120-42	5	38.96	-0.051	0.0202	-2.515	36.44	0.755	37.39	39.55	0.921	12.850	508.20	39.01	78.80%
120-42	6	38.96	0.203	0.0203	10.010	48.96	1.020	50.24	39.55	1.238	12.977	513.22	39.01	79.19%
120-42	7	38.96	-0.203	0.0202	-10.059	28.90	0.599	29.65	39.55	0.731	12.773	505.19	39.01	78.80%
120-42	8	38.96	-0.051	0.0203	-2.502	36.45	0.759	37.40	39.55	0.922	12.850	508.20	39.01	79.19%
120-42	9	38.96	0.000	0.0202	0.000	38.96	0.807	39.97	39.55	0.985	12.875	509.21	39.01	78.80%

Weld No.	Droplet No.	WFS_{DAQ} (mm/s)	Δx (mm)	t_{EN} (s)	$\Delta x/t_{EN}$ (mm/s)	MR (mm/s)	V_d (mm^3)	V_D (mm^3/s)	I_{EN} (A)	BR (mm/(s A))	L_{AVG} (mm)	F_L (mm A)	f (Hz)	%EN (%)
120-42	10	38.96	0.025	0.0203	1.251	40.21	0.837	41.26	39.55	1.017	12.888	509.71	39.01	79.19%
120-42	AVG	38.96	-0.010	0.0202	-0.503	38.45	0.797	39.45	39.55	0.972	12.870	509.01	39.01	78.76%
120-42	STDEV	0.00	0.107	0.0002	5.299	5.30	0.112	5.44	0.00	0.134	0.054	2.12	0.00	0.59%
150-42	1	38.95	0.025	0.0231	1.100	40.05	0.949	41.10	39.55	1.013	12.888	509.71	34.72	80.20%
150-42	2	38.95	-0.127	0.0233	-5.451	33.50	0.801	34.37	39.55	0.847	12.812	506.69	34.72	80.90%
150-42	3	38.95	-0.051	0.0232	-2.190	36.76	0.875	37.72	39.55	0.929	12.850	508.20	34.72	80.55%
150-42	4	38.95	-0.076	0.0231	-3.299	35.65	0.845	36.58	39.55	0.901	12.837	507.70	34.72	80.20%
150-42	5	38.95	0.076	0.0232	3.284	42.24	1.005	43.34	39.55	1.068	12.913	510.71	34.72	80.55%
150-42	6	38.95	0.025	0.0233	1.090	40.04	0.957	41.09	39.55	1.012	12.888	509.71	34.72	80.90%
150-42	7	38.95	-0.229	0.0232	-9.853	29.10	0.693	29.86	39.55	0.736	12.761	504.69	34.72	80.55%
150-42	8	38.95	-0.025	0.0232	-1.095	37.86	0.901	38.84	39.55	0.957	12.862	508.70	34.72	80.55%
150-42	9	38.95	0.025	0.0232	1.095	40.05	0.953	41.09	39.55	1.013	12.888	509.71	34.72	80.55%
150-42	10	38.95	-0.051	0.0231	-2.199	36.75	0.871	37.71	39.55	0.929	12.850	508.20	34.72	80.20%
150-42	AVG	38.95	-0.041	0.0232	-1.752	37.20	0.885	38.17	39.55	0.941	12.855	508.40	34.72	80.52%
150-42	STDEV	0.00	0.089	0.0001	3.833	3.83	0.091	3.93	0.00	0.097	0.044	1.76	0.00	0.26%
0-63	1	59.28	0.102	0.0056	18.143	77.42	0.445	79.44	60.72	1.275	12.926	784.85	66.94	37.49%
0-63	2	59.28	0.076	0.0055	13.855	73.13	0.413	75.04	60.72	1.204	12.913	784.08	66.94	36.82%
0-63	3	59.28	0.076	0.0056	13.607	72.88	0.419	74.78	60.72	1.200	12.913	784.08	66.94	37.49%
0-63	4	59.28	-0.051	0.0058	-8.759	50.52	0.301	51.84	60.72	0.832	12.850	780.23	67.94	39.41%
0-63	5	59.28	0.051	0.0056	9.071	68.35	0.393	70.13	60.72	1.126	12.900	783.31	68.94	38.61%
0-63	6	59.28	0.025	0.0057	4.456	63.74	0.373	65.40	60.72	1.050	12.888	782.54	69.94	39.87%
0-63	7	59.28	0.152	0.0056	27.214	86.49	0.497	88.75	60.72	1.424	12.951	786.40	66.94	37.49%
0-63	8	59.28	0.127	0.0056	22.679	81.95	0.471	84.09	60.72	1.350	12.939	785.63	66.94	37.49%
0-63	9	59.28	0.127	0.0056	22.679	81.95	0.471	84.09	60.72	1.350	12.939	785.63	66.94	37.49%
0-63	AVG	59.28	0.076	0.0056	13.553	72.83	0.420	74.73	60.72	1.201	12.913	784.08	67.61	38.01%
0-63	STDEV	0.00	0.062	0.0001	11.039	11.04	0.060	17.58	0.00	0.182	0.031	1.89	1.12	1.03%
30-63	1	59.28	0.127	0.0086	14.767	74.04	0.653	75.97	62.30	1.188	12.939	806.07	66.07	56.82%
30-63	2	59.28	0.178	0.0086	20.674	79.95	0.705	82.03	62.30	1.283	12.964	807.65	66.07	56.82%
30-63	3	59.28	0.203	0.0086	23.628	82.90	0.732	85.07	62.30	1.331	12.977	808.44	66.07	56.82%

Weld No.	Droplet No.	WFS_{DAQ} (mm/s)	Δx (mm)	t_{EN} (s)	$\Delta x/t_{EN}$ (mm/s)	MR (mm/s)	V_d (mm^3)	V_D (mm^3/s)	I_{EN} (A)	BR (mm/(s A))	L_{AVG} (mm)	F_L (mm A)	f (Hz)	%EN (%)
30-63	4	59.28	0.203	0.0085	23.906	83.18	0.725	85.35	62.30	1.335	12.977	808.44	66.07	56.16%
30-63	5	59.28	0.000	0.0087	0.000	59.28	0.529	60.83	62.30	0.952	12.875	802.11	67.07	58.35%
30-63	6	59.28	0.051	0.0086	5.907	65.19	0.575	66.89	62.30	1.046	12.900	803.69	68.07	58.54%
30-63	7	59.28	-0.178	0.0086	-20.674	38.61	0.341	39.61	62.30	0.620	12.786	796.57	69.07	59.40%
30-63	8	59.28	0.229	0.0086	26.581	85.86	0.758	88.10	62.30	1.378	12.989	809.23	66.07	56.82%
30-63	9	59.28	0.178	0.0086	20.674	79.95	0.705	82.03	62.30	1.283	12.964	807.65	66.07	56.82%
30-63	10	59.28	0.279	0.0086	32.488	91.76	0.810	94.16	62.30	1.473	13.015	810.82	66.07	56.82%
30-63	AVG	59.28	0.127	0.0086	14.767	74.04	0.653	75.98	62.30	1.189	12.939	806.07	66.67	57.34%
30-63	STDEV	0.00	0.135	0.0000	15.770	15.77	0.138	16.18	0.00	0.253	0.068	4.22	1.07	1.04%
60-63	1	59.28	0.152	0.0115	13.252	72.53	0.856	74.42	62.33	1.164	12.951	807.25	57.80	66.47%
60-63	2	59.28	0.229	0.0116	19.707	78.98	0.940	81.04	62.33	1.267	12.989	809.62	57.80	67.05%
60-63	3	59.28	0.279	0.0116	24.086	83.36	0.992	85.54	62.33	1.337	13.015	811.21	57.80	67.05%
60-63	4	59.28	0.127	0.0115	11.043	70.32	0.830	72.15	62.33	1.128	12.939	806.46	57.80	66.47%
60-63	5	59.28	0.229	0.0116	19.707	78.98	0.940	81.04	62.33	1.267	12.989	809.62	57.80	67.05%
60-63	6	59.28	0.178	0.0116	15.328	74.60	0.888	76.55	62.33	1.197	12.964	808.04	57.80	67.05%
60-63	7	59.28	0.279	0.0116	24.086	83.36	0.992	85.54	62.33	1.337	13.015	811.21	57.80	67.05%
60-63	8	59.28	0.000	0.0116	0.000	59.28	0.706	60.83	62.33	0.951	12.875	802.50	58.80	68.21%
60-63	9	59.28	-0.025	0.0115	-2.209	57.07	0.673	58.56	62.33	0.916	12.862	801.71	59.80	68.77%
60-63	10	59.28	0.127	0.0115	11.043	70.32	0.830	72.15	62.33	1.128	12.939	806.46	57.80	66.47%
60-63	AVG	59.28	0.157	0.0116	13.623	72.90	0.865	74.80	62.33	1.169	12.954	807.41	58.10	67.16%
60-63	STDEV	0.00	0.106	0.0001	9.102	9.10	0.110	9.34	0.00	0.146	0.053	3.29	0.67	0.76%
90-63	1	59.28	0.254	0.0145	17.517	76.79	1.143	78.80	62.39	1.231	13.002	811.19	50.03	72.54%
90-63	2	59.28	0.178	0.0146	12.178	71.45	1.070	73.32	62.39	1.145	12.964	808.82	50.03	73.04%
90-63	3	59.28	0.229	0.0145	15.766	75.04	1.116	77.00	62.39	1.203	12.989	810.40	50.03	72.54%
90-63	4	59.28	0.051	0.0146	3.479	62.75	0.940	64.39	62.39	1.006	12.900	804.86	50.03	73.04%
90-63	5	59.28	0.203	0.0145	14.014	73.29	1.090	75.20	62.39	1.175	12.977	809.61	50.03	72.54%
90-63	6	59.28	0.152	0.0145	10.510	69.79	1.038	71.61	62.39	1.119	12.951	808.03	50.03	72.54%
90-63	7	59.28	0.203	0.0144	14.111	73.39	1.084	75.30	62.39	1.176	12.977	809.61	50.03	72.04%
90-63	8	59.28	0.102	0.0145	7.007	66.28	0.986	68.01	62.39	1.062	12.926	806.44	50.03	72.54%

Weld No.	Droplet No.	WFS_{DAQ} (mm/s)	Δx (mm)	t_{EN} (s)	$\Delta x/t_{EN}$ (mm/s)	MR (mm/s)	V_d (mm^3)	V_D (mm^3/s)	I_{EN} (A)	BR (mm/(s A))	L_{AVG} (mm)	F_L (mm A)	f (Hz)	%EN (%)
90-63	9	59.28	-0.025	0.0146	-1.740	57.54	0.862	59.04	62.39	0.922	12.862	802.48	51.03	74.50%
90-63	10	59.28	0.203	0.0146	13.918	73.19	1.096	75.10	62.39	1.173	12.977	809.61	50.03	73.04%
90-63	AVG	59.28	0.155	0.0145	10.663	69.94	1.043	71.76	62.39	1.121	12.952	808.10	50.13	72.84%
90-63	STDEV	0.00	0.088	0.0001	6.035	6.03	0.088	6.19	0.00	0.097	0.044	2.73	0.32	0.66%
120-63	1	59.28	0.406	0.0174	23.356	82.63	1.475	84.79	62.49	1.322	13.078	817.26	42.98	74.79%
120-63	2	59.28	0.432	0.0175	24.674	83.95	1.507	86.14	62.49	1.343	13.091	818.05	42.98	75.21%
120-63	3	59.28	0.305	0.0176	17.318	76.59	1.383	78.59	62.49	1.226	13.027	814.08	42.98	75.64%
120-63	4	59.28	0.229	0.0176	12.989	72.26	1.305	74.15	62.49	1.156	12.989	811.70	42.98	75.64%
120-63	5	59.28	0.406	0.0175	23.223	82.50	1.481	84.65	62.49	1.320	13.078	817.26	42.98	75.21%
120-63	6	59.28	0.356	0.0176	20.205	79.48	1.435	81.55	62.49	1.272	13.053	815.67	42.98	75.64%
120-63	7	59.28	0.305	0.0174	17.517	76.79	1.371	78.80	62.49	1.229	13.027	814.08	42.98	74.79%
120-63	8	59.28	0.330	0.0175	18.869	78.14	1.403	80.18	62.49	1.250	13.040	814.88	42.98	75.21%
120-63	9	59.28	0.610	0.0175	34.834	94.11	1.690	96.57	62.49	1.506	13.180	823.61	43.98	76.97%
120-63	10	59.28	0.279	0.0176	15.875	75.15	1.357	77.11	62.49	1.203	13.015	813.29	42.98	75.64%
120-63	AVG	59.28	0.366	0.0175	20.877	80.15	1.441	82.24	62.49	1.283	13.058	815.99	43.08	75.48%
120-63	STDEV	0.00	0.107	0.0001	6.115	6.12	0.108	6.28	0.00	0.098	0.053	3.33	0.32	0.62%
150-63	1	59.28	0.051	0.0205	2.478	61.75	1.299	63.36	62.33	0.991	12.900	804.08	36.90	75.65%
150-63	2	59.28	0.102	0.0207	4.908	64.18	1.363	65.86	62.33	1.030	12.926	805.67	36.90	76.38%
150-63	3	59.28	0.152	0.0205	7.434	66.71	1.403	68.45	62.33	1.070	12.951	807.25	36.90	75.65%
150-63	4	59.28	0.102	0.0205	4.956	64.23	1.351	65.91	62.33	1.031	12.926	805.67	36.90	75.65%
150-63	5	59.28	0.178	0.0205	8.673	67.95	1.429	69.72	62.33	1.090	12.964	808.04	36.90	75.65%
150-63	6	59.28	0.102	0.0205	4.956	64.23	1.351	65.91	62.33	1.031	12.926	805.67	36.90	75.64%
150-63	7	59.28	0.305	0.0204	14.941	74.22	1.554	76.16	62.33	1.191	13.027	812.00	37.90	77.32%
150-63	8	59.28	0.076	0.0206	3.699	62.98	1.331	64.62	62.33	1.010	12.913	804.87	38.90	80.13%
150-63	9	59.28	0.279	0.0205	13.629	72.90	1.534	74.81	62.33	1.170	13.015	811.21	36.90	75.64%
150-63	10	59.28	0.178	0.0206	8.631	67.91	1.435	69.68	62.33	1.089	12.964	808.04	36.90	76.01%
150-63	AVG	59.28	0.152	0.0205	7.423	66.70	1.405	68.44	62.33	1.070	12.951	807.25	37.20	76.37%
150-63	STDEV	0.00	0.085	0.0001	4.148	4.15	0.085	4.26	0.00	0.067	0.042	2.64	0.67	1.43%
0-85	1	80.34	0.381	0.0041	92.927	173.27	0.729	177.79	97.20	1.783	13.066	1270.01	74.03	30.35%

Weld No.	Droplet No.	WFS_{DAQ} (mm/s)	Δx (mm)	t_{EN} (s)	$\Delta x/t_{EN}$ (mm/s)	MR (mm/s)	V_d (mm^3)	V_D (mm^3/s)	I_{EN} (A)	BR (mm/(s A))	L_{AVG} (mm)	F_L (mm A)	f (Hz)	%EN (%)
0-85	2	80.34	0.305	0.0040	76.200	156.54	0.643	160.63	97.20	1.610	13.027	1266.31	74.03	29.61%
0-85	3	80.34	0.330	0.0040	82.550	162.89	0.669	167.14	97.20	1.676	13.040	1267.54	74.03	29.61%
0-85	4	80.34	0.356	0.0041	86.732	167.08	0.703	171.43	97.20	1.719	13.053	1268.78	74.03	30.35%
0-85	5	80.34	0.406	0.0041	99.122	179.47	0.755	184.15	97.20	1.846	13.078	1271.25	74.03	30.35%
0-85	6	80.34	0.203	0.0040	50.800	131.14	0.538	134.56	97.20	1.349	12.977	1261.37	75.03	30.01%
0-85	7	80.34	0.127	0.0040	31.750	112.09	0.460	115.01	97.20	1.153	12.939	1257.67	76.03	30.41%
0-85	8	80.34	0.102	0.0040	25.400	105.74	0.434	108.50	97.20	1.088	12.926	1256.43	77.03	30.81%
0-85	AVG	80.34	0.276	0.0040	68.415	148.76	0.616	152.64	97.20	1.528	13.013	1264.92	74.78	30.19%
0-85	STDEV	0.00	0.117	0.0001	28.395	28.40	0.123	34.88	0.00	0.292	0.059	5.69	1.16	0.42%
30-85	1	81.10	0.508	0.0069	73.623	154.73	1.095	158.76	96.36	1.606	13.129	1265.11	71.78	49.53%
30-85	2	81.53	0.305	0.0069	44.174	125.70	0.890	128.98	95.45	1.317	13.027	1243.47	71.78	49.53%
30-85	3	81.95	0.584	0.0070	83.457	165.41	1.188	169.72	96.65	1.711	13.167	1272.60	71.78	50.25%
30-85	4	83.64	0.356	0.0070	50.800	134.44	0.966	137.95	96.33	1.396	13.053	1257.38	71.78	50.25%
30-85	5	84.07	0.635	0.0071	89.437	173.50	1.264	178.03	95.95	1.808	13.193	1265.82	71.78	50.96%
30-85	6	84.49	0.381	0.0071	53.662	138.15	1.006	141.75	95.64	1.444	13.066	1249.58	71.78	50.96%
30-85	7	82.37	0.737	0.0071	103.746	186.12	1.356	190.97	97.44	1.910	13.243	1290.43	72.78	51.67%
30-85	8	84.91	0.508	0.0071	71.549	156.46	1.140	160.54	96.12	1.628	13.129	1261.96	71.78	50.96%
30-85	AVG	83.01	0.502	0.0070	71.409	154.42	1.113	158.44	96.24	1.603	13.126	1263.26	71.91	50.51%
30-85	STDEV	1.45	0.149	0.0001	20.709	20.64	0.156	44.33	0.62	0.207	0.074	14.39	0.35	0.76%
60-85	1	81.65	0.457	0.0100	45.720	127.37	1.307	130.69	95.62	1.332	13.104	1252.97	61.51	61.51%
60-85	2	81.65	0.533	0.0101	52.812	134.46	1.394	137.97	95.49	1.408	13.142	1254.90	61.51	62.13%
60-85	3	81.65	0.686	0.0100	68.580	150.23	1.542	154.15	95.19	1.578	13.218	1258.21	61.51	61.51%
60-85	4	81.65	0.432	0.0101	42.752	124.41	1.289	127.65	95.44	1.303	13.091	1249.40	61.51	62.13%
60-85	5	81.65	0.533	0.0100	53.340	134.99	1.385	138.51	95.63	1.412	13.142	1256.74	61.51	61.51%
60-85	6	81.65	0.533	0.0101	52.812	134.46	1.394	137.97	95.08	1.414	13.142	1249.51	61.51	62.13%
60-85	7	81.65	0.533	0.0100	53.340	134.99	1.385	138.51	95.06	1.420	13.142	1249.25	61.51	61.51%
60-85	8	81.65	0.737	0.0101	72.931	154.58	1.602	158.62	95.38	1.621	13.243	1263.15	61.51	62.13%
60-85	9	81.65	0.914	0.0100	91.440	173.09	1.776	177.61	95.79	1.807	13.332	1277.09	61.51	61.51%
60-85	10	81.65	0.559	0.0100	55.880	137.53	1.411	141.12	94.91	1.449	13.154	1248.48	61.51	61.51%

Weld No.	Droplet No.	WFS_{DAQ} (mm/s)	Δx (mm)	t_{EN} (s)	$\Delta x/t_{EN}$ (mm/s)	MR (mm/s)	V_d (mm^3)	V_D (mm^3/s)	I_{EN} (A)	BR (mm/(s A))	L_{AVG} (mm)	F_L (mm A)	f (Hz)	%EN (%)
60-85	AVG	81.65	0.592	0.0100	58.946	140.60	1.448	144.27	95.36	1.474	13.171	1255.96	61.51	61.76%
60-85	STDEV	0.00	0.146	0.0001	14.640	14.64	0.149	15.02	0.29	0.152	0.073	8.82	0.00	0.32%
90-85	1	81.83	0.508	0.0130	39.077	120.91	1.613	124.07	95.21	1.270	13.129	1250.01	51.00	66.30%
90-85	2	81.83	0.610	0.0130	46.892	128.73	1.717	132.08	94.90	1.356	13.180	1250.76	51.00	66.30%
90-85	3	81.83	0.559	0.0130	42.985	124.82	1.665	128.07	94.96	1.314	13.154	1249.14	51.00	66.30%
90-85	4	81.83	0.356	0.0130	27.354	109.19	1.456	112.04	95.28	1.146	13.053	1243.67	51.00	66.30%
90-85	5	81.83	0.508	0.0131	38.779	120.61	1.621	123.76	94.94	1.270	13.129	1246.47	51.00	66.81%
90-85	6	81.83	0.483	0.0131	36.840	118.67	1.595	121.77	94.97	1.250	13.116	1245.66	51.00	66.81%
90-85	7	81.83	0.559	0.0130	42.985	124.82	1.665	128.07	95.15	1.312	13.154	1251.64	51.00	66.30%
90-85	8	81.83	0.584	0.0129	45.287	127.12	1.683	130.44	94.80	1.341	13.167	1248.24	51.00	65.79%
90-85	9	81.83	0.610	0.0128	47.625	129.46	1.700	132.84	94.95	1.363	13.180	1251.42	51.00	65.28%
90-85	10	81.83	0.508	0.0129	39.380	121.21	1.604	124.38	95.56	1.268	13.129	1254.61	51.00	65.79%
90-85	AVG	81.83	0.528	0.0130	40.703	122.54	1.632	125.73	95.07	1.289	13.139	1249.17	51.00	66.20%
90-85	STDEV	0.00	0.076	0.0001	5.952	5.95	0.075	6.11	0.23	0.064	0.038	3.24	0.00	0.47%
120-85	1	81.96	0.660	0.0160	41.275	123.24	2.023	126.45	94.92	1.298	13.205	1253.44	43.99	70.38%
120-85	2	81.96	0.483	0.0158	30.544	112.51	1.824	115.44	95.11	1.183	13.116	1247.49	43.99	69.50%
120-85	3	81.96	0.457	0.0159	28.755	110.72	1.806	113.60	94.93	1.166	13.104	1243.92	43.99	69.94%
120-85	4	81.96	0.508	0.0158	32.152	114.11	1.850	117.09	94.98	1.201	13.129	1246.99	43.99	69.50%
120-85	5	81.96	0.305	0.0160	19.050	101.01	1.658	103.65	95.23	1.061	13.027	1240.60	43.99	70.38%
120-85	6	81.96	0.432	0.0158	27.329	109.29	1.772	112.14	95.32	1.147	13.091	1247.82	43.99	69.50%
120-85	7	81.96	0.508	0.0160	31.750	113.71	1.867	116.68	94.91	1.198	13.129	1246.07	43.99	70.38%
120-85	8	81.96	0.457	0.0160	28.575	110.54	1.815	113.42	94.87	1.165	13.104	1243.14	43.99	70.38%
120-85	9	81.96	0.508	0.0158	32.152	114.11	1.850	117.09	95.36	1.197	13.129	1251.98	43.99	69.50%
120-85	10	81.96	0.457	0.0160	28.575	110.54	1.815	113.42	94.88	1.165	13.104	1243.27	43.99	70.38%
120-85	AVG	81.96	0.478	0.0159	30.014	111.98	1.828	114.90	95.05	1.178	13.114	1246.48	43.99	69.99%
120-85	STDEV	0.00	0.088	0.0001	5.501	5.50	0.090	5.64	0.19	0.059	0.044	4.01	0.00	0.44%
150-85	1	81.25	0.584	0.0189	30.910	112.16	2.175	115.09	94.91	1.182	13.167	1249.69	38.90	73.52%
150-85	2	81.25	0.813	0.0189	43.005	124.26	2.410	127.50	95.31	1.304	13.281	1265.85	38.90	73.52%
150-85	3	81.25	0.406	0.0189	21.503	102.75	1.993	105.43	94.99	1.082	13.078	1242.30	38.90	73.52%

Weld No.	Droplet No.	WFS_{DAQ} (mm/s)	Δx (mm)	t_{EN} (s)	$\Delta x/t_{EN}$ (mm/s)	MR (mm/s)	V_d (mm^3)	V_D (mm^3/s)	I_{EN} (A)	BR (mm/(s A))	L_{AVG} (mm)	F_L (mm A)	f (Hz)	%EN (%)
150-85	4	81.25	0.483	0.0190	25.400	106.65	2.079	109.43	94.95	1.123	13.116	1245.39	38.90	73.91%
150-85	5	81.25	0.533	0.0190	28.074	109.32	2.131	112.18	94.80	1.153	13.142	1245.83	38.90	73.91%
150-85	6	81.25	0.533	0.0189	28.222	109.47	2.123	112.33	94.74	1.156	13.142	1245.04	38.90	73.52%
150-85	7	81.25	0.406	0.0189	21.503	102.75	1.993	105.43	95.00	1.082	13.078	1242.43	38.90	73.52%
150-85	8	81.25	0.660	0.0189	34.942	116.19	2.253	119.22	94.92	1.224	13.205	1253.44	38.90	73.52%
150-85	9	81.25	0.533	0.0190	28.074	109.32	2.131	112.18	94.84	1.153	13.142	1246.36	38.90	73.91%
150-85	10	81.25	0.508	0.0190	26.737	107.99	2.105	110.80	94.60	1.142	13.129	1242.00	38.90	73.91%
150-85	AVG	81.25	0.546	0.0189	28.833	110.08	2.139	112.95	94.91	1.160	13.148	1247.83	38.90	73.68%
150-85	STDEV	0.00	0.120	0.0001	6.391	6.39	0.123	6.56	0.19	0.066	0.060	7.25	0.00	0.20%
0-106	1	102.24	0.229	0.0031	73.742	175.98	0.560	180.57	114.84	1.532	12.989	1491.69	91.04	28.22%
0-106	2	102.24	0.254	0.0032	79.375	181.61	0.596	186.35	106.43	1.706	13.002	1383.80	91.04	29.13%
0-106	3	102.24	0.229	0.0032	71.437	173.68	0.570	178.21	110.88	1.566	12.989	1440.25	91.04	29.13%
0-106	4	102.24	0.178	0.0032	55.563	157.80	0.518	161.92	110.88	1.423	12.964	1437.44	91.04	29.13%
0-106	5	102.24	0.279	0.0032	87.313	189.55	0.622	194.50	109.53	1.731	13.015	1425.50	91.04	29.13%
0-106	6	102.24	0.203	0.0032	63.500	165.74	0.544	170.06	111.78	1.483	12.977	1450.52	91.04	29.13%
0-106	7	102.24	0.127	0.0032	39.688	141.93	0.466	145.63	110.76	1.281	12.939	1433.07	92.04	29.45%
0-106	8	102.24	0.051	0.0032	15.875	118.12	0.388	121.20	111.22	1.062	12.900	1434.78	93.04	29.77%
0-106	9	102.24	0.254	0.0032	79.375	181.61	0.596	186.35	111.89	1.623	13.002	1454.79	91.04	29.13%
0-106	10	102.24	0.381	0.0032	119.063	221.30	0.727	227.07	107.89	2.051	13.066	1409.64	91.04	29.13%
0-106	AVG	102.24	0.218	0.0032	68.476	170.72	0.559	175.17	110.61	1.546	12.984	1436.18	91.34	29.14%
0-106	STDEV	0.00	0.089	0.0000	27.839	27.84	0.091	28.56	2.30	0.268	0.044	28.33	0.67	0.39%
30-106	1	102.24	0.737	0.0062	118.806	221.05	1.406	226.81	112.90	1.958	13.243	1495.17	74.98	46.49%
30-106	2	102.24	0.635	0.0061	104.098	206.34	1.291	211.72	112.90	1.828	13.193	1489.43	74.98	45.74%
30-106	3	102.24	0.660	0.0061	108.262	210.50	1.318	215.99	112.90	1.864	13.205	1490.87	74.98	45.74%
30-106	4	102.24	0.737	0.0062	118.806	221.05	1.406	226.81	112.90	1.958	13.243	1495.17	74.98	46.49%
30-106	5	102.24	0.635	0.0062	102.419	204.66	1.302	210.00	112.90	1.813	13.193	1489.43	74.98	46.49%
30-106	6	102.24	0.711	0.0062	114.710	216.95	1.380	222.61	112.90	1.922	13.231	1493.73	74.98	46.49%
30-106	7	102.24	0.864	0.0062	139.290	241.53	1.537	247.83	112.90	2.139	13.307	1502.34	75.98	47.11%
30-106	8	102.24	0.356	0.0061	58.295	160.54	1.005	164.72	112.90	1.422	13.053	1473.66	76.98	46.96%

Weld No.	Droplet No.	WFS_{DAQ} (mm/s)	Δx (mm)	t_{EN} (s)	$\Delta x/t_{EN}$ (mm/s)	MR (mm/s)	V_d (mm^3)	V_D (mm^3/s)	I_{EN} (A)	BR (mm/(s A))	L_{AVG} (mm)	F_L (mm A)	f (Hz)	%EN (%)
30-106	9	102.24	0.533	0.0062	86.032	188.27	1.198	193.18	112.90	1.668	13.142	1483.70	74.98	46.49%
30-106	10	102.24	0.635	0.0063	100.794	203.03	1.312	208.33	112.90	1.798	13.193	1489.43	74.98	47.24%
30-106	AVG	102.24	0.650	0.0062	105.217	207.46	1.316	212.87	112.90	1.837	13.200	1490.29	75.28	46.52%
30-106	STDEV	0.00	0.136	0.0001	21.674	21.67	0.142	22.24	0.00	0.192	0.068	7.65	0.67	0.50%
60-106	1	102.24	0.584	0.0093	62.817	165.06	1.575	169.36	115.19	1.433	13.167	1516.72	60.99	56.72%
60-106	2	102.24	0.660	0.0092	71.783	174.02	1.643	178.56	115.19	1.511	13.205	1521.11	60.99	56.11%
60-106	3	102.24	0.787	0.0091	86.527	188.77	1.763	193.69	115.19	1.639	13.269	1528.42	60.99	55.50%
60-106	4	102.24	0.864	0.0091	94.901	197.14	1.841	202.28	115.19	1.711	13.307	1532.81	60.99	55.50%
60-106	5	102.24	0.711	0.0092	77.304	179.54	1.695	184.23	115.19	1.559	13.231	1524.03	60.99	56.11%
60-106	6	102.24	0.711	0.0092	77.304	179.54	1.695	184.23	115.19	1.559	13.231	1524.03	60.99	56.11%
60-106	7	102.24	0.584	0.0091	64.198	166.44	1.554	170.78	115.19	1.445	13.167	1516.72	60.99	55.50%
60-106	8	102.24	0.940	0.0092	102.152	204.39	1.929	209.72	115.19	1.774	13.345	1537.20	60.99	56.11%
60-106	9	102.24	0.838	0.0091	92.110	194.35	1.815	199.42	115.19	1.687	13.294	1531.35	60.99	55.50%
60-106	10	102.24	0.686	0.0090	76.200	178.44	1.648	183.09	115.19	1.549	13.218	1522.57	60.99	54.89%
60-106	AVG	102.24	0.737	0.0092	80.503	182.74	1.716	187.51	115.19	1.587	13.243	1525.50	60.99	55.81%
60-106	STDEV	0.00	0.119	0.0001	13.084	13.08	0.120	13.43	0.00	0.114	0.059	6.83	0.00	0.52%
90-106	1	102.24	0.864	0.0120	71.967	174.21	2.145	178.75	115.64	1.506	13.307	1538.80	51.00	61.20%
90-106	2	102.24	0.737	0.0121	60.876	163.12	2.025	167.37	115.64	1.411	13.243	1531.46	51.00	61.71%
90-106	3	102.24	0.889	0.0121	73.471	175.71	2.182	180.29	115.64	1.519	13.320	1540.27	51.00	61.71%
90-106	4	102.24	0.635	0.0122	52.049	154.29	1.931	158.31	115.64	1.334	13.193	1525.58	51.00	62.22%
90-106	5	102.24	0.940	0.0121	77.669	179.91	2.234	184.60	115.64	1.556	13.345	1543.20	51.00	61.71%
90-106	6	102.24	0.762	0.0120	63.500	165.74	2.041	170.06	115.64	1.433	13.256	1532.92	51.00	61.20%
90-106	7	102.24	0.737	0.0122	60.377	162.62	2.036	166.86	115.64	1.406	13.243	1531.46	51.00	62.22%
90-106	8	102.24	0.737	0.0121	60.876	163.12	2.025	167.37	115.64	1.411	13.243	1531.46	51.00	61.71%
90-106	9	102.24	0.813	0.0120	67.733	169.97	2.093	174.41	115.64	1.470	13.281	1535.86	51.00	61.20%
90-106	10	102.24	0.737	0.0122	60.377	162.62	2.036	166.86	115.64	1.406	13.243	1531.46	51.00	62.22%
90-106	AVG	102.24	0.785	0.0121	64.864	167.10	2.075	171.46	115.64	1.445	13.267	1534.25	51.00	61.71%
90-106	STDEV	0.00	0.091	0.0001	7.709	7.71	0.089	7.91	0.00	0.067	0.045	5.25	0.00	0.42%
120-106	1	102.24	0.914	0.0151	60.556	162.80	2.522	167.04	115.60	1.408	13.332	1541.20	42.19	63.71%

Weld No.	Droplet No.	WFS_{DAQ} (mm/s)	Δx (mm)	t_{EN} (s)	$\Delta x/t_{EN}$ (mm/s)	MR (mm/s)	V_d (mm^3)	V_D (mm^3/s)	I_{EN} (A)	BR (mm/(s A))	L_{AVG} (mm)	F_L (mm A)	f (Hz)	%EN (%)
120-106	2	102.24	1.067	0.0151	70.649	172.89	2.679	177.40	115.60	1.496	13.408	1550.01	42.19	63.71%
120-106	3	102.24	0.660	0.0151	43.735	145.97	2.262	149.78	115.60	1.263	13.205	1526.52	42.19	63.71%
120-106	4	102.24	1.168	0.0151	77.377	179.62	2.783	184.30	115.60	1.554	13.459	1555.88	42.19	63.71%
120-106	5	102.24	0.940	0.0151	62.238	164.48	2.548	168.77	115.60	1.423	13.345	1542.67	42.19	63.71%
120-106	6	102.24	0.864	0.0152	56.816	159.06	2.481	163.20	115.60	1.376	13.307	1538.27	42.19	64.13%
120-106	7	102.24	0.889	0.0152	58.487	160.73	2.507	164.92	115.60	1.390	13.320	1539.73	42.19	64.13%
120-106	8	102.24	0.940	0.0151	62.238	164.48	2.548	168.77	115.60	1.423	13.345	1542.67	42.19	63.71%
120-106	9	102.24	0.711	0.0151	47.099	149.34	2.314	153.23	115.60	1.292	13.231	1529.46	42.19	63.71%
120-106	10	102.24	0.813	0.0151	53.828	156.07	2.418	160.14	115.60	1.350	13.281	1535.33	42.19	63.71%
120-106	AVG	102.24	0.897	0.0151	59.300	161.54	2.506	165.75	115.60	1.397	13.323	1540.17	42.19	63.79%
120-106	STDEV	0.00	0.151	0.0000	10.013	10.01	0.155	10.27	0.00	0.087	0.076	8.73	0.00	0.18%
150-106	1	102.24	0.813	0.0181	44.906	147.15	2.733	150.98	115.67	1.272	13.281	1536.26	37.12	67.19%
150-106	2	102.24	0.889	0.0180	49.389	151.63	2.800	155.58	115.67	1.311	13.320	1540.67	37.12	66.82%
150-106	3	102.24	0.787	0.0181	43.503	145.74	2.707	149.54	115.67	1.260	13.269	1534.79	37.12	67.19%
150-106	4	102.24	1.041	0.0183	56.907	159.15	2.988	163.30	115.67	1.376	13.396	1549.48	37.12	67.93%
150-106	5	102.24	0.940	0.0180	52.211	154.45	2.853	158.48	115.67	1.335	13.345	1543.60	37.12	66.82%
150-106	6	102.24	0.940	0.0181	51.923	154.16	2.863	158.18	115.67	1.333	13.345	1543.60	37.12	67.19%
150-106	7	102.24	1.067	0.0181	58.939	161.18	2.993	165.38	115.67	1.393	13.408	1550.95	37.12	67.19%
150-106	8	102.24	0.914	0.0181	50.519	152.76	2.837	156.74	115.67	1.321	13.332	1542.14	37.12	67.19%
150-106	9	102.24	1.168	0.0180	64.911	167.15	3.087	171.51	115.67	1.445	13.459	1556.83	37.12	66.82%
150-106	10	102.24	1.143	0.0180	63.500	165.74	3.061	170.06	115.67	1.433	13.447	1555.36	37.12	66.82%
150-106	AVG	102.24	0.970	0.0181	53.666	155.91	2.892	159.97	115.67	1.348	13.360	1545.37	37.12	67.11%
150-106	STDEV	0.00	0.131	0.0001	7.264	7.26	0.133	7.45	0.00	0.063	0.065	7.55	0.00	0.34%
0-127	1	123.28	0.457	0.0031	147.484	270.77	0.861	277.83	135.00	2.006	13.104	1768.99	91.09	28.24%
0-127	2	123.28	0.330	0.0031	106.516	229.80	0.731	235.79	133.47	1.722	13.040	1740.46	91.09	28.24%
0-127	3	123.28	0.330	0.0031	106.516	229.80	0.731	235.79	133.53	1.721	13.040	1741.24	91.09	28.24%
0-127	4	123.28	0.279	0.0031	90.129	213.41	0.679	218.98	134.37	1.588	13.015	1748.79	91.09	28.24%
0-127	5	123.28	0.432	0.0032	134.938	258.22	0.848	264.96	131.91	1.958	13.091	1726.82	91.09	29.15%
0-127	6	123.28	0.533	0.0031	172.065	295.35	0.939	303.05	133.30	2.216	13.142	1751.79	91.09	28.24%

Weld No.	Droplet No.	WFS_{DAQ} (mm/s)	Δx (mm)	t_{EN} (s)	$\Delta x/t_{EN}$ (mm/s)	MR (mm/s)	V_d (mm^3)	V_D (mm^3/s)	I_{EN} (A)	BR (mm/(s A))	L_{AVG} (mm)	F_L (mm A)	f (Hz)	%EN (%)
0-127	7	123.28	0.559	0.0031	180.258	303.54	0.966	311.46	133.62	2.272	13.154	1757.69	91.09	28.24%
0-127	8	123.28	0.508	0.0031	163.871	287.15	0.913	294.64	133.62	2.149	13.129	1754.30	91.09	28.24%
0-127	9	123.28	0.406	0.0031	131.097	254.38	0.809	261.01	133.62	1.904	13.078	1747.51	91.09	28.24%
0-127	AVG	123.28	0.426	0.0031	136.979	260.26	0.831	267.05	133.60	1.948	13.088	1748.63	91.09	28.34%
0-127	STDEV	0.00	0.098	0.0000	31.677	31.68	0.101	62.28	0.83	0.238	0.049	11.92	0.00	0.30%
30-127	1	123.49	0.787	0.0061	129.082	252.58	1.581	259.16	133.30	1.895	13.269	1768.72	71.83	43.82%
30-127	2	123.49	0.813	0.0060	135.467	258.96	1.594	265.72	133.30	1.943	13.281	1770.41	71.83	43.10%
30-127	3	123.49	0.584	0.0061	95.770	219.27	1.372	224.98	133.30	1.645	13.167	1755.17	71.83	43.82%
30-127	4	123.49	0.533	0.0061	87.443	210.94	1.320	216.44	133.30	1.582	13.142	1751.79	71.83	43.82%
30-127	5	123.49	0.864	0.0062	139.290	262.79	1.672	269.64	133.30	1.971	13.307	1773.80	71.83	44.53%
30-127	6	123.49	0.787	0.0061	129.082	252.58	1.581	259.16	133.30	1.895	13.269	1768.72	71.83	43.82%
30-127	7	123.49	0.787	0.0062	127.000	250.49	1.594	257.03	133.30	1.879	13.269	1768.72	71.83	44.53%
30-127	8	123.49	0.864	0.0062	139.290	262.79	1.672	269.64	133.30	1.971	13.307	1773.80	71.83	44.53%
30-127	9	123.49	0.813	0.0061	133.246	256.74	1.607	263.44	133.30	1.926	13.281	1770.41	71.83	43.82%
30-127	10	123.49	0.711	0.0061	116.590	240.08	1.503	246.35	133.30	1.801	13.231	1763.64	71.83	43.82%
30-127	AVG	123.49	0.754	0.0061	123.265	246.76	1.550	253.20	133.30	1.851	13.252	1766.52	71.83	43.96%
30-127	STDEV	0.00	0.112	0.0001	18.035	18.04	0.118	18.51	0.00	0.135	0.056	7.49	0.00	0.45%
60-127	1	123.55	0.762	0.0091	83.736	207.29	1.936	212.70	132.00	1.570	13.256	1749.79	58.06	52.83%
60-127	2	123.55	0.889	0.0090	98.778	222.33	2.053	228.13	132.00	1.684	13.320	1758.17	58.06	52.25%
60-127	3	123.55	0.762	0.0090	84.667	208.22	1.923	213.65	132.00	1.577	13.256	1749.79	58.06	52.25%
60-127	4	123.55	0.762	0.0092	82.826	206.38	1.948	211.76	132.00	1.563	13.256	1749.79	58.06	53.42%
60-127	5	123.55	1.016	0.0092	110.435	233.99	2.209	240.09	132.00	1.773	13.383	1766.56	58.06	53.42%
60-127	6	123.55	0.813	0.0091	89.319	212.87	1.988	218.43	132.00	1.613	13.281	1753.14	58.06	52.83%
60-127	7	123.55	0.737	0.0091	80.945	204.50	1.909	209.83	132.00	1.549	13.243	1748.12	58.06	52.83%
60-127	8	123.55	0.914	0.0091	100.484	224.04	2.092	229.88	132.00	1.697	13.332	1759.85	58.06	52.83%
60-127	9	123.55	0.610	0.0091	66.989	190.54	1.779	195.51	132.00	1.444	13.180	1739.73	58.06	52.83%
60-127	10	123.55	0.864	0.0091	94.901	218.46	2.040	224.15	132.00	1.655	13.307	1756.50	58.06	52.83%
60-127	AVG	123.55	0.813	0.0091	89.319	212.87	1.988	218.43	132.00	1.613	13.281	1753.14	58.06	52.83%
60-127	STDEV	0.00	0.113	0.0001	12.270	12.27	0.118	12.59	0.00	0.093	0.056	7.46	0.00	0.39%

Weld No.	Droplet No.	WFS_{DAQ} (mm/s)	Δx (mm)	t_{EN} (s)	$\Delta x/t_{EN}$ (mm/s)	MR (mm/s)	V_d (mm^3)	V_D (mm^3/s)	I_{EN} (A)	BR (mm/(s A))	L_{AVG} (mm)	F_L (mm A)	f (Hz)	%EN (%)
90-127	1	123.31	0.864	0.0120	71.967	195.28	2.404	200.37	131.37	1.486	13.307	1748.11	49.68	59.62%
90-127	2	123.31	0.864	0.0121	71.372	194.68	2.417	199.76	131.37	1.482	13.307	1748.11	49.68	60.11%
90-127	3	123.31	0.991	0.0120	82.550	205.86	2.535	211.23	131.37	1.567	13.370	1756.46	49.68	59.62%
90-127	4	123.31	1.041	0.0121	86.066	209.38	2.600	214.84	131.37	1.594	13.396	1759.79	49.68	60.11%
90-127	5	123.31	0.965	0.0121	79.769	203.08	2.521	208.38	131.37	1.546	13.358	1754.79	49.68	60.11%
90-127	6	123.31	0.889	0.0121	73.471	196.78	2.443	201.92	131.37	1.498	13.320	1749.78	49.68	60.11%
90-127	7	123.31	0.965	0.0120	80.433	203.75	2.509	209.06	131.37	1.551	13.358	1754.79	49.68	59.62%
90-127	8	123.31	0.533	0.0121	44.083	167.40	2.078	171.76	131.37	1.274	13.142	1726.43	49.68	60.11%
90-127	9	123.31	0.864	0.0121	71.372	194.68	2.417	199.76	131.37	1.482	13.307	1748.11	49.68	60.11%
90-127	10	123.31	1.168	0.0122	95.770	219.08	2.743	224.80	131.37	1.668	13.459	1768.14	49.68	60.61%
90-127	AVG	123.31	0.914	0.0121	75.695	199.01	2.467	204.20	131.37	1.515	13.332	1751.45	49.68	60.01%
90-127	STDEV	0.00	0.165	0.0001	13.549	13.55	0.171	13.90	0.00	0.103	0.083	10.84	0.00	0.31%
120-127	1	123.21	0.965	0.0150	64.347	187.55	2.887	192.45	131.88	1.422	13.358	1761.60	43.60	65.40%
120-127	2	123.21	0.457	0.0151	30.278	153.49	2.378	157.49	131.88	1.164	13.104	1728.10	44.60	67.35%
120-127	3	123.21	0.305	0.0149	20.456	143.67	2.196	147.41	131.88	1.089	13.027	1718.05	45.60	67.94%
120-127	4	123.21	0.533	0.0150	35.560	158.77	2.444	162.91	131.88	1.204	13.142	1733.13	43.60	65.40%
120-127	5	123.21	0.508	0.0149	34.094	157.30	2.405	161.40	131.88	1.193	13.129	1731.45	43.60	64.96%
120-127	AVG	123.21	0.554	0.0150	36.964	160.17	2.462	164.35	131.88	1.214	13.152	1734.47	44.20	66.21%
120-127	STDEV	0.00	0.247	0.0001	16.411	16.41	0.256	16.84	0.00	0.124	0.123	16.26	0.89	1.34%
150-127	1	123.94	0.686	0.0181	37.890	161.83	3.006	166.05	131.63	1.229	13.218	1739.87	38.06	68.89%
150-127	2	123.94	0.305	0.0181	16.840	140.78	2.615	144.45	131.63	1.070	13.027	1714.80	39.06	70.70%
150-127	3	123.94	1.346	0.0180	74.789	198.73	3.670	203.91	131.63	1.510	13.548	1783.34	40.06	72.11%
150-127	4	123.94	0.813	0.0181	44.906	168.85	3.136	173.25	131.63	1.283	13.281	1748.23	38.06	68.89%
150-127	5	123.94	0.737	0.0181	40.696	164.64	3.058	168.93	131.63	1.251	13.243	1743.22	38.06	68.89%
150-127	AVG	123.94	0.777	0.0181	42.989	166.93	3.097	171.29	131.63	1.268	13.264	1745.89	38.66	69.89%
150-127	STDEV	0.00	0.374	0.0000	20.796	20.80	0.378	21.34	0.00	0.158	0.187	24.59	0.89	1.46%

Weld No.	Droplet No.	WFS_{DAQ} (mm/s)	Δx (mm)	t_p or t_b (s)	$\Delta x/t_p$ or $\Delta x/t_b$ (mm/s)	MR (mm/s)	V_d (mm^3)	V_D (mm^3/s)	I_b or I_p (A)	BR (mm/(s A))	L_{AVG} (mm)	F_L (mm A)	f (Hz)	%p or %b (%)
B-0-42	1	39.09	-0.136	0.01674	-8.1	30.96	0.532	31.77	25.19	1.229	12.807	322.61	41.75	69.87%
B-0-42	2	39.09	-0.397	0.01647	-24.1	14.98	0.253	15.37	25.19	0.595	12.677	319.32	41.75	68.75%
B-0-42	3	39.09	-0.349	0.01566	-22.3	16.80	0.270	17.24	25.19	0.667	12.701	319.93	41.75	65.36%
B-0-42	4	39.09	-0.329	0.00756	-43.5	-4.44	-0.034	-4.55	25.19	-0.176	12.711	320.18	41.75	31.56%
B-0-42	5	39.09	-0.329	0.00675	-48.8	-9.66	-0.067	-9.91	25.19	-0.384	12.711	320.18	41.75	28.17%
B-0-42	6	39.09	-0.310	0.00675	-45.9	-6.85	-0.047	-7.03	25.19	-0.272	12.720	320.42	41.75	28.17%
B-0-42	7	39.09	-0.145	0.01566	-9.3	29.83	0.479	30.61	25.19	1.184	12.803	322.49	41.75	65.36%
B-0-42	8	39.09	-0.242	0.00621	-39.0	0.11	0.001	0.11	25.19	0.004	12.754	321.27	41.75	25.92%
B-0-42	9	39.09	-0.184	0.01755	-10.5	28.60	29.350	29.35	25.19	1.136	12.783	322.00	41.75	73.25%
B-0-42	10	39.09	-0.310	0.00999	-31.0	8.05	8.262	8.26	25.19	0.320	12.720	320.42	41.75	41.70%
B-0-42	AVG	39.09	-0.273	0.01193	-22.9	16.20	0.20	16.62	25.19	0.430	12.738	320.88	41.75	49.81%
B-0-42	STDEV	0.00	0.091	0.00486	15.7	15.72	9.299	16.13	0.00	0.624	0.045	1.14	0.00	20.28%
P-0-42	1	39.09	0.378	0.00216	175.0	214.13	0.474	219.72	362.08	0.591	13.064	4730.21	41.75	9.02%
P-0-42	2	39.09	0.882	0.00162	544.6	583.67	0.970	598.89	362.08	1.612	13.316	4821.46	41.75	6.76%
P-0-42	3	39.09	0.242	0.00189	128.1	167.16	0.324	171.52	362.08	0.462	12.996	4705.59	41.75	7.89%
P-0-42	4	39.09	0.755	0.00135	559.4	598.49	0.829	614.10	362.08	1.653	13.253	4798.47	41.75	5.63%
P-0-42	5	39.09	0.649	0.00189	343.5	382.56	0.742	392.54	362.08	1.057	13.200	4779.27	41.75	7.89%
P-0-42	6	39.09	0.504	0.00135	373.4	412.52	0.571	423.28	362.08	1.139	13.127	4753.02	41.75	5.63%
P-0-42	7	39.09	0.126	0.00135	93.4	132.45	0.183	135.90	362.08	0.366	12.938	4684.59	41.75	5.63%
P-0-42	8	39.09	0.562	0.00216	260.2	299.34	0.663	307.15	362.08	0.827	13.156	4763.52	41.75	9.02%
P-0-42	9	39.09	0.494	0.00162	305.0	344.10	353.079	353.08	362.08	0.950	13.122	4751.21	41.75	6.76%
P-0-42	10	39.09	0.406	0.00108	376.0	415.11	425.936	425.94	362.08	1.146	13.078	4735.28	41.75	4.51%
P-0-42	AVG	39.09	0.500	0.00165	303.5	342.63	0.58	351.56	362.08	0.980	13.125	4752.26	41.75	6.87%
P-0-42	STDEV	0.00	0.228	0.00037	158.9	158.86	164.877	163.00	0.00	0.439	0.114	41.25	0.00	1.54%
B-90-42	1	38.94	-0.040	0.00108	-37.0	1.90	0.002	1.95	24.81	0.076	12.855	318.93	39.51	4.27%
B-90-42	2	38.94	-0.049	0.00162	-30.3	8.69	0.014	8.91	24.81	0.350	12.851	318.82	39.51	6.40%
B-90-42	3	38.94	-0.098	0.00243	-40.3	-1.40	-0.003	-1.43	24.81	-0.056	12.826	318.21	39.51	9.60%
B-90-42	4	38.94	-0.039	0.00135	-28.9	10.05	0.014	10.31	24.81	0.405	12.856	318.94	39.51	5.33%

Weld No.	Droplet No.	WFS_{DAQ} (mm/s)	Δx (mm)	t_p or t_b (s)	$\Delta x/t_p$ or $\Delta x/t_b$ (mm/s)	MR (mm/s)	V_d (mm^3)	V_D (mm^3/s)	I_b or I_p (A)	BR (mm/(s A))	L_{AVG} (mm)	F_L (mm A)	f (Hz)	%p or %b (%)
B-90-42	5	38.94	-0.059	0.00108	-54.6	-15.70	-0.017	-16.11	24.81	-0.633	12.846	318.70	39.51	4.27%
B-90-42	AVG	38.94	-0.057	0.00151	-37.7	1.23	0.002	1.27	24.81	0.028	12.847	318.72	39.51	5.97%
B-90-42	STDEV	0.00	0.024	0.00056	10.3	10.32	0.013	10.59	0.00	0.416	0.012	0.30	0.00	2.21%
P-90-42	1	38.94	0.315	0.00297	106.1	145.03	0.442	148.81	365.32	0.397	13.033	4761.03	39.51	11.73%
P-90-42	2	38.94	0.315	0.00297	106.1	145.03	0.442	148.81	365.32	0.397	13.033	4761.03	39.51	11.73%
P-90-42	3	38.94	0.758	0.00297	255.3	294.22	0.896	301.90	365.32	0.805	13.254	4841.95	39.51	11.73%
P-90-42	4	38.94	0.385	0.00297	129.7	168.60	0.514	173.00	365.32	0.462	13.068	4773.82	39.51	11.73%
P-90-42	5	38.94	0.345	0.00297	116.2	155.13	0.473	159.18	365.32	0.425	13.048	4766.51	39.51	11.73%
P-90-42	AVG	38.94	0.424	0.00297	142.7	181.60	0.553	186.34	365.32	0.497	13.087	4780.87	39.51	11.73%
P-90-42	STDEV	0.00	0.189	0.00000	63.7	63.70	0.194	65.36	0.00	0.174	0.095	34.55	0.00	0.00%
P-150-42	1	38.84	0.346	0.00216	160.2	199.07	0.441	204.26	365.39	0.545	13.048	4767.61	34.72	7.50%
P-150-42	2	38.84	0.317	0.00135	234.9	273.71	0.379	280.85	365.39	0.749	13.034	4762.31	34.72	4.69%
P-150-42	3	38.84	0.231	0.00162	142.6	181.47	0.302	186.20	365.39	0.497	12.991	4746.60	34.72	5.62%
P-150-42	4	38.84	0.019	0.00189	10.1	48.90	0.095	50.17	365.39	0.134	12.885	4707.87	34.72	6.56%
P-150-42	5	38.84	0.009	0.00432	2.1	40.92	0.181	41.99	365.39	0.112	12.880	4706.04	34.72	15.00%
P-150-42	AVG	38.84	0.184	0.00227	81.3	120.17	0.28	123.30	365.39	0.407	12.967	4738.09	34.72	7.87%
P-150-42	STDEV	0.00	0.161	0.00119	101.0	101.01	0.142	103.65	0.00	0.276	0.081	29.46	0.00	4.12%
B-0-127	1	123.28	-0.125	0.00081	-154.4	-31.08	-0.026	-31.89	46.46	-0.669	12.813	595.27	91.09	7.38%
B-0-127	2	123.28	-0.077	0.00081	-95.1	28.20	0.023	28.93	46.46	0.607	12.837	596.38	91.09	7.38%
B-0-127	3	123.28	-0.144	0.00108	-133.4	-10.08	-0.011	-10.35	46.46	-0.217	12.803	594.83	91.09	9.84%
B-0-127	4	123.28	-0.105	0.00081	-129.7	-6.38	-0.005	-6.54	46.46	-0.137	12.823	595.73	91.09	7.38%
B-0-127	5	123.28	-0.125	0.00108	-115.8	7.51	0.008	7.71	46.46	0.162	12.813	595.27	91.09	9.84%
B-0-127	AVG	123.28	-0.115	0.00092	-125.5	-2.24	0.00	-2.30	46.46	-0.051	12.817	595.50	91.09	8.36%
B-0-127	STDEV	0.00	0.025	0.00015	22.0	21.98	0.019	22.55	0.00	0.473	0.013	0.59	0.00	1.35%
P-0-127	1	123.28	0.010	0.00540	1.9	125.14	0.693	128.40	373.14	0.335	12.880	4806.04	91.09	49.18%
P-0-127	2	123.28	-0.058	0.00486	-11.9	111.35	0.555	114.25	373.14	0.298	12.846	4793.36	91.09	44.26%
P-0-127	3	123.28	-0.260	0.00567	-45.9	77.42	0.450	79.44	373.14	0.207	12.745	4755.67	91.09	51.64%
P-0-127	4	123.28	-0.211	0.00540	-39.1	84.20	0.466	86.40	373.14	0.226	12.770	4764.81	91.09	49.18%

Weld No.	Droplet No.	WFS_{DAQ} (mm/s)	Δx (mm)	t_p or t_b (s)	$\Delta x/t_p$ or $\Delta x/t_b$ (mm/s)	MR (mm/s)	V_d (mm^3)	V_D (mm^3/s)	I_b or I_p (A)	BR (mm/(s A))	L_{AVG} (mm)	F_L (mm A)	f (Hz)	%p or %b (%)
P-0-127	AVG	123.28	-0.130	0.00533	-24.3	98.95	0.54	101.53	373.14	0.267	12.810	4779.97	91.09	48.56%
P-0-127	STDEV	0.00	0.127	0.00034	22.5	22.50	0.111	23.09	0.00	0.060	0.063	23.66	0.00	3.09%
B-90-127	1	123.31	-0.188	0.00189	-99.5	23.82	0.046	24.44	46.12	0.516	12.781	589.46	49.68	9.39%
B-90-127	2	123.31	-0.099	0.00108	-91.7	31.62	0.035	32.45	46.12	0.686	12.826	591.51	49.68	5.36%
B-90-127	3	123.31	-0.227	0.00135	-168.2	-44.88	-0.062	-46.05	46.12	-0.973	12.762	588.56	49.68	6.71%
B-90-127	4	123.31	-0.188	0.00162	-116.1	7.23	0.012	7.42	46.12	0.157	12.781	589.46	49.68	8.05%
B-90-127	5	123.31	-0.404	0.00189	-213.8	-90.50	-0.175	-92.86	46.12	-1.962	12.673	584.48	49.68	9.39%
B-90-127	AVG	123.31	-0.221	0.00157	-141.3	-17.97	-0.029	-18.44	46.12	-0.315	12.764	588.69	49.68	7.78%
B-90-127	STDEV	0.00	0.112	0.00035	51.9	51.88	0.092	53.23	0.00	1.125	0.056	2.59	0.00	1.75%
P-90-127	1	123.31	-0.631	0.00405	-155.8	-32.53	-0.135	-33.38	381.48	-0.085	12.560	4791.20	49.68	20.12%
P-90-127	2	123.31	-0.591	0.00432	-136.8	-13.53	-0.060	-13.88	381.48	-0.035	12.580	4798.83	49.68	21.46%
P-90-127	3	123.31	-0.572	0.00486	-117.7	5.59	0.028	5.73	381.48	0.015	12.589	4802.45	49.68	24.14%
P-90-127	4	123.31	-0.523	0.00432	-121.1	2.22	0.010	2.28	381.48	0.006	12.614	4811.80	49.68	21.46%
P-90-127	5	123.31	-0.463	0.00459	-100.9	22.42	0.106	23.00	381.48	0.059	12.644	4823.24	49.68	22.80%
P-90-127	AVG	123.31	-0.556	0.00443	-125.6	-2.28	-0.010	-2.34	381.48	-0.008	12.597	4805.50	49.68	21.99%
P-90-127	STDEV	0.00	0.065	0.00031	20.8	20.79	0.091	21.34	0.00	0.055	0.032	12.38	0.00	1.53%
P-150-127	1	123.94	-0.451	0.00351	-128.5	-4.58	-0.016	-4.70	382.26	-0.012	12.650	4835.40	38.20	13.40%
P-150-127	2	123.94	-0.855	0.00567	-150.8	-26.89	-0.156	-27.59	382.26	-0.070	12.448	4758.18	38.20	21.65%
P-150-127	3	123.94	-0.605	0.00540	-112.1	11.88	0.066	12.19	382.26	0.031	12.573	4805.96	38.20	20.62%
P-150-127	4	123.94	-0.557	0.00405	-137.6	-13.62	-0.057	-13.98	382.26	-0.036	12.597	4815.14	38.20	15.47%
P-150-127	AVG	123.94	-0.617	0.00466	-132.5	-8.56	-0.04	-8.79	382.26	-0.022	12.567	4803.67	38.20	17.79%
P-150-127	STDEV	0.00	0.171	0.00104	16.3	16.28	0.092	16.70	0.00	0.043	0.086	32.72	0.00	3.98%